Technische Universität München
TUM School of Natural Sciences

Cryo-FIB development from unicellular to multicellular organisms - from VIPP1 to *copia*

Sven Dominik Klumpe

Vollständiger Abdruck der von der TUM School of Natural Sciences der Technischen Universität München zur Erlangung eines

Doktors der Naturwissenschaften (Dr. rer. nat.)

genehmigten Dissertation.

Vorsitz: Prof. Dr. Michael Sattler

Prüfende der Dissertation:

1. Hon.-Prof. Dr. Wolfgang Baumeister
2. Prof. Dr. Martin Beck
3. Prof. Dr. Jürgen Plitzko

Die Dissertation wurde am 21.12.2023 bei der Technischen Universität München eingereicht und durch die TUM School of Natural Sciences am 28.02.2024 angenommen.

Abstract

"Insights must precede application" (Max Planck, translated), but to gain insights, the appropriate methods have to be in place. The thesis at hand covers the technological advancements of cryo-focused ion beam (cryo-FIB) milling for visual proteomics by cryo-electron tomography (cryo-ET) and their applications to unicellular and multicellular organisms and tissues, with the aim of exploring cellular ultrastructure at the molecular level. In addressing the specific challenges in the field, techniques and tools for automating cryo-FIB milling procedures, improving the throughput of existing workflows, and expanding the range of accessible samples by cryo-lift-out are presented.

SerialFIB, a modular and versatile software package for automating various cryo-FIB workflows, is introduced, followed by a demonstration of its practical use on a wide range of biological samples. This is followed by novel approaches, such as the use of machine learning for the fully automated selection of suitable lamella positions, especially for on-grid lamella milling. The application of the developed methods for cryo-ET to unicellular samples is then showcased in a collaborative study investigating VIPP1, a protein that is conserved throughout the green lineage, shedding light on the biogenesis of the thylakoid membrane in *Synechocystis* PCC 6803 cyanobacteria and *C. reinhardtii* algae.

As part of an effort to increase the number of samples amenable to cryo-ET, a major part of this thesis focuses on improving cryo-lift-out for the routine characterization of multicellular organisms. The first step in these developments was the ability to transfer and securely attach lamellae using a redeposition approach, eliminating the use of the gas injection system during the cryo-lift-out transfer step. A technical advance that enabled quasi-sequential focused ion beam milling in cryo-lift-out, a technique termed Serial Lift-Out. Yet, the preparation of specific biological structures from bulk HPF material requires a targeted selection by either fluorescence light microscope (FLM) or cryo-FIB-scanning electron microscopy (SEM) volume imaging. Methods to achieve such targeted preparation in cryo-lift-out are presented.

In an effort to demonstrate the application of these workflows to specific biological questions, FLM or SEM-guided cryo-lift-out, cryo-ET, and complementary techniques are used to describe the life cycle of the *copia* retrotransposon. The culmination of these techniques reveals the in-cell structure and *in situ* snapshots of *copia* retrotransposon capsids in intact *D. melanogaster* egg chambers. It further allows for describing the ultrastructural differences between the nuclear envelopes of somatic and germ-line cells of the *D. melanogaster* egg chambers.

In conclusion, ongoing developments in cryo-FIB sample preparation, efforts to expand the SerialFIB platform, and the potential impact on future structural studies is discussed. An outlook is given on how these novel methods may enable the study of biological processes *in situ*, such as the mode of action of VIPP1 or the interaction of capsids of retroviruses and retroelements with other macromolecular complexes such as the nuclear pore complex.

Zusammenfassung

„Dem Anwenden muss das Erkennen vorausgehen“ (Max Planck), doch zum Erkennen braucht es die passende Methodik. Die vorliegende Arbeit behandelt sowohl die Weiterentwicklungen der Technologie fokussierter Ionenstrahlen (kryo-FIB) für die visuelle Proteomik mittels Kryo-Elektronentomographie (Kryo-ET) als auch ihre Anwendungen bei einzelligen und mehrzelligen Organismen oder Geweben um die zelluläre Ultrastruktur auf molekularer Ebene zu erforschen. Zur Bewältigung der Herausforderungen in diesem Bereich werden Techniken und Werkzeuge zur Automatisierung des Kryo-FIBs und optimierte Kryo-Lift-Out Verfahren vorgestellt, welche die Durchsatzleistung bestehender Arbeitsabläufe verbessern und die Vielfalt der zugänglichen Proben in der Kryo-ET erweitern.

Zunächst wird SerialFIB vorgestellt, ein modulares und vielseitiges Softwarepaket zur Automatisierung verschiedener Kryo-FIB-Arbeitsabläufe. Dem folgt eine Demonstration seiner praktischen Anwendung an einer Vielzahl biologischer Proben. Zusätzlich wird die Verwendung von maschinellem Lernen für die vollautomatische Auswahl geeigneter Lamellenpositionen auf Elektronenmikroskopiegrids vorgesetellt. Als Anwendungsbeispiel dient VIPP1, ein konserviertes Protein in Chloroplastida, das an der Biogenese der Thylakoidmembran beteiligt ist. Diesbezüglich werden in einer kollaborativen Studie molekulare Einblicke in Cyanobakterien *Synechocystis* PCC 6803 und Algen *C. reinhardtii* gegeben.

Im Rahmen der Bemühungen, das kryo-FIB Verfahren für neue biologische Proben zu ermöglichen, konzentriert sich ein großer Teil dieser Arbeit auf die Optimierung des Kryo-Lift-Outs für die routinemäßige Charakterisierung mehrzelliger Organismen. In einem ersten Schritt werden Methoden etabliert um Lamellen mittels des Redepositionsfräsen, einer Art Schweißen mittels Ionenfräsen, zu transferieren und sicher zu befestigen. Diese Entwicklungen machen den Einsatz des Gasinjektionssystems beim Kryo-Lift-Out obsolet. Dieser technische Fortschritt ermöglicht außerdem die Produktion quasi-sequentieller Lamellen im Kryo-Lift-Out, dem "Serial Lift-Out". Dennoch erfordert die Präparation spezifischer biologischer Strukturen aus dickem, hochdruckgefrorenem Material eine zielsichere Identifizierung durch Fluoreszenzlichtmikroskopie (FLM) oder Volumenbildgebung via Kryo-FIB gekoppelt mit Rasterelektronenmikroskopie (REM). Methoden, dies zu erreichen, werden in der vorliegenden Arbeit behandelt.

Die entwickelten Methoden und ergänzende Techniken werden angewandt, um den Lebenszyklus des *copia* Retrotransposons in der Fruchtfliege *D. melanogaster* zu beschreiben. Diese Daten erlauben die Auflösung der intrazellulären Struktur und *in situ*-Momentaufnahmen von *copia* Kapsiden in intakten Eikammern von *D. melanogaster*. Außerdem werden die ultrastrukturellen Unterschiede zwischen den Zellkernen somatischer Zellen und der Keimbahn in den Eikammern beschrieben.

Abschließend werden laufende Entwicklungen in der Kryo-FIB-Probenpräparation und Bemühungen zur Erweiterung der SerialFIB-Plattform sowie deren potenzielle Auswirkungen

auf zukünftige strukturelle Studien beschrieben. Anhand von Beispielen wird ausgearbeitet, wie die vorgestellten Methoden die Erforschung biologischer Prozesse *in situ* ermöglichen könnten, z. B. im Hinblick auf die Wirkungsweise von VIPP1 oder um die Interaktion von Retrovirus- und Retroelementkapsiden mit anderen makromolekularen Komplexen wie dem Kernporenkomplex zu untersuchen.

Publications of Sven (Dominik) Klumpe

Publications presented in this thesis

Peer-reviewed publications

A Modular Platform for Streamlining Automated Cryo-FIB Workflows
Klumpe S*, Fung, HKH*, Goetz SK*, Zagoriy I, Hampoelz B, Xiaojie Z, Erdmann PS, Baumbach J, Müller CW, Beck M, Plitzko JM#, Mahamid J#
eLife 10:e70506.
DOI: 10.7554/eLife.70506
2021 December 24

Structural basis for VIPP1 oligomerization and maintenance of thylakoid membrane integrity
Gupta TK*, **Klumpe S***, Gries K*, Heinz S*, Wietrzynski W*, Ohnishi N, Niemeyer J, Spaniol B, Schaffer M, Rast A, Ostermeier M, Strauss M, Plitzko JM, Baumeister W, Rudack T, Sakamoto W, Nickelsen J, Schuller JM#, Schroda M#, and Engel BD#
Cell **184(14)**: 3643-3659
DOI: 10.1016/j.cell.2021.05.011
2021 July 8

Serial Lift-Out – Sampling Molecular Anatomy in Whole Organisms
Schioetz OS*, Kaiser CJO*, **Klumpe S***,#, Morado DR, Poege M, Schneider J, Beck F, Thompson C, Plitzko JM#
Nature Methods
Accepted manuscript.

Invited contributions and book chapters

Recent Advances in Gas Injection System-Free Cryo-FIB Lift-Out Transfer for Cryo-Electron Tomography of Multicellular Organsims and Tissues
Klumpe S#, Kuba J, Schioetz OH, Erdmann PS, Rigort A, Plitzko JM
Microscopy Today
DOI: 10.1017/S1551929521001528
2022 January 31

* equal contribution # corresponding author

Other publications

Peer-reviewed publications

Cryo-plasma FIB/SEM volume imaging of biological specimens
Dumoux M[#], Glen T, , Smith JLR, Ho EML, Perdigao LMA, Pennington A, **Klumpe S**, Yee NBY, Farmer D, Lai PYA, Bowles W, Kelley R, Plitzko JM, Wu L, Basham M, Clare DK, Siebert CA, Darrow MC, Naismith JH, Grange M[#]
eLife 12:e83623
DOI: 10.7554/eLife.83623
2023 March 8

Allosteric control of Ubp6 and the proteasome via a bidirectional switch
Hung KYS, **Klumpe S***, Eisele MR*, Elsasser S*, Tian G*, Sun S, Moroco JA, Cheng TC, Joshi T, Seibel T, Van Dalen D, Feng XH, Lu Y, Ovaa H, Engen JR, Lee BH[#], Rudack T[#], Sakata E[#], Finley D[#] *Nat Commun* 13:838
DOI: 10.1038/s41467-022-28186-y
2022 February 11

In situ Cryo-Electron Tomography Reveals Gradient Organization of Ribosome Biogenesis in Intact Nucleoli
Erdmann PS[#], Hou Z*, **Klumpe S***, Khavenekar S*, Beck, F, Wilfling F, Plitzko J, Baumeister W[#]
Nat Commun 12: 5364
DOI: 10.1038/s41467-021-25413-w
2021 September 10

Cryo-EM structure of the cetacean morbillivirus nucleoprotein-RNA complex
Zinzula L[#], Beck F, **Klumpe S**, Bohn S, Pfeifer G, Bollschweiler D, Nagy I, Plitzko JM and Baumeister W[#]
J Struct Biol 213(3): 107750
DOI: 10.1016/j.jsb.2021.107750
2021 June 3

A streamlined workflow for automated cryo focused ion beam milling
Tacke S*, Erdmann PS*, Wang Z, **Klumpe S**, Grange M, Plitzko JM[#] and Raunser S[#]
J Struct Biol 213(3): 107743
DOI: 10.1016/j.jsb.2021.107743
2021 June 21

* equal contribution [#] corresponding author

Membrane imaging in the plant endomembrane system
Liu Z*, Gao J*, Cui Y*, **Klumpe S**, Xiang Y, Erdmann PS# and Jiang L#
Plant Physiol 185(3): 562-576
DOI: 10.1093/plphys/kiaa040
2022 December 4

High-resolution structure and biophysical characterization of the nucleocapsid phosphoprotein dimerization domain from the Covid-19 severe acute respiratory syndrome coronavirus 2
Zinzula L#, Basquin J, Bohn S, Beck F, **Klumpe S**, Pfeifer G, Nagy I, Bracher A, Hartl FU and Baumeister W#
Biochem Biophys Res Commun 538: 54-62
DOI: 10.1016/j.bbrc.2020.09.131
2021 January 29

Exploring the catalytic cascade of cembranoid biosynthesis by combination of genetic engineering and molecular simulations
Schrepfer P, Ugur I, **Klumpe S**, Loll B#, Kaila VRI# and Bruck T#
Comput Struct Biotechnol J 18: 1819-1829
DOI: 10.1016/j.csbj.2020.06.030
2020 July 16

A low-cost fluorescence reader for in vitro transcription and nucleic acid detection with Cas13a
Katzmeier F*, Aufinger L*, Dupin A*, Quintero J*, Lenz M, Bauer L, **Klumpe S**, Sherpa D, Durr B, Honemann M, Styazhkin I, Simmel FC# and Heymann M#
PLoS One 14(12): e0220091
DOI: 10.1371/journal.pone.0220091
2019 Dec 18

Invited contributions and book chapters

Chapter 23 – Elektronenmikroskopie in *Bioanalytik*
Erdmann PS#, **Klumpe S**, Plitzko JM
Edited by Lottspeich F and Kurreck J
Springer Berlin
2022:553-600

* equal contribution # corresponding author

Contents

1. Introduction

Since the invention of the first compound microscopes in the 17^{th} century and the crucial work by Antonie van Leeuwenhoek that described bacteria, protozoa, and others for the first time , paving the way for advancements in biology [1], microscopy has been widely used to study biological specimen. While limited in resolution, microscopes at the time gave Robert Hooke the tools for the identification of the basic unit of life, that is, the cell. It marked the beginning of cell biology. Yet, it took 2 centuries until researchers recognized the role of the cell in the functioning of living organism. As an example of how technology development like microscopy go hand in hand with new biological discoveries, thanks to advances in microscopy, Matthias Schleiden and Theodor Schwann proposed that plants and animals are organized in cells in 1838 and 1839, respectively [2]. Since then, understanding the intricate details of how living organisms are organized at the cellular and later molecular level have not ceded to fascinate researchers. The invention of the electron microscope in the early 1930s by Ernst Ruska and Max Knoll [3] and its application to biological specimen yielded a breadth of discoveries in structural cell biology [4]. To study biological macromolecules that make about cellular ultrastructure such as proteins, however, the first methods that became available were performed on purified components using X-Ray crystallography [5]. While yielding information up to atomic detail, isolating these proteins took them out of their native environment, the inside of a cell, and required the proteins to be assembled into crystals. Fast forwarding into the late 20^{th} century and early 21^{st} century, advances in electron microscopy at cryogenic temperatures yielded pseudo-atomic structures of isolated macromolecules embedded into a layer of amorphous ice without the need for crystallization [6]. Exploiting similar technological and methodological advances put forth electron tomography at cryogenic temperature and, for the first time, enabled the study of cellular ultrastructure at molecular resolution. It coined the idea of “visual proteomics” [5], the study of the entirety of the proteome within tomographic reconstructions of tilt series acquired by electron microscopy [7]. Initially only small prokaryotic organisms and the thinnest regions of eukaryotic cells could be studied [8] by cryo-ET. With advances in sample preparation for electron microscopy, that is cryo-microtomy [9] and cryo-focused ion beam (cryo-FIB) milling [10, 11], the variety of specimens and structures amenable to cryo-electron tomography (cryo-ET) increased dramatically. While being incredibly time consuming, the milling of thin sections of cells, so called lamellae, using cryo-FIB instruments was shown to prevent the artifacts previously observed for cryo-microtomy, namely knife marks, crevasses, and foremost compression of the sample [12]. In addition, cryo-microtomy remained to require a high degree of ex-

pertise and dexterity. The increasing stability of cryo-FIB instruments promises the possibility of streamlining the process of sample preparation for the visualization of cellular ultrastructure at molecular resolution [13]. At the time the FIB was first applied to unstained, vitreously frozen biological material, ion beam technology had already been explored extensively in the materials science [14] and semiconductor industry [15] for a variety of applications such as surface interfaces and microchip failure analysis. As a result, there was a breadth of methodology that the biomedical sciences could draw from for increasing the variety of samples that are amenable to cryo-ET.

In this thesis, the main bottlenecks that visual proteomics and cryo-FIB sample preparation in particular face will be investigated and techniques and tools will be developed to overcome them. Subsequently, their application to answer biological questions and perform cellular structural biology in both unicellular organisms as well as multicellular organisms and tissues will be showcased.

The limitations that need to be overcome for unraveling the full potential of *in situ* structural biology and visual proteomics are diverse. First, due to the time consuming and manual task of lamella milling, the throughput is insufficient for the study of rare events or low copy number proteins [16]. Furthermore, the development of new workflows using the cryo-FIB-SEM instrument is considerably slowed as high-level scripting interfaces are missing. Second, the variety of samples that can routinely be prepared by cryo-FIB milling is limited to unicellular organisms. The lamella preparation of multicellular organisms and tissues have not gone beyond proof-of-principle experiments mainly due to technical hurdles in the overall workflow [17–19]. Third, targeting of specific membrane-bound or membrane-less organelles inside the cell using fluorescence microscopy-guided site-specific lamella preparation was plagued by low throughput and success rate, especially in the preparation of tissues [17]. Finally, the identification of macromolecules inside tomograms and the interpretation of their three-dimensional reconstructions that result from them require integrated structural biology approaches that take multiple sources of experimental data into account [20]. Improvements and further developments on these limitations and their biological applications will be the main focus in the presented work.

In **Chapter 4.1** of this thesis, I will describe the software package SerialFIB that I developed in collaboration with Dr. Herman K.H. Fung, Dr. Sara K. Goetz and Dr. Julia Mahamid, EMBL Heidelberg[21]. It allows for the automation of several workflows after user setup that are common in cryoFIB applications, that is on-grid lamella preparation, fluorescence-guided site specific lamella preparation, cryo-FIB-SEM volume imaging by iterative ablation and SEM imaging, and cryo-lift-out site preparation.

In addition, SerialFIB's high-level scripting interface enables the rapid development of novel workflows. We exemplify the usage of the developed platform using 6 different specimens ranging from unicellular organisms to *Drosophila melanogaster* tissue. In **Chapter 4.2**, I go on to use SerialFIB's platform in combination with machine learning of cryo-FIB images, automated sample exchange hardware, and inductively coupled plasma ion sources to enable lamella preparation of multiple grids without user intervention or input. I will exemplify the fully automated workflow using *C. reinhardtii* and *S. cerevisiae* cells and I will show that a model trained on one cell types hold the potential to be applicable to other cell types. Within a collaborative study involving multiple researchers from different fields, the application of cryo-electron tomography of on-grid prepared lamellae will be demonstrated to study the vesicle inducing protein in plastids 1 (VIPP1) in **Chapter 4.3**. The cryoEM map derived model of VIPP1 I built informs mutants that probe the function of VIPP1 in thylakoid biogenesis and maintenance in cyanobacteria, specifically the *Synechocystsis sp.* PCC 6803 strain. Based on the model, I will show how a mutant that disturbs VIPP1's ability to bind membranes have an effect on the ultrastructure of thylakoid membranes under high light stress. Furthermore, I will show the usage of cryo-fluorescence microscopy guided lamella milling to study the *in situ* structure of VIPP1 in *C. reinhardtii*.

I will then move beyond unicellular organisms and focus on the preparation of multicellular organisms and tissues for cryo-electron tomography. In **Chapter 4.4**, I will describe the improvements in cryo-lift-out that now enable the multiple usage of a high-pressure frozen sample by abolishing the necessity of using the gas injection system during cryo-FIB lift-out transfer [22]. Rather than using platinum deposition to attach material to the cryo-lift-out needle, micro-welding by FIB milling redeposition of sputtered material is used. This paves the way for quasi-sequential focused ion beam sections in cryo-lift-out, as will be the topic of **Chapter 4.5** in a highly collaborative work with Oda H. Schioetz and Dr. Christoph J.O. Kaiser. While these developments focus on the reusability and throughput of the cryo-lift-out method, **Chapter 4.6** will shortly introduce techniques on how in-chamber light microscopes and cryo-FIB-SEM volume imaging aid in the targeted preparation of lamellae from bulk tissue. As will be seen in **Chapter 4.7**, the correlative preparation enables to compare the germline versus somatic cell nuclear pore complex structure and distribution within the nuclear envelope of *D. melanogaster* egg chambers.

Combining the technology development in the presented thesis, **Chapter 4.7** reveals the structure of *copia* retrotransposon capsids and *in situ* snapshots of their nucleocytoplasmic transport in the follicle cells of high-pressure frozen *D. melanogaster* egg chambers as imaged by SEM-guided cryo-lift-out and cryo-ET. I will go on to describe the biochemical isolation of follicle cells from egg chambers and their on-grid identification and correlative cryo-FIB preparation for cryo-ET. Tomograms of isolated

follicle cells reveal large retrotransposon clusters inside the follicle cell nucleus containing both immature and a small number of mature capsids and, in conjunction with the tomography data from intact tissue, inform the structural differences of the retrotransposon inside and outside the nucleus. Complementary techniques such as immunofluorescence, single-molecule fluorescence *in situ* hybridization, and RNAseq as well as plastic sectioning experiments of the follicle cell epithelium suggest those structures to be Ty1 *copia*-like structure. I will then go on to use subtomogram averaging of the particles found in the cryo-tomograms to elucidate the *in situ* structure of the *copia* gag protein coat at subnanometer resolution.

In the last part of this thesis, I will discuss and give an outlook on further developments needed in sample preparation for cryo-ET to streamline the presented applications and enable the acquisition of big data sets on cryo-lamellae for visual proteomics. I will describe the current efforts to expand the open-source software package SerialFIB to other cryo-FIB-SEM manufacturers and the improvements in hardware and software that hold the potential to expand the molecular targets amenable by cryo-ET. I will discuss how these improvements will contribute to the structural studies of nuclear pore complexes in the different environments explored here. Finally, the thesis will end with a perspective on the nucleocytoplasmic transport of large molecular complexes by the nuclear pore, its potential relevance to transposable elements, and future directions to understand VIPP1's role in thylakoid membranes as studied in this thesis.

2. Aim of the thesis

While the topics of the presented work have benefited immensely from the interplay and complementary nature of the projects, the aims of the thesis can be separated into two objectives: (1) overcoming the technical and technological challenges in improving the sample variety and throughput limiting *in situ* structural biology by cryo-electron tomography (cryo-ET) of cryo-focused ion beam (cryo-FIB) thinned samples by both on-grid and cryo-lift-out sample preparation (2) the technical and technological advances are driven by biological problems and the developments presented are informed by the application to specimens with specific biological questions in mind. The technical and technological pillar of this thesis comprises three major topics:

- Establishing automation in cryo-FIB lamella preparation by developing an open-source software platform that allows for rapid development of future cryo-FIB preparation protocols as well as increasing the throughput of both established workflows and new developments using conventional gallium-based FIB and plasma FIB ion sources
- Advancing the workflows for preparation of high-pressure frozen samples such as tissues and multicellular organisms by cryo-lift-out with increased throughput to enable addressing specific biological questions directly within native tissues
- Developing and enabling correlative approaches to target events within thick specimen by cryo-lift-out

The biological applications of cryo-FIB-SEM presented in this thesis aim at

- Understanding the structure-function relationship of the VIPP1 complex involved in thylakoid biogenesis and maintenance by integrative modeling into the single particle analysis structure of the VIPP1 complex from the cyanobacterium *Synechocystsis sp.* 6803 enabling model-guided site-directed mutagenesis experiment to probe the structure-function relationship of the VIPP1 complex and subsequent in-cell structural analysis of VIPP1
- Visualizing biological ultrastructure at molecular resolution by cryo-FIB lift-out and cryo-ET across a variety of prominent multicellular model organisms in both Developmental and Cell Biology, e.g. *C. elegans* and *D. melanogaster*
- Enabling structural cell biology in *Drosophila* ovaries with a focus on cell-type specific differences in NPC structure and visualization of *copia* retrotransposon capsids

3. Fundamentals

3.1. Electron microscopy of biological specimen

3.1.1. Methodological perspective

Biological discoveries are often driven by observations and technological advances. Whenever a new technology in biology has becoming widely available, there is a wealth of insights that origin from their biological application. Prominent examples would be the discovery of the cell as the minimum building block of life thanks to the availability of the microscopy [1], the elucidation of the first protein structure by X-Ray crystallography [5], the discovery of organelles and description of their structure by electron microscopy, and the elucidation of the human genome through the development of sequencing techniques.

To get the most detailed view into how cells are structured at the nanoscale, the investigation of the different states of biological specimen needs to be performed at the highest resolution and structural preservation possible. Dynamic imaging of live objects is preferred whenever the length scale to be investigated allows it. A wealth of microscopy techniques has been developed that allows to image biological specimen. A summary of the accessible length scales by different techniques is given in **Figure 3.1.1**. The method of choice for a given biological problem is thereby determined by a number of factors, namely the length scale of the studied biological structure, the time scale of the process to be studied, and the volume that needs to be analyzed in order to draw conclusions from the observations. Generally, resolution tends to decrease with an increase in volume analyzed. While e.g. atom probe tomography (APT) [23], nuclear magnetic resonance (NMR) [24, 25], and X-Ray crystallography [26] allow down to atomic resolution, the size of the molecular structure in these techniques is usually limited to tens of nanometers (e.g. the needle specimen in APT or proteins with a molecular mass smaller than 50-100 kDa in NMR spectroscopy). Larger volumes are usually studied by computer tomography (CT) [27], magnetic resonance imaging (MRI) or light microscopy (LM). The latter even allows the study of live objects over extended periods of time by e.g. lattice light sheet live imaging[28]. With the continued development in super-resolution light microscopy techniques, the length scales of processes that can be studied by visible light are steadily decreasing [29]. If nanometer resolution is needed to answer a biological question, electron microscopy by either electron tomography of plastic-embedded samples (ET), sequential focused ion beam milling and scanning electron microscopy (FIB-SEM) are used [30]. The FIB-SEM community is continuing to work towards increasing

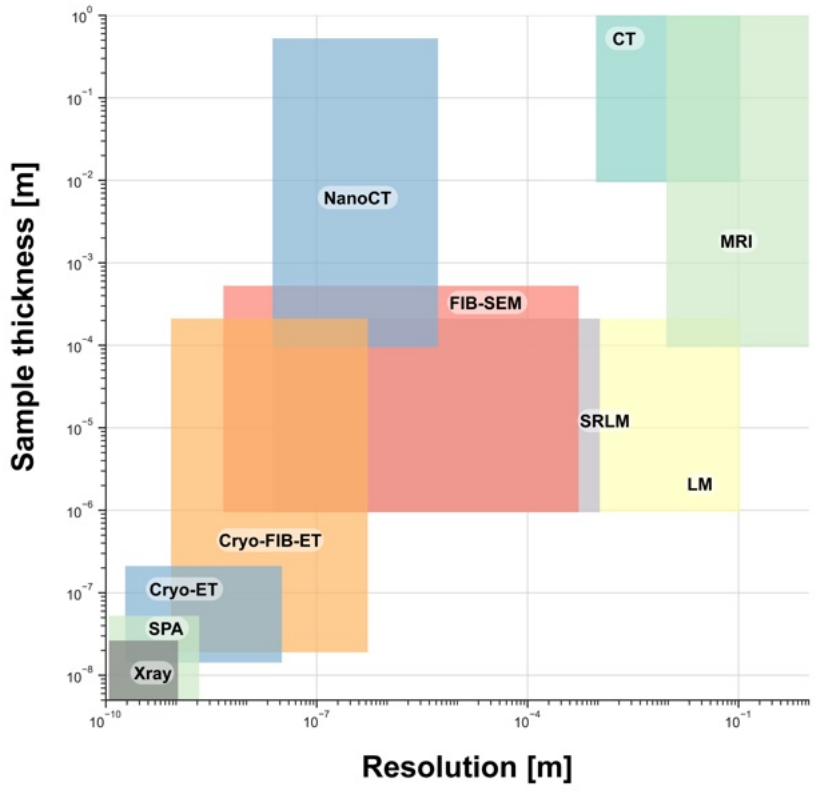

Figure 3.1.1 Overview of the resolution ranges of different imaging and structural technologies. Estimated values for Sample thickness ranges and obtainable resolution are given for following technologies: Xray: X-Ray crystallography, SPA: Single particle analysis by cryo-EM, Cryo-ET: Cryo-electron tomography, Cryo-FIB-ET: Cryo-ET on FIB milled lamellae, FIB-SEM: Volume imaging by iterative ablation and imaging, SRLM: Super-resolution light microscopy,LM: Light microscopy, MRI: Magnetic resonance imaging, CT: Computed tomography.

the maximum size of specimen that can be analysed at isotropic resolution of several nanometers, with the central fly brains [31] or entire small organisms such as *Platerynereiis dumerii* [32] being some of the most recent achievements. Most applications are currently still in plastic-embedded and heavy-metal stained specimen; yet, applications in cryo-FIB-SEM are growing (compare **Chapter 5.1**).

Cryo-electron tomography is to date the only technique that, in conjunction with cryo-FIB-SEM sample preparation, is capable of generating data at sub-nanometer resolution of samples ranging in size from a hundred of nanometers to hundreds of micrometers [33]. As a result, it holds the potential to study macromolecular complexes and biological structures within their native environment, the inside of a cell, at resolutions where sometimes even bulky side-chains of protein can be resolved [34–36]. This opens up the possibility of understanding the architecture of structures in cellular disease states and a variety of relevant biological structures at macromolecular resolution and, thus, seems a promising technique to start answering questions from cell and developmental biology through the eyes of a structural biologist [16, 37].

3.1.2. Electron-sample interaction

When a beam of electrons hits a sample, multiple interaction mechanisms yielding different outcomes occur and can be utilized for imaging and spectroscopy [38]. Those outcomes include:

- transmission of the electron without scattering
- elastic scattering of the electron, where the electron experiences the coulomb potential of the atoms in the sample without losing energy. In conjunction with the unscattered beam it yields the main information content in images by transmission electron microscopy
- inelastic scattering of the electron, where the electron loses energy while scattering and thus damages the sample
- backscattering of electrons at the sample, which yields information on the topography of the sample surface (scanning electron microscopy) and atomic species present
- the generation of secondary electrons, one of the main contrast formation mechanisms in scanning electron microscopy
- the generation of visible light by cathodoluminescence
- the generation of characteristic X-rays, used in electron dispersion spectroscopy (EDS) for elemental analysis
- the generation of Auger electrons, a non-radiative decay following ionization of atoms

In cryo-transmission electron microscopy (cryo-TEM), most information is retrieved through elastically scattered electrons, as inelastically scattered electron lose their phase information relative to the unscattered beam. The amount of inelastic scattering events depends on the sample material and its thickness, with the key component represented by the mean free path of the electron within the sample. Therefore, samples need to be sufficiently thin for high resolution TEM images, as the thicker the sample gets, the more single and multiple inelastically scattered electrons are produced, contributing to the noise level in the image. To that end, the larger the number of scattering events, the harder it is to infer what happened to the electron in the sample, and accordingly to interpret the images. The inelastically scattered electrons can be removed from the final image that reaches the detector with an energy filter, which will be discussed in **Chapter 3.1.3**. Alternatively, a chromatic aberration corrector can be used to bring the electrons that experienced a single inelastic scattering event back into phase with the unscattered beam. While widely applied in the

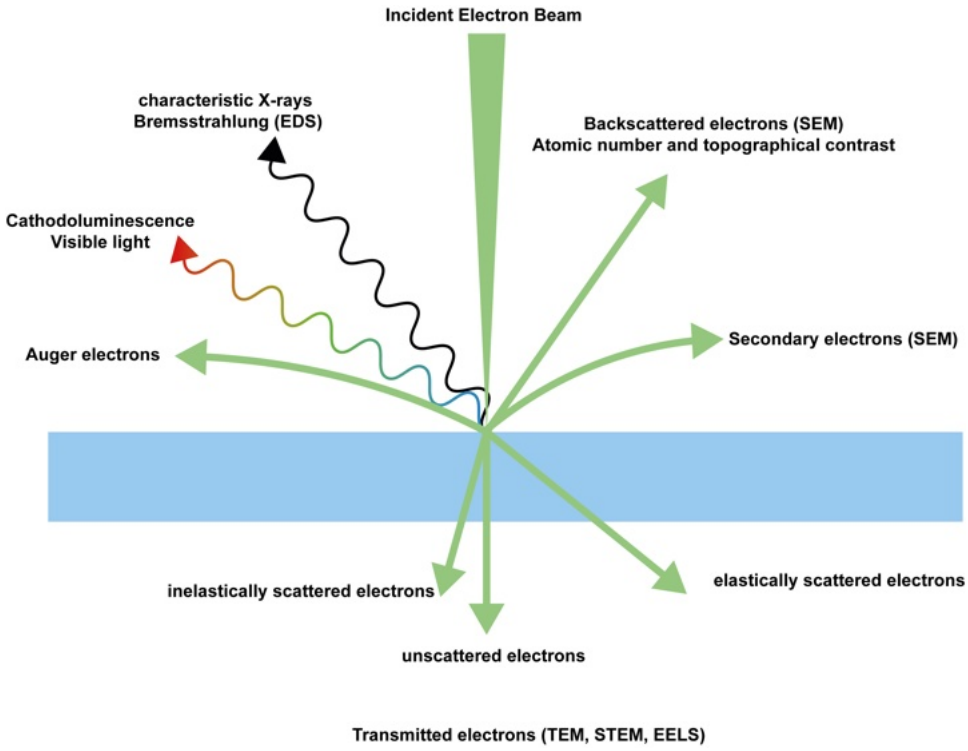

Figure 3.1.2 Schematic of the electron sample interactions and their uses in different imaging and spectroscopic technologies

materials science, aberration correction has only recently been explored for biological samples at cryogenic temperature and is beyond the scope of this thesis. The reader is referred to other resources for a detailed explanation of abberation-corrected TEM [38–40].

To date, the state-of-the-art for imaging of biological samples is energy-filtered TEM (EFTEM), where the signal depends exhaustively on the elastically scattered electrons[41]. The signal-to-noise ratio in an image therein depends on the atomic number of the material of the sample. Heavier elements scatter electrons to higher angles and these electrons can be removed by e.g. the objective aperture, referred to as amplitude contrast. As biological specimen are generally composed of light elements, the amplitude contrast is very low. Additionally, electrons that pass through the sample and are scattered elastically experience a phase shift. These electrons interact with the central beam, leading to phase contrast. In the weak phase approximation used for biological samples [42] that encompass low atomic number elements such as carbon, nitrogen, oxygen, and hydrogen, the amplitude contrast is negligible and the contrast is mainly formed through phase contrast by defocusing the image as will be discusses in a later section on the contrast transfer function (compare **Chapter 3.2.2**).

3.1.3. The transmission electron microscope

The TEM was developed by Ernst Ruska and Max Knoll at the Technische Hochschule Berlin in the 1930s [3] and applications of TEM would years later show that the shorter wavelength of the electron enables overcoming the resolution barrier imposed by visible light. Indeed, the first prototype to perform “Übermikroskopie” (german for “Ultramicroscopy”), so microscopy beyond the resolution of light, was built in 1933. Ernst Ruska realized the commercial value of this groundbreaking invention and the first commercially available TEM was brought to market by Siemens in 1939.

In a nutshell, a TEM consists of five components:

- an electron source to generate electron
- a vacuum tube that allows the electrons to travel through the column
- electromagnetic lenses to focus the electrons
- a stage holding the specimen
- and a camera.

Usually, transmission electron microscopes contain additional parts that are tailored to specific applications or correct for aberrations inherent to the TEM. A detail description of the different components of modern instruments for cryo-electron microscopy is beyond the scope of this thesis and described elsewhere [38, 43]. A brief discussion of the most essential components and a schematic of a modern TEM instrument (**Figure 3.1.3**) is given below.

Vacuum system, stages and robotic sample exchange

High vacuum well below 10^{-7} mbar is needed in order to operate a transmission electron microscope as the elastic mean free path of an electron in atmosphere would be around 60 nm for 10 keV electrons [44]. The vacuum inside an electron microscope is maintained by a series of pumps with sequential optimal efficiency vacuum range that in conjunction pump the chamber to vacuum. Generally, a vacuum of 10^{-3} mbar allows for imaging with electrons, however a much better vacuum is desirable for high resolution work. Pre-vacuum is usually created by a turbo molecular pump (TMP). The final evacuation by an ion getter pump brings the vacuum to working conditions. Modern instruments such as the Titan Krios usually operate at a vacuum of around 10^{-07} mbar or below inside the column. Specific parts such as the electron gun need to have even a better vacuum for operation which is usually achieved by ion getter pumps connected directly to the electron gun [38].

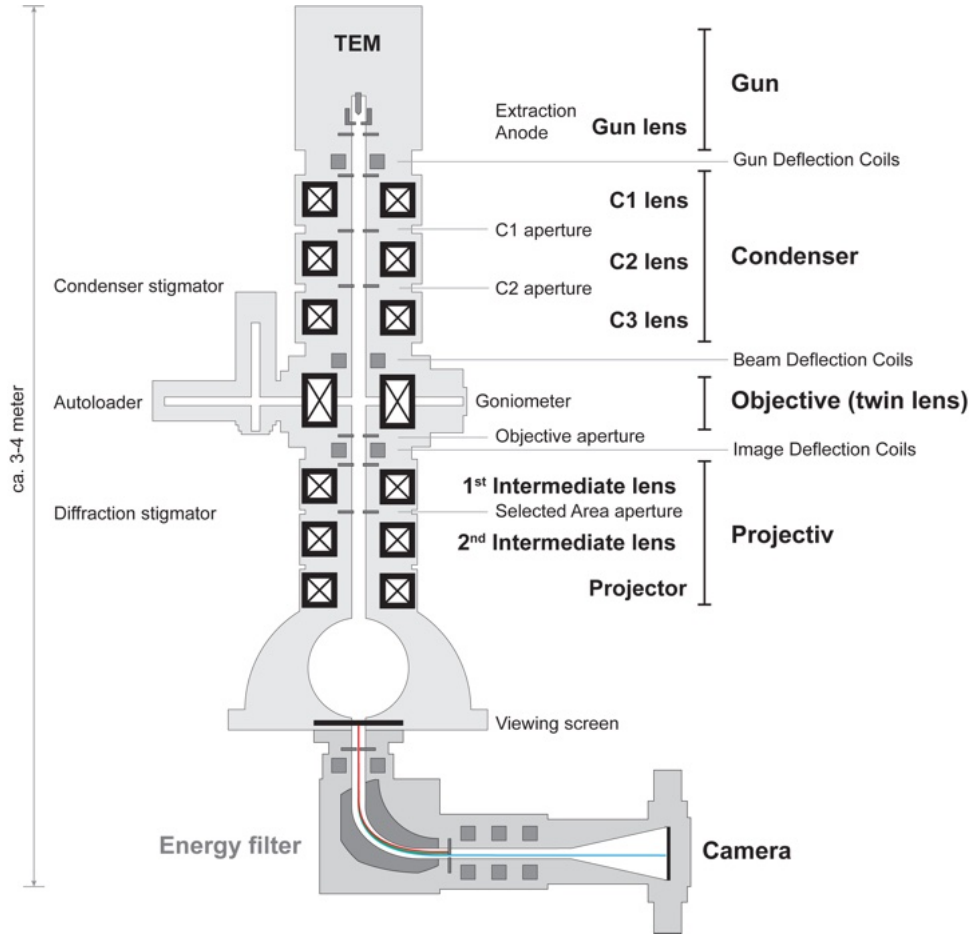

Figure 3.1.3 Schematic of the transmission electron microscope. Courtesy of Dr. Jürgen M. Plitzko.

Different sample stages exist for modern electron microscopes. Available are either mechanical single sample side-entry holders, manual or robotic multi-sample holders that usually load one sample at a time into the electron column [43]. While not commonly used, piezo-driven stages with increased precision as used in other microscopy disciplines are on the horizon to be included into modern electron microscopy hardware.

Electron gun

Several types of electron guns are available. Traditionally, tungsten filaments were used to produce electrons by heating them through their resistance. Later, thermionic emission guns deploying Lanthanum hexaboride (LaB_6) or Cerium hexaboride (CeB_6) were introduced. Modern cryo-electron microscopes are equipped with field emission guns (FEG), which consists of a tungsten wire that is shaped into a sharp tip with a diameter of circa 100 nm and is either operated at elevated temperatures of ca. 1800 K (Schottky FEG; XFEG) or at room temperature (Cold FEG; X-CFEG). While the brightness differs significantly between the sources, the major difference lies in their spatial and temporal coherency, thus the resulting source size and energy spread of the produced electrons. At 100 kV, tungsten filaments produce a beam with an energy spread of 3 eV; LaB_6 thermionic emission guns 1.5 eV, XFEG 0.7 eV and CFEG 0.3 eV [38]. These values are similar at 300 kV [41]. A reduced energy spread as well as increased spatial coherency helps circumvent some of the aberrations of the electron microscope.
In the technical realization, the gun component of a TEM typically consists of an electron source, an extraction anode to emit the electrons, a gun lens creating the first crossover of the electron beam, and gun deflection coils to correct for gun tilt and gun shift. Other emitters such as pulsed electron sources are being explored for specific applications. For further information, please see [43, 45].

Condensor system

The condenser lens system starts with the condensor stigmator coils followed by the C1 lens. In combination with an aperture directly after the lens, the C1 aperture, the C1 lens is used to regulate the illumination strength of the incident beam, therefore also called spot size in the software of some of the electron microscope manufacturers. Following a crossover, the electron beam reaches the C2 lens. By regulating the strength of the C2 lens in combination with the objective lens decides whether the beam is convergent or divergent at the sample. In a C2 system, parallel illumination can only be achieved if the crossover of the C2 lens is set to the front focal plane of the objective lens. A C2 aperture is used to regulate the flux at the sample. Additionally, in some of the modern instruments a C3 lens is added. The additional lens

ensures in conjunction with the C2 lens that the beam at the sample stays approximately parallel. This is achieved by a calibrated interplay between the C2 and C3 lens strength and enables fine-tuning the intensity at the sample with different beam sizes while staying approximately parallel in illumination.

Objective lens

In biological applications at cryogenic temperatures, the objective lens is a twin lens that allows the sample stage to be mounted within the objective lens. When loaded, the sample is surrounded by a cold trap, the cryo-box, to avoid contaminating the sample. Due to the geometry of sample loading and the need to tilt the sample for electron tomographic data acquisition (usually $\pm$ 60 °), the objective lens is one of the main sources of aberrations. For an uncorrected Titan Krios 300 kV instrument with a C-twin lens, the spherical aberration coefficient C_S is 2.7 mm and chromatic aberration coefficient C_C is 3.3 mm. The values of these constants relate the radius of the circle of least confusion. This means it is the minimal diameter of the envelope of rays going through the lens with a defined semi-angular aperture or wavelength for C_S or C_C, respectively. The diameter of the circle or disc of least confusion in TEM is given for spherical aberration by:

$$d_{SA} = C_S * \alpha^3/2 \tag{3.1}$$

where α is the convergence semi-angle. For chromatic aberration in TEM, the diameter of the disc of least confusion can be estimated by

$$d_{CV} = C_C * \beta * dV/V \tag{3.2}$$

where β is the collection semi-angle, V is the accelerating potential, dV the maximum departure from V of an electron contributing to the image. The same holds for fluctuation in current

$$d_{CI} = C_C * \beta * dI/I \tag{3.3}$$

where I is the lens current and dI is the dV the maximum departure from I of an electron contributing to the image. As lenses in modern electron microscopes are generally constant current lenses, d_{CI} is negligible for cryo-TEM.

Projection system

The projection system of the electron microscope comprises a number of lenses that are relevant for the magnification of the final image. Generally, the overall magnification is given by the product of the magnification of the individual lenses. The projection system consists of two or three lenses, the intermediate lens(es) and the projector lens. Together with the magnification of the objective lens, these lenses generate the magnification of the final image at the detector. In energy-filtered transmission electron microscopy, the optical system of the energy filter adds to the overall magnification, leading to different magnification steps in EFTEM compared to TEM mode.

Energy filter

As described in **Chapter 3.1.2**, while the beam of high energy electrons passes through the sample, it interacts in different ways with it. In a conventional electron microscope, only the elastically scattered electrons provide interpretable signal at the detector plane. All other interactions, such as inelastic scattering and the generation of secondary electrons, contribute to noise and sample damage. Interactions that lead to noise generally increase with sample thickness; generally speaking, the thinner the sample, the higher resolution information can be retained in the image. Therefore, to reduce noise in imaging, it is generally favorable to filter out electrons that have been inelastically scattered. The energy filter achieves this with an electromagnetic prism that separates the electrons according to their energy level. By placing a slit at the “zero-loss” peak, so only allowing electrons that have only been elastically scattered, the image contrast of thick samples can be increased significantly. For electron tomographic studies at cryogenic temperatures, an energy filter is hence favorable as samples tend to be much thicker (circa 200 nm) compared to common single particle analysis samples (around 50 nm). An energy filter can also be used to perform electron energy loss spectroscopy (EELS) studies, which yields spectra of the energy levels of electrons and reveals element specific losses that allow for elemental mapping of the sample, referred to as electron spectroscopic imaging or ESI.

Image Detection

The final image formed by the electron microscope needs to be detected, usually with a camera, an array of pixels. The quality of a camera is measured by two properties: the modulation transfer function (MTF) and the detection quantum efficiency (DQE) [46]. DQE is defined as the ratio of the square of the output signal to noise ratio ($(S/N)_{out}$) to the square of the input signal to noise ratio ($(S/N)_{in}$) :

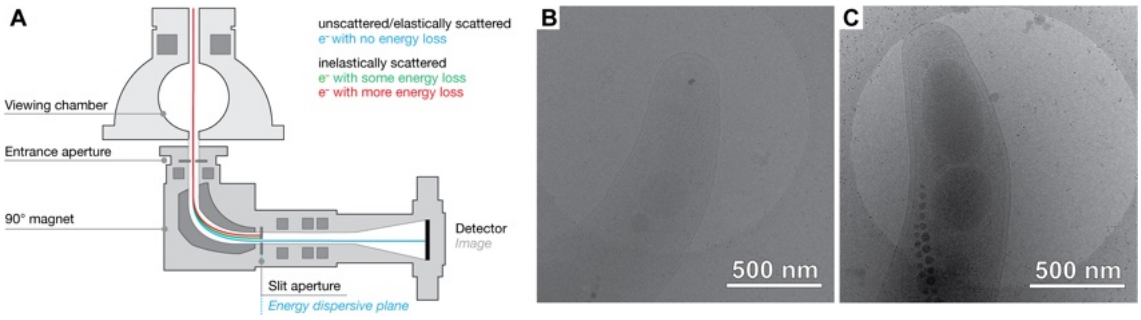

Figure 3.1.4 Energy-filtered TEM. A: Schematic of the path through the energy filter. **B:** An unfiltered projection image of a magnetotactic bacterium. **C:** A filtered projection image. Courtesy of Dr. Jürgen Plitzko.

$$DQE = (S/N)^2_{out}/(S/N)^2_{in} \tag{3.4}$$

Until recently, the only digital cameras available for electron microscopes were charge-coupled devices, or “CCD”s. Due to their architecture, the DQE was generally worse than collecting on electron sensitive film for a long time. That is because of the scintillator layer (usually a single crystal Yttrium aluminium garnet (YAG) for electron up to 120 kV and phosphor alloys for electron with higher velocity) [38]. The photons that are generated are guided via glass-fiber optics that attenuate the signal and increase in the end the noise contribution to the image. Thus, for the highest quality images, researchers had to develop the exposed film and scanned the resulting image to digitalize them, enabling image processing. Until direct detection devices (DDD) became available [6], reconstructions of macromolecular complexes were generally limited to resolutions in the range of a nanometer and above. DQE and throughput had to be traded off: while detection on film gave higher DQE than CCD detectors, the film had to be developed and, thus, throughput was limited. Furthermore, only 50 negatives could be taken at a time, limiting the achievable throughput with film immensely. Direct electron detectors, however, allowed for higher throughput with little trade off on the DQE [46], enabling the collection of a large number of images and, thus, millions of particles. Additionally, direct electron detectors became fast enough in readout to collect frames rather than integrated images, which in conjunction with computational advances allowed for beam-induced motion correction of the images [47]. These technological advances lead to more routine reconstructions at resolutions where clear side-chain specific density becomes visible, i.e. at around 4 Å [6]. Since then, further optimization of the microscope as well as the detectors has led to sub-2.5 Å resolution reconstruction of biomedically relevant macromolecules such as GPCRs [48].

3.2. Cryo-electron microscopy

To study biological macromolecules, several steps are needed to get from the sample in solution to a three-dimensional reconstruction of the protein or protein complex. Initially, the structure has to be fixated by embedding them in a layer of vitreous ice. Subsequently, transmission electron microscopy images of the specimen are taken. Those images are computationally reconstructed and the resulting reconstructions are interpreted by structural modeling. This subsection describes the key steps and considerations in this workflow.

3.2.1. Water and its states

The first step in any electron microscopy workflow is the fixation of the biological sample. In cryo-electron microscopy, the aim is to freeze the sample with cooling rates of 10^5 - 10^6 °K/s to avoid crystal formation. Crystalline ice would be detrimental to cryo-TEM imaging of the sample as the electron beam will be diffracted by the crystal lattice of the ice, resulting in Bragg reflections distorting the projection images. Additionally, the formed ice crystals will expand within the biological material, potentially damaging its ultrastructure. There are many phases of solid-state water; the most relevant to cryo-electron microscopy are hexagonal and cubic ice crystals. If the sample is cooled quickly enough to suppress crystal formation in the sample, a vitreous, glass-like state of water is reached. If the sample is warmed up from this state, cubic ice can be formed. If the cooling rates to form vitreous ice are not reached, hexagonal ice is formed within the sample, potentially destroying the ultrastructure of the specimen. The different fixation techniques for biological specimens are discussed in **Chapter 3.4.2**.

3.2.2. Image formation and the Contrast transfer function (CTF)

For elastically scattered electrons, one differentiates two main mechanisms of contrast formation in transmission electron microscopy: amplitude contrast and phase contrast. When an electron beam interacts with a sample, both its amplitude and phase change, which can give rise to contrast in the resulting image. Amplitude contrast is formed by scattering of electrons to high angles which can be cut off via apertures, removing them from the incident beam. The effects is also referred to as mass-thickness as it depends on the atomic mass of the elements in the samples and its thickness. Phase contrast is formed by the interaction and superposition of the phase information of the elastically scattered wave with the incident unscattered wave. Biological samples are composed of atoms with a relatively low atomic number, mostly carbon, nitrogen, oxygen, and hydrogen. Thus, the number of electrons

that are scattered to high angle is small and phase contrast is the major component in contrast formation when investigating frozen-hydrated biological samples. In the weak phase approximation, considering the microscope parameters such as wavelength, focus, and spherical aberration coefficient, the phase contrast transfer function can be derived to be

$$CTF_{ideal}(k, \Delta z) = -2sin[\pi * (-\Delta z * \lambda * k^2 + C_S * \lambda^3 * k^4/2)] \tag{3.5}$$

with spatial frequency k, defocus Δz, wavelength of the electron λ, and spherical aberration coefficient C_S.

Due to temporal and spatial incoherence, the transfer function decays to 0 at higher frequencies, described by the temporal E_t and spatial E_c coherence envelope functions. For their derivation, the reader is referred to thorough description elsewhere [49].

The resulting contrast transfer function is given by the product of the ideal phase contrast transfer function and the envelope functions

$$CTF = CTF_{ideal} * E_t * E_c \tag{3.6}$$

Practically, the CTF describes the information transfer in the image at a specific spatial frequency. In absence of a phase plate, the CTF starts at 0 for low spatial frequencies. In order to increase contrast in weak phase object samples, the defocus can be increased at the expense of resolution in the image due to the envelope dependency on the defocus. Generally, the point resolution of the image is given by the first zero crossing of the CTF. The defocus at which the first zero crossing of the CTF is pushed to the highest spatial frequencies is the Scherzer defocus. The Scherzer defocus is defined as:

$$\Delta f_{Scherzer} = -\sqrt{\lambda * C_S} \tag{3.7}$$

After the first zero crossing, the CTF oscillates, ideally between 1 and -1 but with decreasing amplitude due to the envelope given by limited temporal and spatial coherence of the incident electron beam. The CTF is plotted for different defoci in **Figure 3.2.1**. While the oscillations can be corrected for by approximating the CTF from the image itself and correcting for it, the information at the zero crossing of the CTF

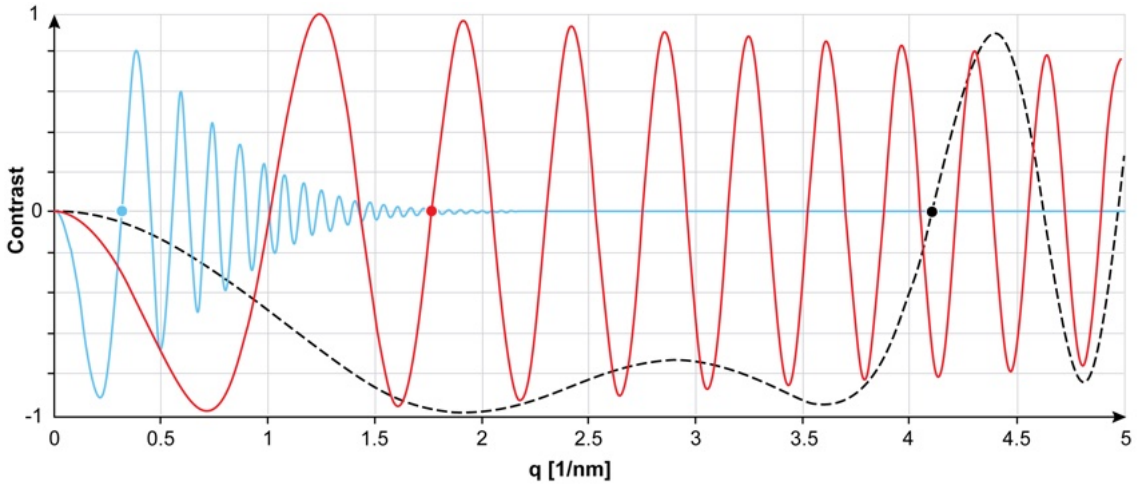

Figure 3.2.1 Contrast transfer function. The different colours indicate different defocus values of 0.5 μm (red), 5 μm (blue) and at Scherzer focus (black).

cannot be restored. Thus, for single particle and cryo-electron tomography workflows it is essential to collect the images at different defoci to fill in the missing information introduced by the CTF zero crossings during averaging.

Phase plates such as the Volta phase plate or the more recently developed laser phase plate generally shift the CTF, ideally by a factor of $\pi/2$, to increase the information transfer at low spatial frequencies. To date, routine imaging is still performed with several hundreds of nanometers defocus to allow for fitting and correcting the CTF. Furthermore, since the introduction of a physical phase plate reduces the signal-to-noise ratio in the final image, the Volta phase plate is not routinely applied [50]. Future phase plate developments such as the laser phase plate [51] based on the ponderomotive force created through a Fabry-Perot cavity [52] promise to solve these problems and are under active development.

3.2.3. Principle of single particle analysis

Reconstructing the structure of isolated particles such as protein complexes by cryo-electron microscopy has become a widespread application of TEM for biological specimen. Single particle analysis depends on the assumption that the object of interest is identical (or very similar) for the entire population. The signal-to-noise ratio of the noisy projection images is then increased via computationally averaging thousands of projection images of the particles, thus a significant amount of time is spent on the image processing of the acquired images [53]. First, as the sample tends to drift under the irradiation with the electron beam, the acquired movies from high-speed direct detection cameras (modern cameras include e.g. Gatan K2/K3, Falcon 3/4i, and DE64, compare **Chapter 3.1.3**) need to be aligned and averaged to

get the final beam-induced motion corrected image [47]. Based on that image, using prior information on the imaging conditions such as estimated defocus, magnification, acceleration voltage, and spherical aberration of the microscope, the contrast transfer function (CTF) can be estimated [54, 55]. Correcting for the CTF normalizes the images in an acquisition parameter-specific manner such that during particle averaging the image frequency-dependent modulation of the image is taken into account [56, 57]. Subsequently, particles need to be identified in and extracted from the images acquired. A further alignment and 2D classification step will remove false-positively picked particles and make sure that the extracted particles are similar in their projection. The projection images can subsequently be matched to projection angles of the particle either by including a low-pass filtered reference or an *ab initio* reference by e.g., stochastic gradient descent [58]. Once projection matching has been performed, the particles can be reconstructed to a model of the imaged 3D object by classical weighted backprojection (compare **Chapter 3.3**) and 3D classification on resulting reconstructions can be used to increase the structural homogeneity of the object of interest [59–61]. The resulting 3D object can be used to refine the projection angles assigned to the original extracted particles to improve the accuracy of the 3D reconstruction. Finally, post-processing methods (e.g. the application of a blurring factor) can improve the visualization of the resulting Coulomb potential map of the object of interest. The single particle workflow is illustrated in **Figure 3.2.2**. Together with other developments in the field of cryo-EM, single-particle image processing has been recognized by the Nobel prize to Joachim Frank, Jaques Dubochet, and Richard Henderson in 2017 [62].

The resolution of the reconstruction dictates the subsequent analysis and molecular interpretation of the map. If high enough resolution (< 1.5 Å) is reached, atom positions can be deduced unambiguously from the map alone. This, however, is a luxury that is to date still reserved to the most rigid and well behaving proteins that have been subjected to single particle analysis by cryo-electron microscopy. However, even if this resolution is not met by the reconstruction, prior knowledge on the physical and structural properties of biological macromolecules may still allow for the interpretation of the map. The algorithms and strategies used in model building are described in the following chapter.

3.2.4. Model building

When it comes to building models into the electron microscopy map produced by single particle analysis or subtomogram analysis, the attained resolution dictates the possible analysis. Generally, the level of detail representing the biological macromolecular is determined with the attained resolution in mind. For the low-resolution regime, coarse-graining residues according to common schemes such as the MARTINI models (4 to 1 residue mapping) [63] or even coarser representation such as

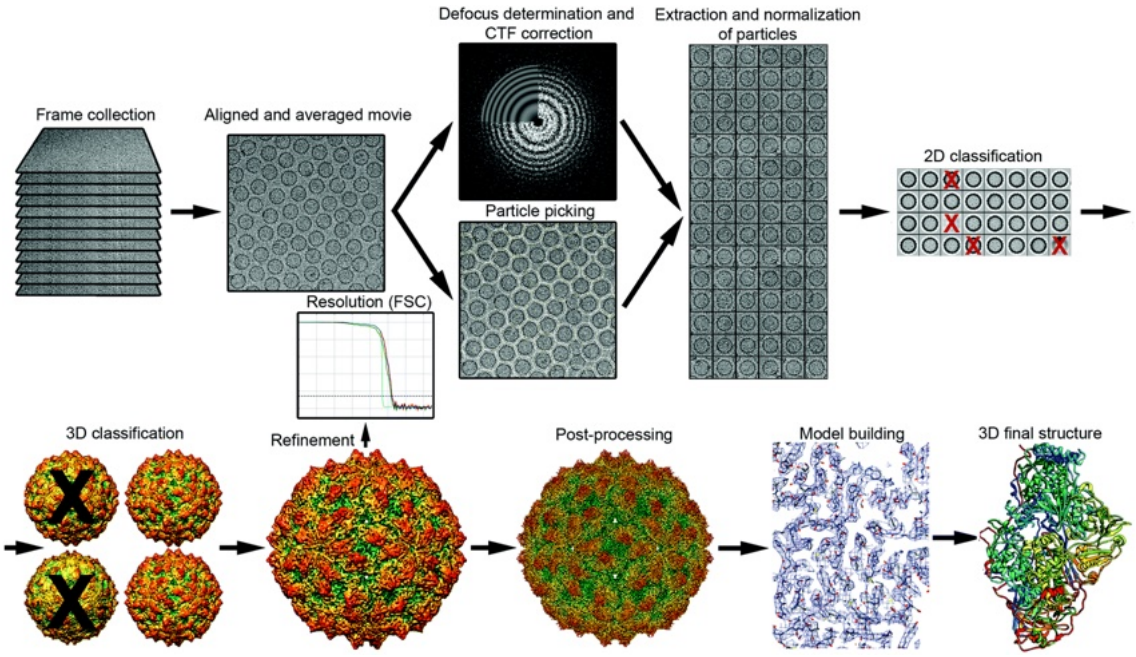

Figure 3.2.2 The single particle analysis workflow. Adapted from [53] with permission.

spheres representing whole subunits may be sensible. From sub-nanometer resolution, atomic models as a physical basis to fit either secondary structure or even side-chains at very high resolution are used. If side-chains are clearly visible in the map, the model can be built *de novo* from sequence information alone. Results from homology modeling [64] or more recently structure prediction algorithms such as AlphaFold [65] or RosettaFold [66] can be used as template for refinement in a manual or automatic fashion. The refinement algorithms use libraries of side-chain geometries and physical description of the molecule's topology while taking the experimental data into account by comparing the fit of the model to the map. Manual inspection of the side-chain to density fit is needed either way. Adjustments and refinements are commonly based on the potential energy surface of the molecule approximated by so-called force fields that are parameterized using experimental structures and quantum chemical calculations.

Commonly available force fields can usually be split into two types of interactions: non-bonded interaction represented by the potential U_{nb} and bonded interactions given by U_b. It holds that

$$U_{total} = U_{nb} + U_b. \tag{3.8}$$

The bonded interactions correspond to bonds, angles, and dihedrals, mathematically described by a Morse potential. However, since the integration of Morse potentials are computationally expensive, harmonic potentials are used, approximating the

Morse potentials at the equilibrium position r_e

$$U_b = U_{bond} + U_{angle} + U_{dihedral} \tag{3.9}$$

with

$$U_{bond} = \frac{1}{2} \sum_{bonds_i} k_i^{bond} (r_i - r_{0i})^2 \tag{3.10}$$

,

$$U_{angle} = \frac{1}{2} \sum_{angles_i} k_i^{angle} (\theta_i - \theta_{0i})^2 \tag{3.11}$$

and

$$U_{dihedral} = \sum_{dihedral_i} \begin{cases} k_i^{dihedral}[1 + \cos(n_i \phi_i - \gamma_i)], & \text{if } n_i \neq 0 \\ k_i^{dihedral}(0_i - \gamma_i)^2 & \text{if } n = 0 \end{cases} \tag{3.12}$$

When performing molecular dynamics or molecular dynamics flexible fitting simulations, parametrization of the force field is the crucial step for achieving close to 'physical' behavior of the model. Bonds are modeled using harmonic potentials with a force constant k_i^{bonds} derived from quantum chemical calculations, equilibrium distance r_{0i} derived from experimental structure information, and atom-atom distance r_i. The angles are described equivalently with force constant k_i^{angles}, equilibrium angle θ_{0i} and angle θ_i. Dihedrals and torsions within a group of four atoms are approximated using a fourier series of even functions, thus only containing cosines. The constant is given by $k_i^{dihedral}$, multiplicity of minima n_i, torsion angle ϕ_i and phase shift γ_i.

The non-bonded interaction potential U_{nb} is described by two terms: the van-der-Waals interaction potential U_{vdW}, usually described using the mathematically simpler Lennard-Jones potential, and the Coulomb potential $U_{Coulomb}$. They are given by

$$U_{nb} = U_{vdW} + U_{Coulomb} \tag{3.13}$$

where

$$U_{vdW} = \sum_i \sum_{j>i} 4\epsilon_{ij} [(\frac{A_{ij}}{r_{ij}})^{12} - (\frac{B_{ij}}{r_{ij}})^6] \tag{3.14}$$

and

$$U_{Coulomb} = \sum_i \sum_{j>i} \frac{q_i q_j}{4\pi\epsilon_0 r_{ij}}. \tag{3.15}$$

The Van-der-Waals parameters A_{ij}, B_{ij} describing the distance at which the interparticle potential is zero, and partial charges q_i q_j need to be derived from quantum mechanical calculations. ϵ_0 refers to the permittivity of vacuum. During a molecular dynamics simulation, Newton's equation of motion including these potentials are integrated with a time step of usually 1 fs or 2 fs with free or fixed hydrogen bonds, respectively.

In molecular dynamics simulations, one frequently applies user-defined forces in order to sample a specific region of the Free Energy Surface (FES) of a biomolecule. A similar approach to forcing a simulation into the conformational state of a protein to be studied can be performed when building models into experimental electron densities of a biomacromolecule, the Molecular Dynamics Flexible Fitting (MDFF) algorithm. The potential from the electron density is created by weighting a localized potential at every position in space:

$$U_{EM}(R) = \sum_j w_j V_{EM}(r_j) \tag{3.16}$$

with

$$V_{EM} = \begin{cases} \xi[1 - \frac{\Phi(r) - \Phi_{thr}}{\Phi_{max} - \Phi_{thr}}], & \text{if } \Phi(r)\Phi_{thr} \\ \xi & \text{else} \end{cases} \tag{3.17}$$

where w_j denotes the per-atom scaling, chosen to be the atom's mass, Φ is the value of the density at each grid point, Φ_{thr} and Φ_{max} is the threshold and maximal value for density included in the potential. ξ is a scaling factor. The higher ξ, the stronger the forces will be acting on the system to fit the map. Typical values are 0.3 for initial fitting.

The MDFF algorithm can also be used at lower resolutions, e.g. sub-nanometer resolution where secondary structure becomes observable or even lower resolution where only subunits are distinguishable. At the mid- to low-resolution regime, strong secondary structure constraints and short simulation are often required to prevent secondary structures from being disrupted by the map-derived potential. Additionally, domain restraints are usually necessary when working with low resolution maps.

In the mid- and low-resolution regime, other sources of information can become essential to generate a sensible molecular model. This includes knowledge from physical principles and statistical inference, i.e. molecular dynamics, comparative modeling, structure prediction, and steric effects[65, 67, 68]. Furthermore, other sources of experimental data such as X-ray crystallography, nuclear magnetic resonance spectroscopy, cross-linking mass spectrometry, yeast to hybrid interaction assays, and other techniques can help in generating consensus models. This is usually referred to as "integrative structural biology", and a number of software packages such as HADDOCK [69, 70], the Integrative Modeling Platform (IMP) [71, 72], and others are available to perform these modeling tasks[73–77]. The different approaches as soft-

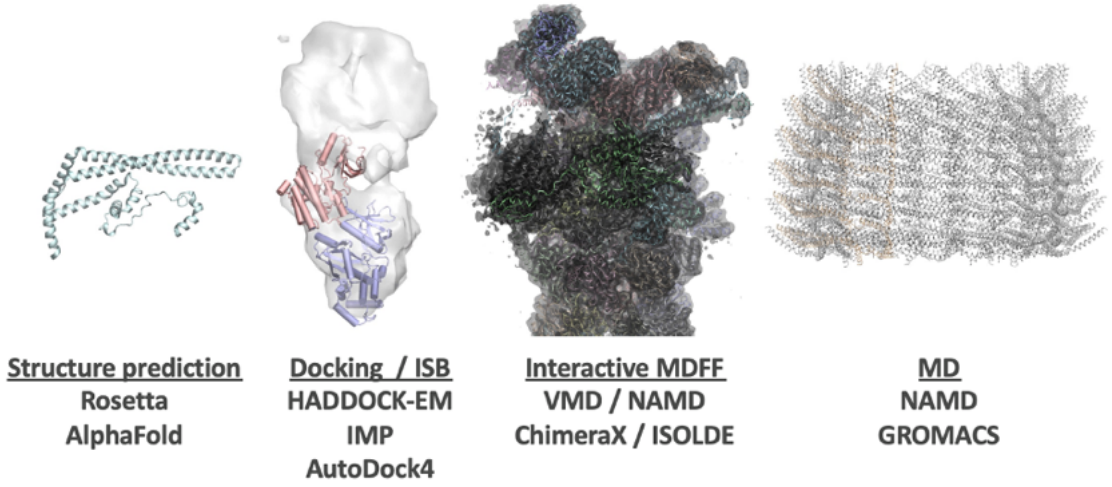

Figure 3.2.3 Overview of different modeling strategies Modeling approaches and their corresponding software packages used throughout this work include structure prediction, integrative structural biology suites such as HADDOCK [69, 70] and IMP [71, 72], interactive molecular dynamics (MD) and flexible fitting (MDFF) packages [75, 76].

ware packages used throughout this thesis for integrative modeling are summarized in **Figure 3.2.3**.

3.3. Cryo-electron tomography

The general principle of cryo-electron tomography goes back to the polytropic montage introduced by Roger Hart in 1968 [78]. Though he did not reconstruct the three dimensional object at the time, the demonstration of collecting multiple images of the same object at different angles should allow to reconstruct the original object through back-projection. While Hart identified the possibility of doing so in unstained biological material, a major obstacle to achieve such three-dimensional reconstruction is the dose sensitivity of the sample: with increasing electron dose, the sample damages during irradiation. While the limited dose that the sample can be irradiated with could be spent on a single image in single particle analysis, cryo-ET needs to distribute that dose to a number of projections at different tilts, increasing the noise level per image significantly. Sample preparation methods such as chemical fixation, plastic embedding and negative staining of biological material overcome the dose problem by embedding and contrasting the specimen but the artifacts introduced during these preparations precluded the structural analysis of features beyond tens of nanometer resolution [79]. It took until the 1990s for the TEM hardware in cryo-EM to mature to the point that the first tomograms could be collected in unstained biological material at cryogenic temperatures, with an early application on lipid vesicles [80].

3.3.1. Principle and challenges of cryo-electron tomography

The general principle of tomography is relatively straight forward: by taking several projection images at known angles of the same object, a reconstruction of the three-dimensional structure of the imaged object can be obtained. If an infinite number of projections or “tilts” is recorded, the reconstruction of the object would be exact. With decreased number of projections, the resolution of the reconstruction decreases. The relationship of the number of tilts to the attainable resolution is thereby described by the Crowther criterion:

$$d \simeq \pi * D/N = \Delta\alpha * D \tag{3.18}$$

Where d is the reachable resolution, D is the diameter of the (spherical) object, N is the number of recorded tilts of the object, and $\Delta\alpha$ is the angle incremental. According to the Crowther criterion, the more tilts are recorded, the higher the obtainable resolution. However, in cryo-electron tomography the damage that the incident electron beam causes decreases the high-resolution information obtainable from the sample. Generally speaking, a dose of anywhere between 50-200 e/Å^2 leads to severe damage of the sample, usually visible through the release of hydrogen or different radical species [81] due to radiation damage by the bombardment with the high energy electron beam [82, 83]. Furthermore, the available stages and sample holder have a limitation to how high they can tilt. As a result, not the entire 180 $^\circ$ tilt range can be collected. Usually, a tilt range from -60° to 60° can be achieved [80]. The missing information due to missing tilts leads to artifacts in the reconstruction and since the missing information leaves a “wedge” in Fourier space unassigned, it is referred to as the “missing wedge” problem (compare **Chapter 3.3.3**). Due to both the missing wedge and dose limitation in cryo-ET, significant efforts have been undertaken to determine the most efficient way of data collection to retain the highest resolution information from delicate biological samples in vitreous ice [84].

3.3.2. Tilt series data acquisition schemes

Several ways of collecting tomography data of vitreous samples have been developed. The main limitation in tilt schemes is the limited dose that can be spent on the dose sensitive material. Therefore, tilt series acquisition schemes are essential to make the most out of the limited dose budget and are still subject to research and optimization [84–86]. The simplest way to collect a tilt series is unidirectional: one starts at the highest negative angle to be collected and incrementally moves towards the highest positive angle. As resolution scales with thickness and the sample increases dramatically in thickness at high tilts, the highest information obtainable is at 0°. As a

result, in the unidirectional tilt scheme, most of the high-resolution information is lost to beam damage by the time that the 0 ° tilt projection is collected. This was partially mitigated by the bidirectional tilt scheme: one starts at low tilt on the negative side or at 0° tilt, goes up the positive side and once the tilt limit of the stage is reached, the missing tilts in the negative direction are collected. While this tilt scheme does retain more information in the initial tilts, it loses some obtainable information as the negative direction is corrected only after all tilts of the positive direction have been collected; the accumulated dose then decreases the information content in the negative tilts. Finally, the dose-symmetric or Hagen scheme distributes the dose symmetrically. First, the projection at 0° is collected. Then, the tilt is moved up an increment in the positive direction $+\Delta$ for the next projection, returned to the same angle in the negative direction $-\Delta$, and moved to -2Δ to collect the next projection. Finally, the stage returns to the positive equivalent 2Δ and so on [84, 86]. The tilt scheme has been benchmarked to be the most efficient of the three tilt schemes mentioned regarding obtainable high resolution information. Additional data acquisition schemes have been developed, such as data collection strategies that emphasize the 0° tilt by increasing the dose spent on it [85]. The rest of the tilt series is collected at lower dose. The rationale is that a large fraction of the dose budget is spent on the 0° tilt which contains the highest-resolution information. The subsequent tilts are collected with a high accumulated dose to reconstruct the tomograms and identify particles and their orientations from it. They will not contribute to the high-resolution information in e.g. subtomogram averaging workflows as the projections will be dose-filtered. Finally, additional data collection and analysis schemes have become available. For example, in montage tomography one condenses the beam such that not the entire camera is exposed and distributes the dose in a hexagonal shape with sufficient overlap to obtain a tomogram of a larger region than the illumination area of the beam. In 2D template matching on complex samples only a single tilt is collected, from which particle positions are determined by searching for a template at different applied defoci to search for the highest cross-correlation. The defocus applied to the template with the highest cross-correlation then gives information on the position of the particle along the z axis. Additionally, the acquisition of multiple tilt series at a time by multishot acquisitions have become common, increasing the throughput by an order of magnitude. The tilt schemes and acquisition strategies are summarized in **Figure 3.3.1**.

3.3.3. Reconstruction algorithms

In order to reconstruct the three-dimensional density map or “tomogram” of the pleomorphic structure imaged, the collected tilt series needs to be aligned by comparing images throughout the tilt series. In the simplest case, fiducial markers such as gold nanoparticles can be added to the sample prior to freezing. The markers are easily

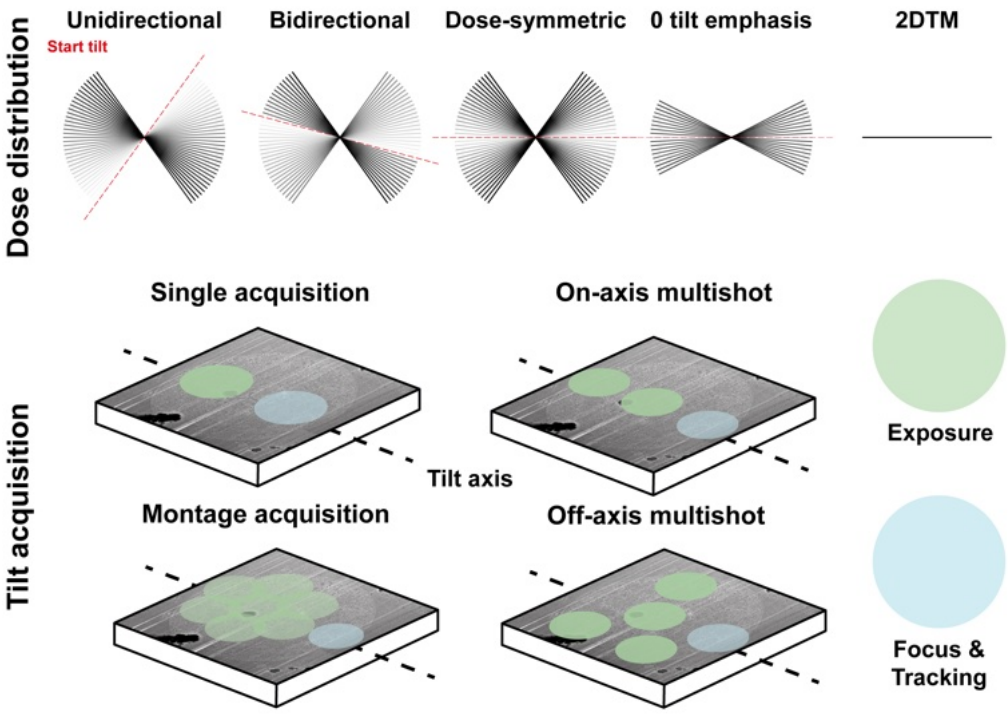

Figure 3.3.1 Data acquisition schemes in *in situ* structural biology by transmission electron microscopy. The gray values in the dose distribution color code the accumulated dose from white (unexposed) to black (100% of the dose). The focusing and tracking regions and exposure positions in typical acquisition scenarios are displayed and now commonly available in commercial e.g. Tomography 5 (Thermo Fisher Scientific), Latitude (Gatan), and Recorder (JEOL) as well as academic software packages, SerialEM [87] and Leginon [88].

recognizable in the different projections of the sample and can be tracked throughout the tilt series for subsequent alignment. If such fiducial markers are not readily available, e.g. on cell or tissue sections, the images can be divided into patches which are then tracked through the tilt series by stretching or compressing them according to the tilt angle and comparing them via cross-correlation to the tilt image. The latter method is generally referred to as “patch tracking” and available in common software packages for reconstruction such as imod/3dmod [89]. The cross-correlation based algorithms usually require manual cleaning of the results to generate high-quality alignment. More recently, robust fully automated tilt series alignment by AreTomo has become available [90].
A number of reconstruction algorithms to generate the tomogram from the aligned projections exist. Most common are algebraic reconstruction techniques (ART) [91], e.g. simultaneous ART (SART), and weighted backprojection (WBP) using standard tomographic programs [89]. For an in-depth discussion of these techniques and available software packages, the reader is referred other sources [92]. In brief, weighted back-projection relies on the Fourier slice theorem. The theorem states that the projection of a three-dimensional object represents a slice in Fourier space of the object. Thus, a model of the object can be created from its projections by filling the Fourier space with the Fourier transform of the projection at the tilt angle that the projection was collected. Due to the limited tilt range obtainable in cryo-ET (usually -60 to +60 degrees), not the entire Fourier space can be sampled and angles are missing. As the tilt series are nowadays commonly collected from a single tilt angle, the resulting missing information resembles a wedge in Fourier space, generally referred to as the “missing wedge”, giving the “missing wedge problem” its name. Pratical solutions to the missing wedge problem are still lacking, though interesting ideas have been explored [93]. Furthermore, discrete tilt angles are collected, reducing the obtainable resolution within the 3D reconstruction as described in **Chapter 3.3.1**. The concepts of weighted back-projection is visualized schematically for a 2D object in **Figure 3.3.2**.

3.3.4. Particle picking and subtomogram analysis

While techniques to compensate the low signal-to-noise ratio by machine learning algorithms are an active field of research [94–96], cryo-electron tomograms are inherently noisy. However, as common practice in single particle analysis and discussed in **Chapter 3.2.3**, the tomograms tend to contain multiple copies of quasi-identical particles of biological macromolecules such as ribosomes, proteasomes, nuclear pore complexes etc. that can be identified in the tomogram and averaged to increase the signal-to-noise ratio. To this end, one way to identify the particle positions in a tomogram is template matching with a reference. Template matching essentially convolutes the Fourier transform of the particle containing volume with the Fourier

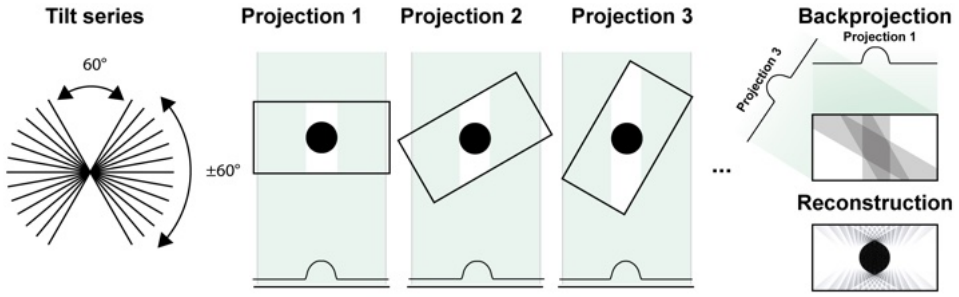

Figure 3.3.2 Schematic representation of the reconstruction from projections: The process of reconstruction is exemplified on a 2D example of a sphere. The missing wedge from the tilt series collected is usually in the range of 60°. The signal from the projections is used to reconstruct the original object using weighted backprojection. The missing wedge leads to elongation of the sphere in the reconstruction due to missing information.

transform of the reference rotated in all expected angles. The inverse Fourier transform then gives the cross-correlation map of the used reference. This is repeated at the expected angles, where increments are chosen taking the computational cost of very fine sampling into account. The highest cross correlation value per tomogram position is determined. The process results in a scoring and an orientation map, where the scores of each position within the tomogram and the corresponding Euler angles of the reference are stored. It is worth noting that to date, this is only working reliable for relatively large macromolecules, usually >500 kDa, and a lot of manual intervention and confirmation is still needed.

Based on the determined positions, particles can be extracted in subtomograms, boxing a volume around the identified positions. These subtomograms can be used for iterative alignment and averaging to refine the angular distribution of the particles to the novel reference created from the previous averaging procedure. If performed correctly, the procedure increases the signal-to-noise ratio, creating a better resolved structure. In the case of false-positively identified particles or biological heterogeneity in the composition and/or conformational state of the studied macromolecules, classification can help in identifying and disentangling this heterogeneity. The process is illustrated in **Figure 3.3.3**. More recently, machine learning models have become available to perform the task of particle identification within tomograms and are improving constantly. While training these networks is computationally more expensive than template matching runs, deploying the models on tomograms after training becomes much more efficient and requires a small fraction of the time needed for classical approaches.

The strength of subtomogram analysis from cellular tomograms is that in addition to the elucidated structure, the identified and refined particle positions can be placed back into context within the acquired tomograms. Consequently, the relative orientation and distances between different structures within the tomogram can be analyzed, e.g., the spatial relation of the macromolecular complex to membranes in the

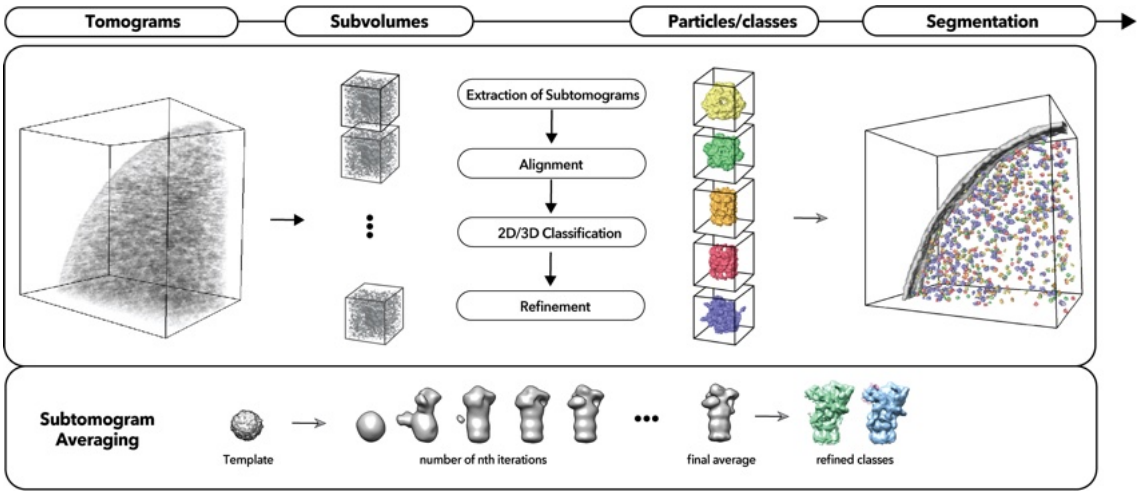

Figure 3.3.3 The subtomogram averaging workflow. Adapted from [97] with permission.

tomogram or potential interactions and co-dependent distribution of macromolecular complexes. Thus, the method retains the contextual information of the near-native cellular environment.

3.3.5. Thickness limitation in electron microscopy

For all the data acquisition and subsequent analysis of images obtained, the sample is essential to the success of *in situ* structural biology projects. The majority of cellular cryo-ET imaging is performed with transmission electron microscopy at 300 kV. In this setup, the electron's inelastic mean free path within biological material is approximately 300-400 nm [98]. As a result, when dealing with thicker samples, the signal-to-noise ratio decreases rapidly. Consequently, most cells, with the exception of the thinnest regions of adherent eukaryotic cells, are not directly suitable for cryo-ET. Hence, sample preparation for cellular tomography is essential. Required is a vitreously frozen thin section of the cellular or tissue material below 300 nm, ideally 200 nm in thickness, prepared minimally invasive, and at the highest throughput possible. In the following, we will focus on the sample preparation techniques available to achieve this goal and the hurdles that come with it.

3.4. Sample preparation for electron microscopy

3.4.1. Samples in electron microscopy

The sample in electron microscopy in the biological sciences are as diverse as biology itself. They can range from purified proteins and viruses to entire tissues and small organisms (**Figure 3.4.1**) [22]. Generally, the thicker the sample, the more complex is the preparation method required to obtain a vitreous section in the TEM

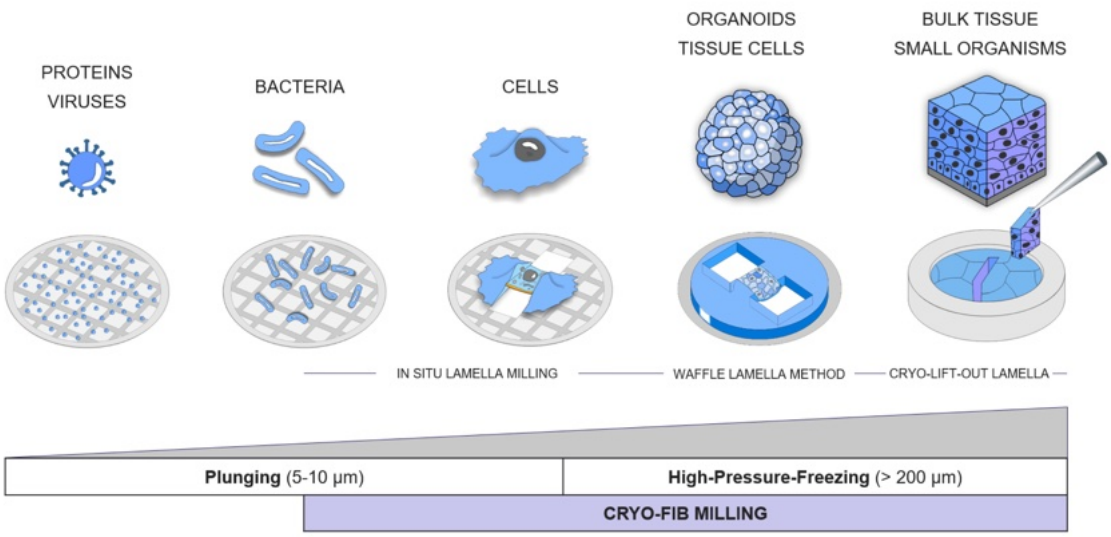

Figure 3.4.1 Overview of the biological samples in cryo-ET. Adapted from [22] with permission.

that is suitable for cryo-ET data acquisition. While proteins and viruses can usually be plunge frozen and imaged directly in the TEM, bacteria and eukaryotic cells, while still amenable to plunge-freezing, usually need to be thinned to be imaged in the TEM. For thicker samples, high-pressure freezing is required, making the workflow even more challenging. This chapter will focus on the fixation and preparation techniques and their challenges when preparing biological samples for TEM imaging and cryo-ET.

3.4.2. Fixation techniques for biological specimen

Every workflow in electron microscopy starts with sample fixation. As biological objects are generally dynamic and aqueous in nature, high-resolution imaging in the TEM requires the reduction of this dynamics and the stabilization of the sample such that it withstands the high vacuum systems of the electron microscope. Several fixation methods are available [99, 100]. Generally, the fixation techniques can be classified into fixation by chemical reactions that alter the chemical topology of the specimen [101] and cryo-fixation techniques that leave the covalent bonds within the molecules of interest generally intact and unchanged.

Chemical fixation

Chemical fixation has generally been used to fix and preserve the ultrastructure of the sample by cross-linking the biological molecules, namely proteins, lipids, and nucleic acids present within the sample. This way, the morphology of the sample can be maintained during further sample processing without risking the degradation of the biological specimen by e.g. enzymatic reactions. The procedure can also become

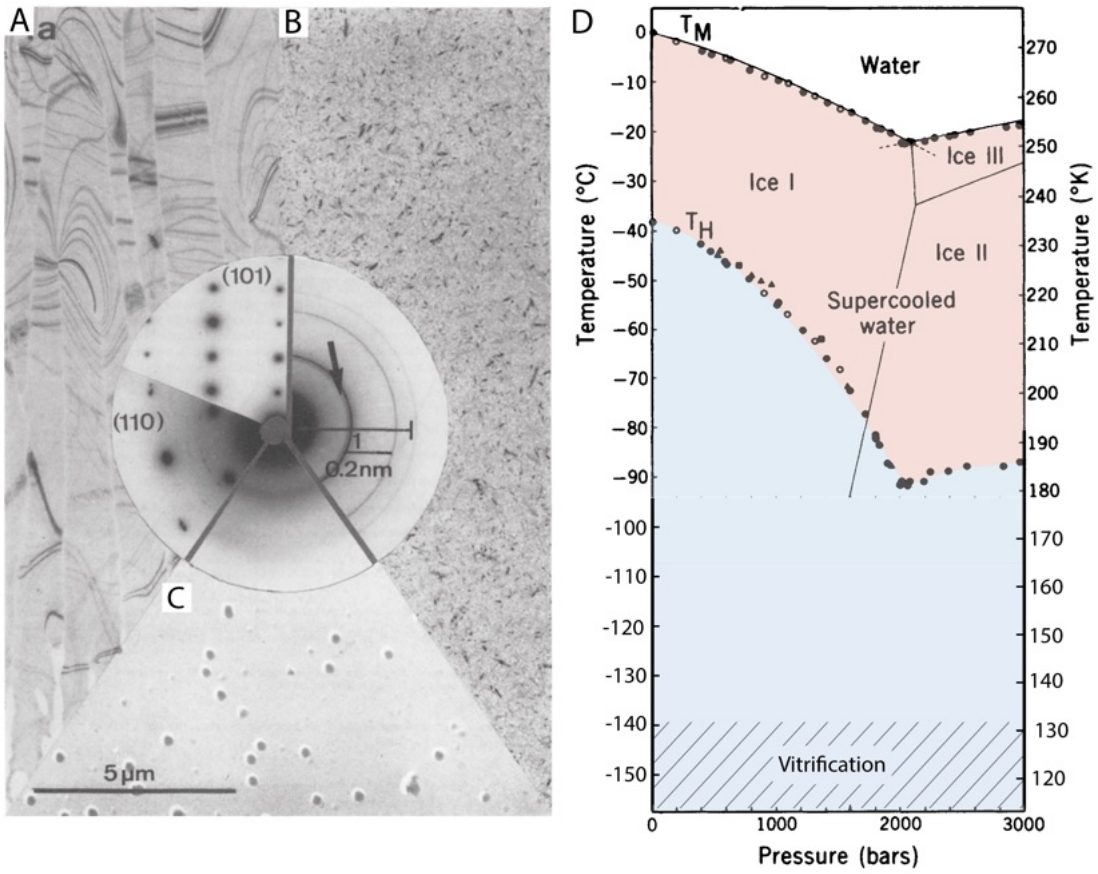

Figure 3.4.2 Micrographs and phase diagram for different states of ice relevant to cryo-EM A: Micrograph and diffraction pattern for the (101) and (110) axis of hexagonal ice crystals. **B:** Micrograph and diffraction pattern of cubic ice. **C:** Micrograph and diffraction image of vitreous, amorphous ice. Note the absence of reflexes in the diffraction pattern. Adapted from [102], with permission. **D:** Phase diagram of water illustrating the peculiar properties of water at 2000 bar exploited in vitrification by high-pressure freezing. Adapted from [103], with permission.

necessary to chemically inactivate potentially hazardous or infectious samples such as viruses. Chemical fixation, while used for classical EM sample preparation, therefore also finds applications in cryogenic workflows as inactivation method when high biosafety level samples need to be imaged in lower biosafety laboratories.

In more traditional cell biological specimen preparation, the sample is dehydrated after chemical fixation and subsequently embedded in a resin to allow for sectioning with a diamond knife. The dehydrated sections are compatible with the high vacuum system of the TEM and can be stained with heavy metals to increase contrast. While chemical fixation may be the method of choice for certain biological applications, it generally can be assumed that it alters ultrastructure to an extent as not the actual biological molecules but rather the accumulated stain is imaged. Thus, it is important to choose the gentlest chemical fixation method possible to preserve as much of the ultrastructural detail of the biological specimen as possible.

Vitrification

As described in **Chapter 3.2.1**, the cooling of water can lead to different states, hexagonal (compare **Figure 3.4.2A**), cubic (compare **Figure 3.4.2B**), and amorphous or vitreous ice (compare **Figure 3.4.2C**). Which state of ice is formed during freezing depends on the cooling rate and environmental factors. The common methods for vitrification are discussed below.

Plunge freezing

Plunge freezing was the first practical technique to be developed to produce vitreous ice on electron microscopy grids by Jacque Dubochet at the European Molecular Biology Laboratory Heidelberg in the 1970-80s[100]. At ambient pressure, a cooling agent, usually ethane, propane or a mixture thereof, is cooled just above their melting temperature in a bath of liquid nitrogen. The solution containing the sample is pipetted onto the grid, excess liquid is removed by backside or double-side blotting using filter paper in a humidity chamber and the resulting thin film is plunged into the cooling agent, vitrifying the sample [104]. The device and workflow is shown in **Figure 3.4.3**. Nowadays, plunge freezing is a wide-spread technique to vitrify thin films of aqueous protein solutions for single particle analysis as well as cellular samples such as prokaryotic and eukaryotic cells up to a thickness of 10 μm for cryo-FIB milling (compare **Chapter 3.4.10**) and cryo-ET.

High-pressure freezing

When samples thicker than 10 μm up to a thickness of 200 μm are to be vitrified, high-pressure freezing is the method of choice, initally developed by Hans Moor from the 1960s onwards [105]. In first approximation, the freezing under high-pressure can be understood by remembering the principle of Le Chatelier. Freezing increases the volume of water. Pressure hinders the expansion upon freezing. Thus, pressure has to disfavor crystallization [106]. This principle can be observed in a particularity in the phase diagram of water: the freezing point of water is lowered at high pressure, allowing it to be cooled to -92 °C (181 °K) at a pressure of approximately 200 MPa (2000 bar) (compare **Figure 3.4.2D**). This leads to a reduction in the cooling rate necessary for vitrification [103, 106]. In practice, high-pressure freezing is performed by applying the biological sample to a sample carrier that is inserted into a pressure chamber and exposed to a pressurized stream of liquid nitrogen that cools the sample rapidly, allowing it to vitrify. A vitrification limit of around 200 μm is generally cited [107].

Other rapid freezing techniques

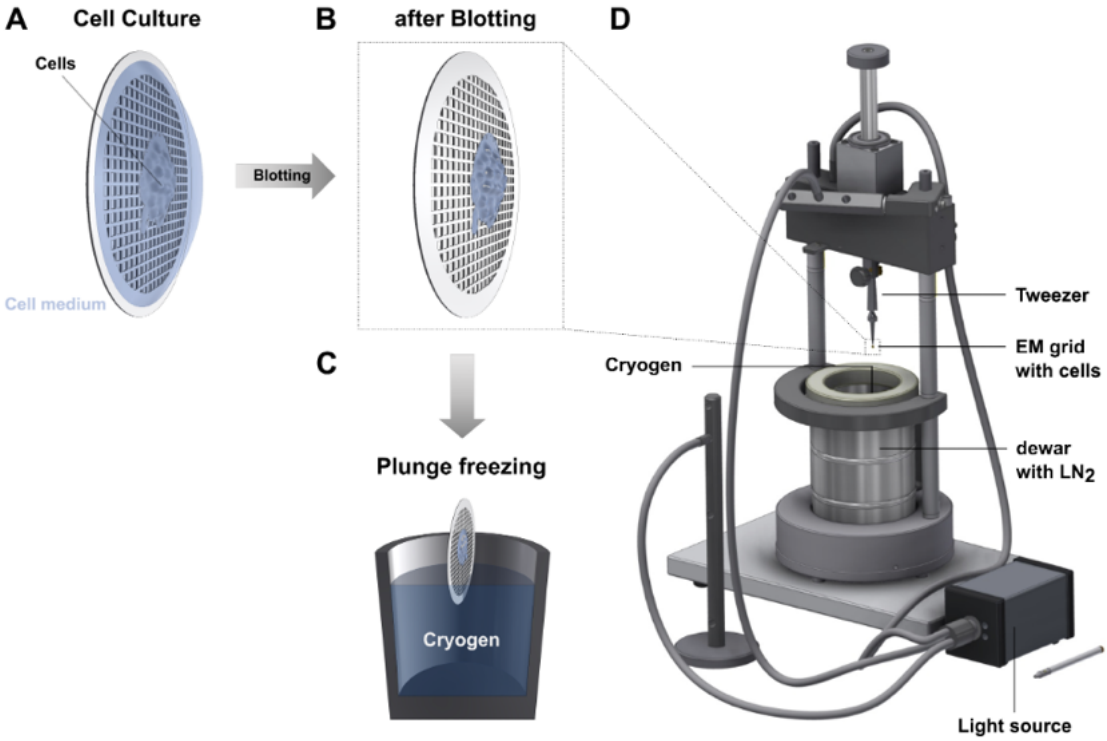

Figure 3.4.3 Manual plunge freezing. A: Cells are grown on the grid or applied with a pipette prior to plunge freezing. **B:** The access liquid is moved using plotting paper and **C:** the grid is plunged into cryogen. **D:** Shows a schematic of a manual plunge freezer as developed in the CryoEM technology workshop at the MPI of Biochemistry. Provided by Tim Laugks, used with permission.

A multitude of other sample preparation and rapid freezing techniques for fixation of biological specimen have been explored. While these systems are to date experimental, there are promising developments such as jet freezing for samples of intermediate thickness of circa 10 - 25 μm. Additionally, time resolution in freezing has also become an active field of research [110–112]. These developements are, however, beyond the scope of this thesis, and the reader is referred to excellent reviews elsewhere [108, 109].

3.4.3. Sample thinning

A technique that has dominated the sample preparation of cells and tissues for a long time was the usage of very sharp knife edges made from diamond to produce thin sections of plastic embedded or cryogenically frozen materials [113]. The "ultramicrotomy" technique has many advantages such as low cost compared to other thinning methods, high throughput, and the potential for consecutive sections from the sample to be investigated. However, the sections produced by ultramicrotomy show severe artifacts from the force applied to the sample by the diamond knife [12]. These artifacts include knife marks, crevasses, and compression of the sample. Thus, while still widely used in the preparation of plastic-embedded samples for electron microscopy, the cryogenic applications of diamond knife sectioning have decreased as they require significant user expertise and other techniques that largely preserve ultrastructure have become available, namely cryogenic focused ion beam - scanning electron microscopes [114].

3.4.4. The Focused Ion Beam - Scanning Electron Microscope

In replacement of diamond knife-based ultramicrotomy for cryogenic sample preparation, the focused ion beam - scanning electron microscope (FIB-SEM) is constantly gaining popularity in cryogenic sample preparation of cells and tissues for cryo-ET. This results mainly from the superior preservation of sample using the focused ion beam, enabling the elucidation of structures directly within thinned cell sections [10, 11]. While the FIB-SEM instrument originated in semiconductor applications [15] and the materials science [14], the following chapter describes the instrumentation and applications to biological systems at room temperature and in cryogenic conditions.

3.4.5. The FIB-SEM instrument

The FIB-SEM instruments consists of a scanning electron microscope and a focused ion beam that is oriented at 52° to 54° relative to the electron column. The exact angle

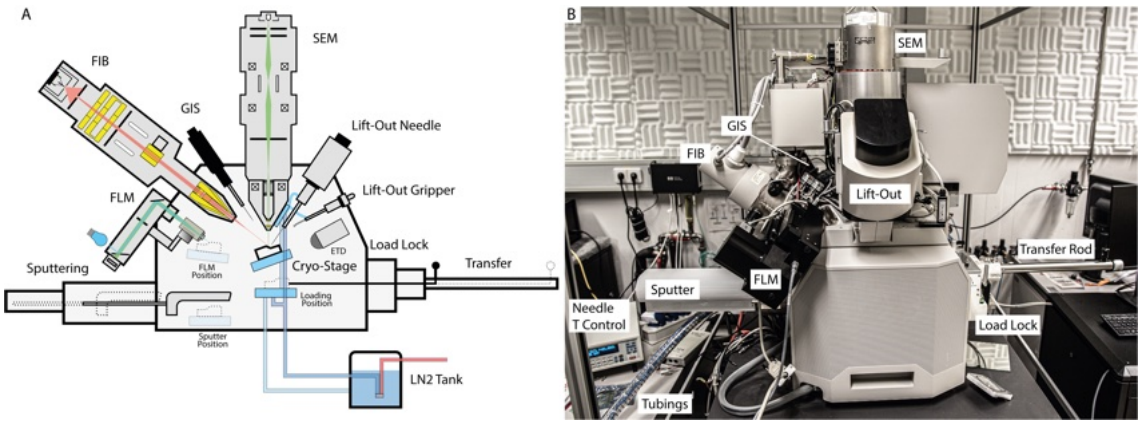

Figure 3.4.4 The modern cryo-FIB-SEM instrument. A: Schematic representation. **B:** Image of a Thermo Fisher Scientific Scios cryo-FIB-SEM with annotated main components.

depends on the microscope provider: Thermo Fisher Scientific instruments have a relative angle of 52°, Zeiss instruments 54°, and other instrument providers may vary as well. In a FIB-SEM instrument, the focused ion beam is used to site-specifically ablate sample material by continuous scanning with the ion beam. The SEM is used to monitor the cutting process or as imaging modality for volume electron microscopy applications [115].

A modern FIB-SEM instrument [22] comes with a number of accessories that allow for specific workflows. Such accessories comprise: a gas injection system (GIS) that is used to deposit protective layers such as organometallic platinum onto the sample to protect it from unspecific ablation during FIB milling; a sputtering system to increase the conductivity of non-conductive samples such as frozen-hydrated material by sputtering of atomic platinum; micromanipulation systems, either a gripper- or needle-type system that is cooled via a connection to an contaminator, the cryo-shield, inside the chamber to allow for cryogenic lift-out experiments; an in-chamber wide-field fluorescence light microscope to guide lamella preparations via e.g. endogenous fluorescence tags. Finally, the instrument usually comes with a multitude of detectors, such as backscattered electron detectors (T1) or secondary electron detectors (T2, Everhart Thornley Detector ETD). A cryo-stage and dedicated transfer system allow for vacuum transfer of frozen-hydrated samples at liquid nitrogen into the chamber. The stage usually has a tilt range of roughly 45° to -20° and is fully rotatable around its own axis. Whether tilting can be done at eucentric height depends on the specific cryo-stage.
More recently, stages similar to TEM stages, namely the 'CompuStage' (TFS) systems have been adapted to FIB-SEM instruments that include an automated sample exchange system on a plasmaFIB-SEM (PFIB-SEM) instrument and, thus, enable simultaneously pre-loading 12 grids into the instrument that then can be introduced into the microscope's chamber by automated sample exchange [36]. The CompuStage in this case has been modified such that the tilt range is -190° to +10°, making imag-

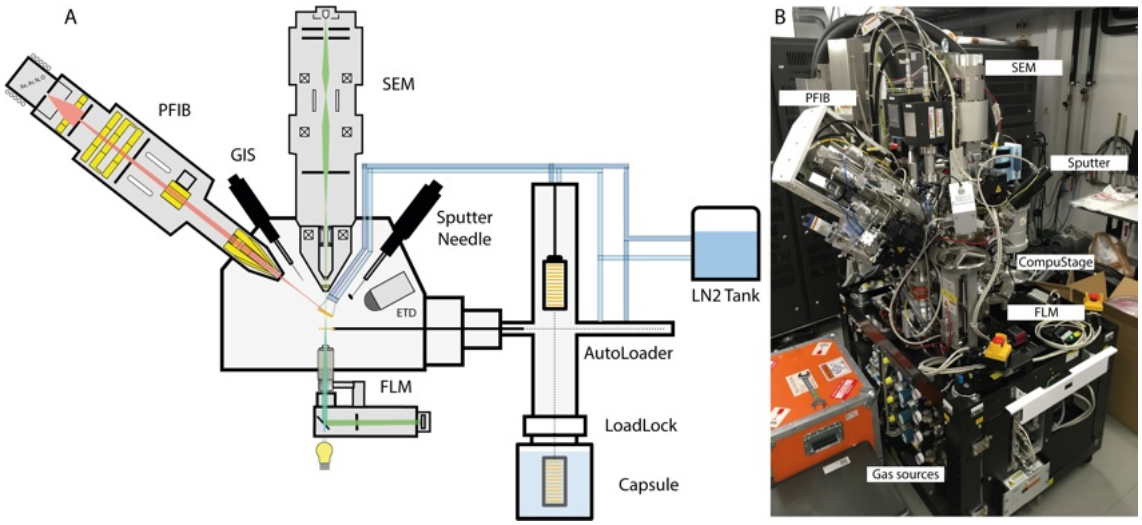

Figure 3.4.5 The next generation cryo-PFIB-SEM instrument. A: Schematic representation. **B:** Image of an Arctis cryo-PFIB-SEM with annotated main components.

ing the bottom of the grid accessible. However, perpendicular imaging from the top cannot be achieved, requiring adaptation to specific workflows such as the 'waffle' method [116].

3.4.6. Principle of Scanning Electron Microscopy (SEM)

While the development of scanning electron microscopes (SEM), by Max Knoll among others, started around the same time as TEMs, it took significantly longer until the first commercial SEMs were available. The prototype of the modern SEM goes back to Vladimir Zworykin in the 1940s [117] but it took many years of development at Charles Oatley's laboratory at the University of Cambridge until in the 1960s, the first commercial SEM produced by Cambridge Instruments became available [118]. The SEM focuses the electron beam to a spot and rasters the sample to collect electrons that are emitted from its surface and captured by a detector either within the chamber (Everhart-Thornley detector) or within the SEM column itself by applying a voltage to the column that collects electrons higher up the column (in-lense detectors). By corresponding the detected signal strength at the scanning position of the electron beam to a pixel value in an image, the SEM micrograph can be formed. In principle, all electrons that are shown to move upwards from the excitation volume of the electron beam in **Chapter 3.1.2** can be used in creating an image in SEM. Most commonly used, however, are secondary electrons as well as backscattered electrons (**Figure 3.1.2**).

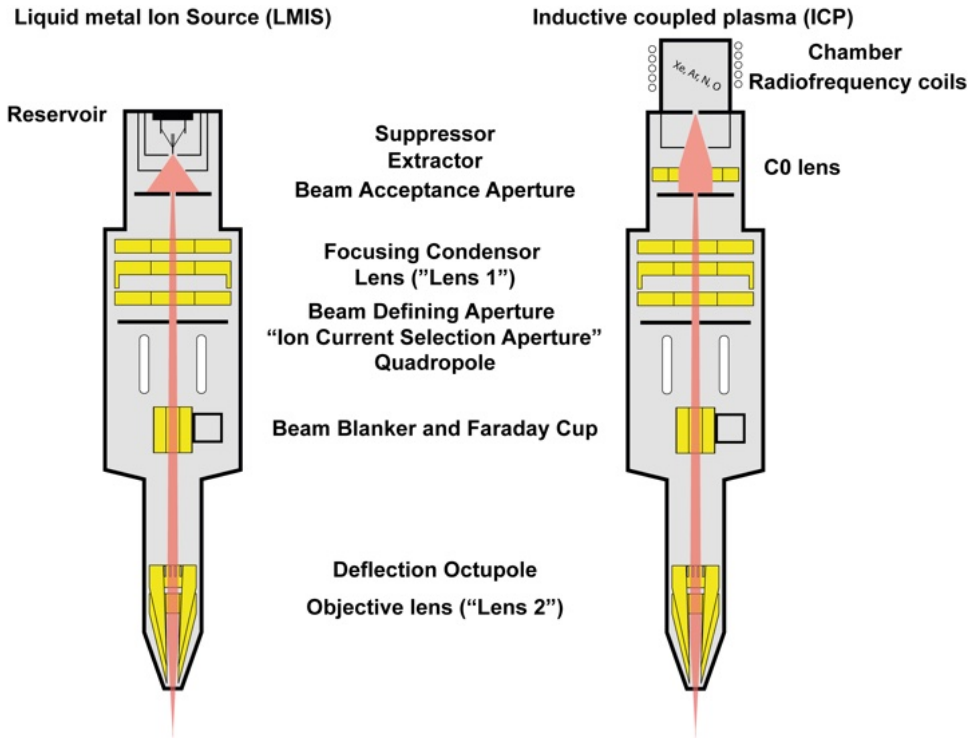

Figure 3.4.6 Comparison of an liquid metal ion source (LMIS, left) and inductively coupled plasma (ICP, right) ion column.

3.4.7. Principle of Focused Ion Beam (FIB) Technology

Similar to scanning electron microscopy, in FIB instruments the beam is focused to a spot that is rastered over the sample surface. The interaction of the ions with the sample created secondary electrons that can be detected using the same detectors as used in SEM. As described in the section on SEM imaging, the detected signal at an ion beam position can be translated into a pixel value in the FIB micrograph, generating the FIB scanning image. Other interactions of the FIB are used for nanomachining and other applications, as discussed below.

The FIB column

The lens system of FIB instruments differs from electron microscopes. Contrary to SEM columns, which can be operated with both electrostatic and electromagnetic lenses (where the latter usually give the better performance), ion beam lenses use electrostatic lenses as the mass of the ions is much higher than that of electrons. Therefore, creating enough force to focus ions by electromagnetic lenses would require lenses that weigh tons and are thus not practical [119]. While ion sources orginiated from gas-field ion sources (GFIS) [120], a number of different focused ion sources are currently in use in the field of cryo-FIB lamella preparation: Liquid metal ion sources (LMIS) [121], with a variety of metals, most commonly gallium, and plasma ion sources from either inductively coupled plasma (ICP) [122] or electron

cyclotron resonance (ECR) [123]. Throughout the rest of the thesis, the PFIB ion source is referring to an inductively coupled plasma, as those are the sources available in the lab. The structure of both LMIS and ICP columns are similar [124]. Ions are extracted from a source by an extraction voltage. The ion beam passes a first aperture, the beam acceptance aperture, which cuts off incoherent ions. After passing the focusing condenser lens or "lens 1", a second aperture, the beam defining aperture allows for the selection of the ion beam current. A beam blanker is used to quickly toggle between scanning mode and a Faraday cup, which allows for current measurement inside the column. Finally, a set of deflection octupoles inside the objective lens or "lens 2" is used for stigmating and scanning the focused beam on the sample. Plasma focused ion beam columns contain an additional lens, the C0 lens, directly after the extractor that aid in decreasing the spread of the beam at the beam acceptance aperture. The main difference of the two columns, however, lies in the nature and source of the ion beam. Liquid metal ion sources (LMIS) traditionally are based on gallium. This is mainly due to the low melting temperature of gallium, which is only a few degrees above room temperature and thus readily available as liquid. A LMIS works by extracting ions from a liquid metal, usually gallium, that forms a film around a tungsten needle [124]. The extraction electrode leads to the liquid metal film to form a Taylor cone [125] at the tip of the tungsten needle from which the ions are brought into the gas phase. This results in a virtual source size in the tens of nanometers [125] . An ICP ion source uses a ceramic chamber filled with a gas, e.g. xenon or argon, that is exposed to a radiofrequency (RF) pulse starting the plasma and continuously maintained by RF pulses. An opening at the bottom of the plasma chamber allows ions to be extracted but results in a much larger virtual source size in the range of several micrometers [124]. The extracted ions travel through the column and are focused onto the sample, leading to a number of interactions that can be used for specific applications and are discussed in the following chapter.

3.4.8. Ion-sample interactions and site-directed material ablation

The interactions of an incident ion beam with a sample are manifold and happen simultaneously (**Figure 3.4.7**). There are many different applications exploiting these interactions. On the one hand, the incident ion beam creates secondary electrons that can be detected by conventional electron detectors such as the Everhart-Thornley detector (ETD) or in-lens secondary electron detector (T2) [126]. Furthermore, the incident ions are going to ablate material in an acceleration voltage, current and incidence angle dependent manner, a phenomenon exploited for nanomachining of samples, e.g., for TEM lamella preparation. However, some of the incident ions are also going to implant into the sample. Applications of this phenomenon can be found in the material sciences, where the ion beam is used for doping materials. Furthermore, the ablation of material also creates secondary ions which can be detected us-

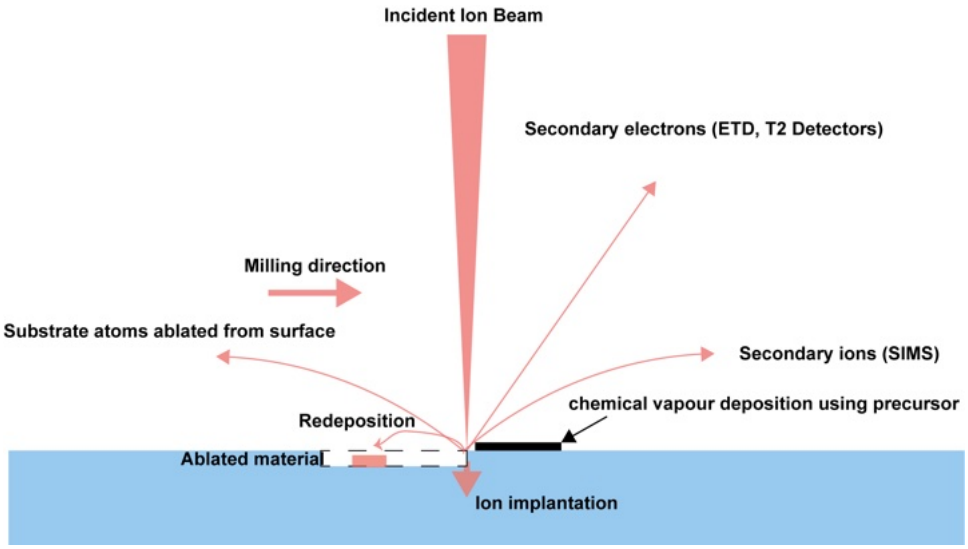

Figure 3.4.7 Ion-sample interactions

ing e.g. in-chamber time-of-flight (TOF) mass spectrometers in secondary ion mass spectrometry (SIMS) [127]. If specific precursor molecules are introduced into the chamber by for example a gas injection system (GIS) [22], the ion beam can be used to cure the precursor to fabricate nanostructures, commonly referred to as chemical vapor deposition (CVD). Finally, some of the ablated ions will not go into the gas phase within the vacuum chamber but rather redeposit on the sample itself. Redeposition can be used for micro-welding material and its application will be explored throughout this thesis for attachments in lift-out preparation at cryogenic conditions where site-specific CVD is not possible. For a exhaustive discussion on the applications of ion beams, the reader is referred to the recent FIB roadmap put together by a consortium of materials scientists in the FIB field [124].

3.4.9. Room temperature applications of (FIB-)SEM instruments: Volume SEM and other EM workflows

Scanning electron microscopy has found many applications for the characterization of biological specimen. Traditionally, the samples were prepared by shadowing metals onto them to make them conductive and, therefore, well behaving in the SEM [128]. While especially freeze-fracture techniques have given a breadth of insights into the ultrastructure of biological specimen, these techniques usually allow for a single surface to be characterized per sample. Ablation techniques, either using focused ion beams or diamond knifes, have enabled to expose sequential surfaces from a sample to be imaged within the vacuum chamber of the SEM. Combined with contrasting methods, these techniques have given unprecedented insights into the ultrastructure of large volumes on the cell and organelle level, most prominently creating the field of connectomics, the mapping of an entire neuronal circuit. Alternatively, the collec-

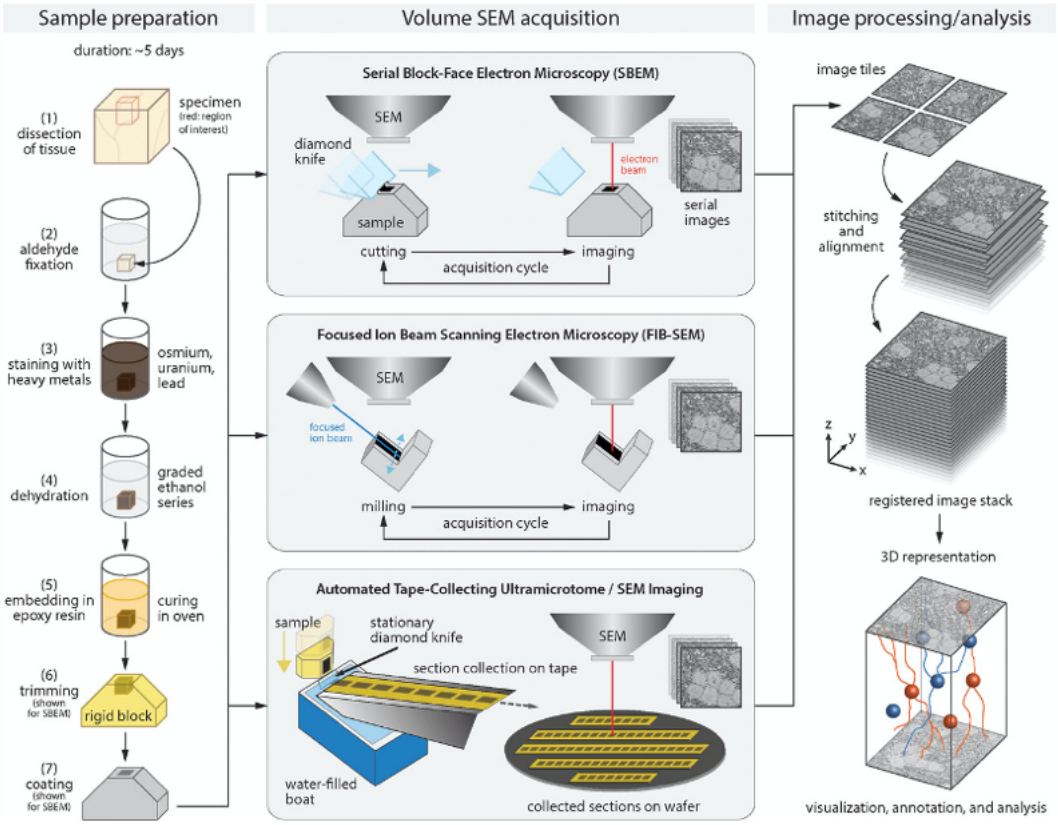

Figure 3.4.8 Overview of volume electron microscopy (vEM) techniques. Adapted from [132] with permissions.

tion of serial sections by automated tape-collecting ultramicrotomy and subsequent SEM imaging can be used to quasi-continuously map tissues at similar scales [129]. These techniques have seen immense developments over the last decades and are summarised in (**Figure 3.4.8**). The interested reader is referred to fabulous reviews on the topic [130, 131]. While vast amounts of valuable information on large volumes can be obtained by these techniques, the obtainable resolution is limited and macromolecular complexes have remained elusive to these techniques. If research questions require molecular resolution, to date focused ion beam milling at cryogenic temperature is the only method that has been demonstrated to yield samples that are sufficiently preserved to allow for obtaining structures directly from within the native cellular environment. The preparation techniques using cryo-FIB instruments will be discussed in the following sections.

3.4.10. Focused ion beam milling for cryo-ET sample preparation

Since the first proof-of-principle experiments of thinning *E. coli* cells with the focused ion beam for subsequent TEM experiments by M. Marko in 2007 [11], the manipulation of biological samples with a FIB at cryogenic temperatures has undergone tremendous development. Nowadays, many cryo-FIB workflows for biological samples have been developed and spread into electron microscopy labs and facilities

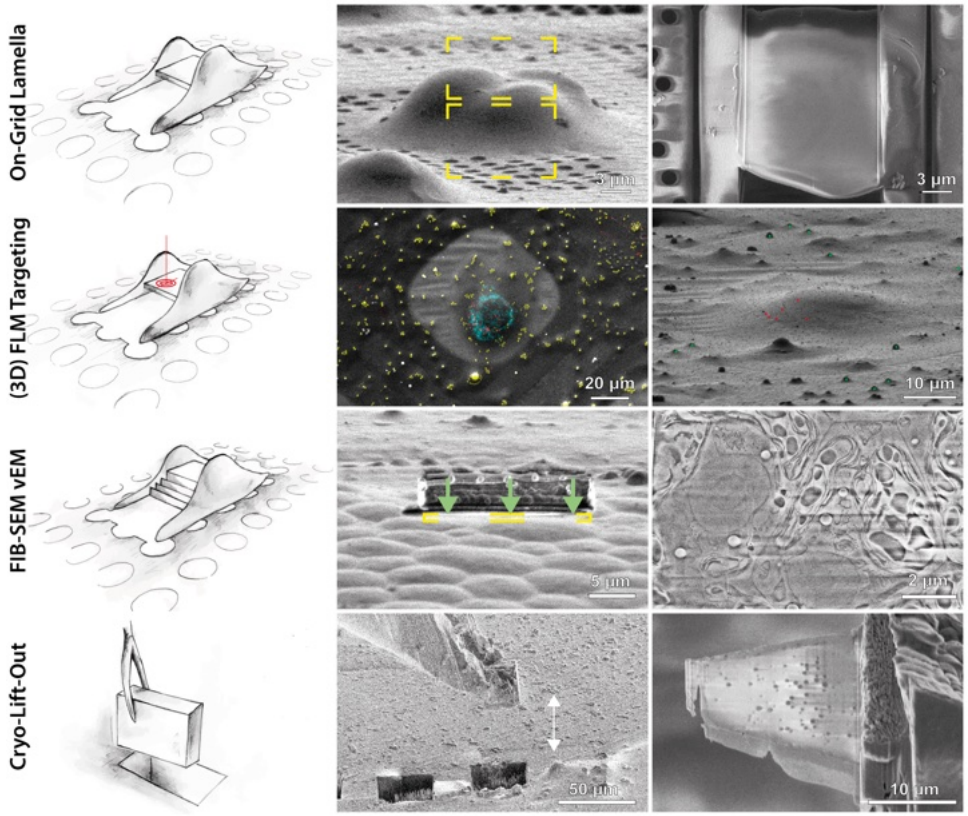

Figure 3.4.9 Overview of cryo-FIB applications. Images in 3D-FLM Targeting produced in collaboration with Dr. Sara K. Goetz and Dr. Herman K.H. Fung. Drawings by Dr. Jürgen M. Plitzko, with permission.

around the world. The most common workflows are described below and summarized in **Figure 3.4.9**.

On-grid thinning of specimen

Multiple ways of thinning biological specimen on the grid have been developed and optimised [10, 133–136]. They can be separated by the type of cryo-fixation that was used to prepare the sample. The resulting sample is very different depending on the freezing method and, thus, the workflow has to be adapted for plunge frozen and high-pressure frozen samples. The main differences in these two cryo-fixation approaches lies in the amount of buffer remaining on the sample surface: plunge freezing generally tries to reduce the amount of buffer as much as possible without drying out the sample. Cells on a plunge-frozen grid appear as easily identifiable bumps on the surface; as the buffer is removed, the outline of the cell is clearly visible. For grids prepared by high-pressure freezing, this is not the case as the sample is embedded in a thick layer of ice. Its thickness depends on the cavity height of the sample carrier used [21, 106]. Therefore, identification of positions has to either be done based on surface features, SEM imaging [21, 137], or fluorescence microscopy [138]. If the sample is dense enough in biological material, no targeting may be needed. In either method, on-grid thinning relies on ablated material from

either one or both sides of the sample until a thin region suitable for TEM imaging is created. For plunge-frozen samples, there are two methods of on-grid preparations: lamella and wedge milling. Lamella milling creates a thin section by ablating material above and below the target volume from an angle of 8° to 12° or higher. To protect the sample and avoid the ablation of regions around the exposed area, a protective layer of organometallic platinum (trimethyl(methylcyclopentadienyl) platinum) [10, 22] is deposited onto the sample using the gas injection system. To mitigate sample charging, metallic platinum can be sputtered onto the sample before or after GIS-assisted organometallic platinum deposition. For heavily charging samples, doing both before and after GIS deposition may help. During the subsequent shaping of the lamella, the beam current is sequentially lowered from approximately 1-3 nA in rough milling down to 30 to 50 pA for final thinning. To compensate for the ablation divergence that leads to a wedge-shape lamella rather than a flat surface, the stage can be tilted up or down from the original milling angle by 0.5 - 2 degrees to allow for backthinning of the lamella. This compensates the wedge-shape and flattens the lamella surface, giving close to homogeneous lamella thickness along its length.

Correlative lamella preparation

As the mean free path of an electron in biological material is around 300-400 nm [98], the imageable volume generally has to be below 200 nm in thickness to obtain good results. However, this means that only about 1% of the cell ends up in the lamella that makes it into the transmission electron microscope, though the percentage may differ according the size of the organism of interest. As a result, when one is interested in specific events inside the cell, the probability of retaining the feature of interest diminishes rapidly with decreasing feature size and number of events per cell. Fluroescence light microscopy probes are, however, widely available for a wide range of organisms used in the biological sciences. Correlative light and electron microscopy (CLEM) can help in targeting specific events within a cell by correlating the fluorescence images with the cryo-FIB images to allow for site-specific preparation of lamellae [138–144]. This significantly increases the success rate for rare events, as lamellae are only prepared in regions where the feature of interest has been observed. Fiducials that are visible in both FLM and FIB imaging modality can further help improve the targeting accuracy through 3D correlation [138].

Cryogenic FIB-SEM tomography volume imaging

Similar to workflows described in **Chapter 3.4.9**, volume electron microscopy by FIB-SEM tomography can be applied at cryogenic temperatures as well [21, 115, 137, 145, 146]. The difference is in the contrast mechanism. As plastic embedded biological samples FIB-SEM tomography are generally stained with heavy metals, the

contrast generated by SEM imaging on the block face of such a sample is dominated by secondary electrons formed by the interaction of the electron beam with the high atomic number elements in reagents used for staining such as osmium (VIII) tetroxide (OsO_4), uranyl acetate ($UO_2(CH_3CO_2)_2$ (H_2O) * H_2O), and lead citrate.

In an unstained biological sample at cryogenic temperatures, however, contrast is mainly formed due to the local differences in the potential of different cellular constituents, usually referred to as charging contrast. The yield in secondary electrons from the sample surface is hereby relatively low. Additionally, as the biological sample is generally not conductive, the electrons of the incident beam cannot dissipate in the sample leading to charging artifacts during scanning of the block face. To mitigate the charging artifacts, imaging is generally aimed to be performed at the lowest voltage possible that still yields sufficient electrons for contrast formation (usually 1-3 kV) and short dwell times (around 100 ns) combined with high line integration are used [115, 147]. Line integration, image integration, alternative scanning strategies, and combinations thereof, may help in reducing noise or charging artifacts in the SEM images.

Lift-out at cryogenic temperatures

If thick samples up to 200 μm are to be investigated, ablating the material above and below the target volume as in preparations on the grid becomes impractical as the ablation rates of gallium-based FIBs is too low to be able to mill through more than around 30 μm in a reasonable amount of time. While plasma focused ion beams can in principle mitigate this problem, they have only recently been introduced to the field and many problems regarding damage of the surrounding material by the beam remain to be solved. An alternative to ablating the entire material during lamella preparation is the extraction and deposition of a tiny fraction of the material to a receiver grid using micromanipulation devices [22]. This process is called lift-out. While a standard procedure for TEM lamella preparation in the materials science at room temperature, the routine adaptation to cryogenic temperatures is difficult [17–19, 148–151]. There are several challenges when adapting the lift-out workflow to cryogenic conditions. First, the micromanipulation device needs to be kept at low temperature to prevent the crystallization of the vitreous ice in the sample during transfer. Second, the workflow needs to be adapted to accommodate the TEM cartridges (e.g. the AutoGrid), which implies geometrical constraints on the receiver grid and lift-out procedure. Third, performing the attachment the same way as at room temperature is suboptimal or even impossible. At room temperature, the GIS is used to deposit platinum site-specifically to weld the lift-out device and the sample together via (electron or ion) beam-assisted deposition. At cryogenic conditions, the precursor gas condensates onto the entire sample, thus increasing the thickness of the protec-

tive platinum layer in every step of the lift-out process. In consequence, if multiple lift-out preparations are performed on the same sample, the platinum layer becomes thicker and thicker until the biological material cannot be reached anymore without ablation large amounts of material, rendering the sample unusable with gallium ion sources. As we will see in **Chapters 4.4 and 4.5**, alternative transfer strategies have been developed and are now commonly used in cryo-lift-out.

3.4.11. Challenges in sample preparation of vitreously frozen cells and tissues

Limitations in the preparation of samples by cryo-FIB milling are manifold. First of all, on-grid sample preparation is limited in throughput, thus automated procedures are essential to streamline the lamella preparation process [21, 152–154]. Furthermore, the amenable sample size for plunge freezing is limited. Consequently, if biological questions are to be tackled in intact tissue samples, high-pressure freezing needs to be deployed. However, the success rate of high-pressure freezing of thick specimen, though hard to quantify due to lack of suitable methods, is low. Combined with the low throughput of lift-out sample preparation, it makes the application of cryo-ET to specimen > 20 μm in thickness very challenging [149]. Finally, targeting strategies using either SEM volume imaging or FLM are time-consuming and manual. Therefore, technical and technological advances in lamella preparation are needed to enable the tackling of novel biological questions within specimen previously unamenable to molecular resolution imaging, some of which will be presented throughout this thesis.

3.5. Visual proteomics and *in situ* structural biology

Structural biology in the reductionist's approach of studying isolated macromolecules by X-ray crystallography, nuclear magnetic resonance spectroscopy or more recently cryo-electron microscopy has given invaluable insights into the mechanisms of important biological processes such as transcription [155], translation [156], and many others [157, 158]. However, all of these techniques require the purification of the complexes from the cellular environment of the organisms of origin or from expression vessels, e.g., *Escherichia coli* or *Drosophila melanogaster* S2 cells, by recombinant protein expression. Due to the disruptive nature of purifying the proteins of interest, all information of the transient interactions or spatial relationship of the protein of interest with the proteome are lost. Since cryo-ET allows the detection and structure determination of macromolecules within a tomogram, it opened the prospects of visual proteomics: Studying proteins and their interactions within the native environment of the cell by creating snapshots of the cellular ultrastructure using rapid freezing and

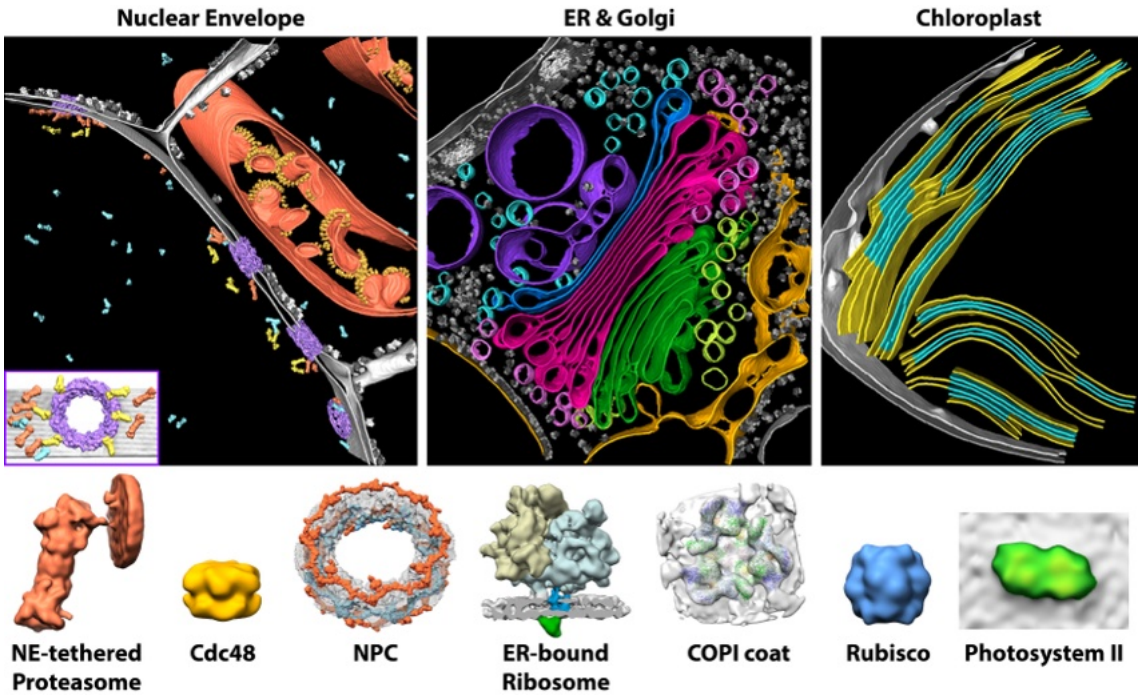

Figure 3.5.1 Visual proteomics by cryo-electron tomography of FIB-milled lamellae. Overview of the different organelles and macromolecular structures studied in *C. reinhardtii* as an example for the potential of cryo-ET for visual proteomics. Kindly provided by Dr. Ben Engel. Original work in [160–168]

tomographic reconstruction [16, 159]. Cellular tomograms are, thus, a rich source of information on local molecular interactions that form the basis of biological functions within the cell.

Examples of proteins studied by cryo-ET *in situ* have become numerous in recent years [160–168]. Due to the reproducible anatomy and relatively low crowding in *C. reinhardtii* cells resulting in great contrast, the alga has been the subject of extensive study by cryo-ET with many structures determined (**Figure 3.5.1**) and represents a great example of the information obtainable by *in situ* structural biology.

While to date the protein structures determined *in situ* are generally limited by size to macromolecular complexes of 500 kDa and above (**Chapter 3.3.4**), the field is continuously evolving and the lower size boundaries of the complexes studied are being pushed by technological advances such as detectors and phase plates [51]. Additionally, the spectrum of organisms deemed amenable to cryo-ET studies is also widened by continuous development in cryo-FIB technology such as cryo-lift-out and the use of plasma ion sources as described above. The field of *in situ* structural biology therefore awaits application to disease models, patient biopsies, and the wide variety of model and non-model organisms to understand biological processes and describe new phenomena in cellular structural biology that hold the potential to deepen our understanding of how cellular systems work at the molecular scale.

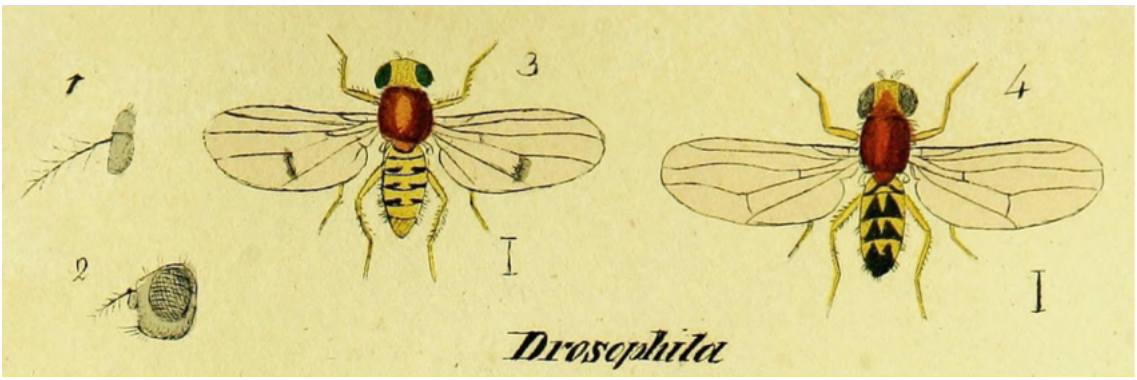

Figure 3.6.1 Meigen's first drawing of the *Drosophila* fruit fly. Adapted from [169], with permissions.

3.6. *Drosophila* as a model organism for molecular and developmental biology

3.6.1. Oogenesis in *Drosophila melanogaster*

Drosophila melanogaster, first described by Johann Wilhelm Meigen in 1830 (**Figure 3.6.1**) [169] and commonly known as the fruit fly, has been cultivated and documented in biological research laboratories for the first time in 1901 in the laboratory of William Ernest Castle [170]. Later, Thomas Hunt Morgan adopted it for genetic studies which should later award him the Nobel Prize in Physiology and Medicine in 1933 "for his discoveries concerning the role played by the chromosome in heredity" [171], the first of six Nobel prizes related to fruit fly research. Nowadays, many research fields such as Genetics and Developmental Biology are no longer imaginable without seminal contributions from the findings obtained by studying this fascinating model system [172].

Since its establishment as a model organism by the Morgan laboratory, *D. melanogaster* has been widely adopted and appreciated for its relatively short generation time, easy handling, inexpensive cultivation and large number of progeny as well as externally laid embryos, making it well suited to study embryogenesis. Also, *Drosophila* has served as common model for the molecular and cellular mechanisms of mRNA localisation, polarity and other principles of development [175]. In the fly, the process of oogenesis takes places within the ovaries of the adult female. The ovaries come in pairs and are connected to the oviduct. The ovary's structure is maintained by a layer of muscles, the peritoneal sheath. Each ovary is composed of multiple smaller structure called ovarioles, which are individually enveloped by the epithelial sheath muscles. An ovary holds approximately 16 to 18 ovarioles (**Figure 3.6.2**). The maturation of the egg takes place in each of them simultaneously, progressing from the anterior positioned stem cells to fully developed eggs at the posterior end. The development of the egg starts in the germarium, a structure at the anterior tip. For each developed egg, a stem cell in the germarium divides 4 times by incomplete cytokinesis to form a

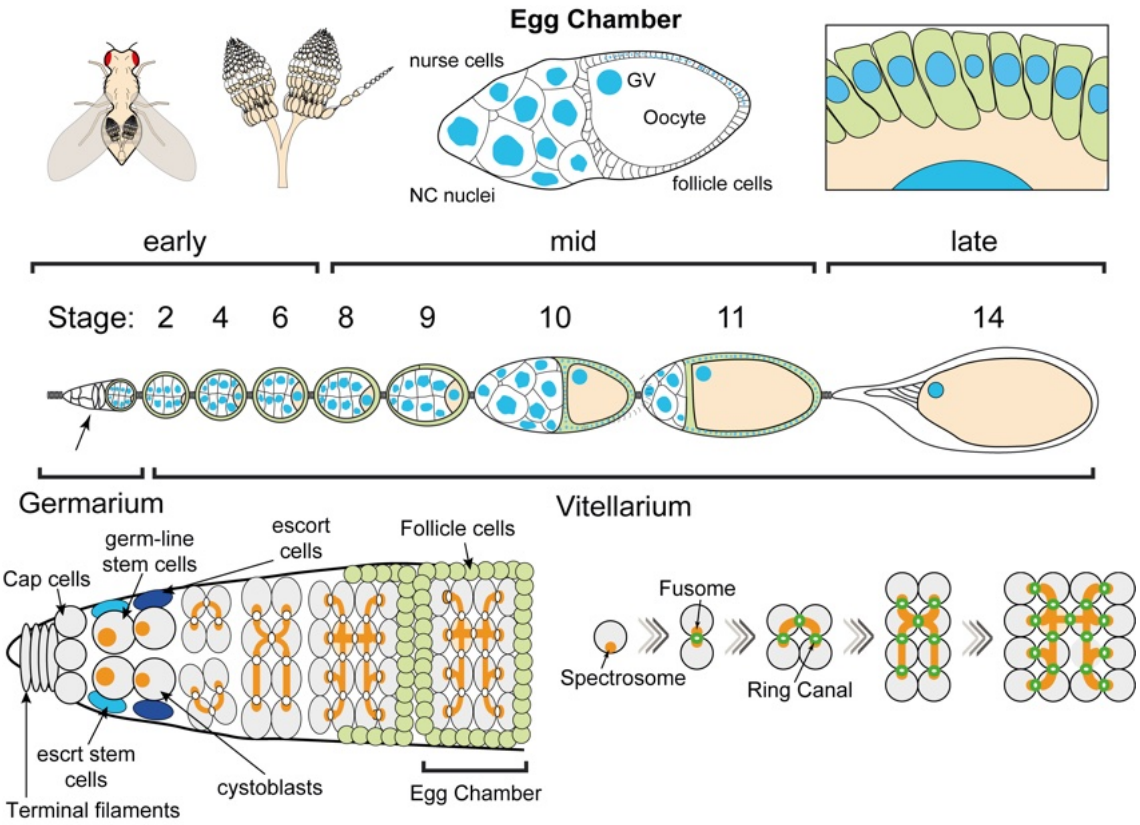

Figure 3.6.2 The anatomy and cell biology of oogenesis in *D. melanogaster*. Drawn with inspirations from [173, 174].

16-cell cyst. Of these 16 cells, 1 is determined to be the oocyte and transcriptionally silenced (**Figure 3.6.2**) [176]. The 15 remaining germ-line cells become 'nurse cells', supporting cells that feed the oocyte with the maternally deposited protein and mRNA load needed for embryogenic development through cytoplasmic bridges called ring canals that originate from the incomplete cytokinesis during cyst formation. The 16 germ-line cells are engulfed by an epithelial layer formed by follicle cells, the 'somatic follicular epithelium'. Follicle cells are excreting factors essential for oogenesis and form the mechanical barriers of the egg, the vitelline membrane and chorion. The tissue comprising nurse cells, oocytes, and follicle cells is called the egg chamber. The stages of the egg chamber are categorized by specific cell-cycle programs of the follicle cells, namely mitosis during early stages 1-6, endocycle (i.e. replication of the genome without segregation during mitosis) during middle stages 7-10A, and gene amplification for the late stages 10B-14 (**Figure 3.6.2**) [177]. During ovulation, the mature egg detaches from the epithelium and passes into the uterus. The epithelial layer left behind forms a structure resembling the *corpus luteum* found in mammals that is involved in the secretion of reproduction-specific hormones [178].

Throughout oogenesis, the delivery of proteins and RNAs from the nurse cells to the oocyte forms the important gradients of morphogens that define the animal's body axes during embryogenesis [179, 180]. Due to the specialized nature of the cell

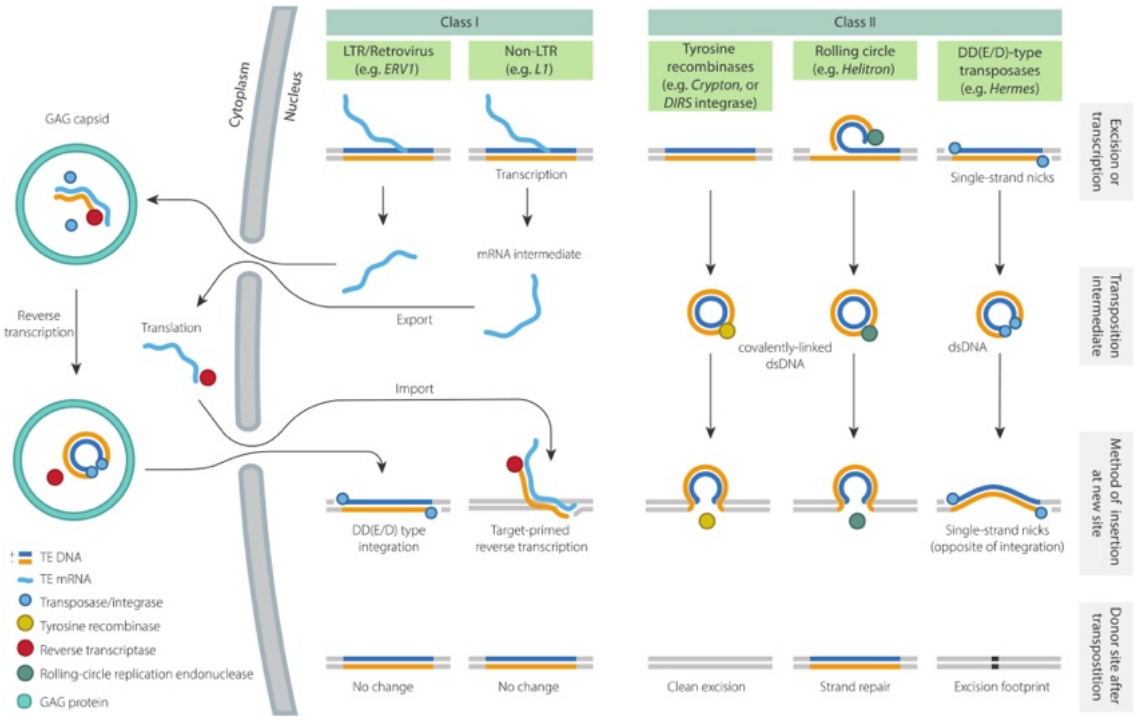

Figure 3.6.3 Classification of transposable elements. Schematic of the life cycle of the different classes of transposable elements. Class III that usually incorporates elements that do not fit into neither Class I nor Class II is not shown. Taken from [181], with permission.

types in the egg chamber, their morphological differences are striking, e.g. on the level of nuclear structure: while the follicle cells show typical nucleus sizes of 5-10 μm as known from other somatic cells, the germ line nuclei of oocytes (also known as 'germ vesicle') and nurse cells are significantly larger, with a diameter of about 40 μm. As the organization and structure of the nuclei changes, it is imaginable that also its ultrastructure and distribution of macromolecular complexes within the nuclear envelope may be different. This will be investigated in **Chapter 4.7**. As we will see, there are ultrastructural differences going from germ-line nuclei to a highly actively transcribing somatic follicle cell nuclei. However, at the preservation of plastic embedded samples, it is challenging to observe. Therefore, the technical advances presented throughout this thesis are needed to perform cryo-ET inside these large samples to be able to tackle questions on the cell-type specific ultrastructural differences in multicellular organisms.

3.6.2. Transposable elements and their regulation

Transposable elements

Transposable elements (TEs), "transposons" or "jumping genes", are DNA sequences that have the ability to move or "transpose" within the genome of an organism. After their discovery and description as dispersed genes by Barbara McClintock in the

1940s, TEs remained understudied and their biological relevance on genome integrity and biological evolution underappreciated for decades. Only when the process of transposition were discovered in other systems such as bacteria, yeast, and bacteriophages in the 1960s to 1970s, the appreciation for McClintock's work grew, leading to her winning the Nobel prize in 1983 "for the discovery of mobile genetic elements" [171].
In *Drosophila*, transposable elements have most probably been first examined as the unknown triggers of hybrid dysgenesis, a condition in which the male transmission of a certain genetic factor results in a sterile offspring, while the female transmission does not. It took until the 1980s for the field to realize that the underlying mechanism of hybrid dysgenesis were transposable elements. Since then, research on TEs in *Drosophila* has greatly benefited from the advantages provided by the model organism for genetic studies, such as genetic engineering, a small number of chromosomes and continuously developed sequencing techniques, most of the time tested specifically on the fruit fly. It paved the way for the use of transposable elements in first genetically transformation of a higher eukaryote, the fruit fly [182]. Additionally, it led to improvements in the understanding of the molecular mechanisms of TEs and noteworthy discoveries in TE regulation and host defense mechanisms such as the regulation by small RNAs, e.g. the piRNA pathway [183–185].

Following a classification introduced by David Finnegan in 1989 [186], transposable elements can be divided into two major classes by the chemical nature of the intermediates that are produced from their genomic information: Class I TEs or retrotransposons transpose via an RNA intermediate that is reverse-transcribed into DNA by a reverse transcriptase. Class II TEs or DNA transposons lack an RNA intermediate and transpose via a DNA intermediate (**Figure 3.6.3**). Some transposable elements show a mixture of the two mechanisms and are usually referred to as Class III TEs. Subclassification of these classes are based on the mechanisms of chromosomal integration. Class I TEs contain five subclasses: long terminal repeats (LTR) retrotransposons, *Dictyostelium* intermediate repeat sequence (DIRS)-like elements, Penelope-like elements (PLEs), long interspersed nuclear elements (LINEs) and short interspersed nuclear elements (SINEs). LTRs and LINEs are the most abundant in *D. melanogaster*. LTR retrotransposons are of specific interest as they show an genome integration reaction catalyzed by an integrase much like retroviruses. The superfamilies of the LTR subclass are Ty1/copia, Ty3/gypsy, and endogenous retroviruses (ERVs) [181].

Transposable elements are regulated by multiple mechanisms, the most prominent being the small RNA pathways such as the PIWI-interacting RNA (piRNA) and small interfering (siRNA) pathway [184]. piRNAs are the main silencing mechanism of

transposable elements in animal gonads. They consist of 23- to 30-nucleotide small RNAs that guide PIWI-clade Argonaute proteins to recognize and silence TEs. PiRNAs are found in discrete genomic loci that seem to be of TE remnant origin. These arrangement of piRNAs on the genome were thus termed piRNA clusters. In consequence, there is a constant evolutionary race between the transposable elements present in a genome and the defense mechanisms that evolve to regulate them. Notably, if the defense mechanisms are defect or genetically knocked out, many of the ancient transposable elements present in the genome are de-repressed and start to appear in their proteineous components within the cell again. Some transposable elements are even currently active in the *D. melanogaster* model. A member of the LTR retrotransposons in the *D. melanogaster* genome is *copia* [187], also known as Ty1 in yeast [188] and other organisms [189]. In *Drosophila* S2 cell culture, virus-like particles were observed inside the nucleus in the wildtype background (**Figure 3.6.4**) [190]. Other elements such as Ty3 are only observed in the cytoplasm of *S. cerevisiae* cells [191, 192]. However, in mutants that remove the nucleocapsid proteins from the macromolecular assembly, localization of these larger clusters of capsids changes from the cytoplasm to within the nucleus [193]. While nucleocytoplasmic transport mechanisms of retrotransposons are largely unknown, LTR retrotransposons have many parallels to retroviruses such as human immunodeficiency virus 1 (HIV-1) [192, 194, 195]. In fact, it is thought that from an evolutionary perspective, retrotransposons may be retroviruses that lost the ability to transposition by loss of genes such as the ENV gene. Therefore, it is imaginable that the nucleocytoplasmic transport routes of the genetic information of the retrotransposons may be similar to HIV-1, which is through interaction with or transport through the nuclear pore complex. Thus, it is worthwhile to review the structure of the nuclear pore complex and its mechanisms of nucleocytoplasmic transport with respect to the replication cycle of transposable elements.

3.6.3. Nuclear pore complex structure and nucleocytoplasmic transport

Different degrees of compartmentalization represent a hallmark of biological evolution [197, 198]. The evolution of the plasma membrane allowed for the differentiation of 'outside' and 'inside' the organism, allowing for the upholding of the non-equilibrium state of life forms as we know them today [199, 200]. The evolution of eukaryotes gave rise to another compartment containing most of the genetic information in eukaryotic organisms: the nucleus [201]. Compartmentalization by membranes poses a logistic problem: Macromolecules such as proteins and RNA have to pass the membranous bilayers separating the compartments to get to their location of action. In the case of the nucleus, the barrier even consists of a double membrane, the inner and outer nuclear membrane. Nuclear pore complexes span the two membranes, fusing outer and inner nuclear membrane and allow for nucleocytoplasmic transport [202].

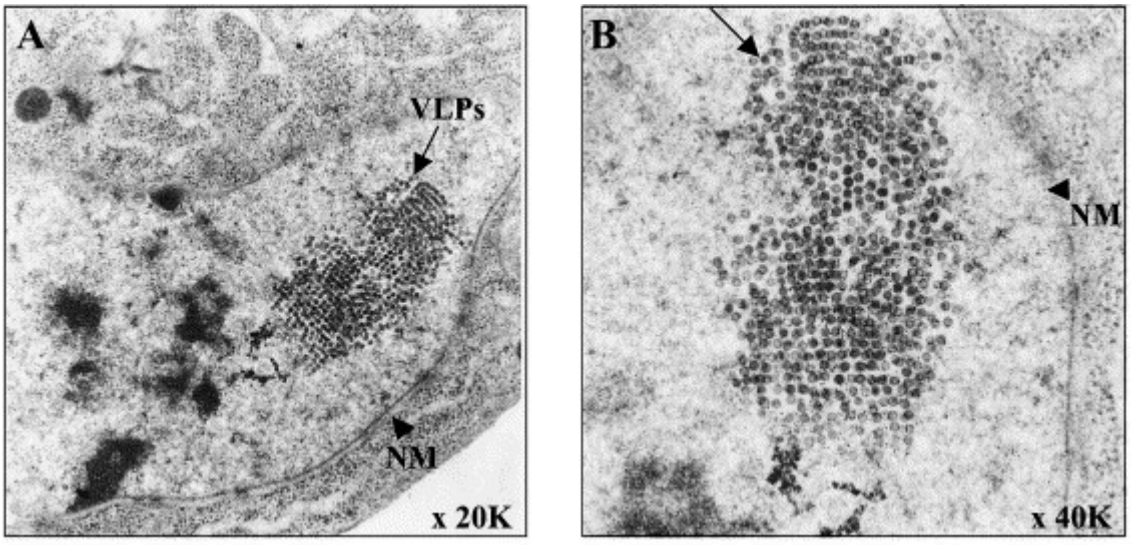

Figure 3.6.4 Classic TEM observation of *copia* in *D. melanogaster* S2 cells. A: TEM section showing the virus-like particles accumulate in the nucleus. Adapted from [190], with permission.

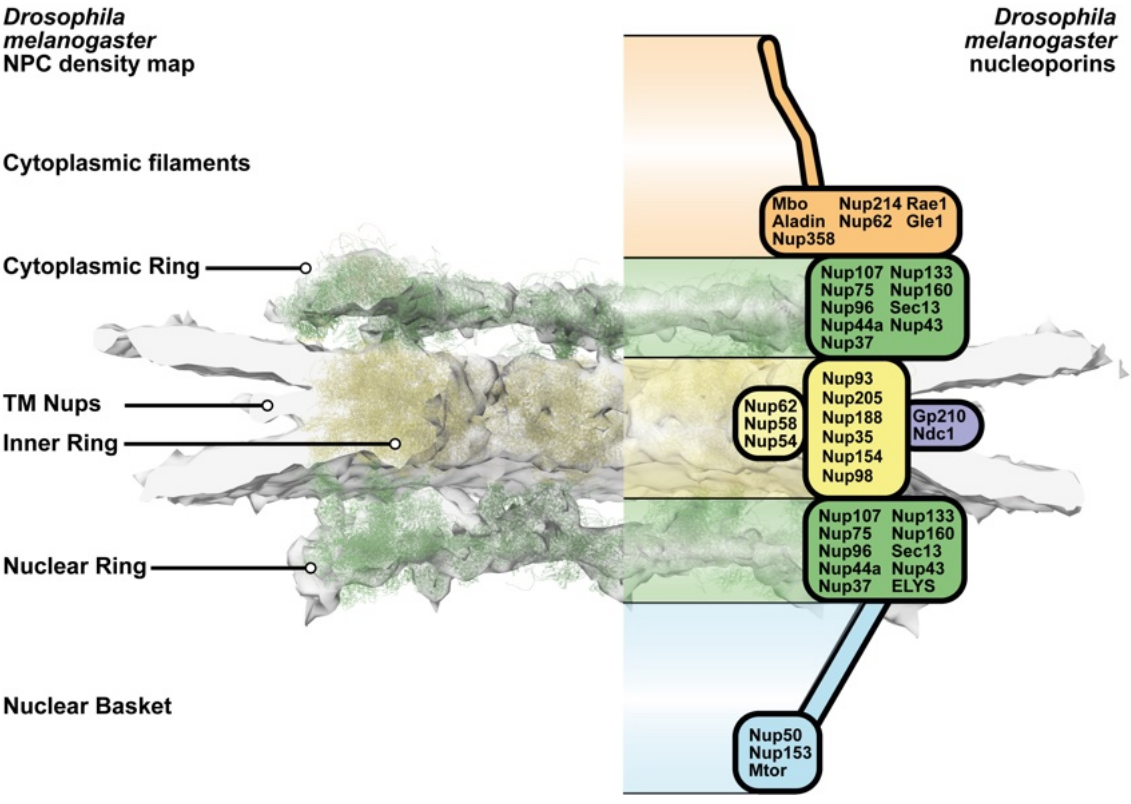

Figure 3.6.5 The *D. melanogaster* nuclear pore complex and its components. On the left, the structure as determined in **Chapter 4.7** is shown with annotations of the different subcomponents of the pore on the cryo-ET density. Cytoplasmic filaments and nuclear basket proteins are not captured in the subtomogram average. On the right, the individual proteins that make up the components are listed. Inspired by [196] and adapted, with permission, using the NPC density of *D. melanogaster* determined in **Chapter 4.7**.

Not only do NPCs form the scaffold for nucleocytoplasmic transport, they also have an important role in regulation by tightly controlling the import and export of e.g. transcription factors and other macromolecules. NPCs are therefore essential to a wide variety of biological processes such as cell cycle and cellular growth regulation.

The nuclear pore complex (NPC) is formed by nucleoporins or Nups that are encoded in about 30 genes. The Nup proteins span a wide size range from several 10s of kDa up to 358 kDa [202]. They can be divided into scaffold and phenylalanine-glycine (FG) Nups and assemble in subcomplexes that come together in multiple copies to form the modules of the NPC. The different modules consist of (from cytoplasm to nucleoplasm) (1) the cytoplasmic filaments, (2) the cytoplasmic ring, (3) the inner ring and transmembrane Nups, (4) the nuclear ring and (5) the nuclear basket [203–207]. FG-Nups form the size discriminating matrix within the central channel of the NPC, allowing small molecules <30 kDa to diffuse freely through the pore; larger macromolecules need to be actively transported. Scaffold Nups form the structural basis of the nuclear pore complex and generally form stable protein-protein interactions. The different modules and the nucleoporins forming them are illustrated on the subtomogram average of a *D. melanogaster* nuclear pore complex in **Figure 3.6.5**, derived from work presented in **Chapter 4.7**.

While showing a large size range, Nups are generally composed of similar secondary structures: beta propeller domains, alpha solenoids and coiled coil elements [202]. In general, the nuclear pore complex shows similar structural architecture as other membrane-binding complexes such as COPI and COPII vesicles [208]. Interestingly, some Nups form incomplete beta propellers to form protein-protein interactions. The last blade is filled by an interaction partner completing the beta propeller such as Sec13, which is a component of both the NPC and COPII vesicles. The different modules of the NPC are formed from several subcomplexes. The inner ring ring complex is the anchor point for the central channel complex. In *D. melanogaster*, the inner ring complex consists of Nup93, Nup205, Nup188, Nup35, Nup154, and Nup98 [202]. The central channel complex or Nup62 complex consists of three FG Nups: Nup62, Nup58 and Nup54 [202]. The cytoplasmic and nuclear ring are assembled from a similar pool of proteins, with ELYS being the exception and only present on the nuclear ring in human, presumably similar in *Drosophila*. The cytoplasmic filaments and nuclear basket are assembled from distinct proteins of which Nup153, a FG-Nup component in the nuclear basket, and Nup358 (also known as Ran binding protein 2 or RanBP2) are of particular importance to the transport of the mature HIV-1 capsid through the nuclear pore complex (**Figure 3.6.6**) [209].

The transport of the mature human immunodeficiency virus 1 (HIV-1) capsid through the nuclear pore complex has recently been visualized by cryo-ET [210]. It represents

one of the first studies of nucleocytoplasmic transport of viral capsids at the structural preservation of cryo-FIB milling and cryo-ET. It was found that fully assembled capsids are transported through the pore. In the current model of the nuclear entry of HIV, the capsids are transported to the nucleus via active transport by microtubule-assisted motor complexes. At the nucleus, the cytoplasmic filaments, predominantly Nup358, bind to the capsid and cytosolic factors dissociate from the capsids surface, allowing the transport of the capsid as a whole. Once reaching the nuclear ring, Nup153 and CPSF6, a nuclear factor, bind the capsid and it is driven into the nucleus. In the nucleus, CPSF6 replaces the Nup153 binding sites and the HIV capsid is released into the nucleus and disassembled to allow for genome integration [209, 211]. While the mechanisms are unknown, nuclear pore complex components have been implicated in the transposition and regulation of transposable elements. For the Ty3/gypsy family in *S. cerevisiae* for example, it has been suggested that the docking of virus-like particles to GLFG-Nups rather than FG-Nups is initiating nuclear entry [212]. Furthermore, as the nucleus does not break down during mitosis in *S. cerevisiae* [213], accessing the nucleus will most likely need an entry route via the NPC. The Ty1/copia family in *S. cerevisiae* has also been shown to require components of the nuclear pore complex for transcription and genomic integration [214]. Thus, there seems to be a relationship between the replication cycle of LTR retrotransposons and nucleocytoplasmic transport via the nuclear pore complex.

Intriguingly, some of the nucleoporins have also been found to be involved in transposon silencing by the PIWI pathway in *D. melanogaster*. The loss of two of the inner channel nucleoporins, Nup54 and Nup58, compromise the piRNA biogenesis in the ovarian follicle cells [215]. Interestingly, the loss of these two proteins has been shown to be specific to the *flamenco* locus, a small RNA cluster that controls Ty3/gypsy and other TEs [216], while knockdowns of other NPC components lead to widespread consequences. Thus, Nup54 and Nup58 specifically seem to be important for the molecules encoded by *flamenco* to reach their dedicated location in the cytosol.

Consequently, NPC-mediated nucleocytoplasmic transport seems to be of specific relevance to the replication cycle and regulation of LTR retrotransposons and potentially other transposable elements. The specific mechanisms of how the genomic information of the retrotransposon enters the nucleus and how these mechanisms may be similar among retroviruses and -transposons remains a subject of active research [217, 218].

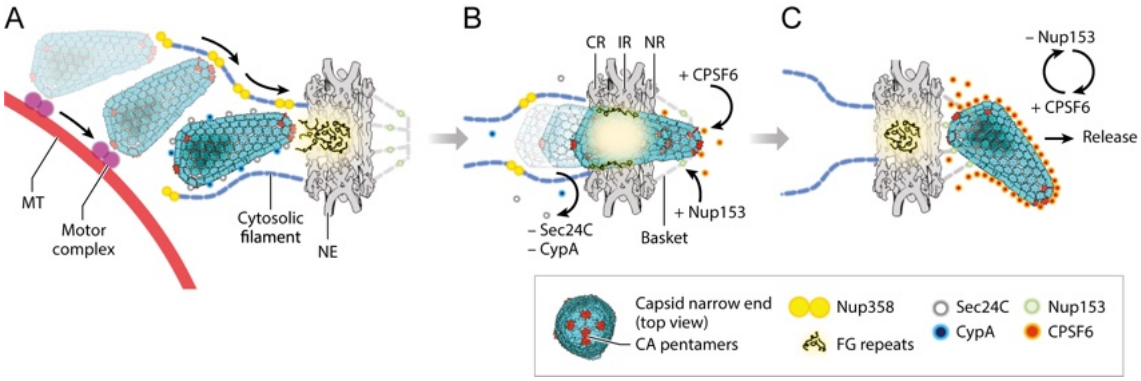

Figure 3.6.6 Nucleocytoplasmic transport of HIV. A: The HIV capsid is actively transported to the nucleus via microtubules(MT)-associated motor complexes. Once it reaches the nuclear pore, the interacts with the cytoplasmic filaments, most prominently Nup358 (also known as RanBP2). **B:** Cytosolic factors dissociate from the capsid's surface and the assembled capsid is transported through the nuclear pore as whole, with the narrow end first. This is most probably due to differences in affinity of the nuclear pore components to the capsid proteins. At the nuclear ring, Nup153, a component of the nuclear ring, and CPSF6, a nuclear factor, bind to the capsid. **C:** In the nucleus, Nup153 binding is replaced with CPSF6 and the capsid is disassembled. Adapted from [209], with permission.

3.7. Thylakoid membrane biogenesis and maintenance

Thylakoid membranes play a crucial role in coordinating the light-dependent stages of oxygenic photosynthesis, which involves the splitting of water into oxygen and hydrogen, providing the oxygen in the air we breath [219]. Additionally, they use the electrons and protons released from this process to generate NADPH and ATP. These bioenergetic molecules are subsequently utilized to capture atmospheric CO2 and convert it into the sugars that nourish all heterotrophic life [220]. Consequently, the thylakoid membranes found in plants, algae, and cyanobacteria serve as the primary source of energy for the intricate web of life on Earth (**Figure 3.7.1**). Despite the pivotal role that thylakoids play in our biosphere, our understanding of their detailed architecture, biogenesis, and maintenance in the face of environmental stress remains limited [221].

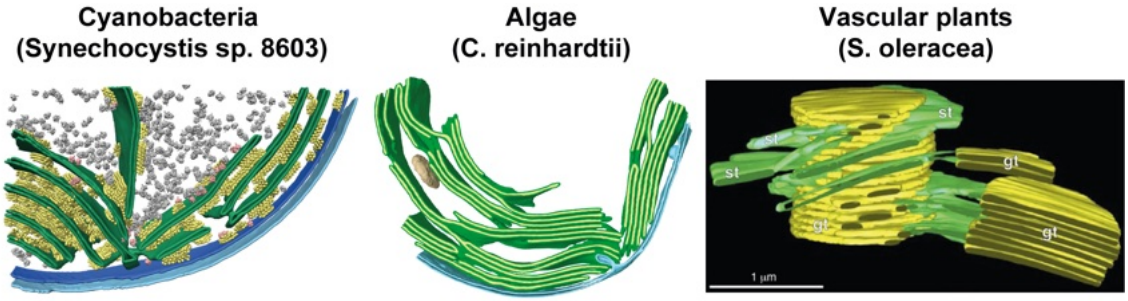

Figure 3.7.1 Morphology of thylakoid membranes for several examples across the green lineage. Cyanobacteria adapted from [222], *C. reinhardtii* from [160] and *S. oleracea* adapted from [223], with permissions.

The 'Very Important Protein in Plastids 1', originally named 'Vesicle-Inducing Protein in Plastids' and abbreviated as VIPP1 is an essential protein across the green lineage [224–230]. VIPP1, also known as IM30 [231], has been implicated in the

biogenesis and maintenance of thylakoids, alongside other crucial proteins such as CURT1 [232], PratA [233], DnaK [234], and others [235, 236]. In both cyanobacteria and chloroplasts, VIPP1 is found in abundance and indications exist that it co-evolved with thylakoid membranes [237]. In vascular plants, VIPP1 is nuclear-encoded and a N-terminal signal peptide is likely ensuring its localisation in the chloroplast through the TIC-TOC system.

Due to its essential role in thylakoid biogenesis and maintenance, knock-down mutants of VIPP1 show strong phenotypes [225, 226], especially under high-light conditions, leading to drastic swelling of the thylakoid lumen. A knock-down of VIPP1 leads to almost complete loss of thylakoid membranes in the cyanobacterium *Synechocystis sp.* PCC 8603 (**Figure 3.7.2**) [224]. A complete knock-out of VIPP1 blocks the assembly of thylakoid membranes and has been shown to be lethal [226]. Little was understood on the structural basis of how VIPP1 is able to perform its vital role in maintaining thylakoid integrity [238]. VIPP1 consists of seven predicted helices that are thought to form a coiled-coil structure from helix 2 and 3 [239]. *In vitro*, VIPP1 assembles oligomeric structures of different shapes, of which rings and rods have been observed across the green lineage (**Figure 3.7.2**). For example, *Synechocystis* VIPP1 (*syn*VIPP1) has been observed to form rings, of which negative stained electron microscopy structures have been reconstructed suggesting a vertical placement of the monomer of VIPP1 within the symmetric ring (**Figure 3.7.2**). However, in *C. reinhardtii*, VIPP1 seems to mostly form helical rods [163]. The luminal side of these structures have been observed to bind membranes such as liposomes or encapsulate them [240]. Additionally, VIPP1 has been reported to show nucleotide hydrolysis activity [241]. How it performs these functions from a structural viewpoint has remained elusive and will be addressed in **Chapter 4.3**.

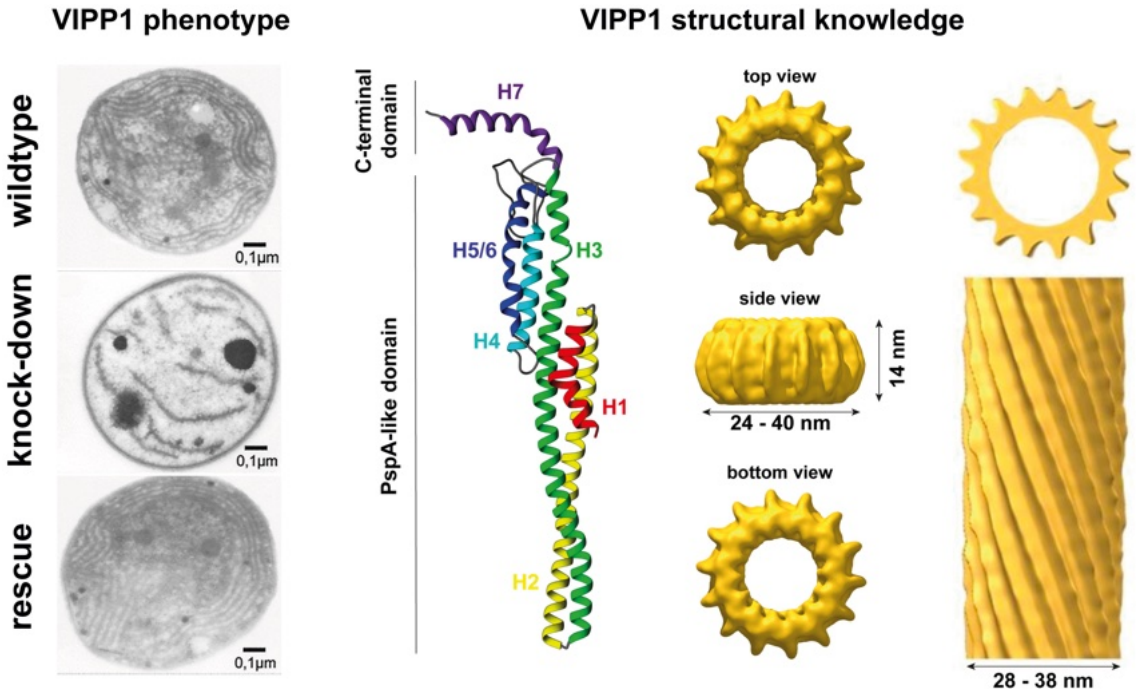

Figure 3.7.2 Cell biological consequences of VIPP1 knockdown and previous structural knowledge about VIPP1 oligomers. VIPP1 knockdown leads to almost complete loss of thylakoids in the cyanobacterium *Synechocystis sp.* PCC 8603. The introduction of VIPP1 rescues the phenotype. Adapted from [224] with permission, Copyright (2001) National Academy of Sciences. Structure predictions of the VIPP1 monomer yield 7 helices, of which 6 form a PspA-like domain. The monomer forms oligomers of varying size from 24-40 nm in diameter. In *C. reinhardtii*, *in vitro* assemblies of VIPP1 encapsulate liposomes forming striated structures with a diameter of 28-38 nm. Adapted from [239] with permission.

4. Results

4.1. A modular platform for automated cryo-FIB workflows and development

This chapter is published as an article in eLife. I developed and currently continue to maintain, adapt, and improve the code-base of SerialFIB. The beta phase of deploying the presented workflows was done in collaboration the the group of Dr. Julia Mahamid at the European Molecular Biology Laboratory (EMBL) in Heidelbeg. Thus, the code includes contributions from Dr. Herman K. H. Fung and Dr. Sara K. Goetz. Images, available under the Creative Commons license (CC BY 4.0), are reproduced from the published article [21].

At the start of the work presented throughout this thesis, the cryogenic preparation of lamellae was a purely manual task. Hardware solutions to keep samples at cryogenic temperature throughout the lamella preparation workflow, such as a in-vacuum transfer into the FIB-SEM instrument and a cryogenic stages within the instrument, were home-built. It led to an unstable stage and automated solutions for the process, while commonly available in the materials science, were therefore lacking. Due to continuous development in the field, however, improved cryo-stages with decreased drift became available, allowing for the development of automated procedures. As further improvements to cryogenic sample preparation using the FIB instrument were needed, I envisioned a modular and extensible platform across manufacturers that would allow researchers to deploy standard procedures and develop novel workflows that are easily shareable. To that end, we developed the SerialFIB platform. The architecture and modules are shown schematically in **Figure 4.1.1**. It encompasses a graphical user interface, depicted in **Figure 4.1.2**, that is decoupled from the instrument hardware through a microscope-specific driver that talks to the instrument hardware using the provider's application programming interface (API). Thereby, only the driver needs to be exchanged when installing and deploying the software on different instruments. The application specific parameters are defined using the so-called 'Designer' submodules. These modules directly correspond to the use cases that have been considered during development. Additionally, a scripting editor is provided that allows for scripting of novel workflows using and extending the already available use cases. An example of such an extension will be discussed in **Chapter 4.2**. In the following, I will showcase the different use cases developed for the SerialFIB software package.

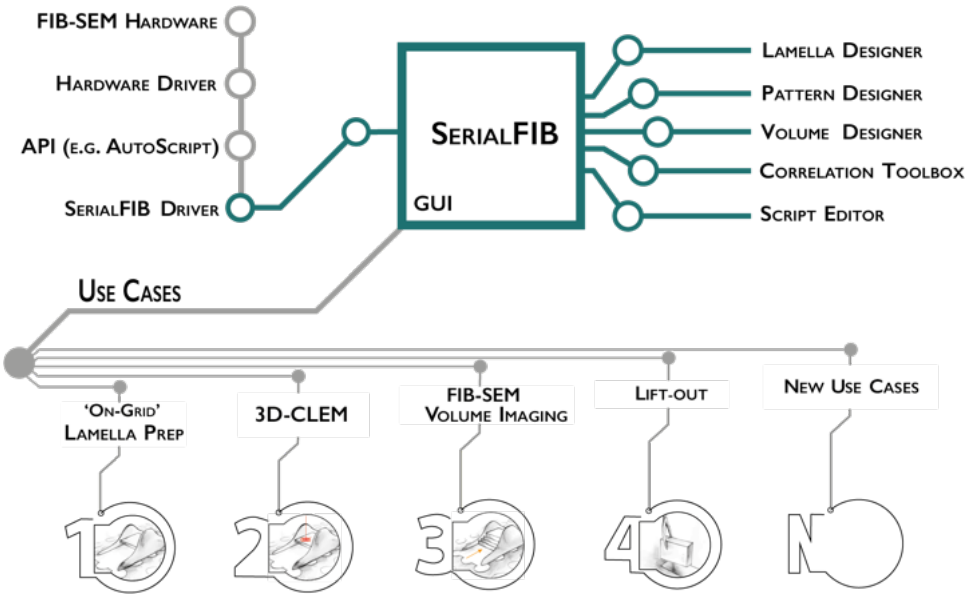

Figure 4.1.1 Overview of the SerialFIB software package. The graphical user interface is decoupled from the hardware of the microscope by an abstraction layer, the SerialFIB driver. The driver communicates with the FIB-SEM Hardware driver (e.g. xT server) via an application programming interface (API), e.g. AutoScript for Thermo Fisher Scientific instruments. The developed use cases are accessible via designated 'Designer' modules and encompass on-grid lamella preparation, 3D-correlative light and electron microscopy via 3DCT (3D-CLEM), FIB-SEM volume imaging and lift-out site preparation. New use cases can be developed using the ScriptEditor. Figure reproduced from [21], with permission.

4.1.1. On-grid lamella preparation using SerialFIB

Similar to other contemporaneous developments in the field (20, 21, 23), SerialFIB offers an automated solution for preparing on-grid lamellae for cryo-ET. For each area of interest, the user specifies the desired lamella width and position, along with milling points on a reference image. These milling points ensure that grid bars and other objects, which can deflect the ion beam and potentially harm the lamella, are avoided (**Figure 4.1.5 A**). Next, we create micro-expansion joints (26) to relieve tension in the frozen specimen (**Figure 4.1.5 B**), followed by a two-stage material removal process: (i) rough milling, reducing all areas of interest to a 1 μm thickness, and (ii) fine milling, thinning the resulting slices to approximately 200 nm thickness to achieve electron transparency (**Figure 4.1.5 C**). Fine milling all areas within a short time frame minimizes amorphous ice contamination on the lamella. While recent hardware advances have diminished this problem, the time frame is usually kept below 1 hour on older hardware. This represents a compromise between lamella production rate and the extent of amorphous ice contamination, contingent on the cryo-FIB-SEM system's condensation rate.

The entire workflow of on-grid lamella preparation using SerialFIB is illustrated in **Figure 4.1.4**.The process uses image cross-correlation to the collected reference image for the realignment procedures to recall positions defined by the user for each milling step. Realignment is performed whenever stored stage positions are navigated to or when the FIB current is changed to compensate for imperfect microscope alignment. For realignment after stage movement, large discrepancies above 10 μm are

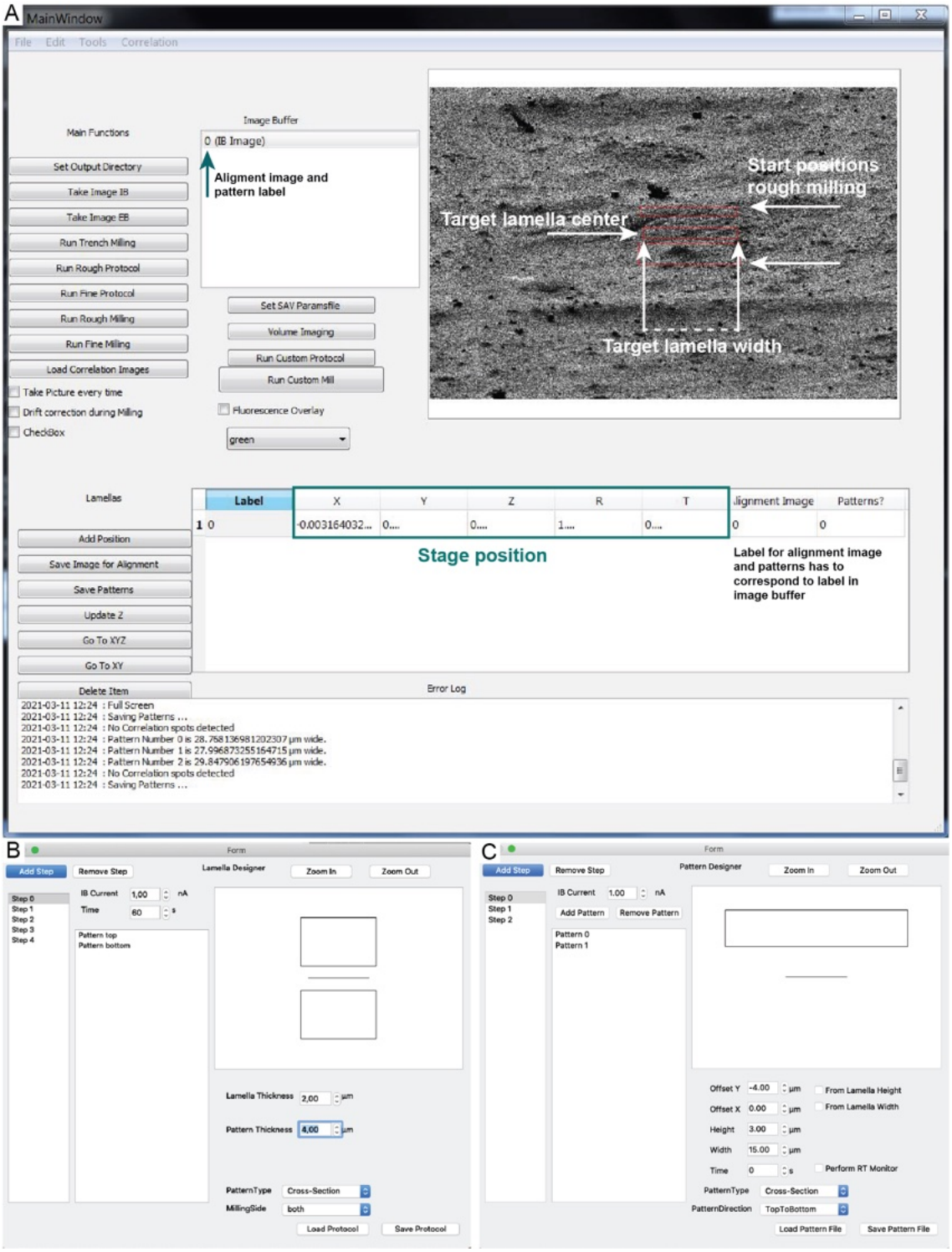

Figure 4.1.2 SerialFIB graphical user interface. A: The main window gives access to the different use cases and protocols. Lamellae positions are defined and saved in the list on the bottom. Alignment images and their corresponding lamella positioning are associated to their corresponding lamella position. Designers and ScriptEditor is selected from the Tools tab. **B:** The lamella designer allows for the preparation of milling protocols with arbitray number of thinning steps. Defined are the pattern thickness, the lamella thickness defining the distance of the milling pattern to the lamella, the current and time per milling step, and finally whether patterning is supposed to happen from the top, bottom, or both sides of the lamella. **C:** Rather than allowing for lamella protocols, the PatternDesigner only incorporates offsets and size of the pattern from a reference point (the central point of the lamella pattern in the SerialFIB GUI) and, thus, allows for arbitray milling shapes using rectangular patterns. Data collected with Dr. Herman Fung and Dr. Sara Goetz. Figure reproduced from [21], with permission.

Sample	# Target sites	# Polished lamellae	Lamella thickness [nm]
Sum159	22	19	70-410
HeLa	22	18	100-450
E. huxleyi	9	9	175-470
C. rheinhardtii	16	10	140-350
S. cerevisae	8	8	190-300
Total	77	64	
Success rate [%]		**83.1**	

Table 4.1.1 Statistics of automated on-grid lamella milling with SerialFIB and corresponding success rates for five different cell types.

compensated for by additional stage movements while smaller corrections are performed using the beam shift. While the current used for alignment can be chosen by the user, it is generally performed at low ion beam currents of 10 pA to 30 pA. For changes in FIB apertures, a reference image is taken before the aperture position change and a new image is acquired after the aperture change. The shift is compensated by cross-correlating the two images and shifting the beam by the determined amount. To define the milling protocol, meaning the parameters for lamella preparation, the milling steps of the intended lamella thickness and exposure pattern are linked to a specific milling time and an ion beam current. These parameters need to be optimized per sample but benchmarking experiments for a variety of plunge-frozen samples are available and can be used as a reference point for future adaptations. The success rate and obtained lamella thickness range are shown in **Table 4.1.1**. From 77 positions, 64 lamellae were generated with a width ranging from 5.6 to 25.6 μm determined from the SEM images and 70-470 nm in thickness as determined by cryo-ET tilt series acquisition and tomogram reconstruction. The data points of width and thickness determination are visualized in **Figure 4.1.3**. This yields a milling success rate of 83 % which is comparable to manual operation.

4.1.2. Targeted lamella preparation by 3D-correlative light and electron microscopy (CLEM)

In order to target biological events into the limited volume of a cryo-FIB lamella, site-specific targeting using cryo-fluorescence data has become the method of choice. It is indispensible for rare events, as the final lamella will only encompass a fraction of the original cell, approximately 0.01-0.1 $\%$ for HeLa and *C. reinhardtii* cells, respectively. While many different possible implementations exists, the most widespread in the community is the usage of autofluorescent beads as fiducials that are added to the sample prior to cryo-fixation. The fluorescent beads are chosen to be large enough, usually 1 μm in size, to identify them in the different imaging modalities (compare **Figure 4.1.6 A-B**). By identification of the fiducials in the imaging modal-

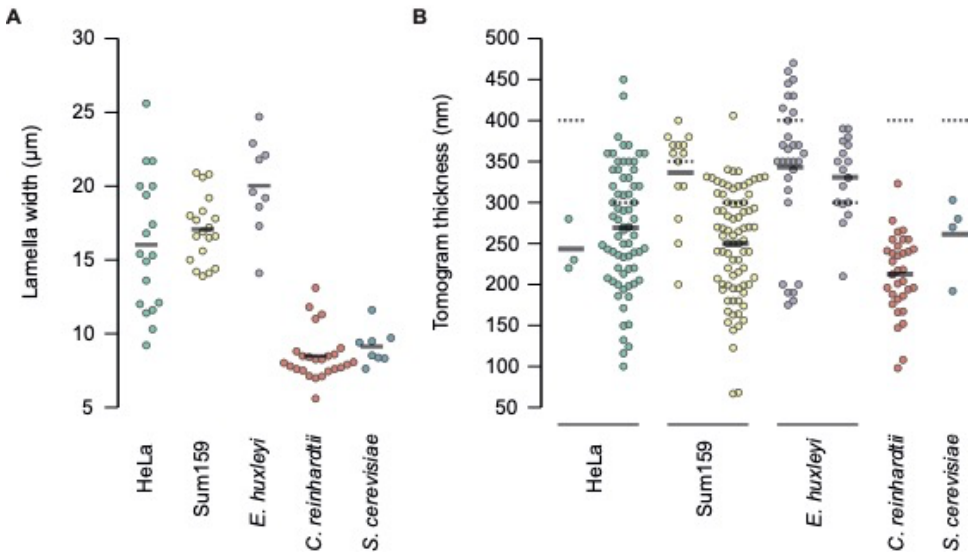

Figure 4.1.3 A: Width and B: tomogram thickness distribution of SerialFIB lamellae from five eukaryotic cell types. Lamellae were prepared in independent FIB sessions and in total 14 grids encompassing HeLa (6), Sum159 (3), *E. huxleyi* (2), *C. reinhardtii* (2), and *S. cerevisiae* (1) grids. Data collected with Dr. Herman Fung and Dr. Sara Goetz. Figure reproduced from [21], with permission.

ities and after their registration, a composite image of SEM and FIB image with the fluorescent data can be produced. Multiple softwares exist to perform this task. In the Plitzko group for CryoEM Technology at the MPI of Biochemistry, Martinsried, Germany, a software package called 3D correlation toolbox (3DCT) had previously been developed. The output of that software can be loaded into the SerialFIB user interface. From these images, lamella positions in the FIB reference image can be chosen (**Figure 4.1.6 C-D**)), allowing for the targeted preparation of specific fluorescent events within the lamella volume (**Figure 4.1.6 E-G**)).

After milling, 3DCT can be used to overlay the cryo-FLM data with the SEM images of the milled lamella for subsequent navigation during cryo-ET data acquisition. In order to evaluate the success of 3D-CLEM-guided lamella preparation, lipid droplets were chosen as a target in plunge-frozen grids of HeLa cells. Two different substrates were chosen, titanium grids with holey 1/20 SiO_2 support and gold grids with holey 1/4 SiO_2 support. To assess the success rate, two images were compared. First, a FLM virtual slice was generated based on the image registration of the light microscopy volume with the FIB image before milling. Subsequently TEM image montages were collected. In 7 out of 10 lamellae on titanium SiO_2 1/20 grids, the targeted lipid droplet was retained. In contrast, 0 out of 4 lamellae contained the targeted lipid droplets on the gold SiO_2 1/4 grids. We attribute this mismatch to movement of the support film upon ion beam irradiation, which can be observed when comparing FIB images before and after lamella milling and analyzing the differences by elastic 2D B-spline registration (**Figure 4.1.7**). While the reasons for the increased movement can only be speculated on and likely has to do with the strain in the material from rapid freezing, the reduced support film movement led to an increased success rate in the

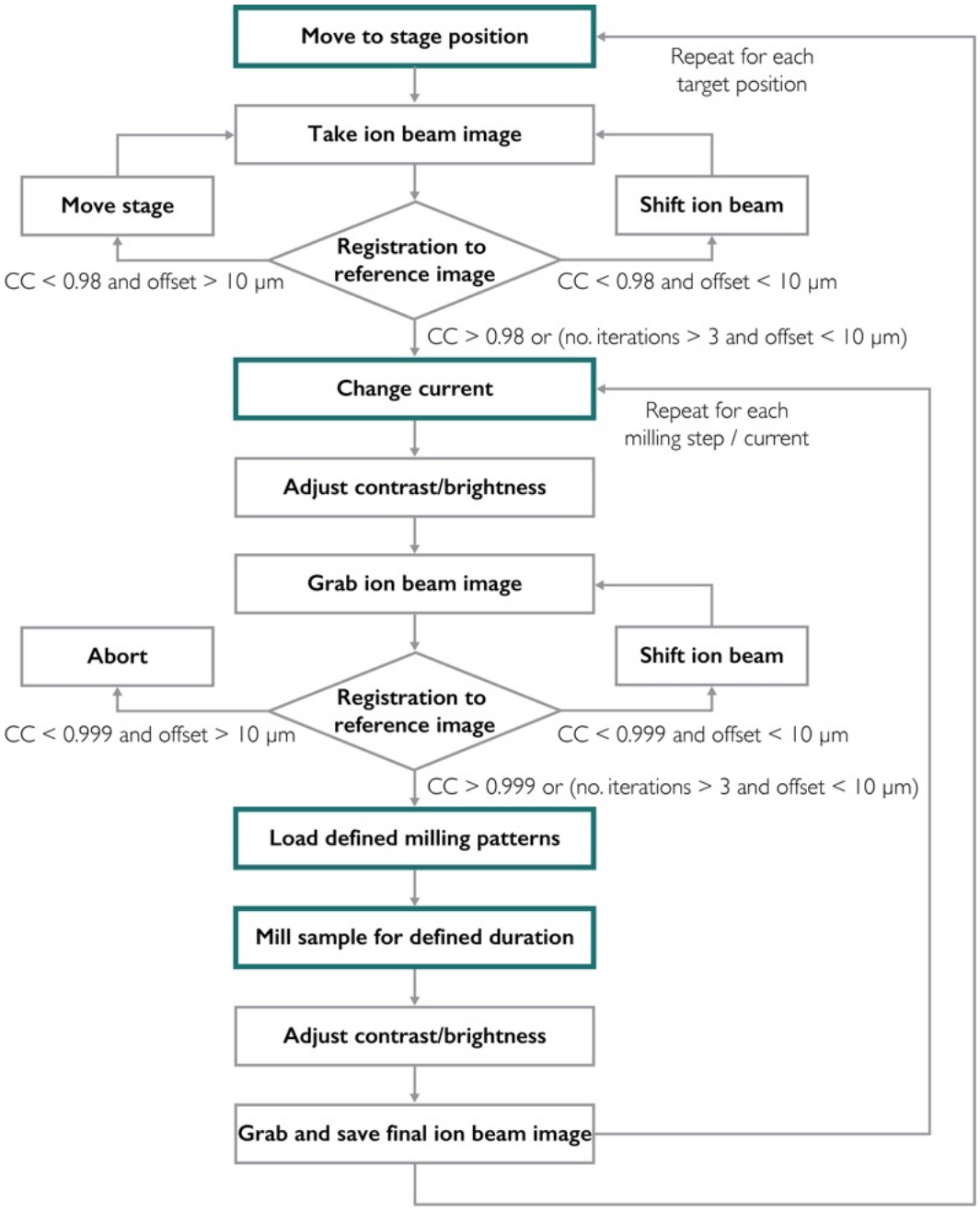

Figure 4.1.4 Workflow diagram of the on-grid lamella preparation routine in SerialFIB. Main steps (dark green) and decision points for alignment via image correlation (rhombus) are indicated as colored boxes. Data collected with Dr. Herman Fung and Dr. Sara Goetz. Figure reproduced from [21], with permission.

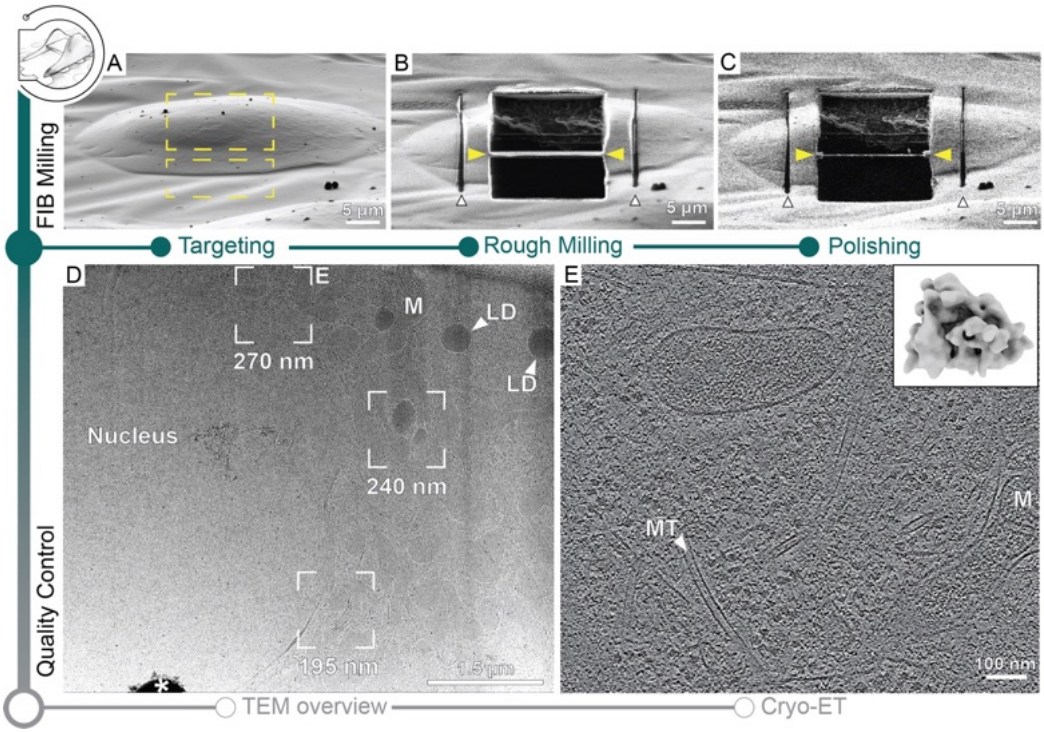

Figure 4.1.5 On-grid lamella preparation in SerialFIB. A: Ion beam image of a Sum159 cells prior to lamella milling. Dashed rectangles indicate the rough milling volume. **B:** Ion beam image of the lamella after rough milling. Yellow arrowheads indicate the lamella at a target thickness of 1 μm. White arrowheads show the micro-expansion joints. **C:** Ion beam image of the final lamella at a target thickness of 300 nm. **D:** Overview of a subregion of the lamella with the nucleus, lipid droplets (LD) and mitochondria (M) distinguishable. The white rectangles indicate tomogram positions and corresponding thickness measurements within the tomogram. **E:** Slice of the tomogram indicated in D. The tomogram shows the cytosol with microtubules (MT) and a mitochondrion (M). The inset shows the subtomogram average obtained from 4 tomograms and 4378 subtomograms extracted collected on the shown lamella resulting in a resolution of 24 Å. Data collected with Dr. Herman Fung and Dr. Sara Goetz. Figure reproduced from [21], with permission.

cryo-CLEM workflow. It illustrates the importance of mechanically stable specimen supports for site-specific 3D-CLEM targeted lamella milling.

4.1.3. Cryo-FIB-SEM volume imaging of vitrified cells in SerialFIB

The acquisition of serial SEM images of FIB milled surfaces produces a 3D representation of specimen at the nanometer scale. The technique, commonly referred to as FIB-SEM volume imaging or tomography, can in principle reveal organelle size and distribution while allowing for subsequent lamella preparation. It involves the incremental removal of material from a specimen in several nanometer-thick slices, followed by SEM imaging. Within SerialFIB, I developed an automated cryo-FIB-SEM volume imaging routine. In testing this workflow on Sum159 breast cancer cells, a window into the cellular material is milled. Then, one selects the volume to be imaged within a reference FIB image. The software will subsequently alternate between removing cellular material in defined steps and imaging the freshly exposed surface with the SEM. We optimized SEM imaging conditions to highlight specific cellular structures while minimizing acquisition times. This optimization involves a trade-off between acquisition speed, image quality, and applied dose (typically between 0.5 - 1.5 e/Å^2 per slice). In the case of *Chlamydomonas reinhardtii* cells, we used line integration to enhance the signal-to-noise ratio, albeit with longer acquisition times (**Figure 4.1.9 A**). Generally, for a typical image with 100 ns pixel dwell time at 100 line integration and an image size of 3072x3072, this results in a SEM imaging time of approximately 100s. While slicing thickness dependent, this allows for an acquisition volume of 20 μm in depth with a slicing thickness of 50 nm within a working day. Additional image processing on the resulting SEM images helped to identify cellular compartments such as the nucleus (**Figure 4.1.9**E). The algorithm encompassed (1) a wavelet decomposition, gaussian blurring of the vertical features and reconstruction to reduce streaking caused by curtaining from uneven milling of the surface, (2) a subtraction of a gaussian blurred and eroded image from the original image to reduce charging gradients in the image, and (3) a CLAHE filter to increase contrast in the final image. While the algorithm is partially described elsewhere [145], the reimplementation in python and incorporation in SerialFIB enables the direct analysis of images during data acquisition. It further allows for cellular features such as the nuclear pore complexes, the thylakoid membranes, and the Golgi apparatus to be resolved (**Figure 4.1.9E-G**). Following volume imaging, the patterns defined in the user interface can be used to prepare a lamella below the final surface of the volume imaging, and thus lets the operator perform a correlative experiment from FLM to FIB-SEM volume imaging to cryo-electron tomography, here exemplified for Sum159 cells (**Figure 4.1.8**). However, the SEM imaging will damage the underlying material to a thickness that is dependent on the acceleration voltage of the electrons used. Here, lamellae were prepared approximately 100 nm below the final SEM imaging

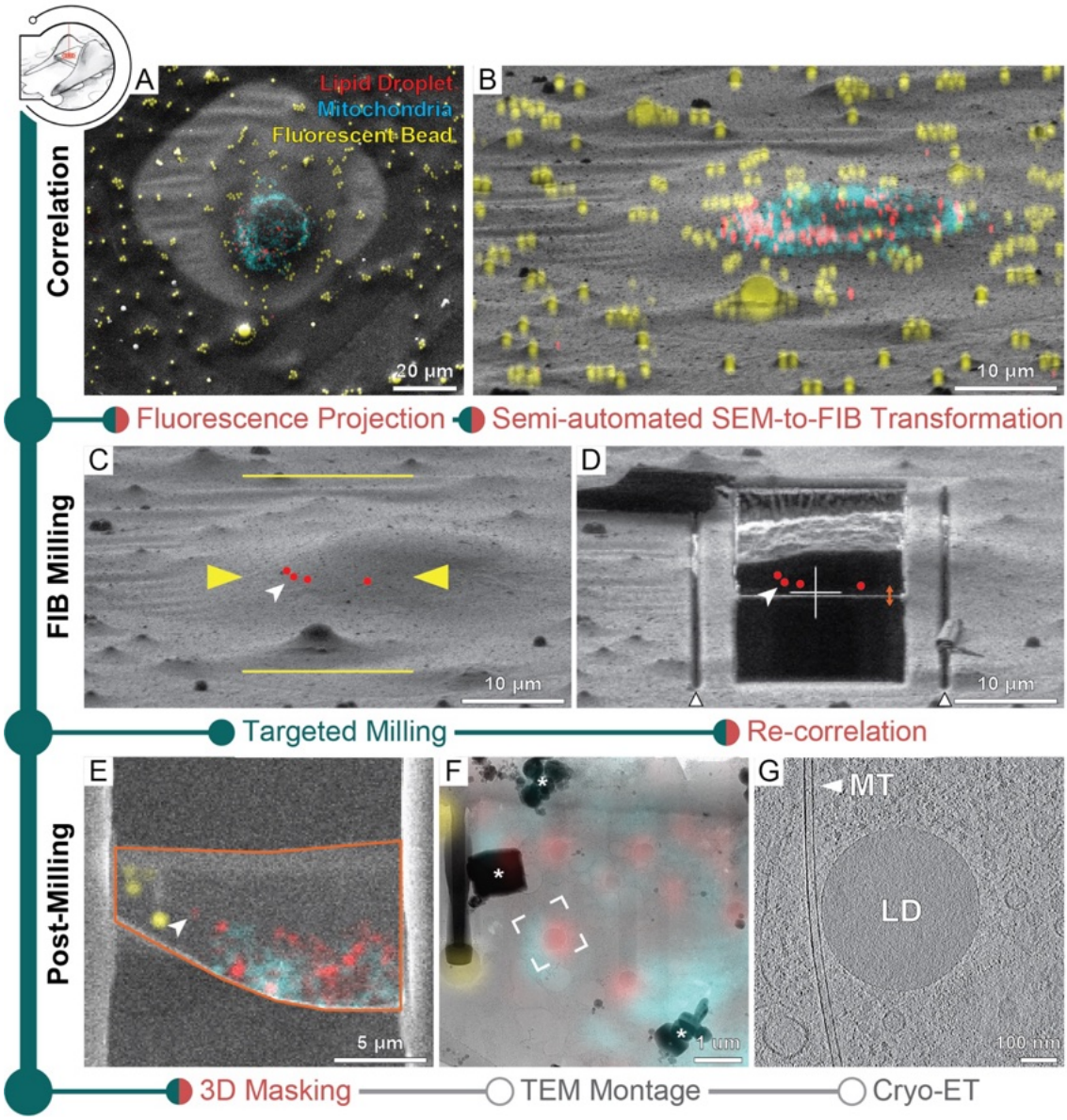

Figure 4.1.6 3D-CLEM targeted lamella preparation in SerialFIB. A: Overview SEM and **B:** FIB image of the lamella site on a HeLa grid overlaid with fluorescent stack after correlation. **C:** Setup within SerialFIB. The red dots indicate user defined regions of interest from the fluorescent stack as determined by the correlation. Yellow lines indicate extreme positions for rough milling. The yellow arrowheads show the lamella position. The white arrowhead indicates the lipid droplet targeted. **D:** FIB image after lamella preparation. Note the offset from the original correlation position as a result of grid deformations during milling. **E:** SEM image of the final lamella with 300 nm FLM slice centered on the lamella. **F:** TEM overview of the lamella. Tomogram position (white frame) and ice contamination (asterisks) are indicated. **G:** Slice through the tomographic reconstruction of the tilt series showing cytosol with the lipid droplet (LD) targeted and microtubules (MT) in its vicinity. Data collected with Dr. Herman Fung and Dr. Sara Goetz. Figure reproduced from [21], with permission.

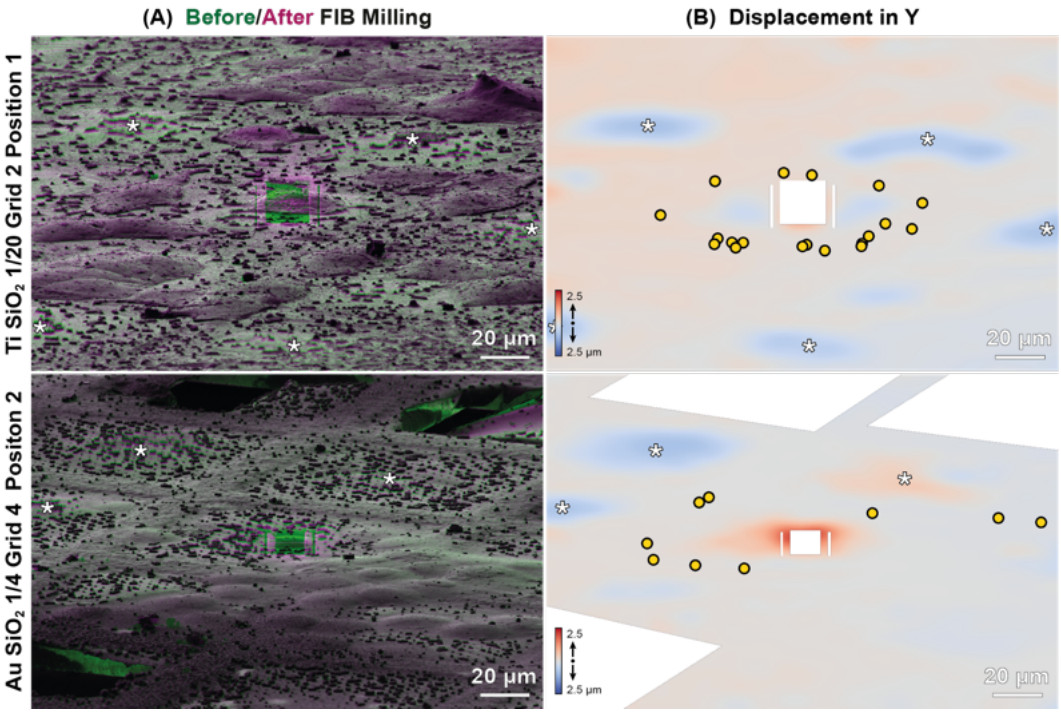

Figure 4.1.7 Support film movement upon lamella milling as visualized by B-spline fitting. A: Overlayed FIB images of a Ti SiO_2 and a Au SiO_2 grid before and after lamella preparation. **B:** The difference of the two images color coded by Y displacement from +2.5 μm (red) to -2.5 μm (blue). Data collected with Dr. Herman Fung and Dr. Sara Goetz. Figure reproduced from [21], with permission.

surface for 3 kV electrons and the 3380 subtomograms of ribosomes obtained from these 2 tomograms could still be averged to 24 Å resolution, comparable to the 4738 subtomograms from the on-grid experiments without SEM imaging (**Figure 4.1.5E**). The tomograms reconstructed from the tilt-series collected either way were visually undistinguishable. Thus, for molecular resolution multi-scale 3D cryogenic imaging, the presented approach gives similar results for the low resolution regime. For high-resolution subtomogram analysis below approximately 1 nm resolution, it cannot be ruled out that the exposure would damage the macromolecules to an extent that would prevent the analysis.

4.1.4. Accelerating lift-Out lamella preparation with SerialFIB

The preparation of lamellae from high-pressure frozen material is a time-consuming endeavour, especially when using gallium ion sources that are limited in current. The most tedious step for this process was and remains to be the preparation of trenches that are wide enough to give access to cryo-micromanipulator devices such as a cryo-gripper or a tungsten needle (see also **Chapter 4.4**).

Two types of samples are usually considered in high-pressure freezing, so called 'waffle' samples that have a layer of ice typically between 10 to 30 μm in thickness, and samples directly frozen in high-pressure freezing planchettes. In the latter, the specimen is embedded in a 50 to 200 μm layer of ice. As introduced in **Chapter**

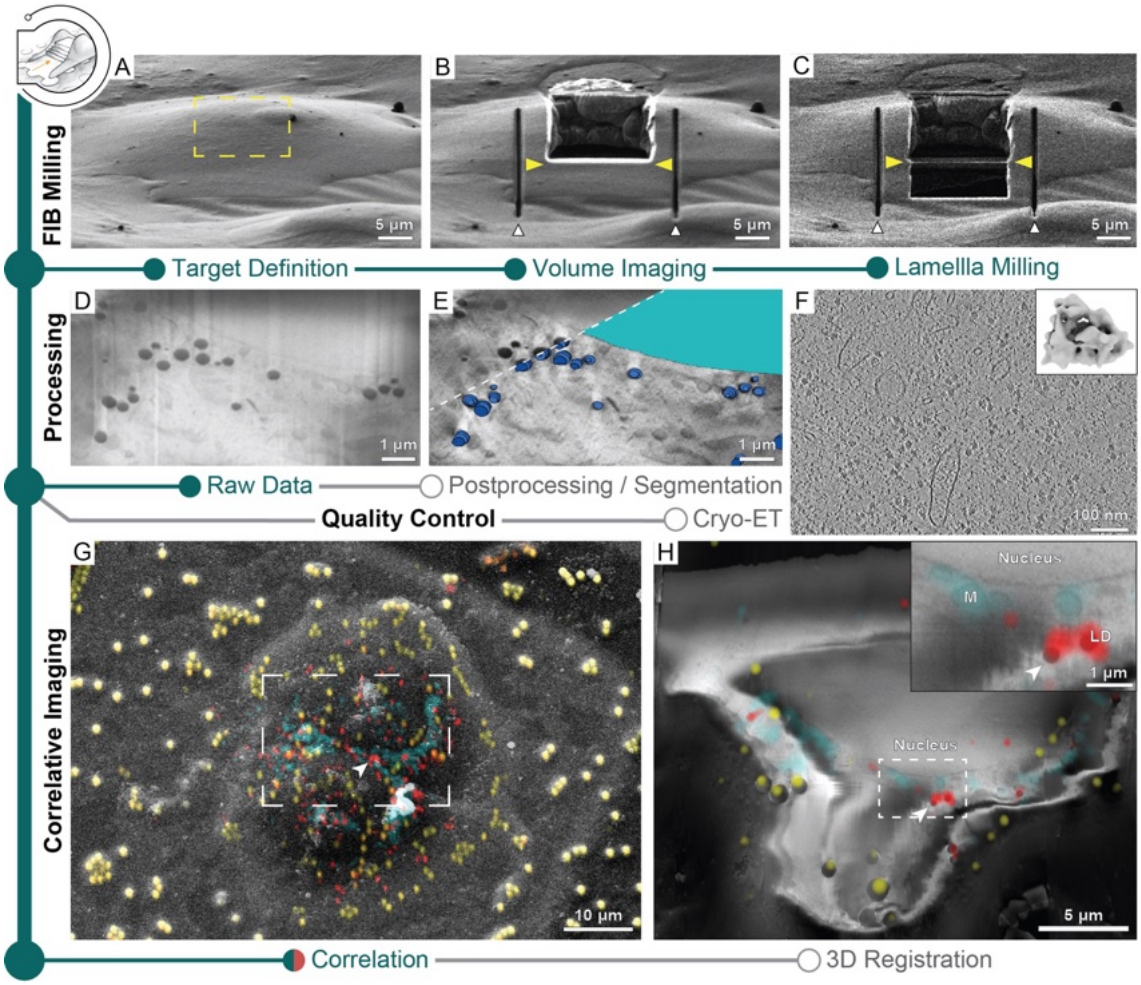

Figure 4.1.8 Multi-scale 3D crogenic imaging of Sum159 breast cancer cells by fluorescence microscope, FIB-SEM volume imaging, and cryoET. A: FIB image of a Sum159 cell prior to imaging. Yellow rectangle indicates the volume to be imaged. **B:** FIB image after volume imaging. Yellow arrowheads indicate the lamella. White arrowheads show the micro-expansion joints. **C:** FIB image of the final lamella. **D:** SEM image of the cell's surface as collected by SerialFIB. **E:** Postprocessed and segmented image. Segmented is the nucleus (cyan) and lipid droplets (blue). **F:** Slice through the reoconstructed tomogram of a tilt series collected on the final lamella. Inset shows the ribosome structure determined on the lamella from 2 tomograms and 3380 subtomograms at 24 Åresolution. **G:** SEM view of the two HeLa cells overlaid with a maximum intensity projection of the mitochondria(cyan), lipid droplets(red), and fiducial bead (yellow) fluorescence.. **H:** A selected cross-section from the processed FIB-SEM volume is superimposed with a 200-nm simulated cross-section from the 3D-registered fluorescence volumes after applying an affine transformation. The white arrowhead indicates a pair of lipid droplets, which can be viewed in closer detail in the inset. Data collected with Dr. Herman Fung and Dr. Sara Goetz. Figure reproduced from [21], with permission.

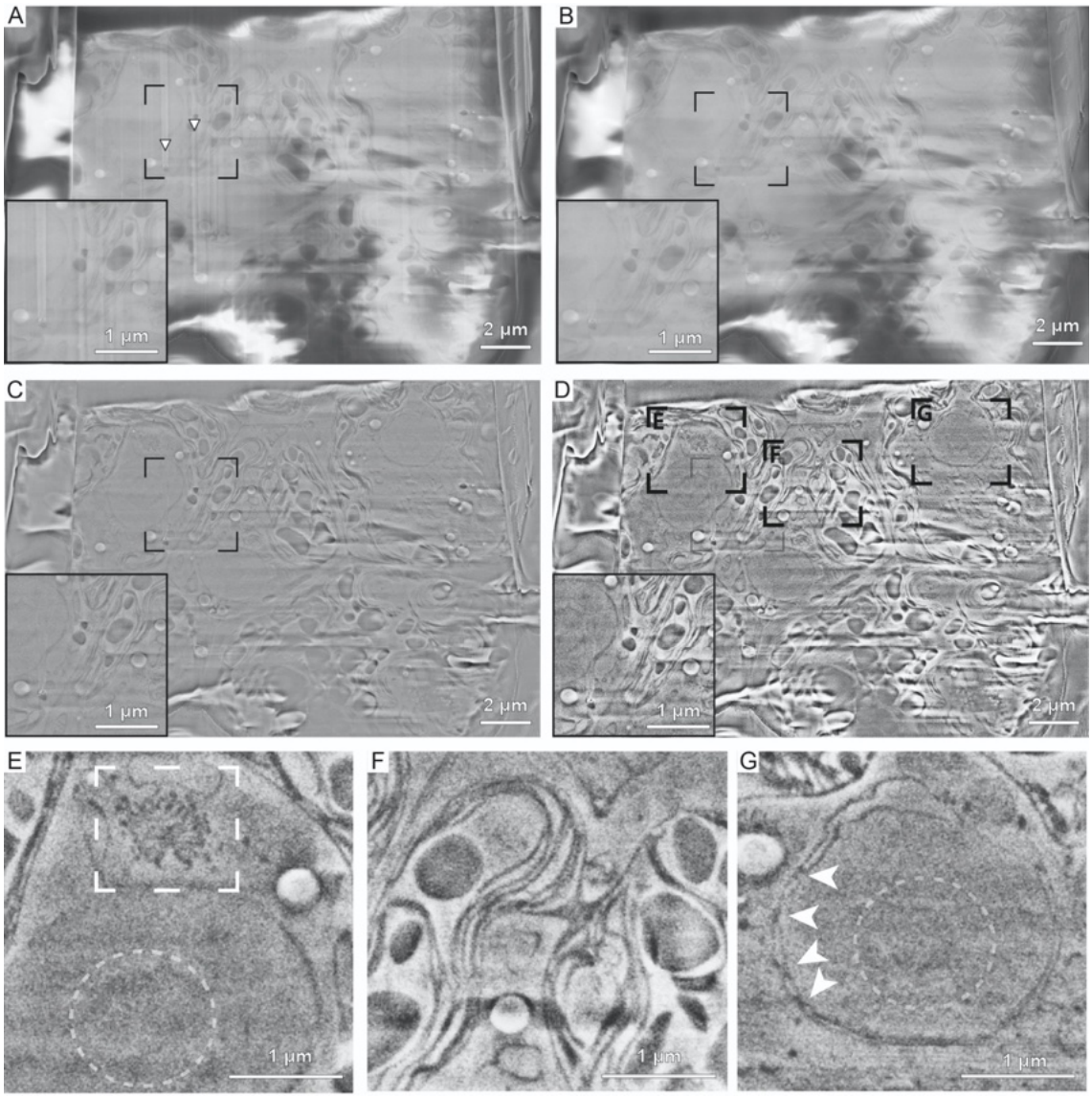

Figure 4.1.9 Sequential volume imaging and processing of *Chlamydomonas reinhardtii*. Image processing steps inspired by [145]. **A:** Original data, with arrowheads highlighting curtaining artefacts caused by ion beam milling. **B:** The image after the removal of stripes using wavelet decomposition to the 8th level, Coiflets family 3, and vertical component smoothing with Gaussian blurring (sigma = 6). **C:** Local charge adjustment achieved through image subtraction from a Gaussian blurred (sigma = 35) image, followed by three rounds of erosion, applied to the image in B. **D:** The image post-processing, which includes median filtering (3.0 pixels) and local contrast enhancement using CLAHE (Contrast-Limited Adaptive Histogram Equalization) with a slope of 3.0. **E-G** Close-up views of the regions marked in D, revealing a Golgi stack (E, within the rectangle), thylakoid membranes (F), the nucleolus (E and G, within dashed circles), and nuclear pore complexes in the nuclear envelope (G, indicated by arrowheads). Figure reproduced from [21], with permission.

3.4.10, lift-out physically extracts material from the bulk sample to prepare electron-transparent lamellae on a receiver grid, classically a half-moon grid, which will be explored later in this thesis (compare **Chapter 4.5**).
Using SerialFIB, the time consuming milling for lift-out site preparation can be automated, as demonstrated here for the trench milling in a high pressure frozen *Drosophila* egg chamber specimen (**Figure 4.1.10A-C**). To find the positions within the bulk material, 3DCT can be used to correlate surface features with the fluorescence microscopy data, exemplified in (**Figure 4.1.11**). The milling is subsequently performed using a custom pattern sequence file in the Pattern Designer (**Figure 4.1.2**). As high-pressure frozen samples contain much thicker layers of ice compared to plunge-frozen samples and are thus highly non-conductive, even in-chamber sputtering tends to only help mildly. Therefore, the entire process is done with the "Drift Suppression" function within the FIB-SEM, where the electron beam is used as a flood gun to neutralize the charges the ion beam is generating during milling. By milling with the ion beam perpendicular to the sample surface, the process yielded 20 μm x 20 μm extractable chunks ready for lift-out (**Figure 4.1.10D**). The preparation time per position is dependent on the sample type and ranges anywhere between 30 and 60 minutes for the horse-shoe shaped patterns shown. After lift-out, transfer and attachment to the receiver grid (**Figure 4.1.10E**), the automated lamella milling routines can be used to mill down the extracted material to 1 to 5 μm depending on sample stability(**Figure 4.1.10F**). At the time of this experiment, the lift-out system used was a cryo-gripper and the attachment only single-sided, leading to relatively low lamella stability during the thinning process. We will see ways to improve on this in **Chapter 4.5**. Due to this instability, lamellae were still polished to below 200 nm manually. Within the TEM, overviews of the lamellae can be collected to decide on tilt series positions based on the ultrastructure of the material (**Figure 4.1.10G**). A slice through a tomogram collected on the lamella is shown in (**Figure 4.1.10H**). Subtomogram averaging of 20284 particles from 8 tomograms yielded a structure of the *D. melanogaster* ribosome at 20.8 Å resolution.
The presented lift-out experiment is an example of a custom task using the Pattern-Designer for lift-out site preparation in SerialFIB. As the technology evolved, novel workflows such as 'waffle' milling are beeing incorporated into SerialFIB, as will be discussed in **Chapter 5.1** and **Chapter 5.2**.

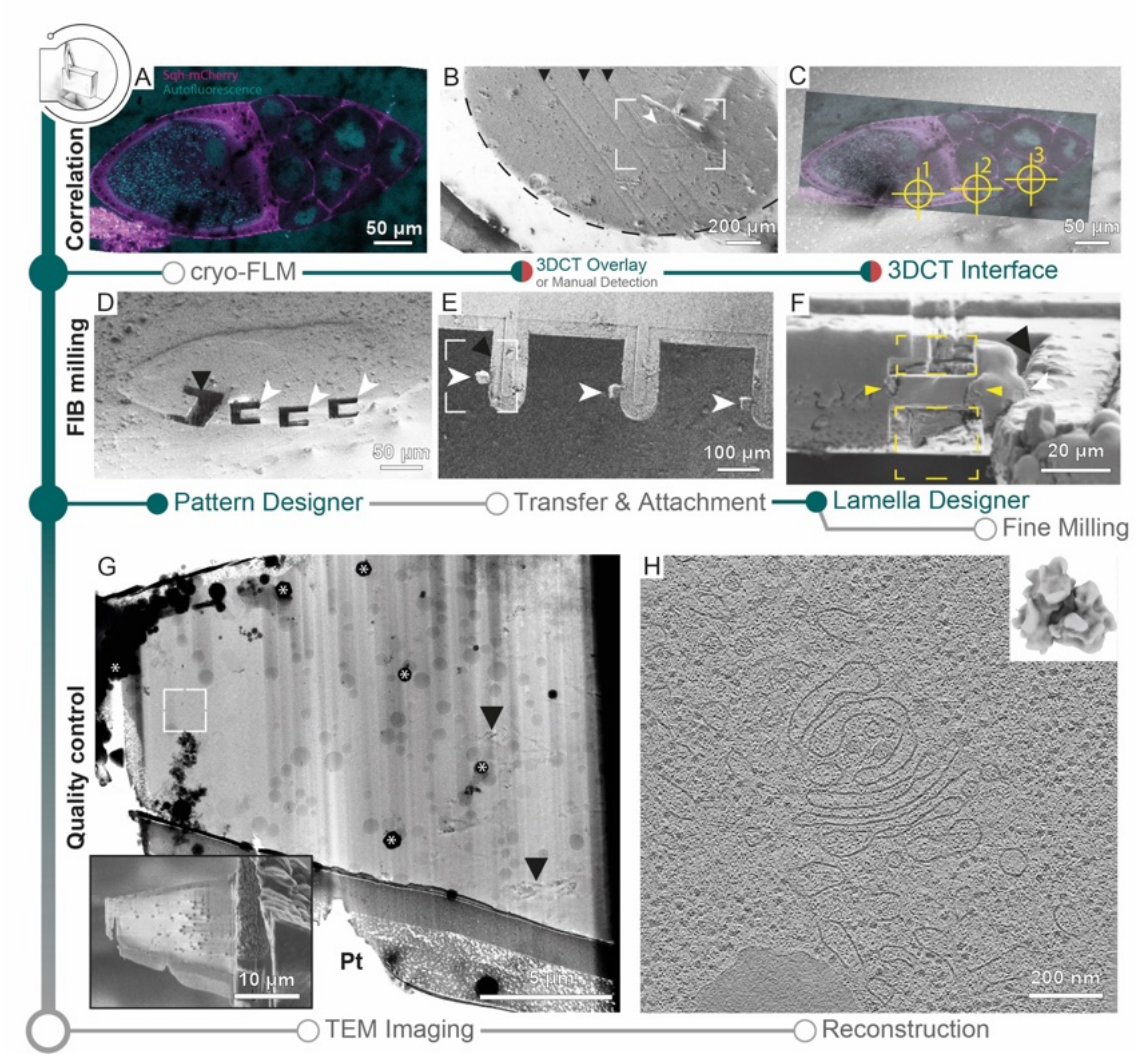

Figure 4.1.10 Cryo-FIB lift-out from HPF *D. melanogaster* egg chambers. A: Fluorescence light microscopy image of the *D. melanogaster* egg chamber subjected to cryo-lift-out. Due to the orientation of the subsequent images, the anterior is shown to the right. **B:** SEM overview of the sample from A. Black arrowheads indicate knife marks from diamond knife pre-trimming. The dashed line outlines the HPF planchette. The white rectangle indicates the position of the egg chamber (white arrowhead). **C:** Overlay of fluorescence data on the SEM imag for lift-out site preparation. Three target sites were prepared. **D:** SEM image of the automated lift-out sites (white arrowheads) prepared with SerialFIB. The black arrowhead indicates the volume imaging site for confirmation of the egg chamber position. **E:** Lift-out volume (white arrowheads) attached to the sides of a half-moon pin (black arrowhead) after cryo-lift-out. The rectangle shows the lamella site of the subsequent images. **F:** FIB image of the lamella after automated rough milling in SerialFIB. Yellow rectangles indicate the rough milled volume, yellow arrowheads show the lamella position. **G:** TEM overview of the lamella prepared in F. Asterisks show ice contamination, black arrowheads indicate reflections from bad vitrification. The white rectangle shows the tilt series position of the reconstructed tomogram in H. Inset shows the final SEM image of the lamella. Pt indicates the platinum layer. **H:** Slice through the tomogram collected. Visible is a golgi apparatus and cytosolic regions. The inset shows the subtomogram average of the *D. melanogaster* ribosome from 8 tomograms (20284 subtomograms) collected on lift-out lamellae at a resolution of 20.8 Å. Figure reproduced from [21], with permission.

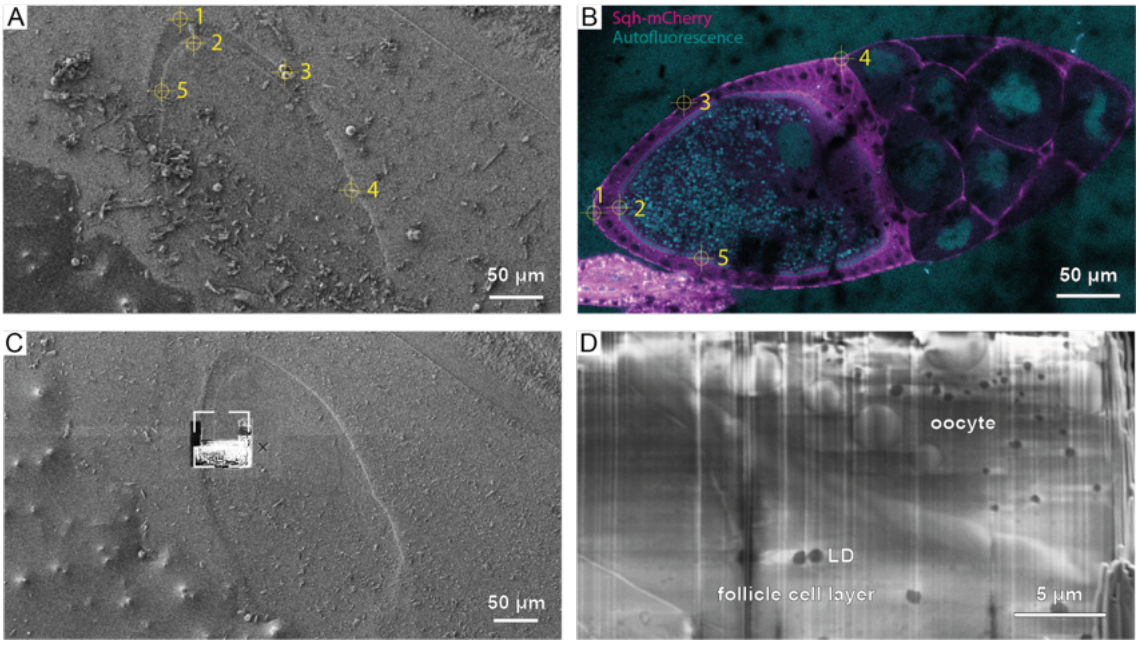

Figure 4.1.11 Correlation for cryo-FIB lift-out from HPF *D. melanogaster* egg chamber. A: FIB and **B:** FLM image (anterior to the right) of the egg chamber that are used in 3DCT for correlation. Crosshairs and numbering show the features that are used for correlation. **C:** FIB image of the region milled for SEM volume imaging. The white frame indicates the region imaged in D. **D:** SEM image from a volume imaging run on the egg chamber showing oocyte as well as the follicle cell epithelium layer with cellular features distinguishable such as lipid droplets. Figure reproduced from [21], with permission.

4.2. Machine Learning and automated sample exchange hardware enables fully automated cryo-FIB lamella milling of multiple grids

The following chapter is in preparation to be submitted for publication. The machine learning code was developed in collaboration with Marina Luchner, a Master's internship student at the time in the research group CryoEM Technology, who trained some of the neural networks deployed in this chapter throughout her internship. I supervised the algorithm development, collected the training data, developed the interface with SerialFIB and performed the FIB-SEM and TEM experiments.

4.2.1. General considerations for a fully automated cryo-FIB lamella preparation workflow

Creating an automated lamella preparation workflow without human intervention presents several challenges. It involves automating various steps, such as GIS platinum deposition, grid screening, selection of optimal milling positions for lamellae, and potentially applying sputter coating after lamella preparation. While most of these tasks can be addressed by defining specific stage positions, the most complex aspect is grid screening and subsequent lamella site selection. Initially, the process requires detecting cells from the images. As in manual lamella preparation, certain criteria must be fulfilled for the position to yield a suitable lamella:

- Visibility of cells from the ion beam view at the chosen milling angle
- Ensuring the cell colony size provides sufficient material for a lamella of adequate size for cryo-electron tomography (cryo-ET) data collection
- Avoidance of positions with an excessive number of cells to circumvent targeting thicker and therefore potentially devitrified regions
- Positions with cells in the center of a grid square with sufficent distance from grid bars to prevent interferences during lamella preparation or data collection

Additionally, though scanning electron microscopy (SEM) imaging can be beneficial for optimizing lamella milling protocols, it is not strictly necessary for the lamella preparation process. We developed the workflow to exclude the SEM in order to show that a minimal instrument encompassing only the FIB would potentially suffice for lamella preparation. The only exception in the presented work is during GIS platinum deposition, where it serves as a safety measure enforced by the microscope

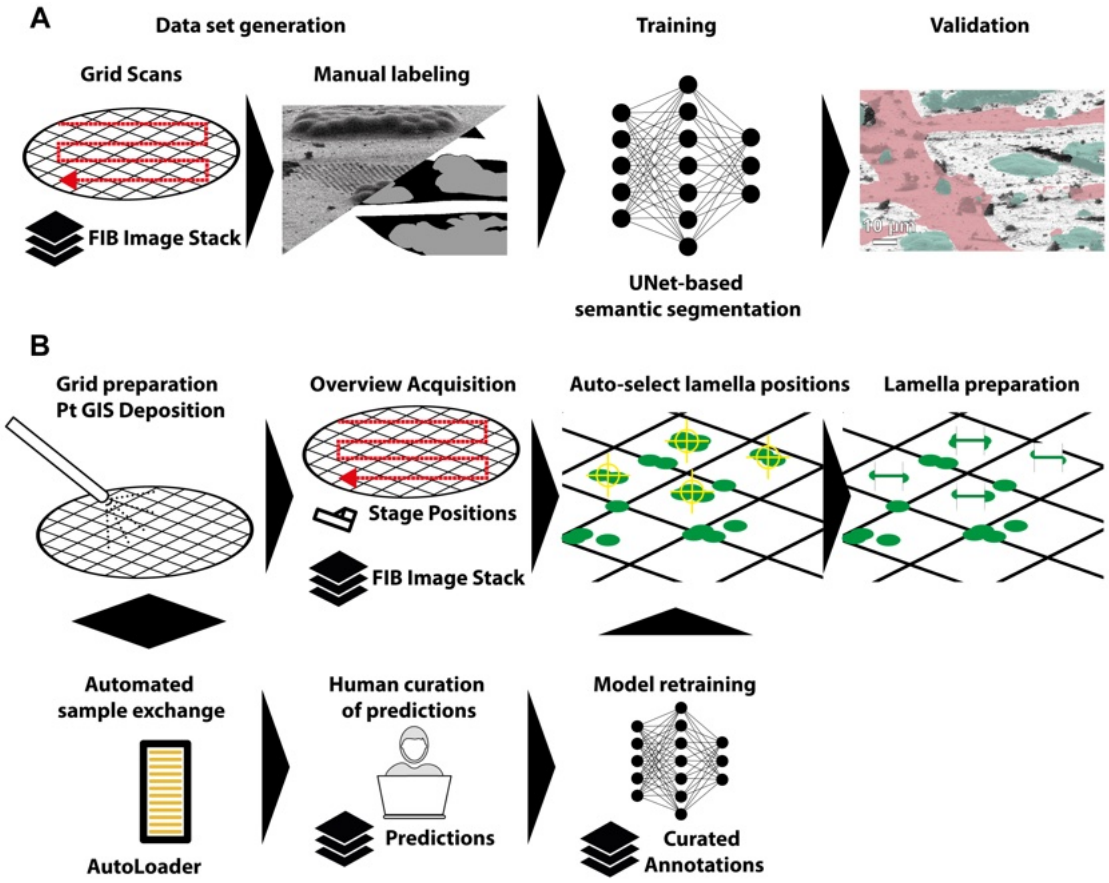

Figure 4.2.1 A: Model generation for automated lamella site selection. Grid scans are created, acquiring initial training data. The first images were manually labeled, following subsequent U-Net model training and validation. **B**: During model deployment, grids are loaded into the cryo-FIB and automatically GIS deposited and screened. During the screening, the acquired images and their corresponding stage positions are stored. Lamella sites are selected automatically and lamella are prepared based on a user-defined sequential milling protocol. In a human-in-the-loop approach, the images acquired during model deployment are manually curated and can be used in subsequent training to improve the site selection model for the next deployment.

provider. This can, however, be circumvented if no SEM column is present. Based on these criteria, the objective was to develop models for site selection and create a corresponding pipeline to deploy these models effectively. The software automates the platinum deposition on the grid, conducts a comprehensive grid screening, identifies suitable lamella positions solely from the screened FIB images, and ultimately prepares lamellae at these selected positions completely autonomous. The workflow is summarized in **Figure 4.2.1B**. If automated sample exchange hardware is available (compare **Chapter 3.4.10**), it can be used to prepare multiple samples via full automation, loading and unloading them one after the other.

4.2.2. Training a U-Net segmentation model for the detection of suitable lamella sites

The main task of the semantic segmentation is to determine the grid bar orientation on the image and cell colonies of suitable size and location (**Figure 4.2.2**). Thus, the

training dataset was manually labelled for 2 classes: grid bars and cells. To identify how many images were needed to train the U-Net-based semantic segmentation using the nnU-Net architecture, we trained two test models models on 45 and 164 images of *C. reinhardtii* cells, subsequently referred to as Chlamy45 and Chlamy164. The learning curves suggest overfitting of the training data already in the first epochs. Overfitting at this stage was, to the best of our knowledge, inevitable due to the limited data set size. Surprisingly, predictions from Chlamy45 on a novel image taken during a model deployment session on the microscope (**Figure 4.2.2A**) still yielded results on both grid bars (rose) and cells (cyan), that were successfully used for lamella site selection (**Figure 4.2.2**). This is most likely the result of the post-processing used in lamella site selection that is more robust in terms of positioning than the per-pixel evaluation in the network training. The semantic segmentation of the image is subsequently processed for lamella site selection. First, cell colonies of suitable size are determined based on their location in the image. This yields instance segmentations from the semantic segmentation where each instance is a cell colony of a user-defined desired size. Colonies that are larger or smaller than the given thresholds are ignored. Next, the grid bar positions need to be determined. Grid bars tend to be partially or fully covered by either a thick layer of ice or cellular structures. Thus, the prediction of grid bars based on the image alone only yields incomplete grid bar detection (**Figure 4.2.2B**, rose). To overcome the problem of imperfect visibility of the grid bars in cryo-FIB images, we used prior knowledge of the geometry of grids for inference of grid bar orientations. A grid mask with measured dimensions of the physical grid bars based on the pixel size is created, rotated in 5° increments to 90 ° and each rotation is projected to the corresponding 11° viewing angle of the focused ion beam. The resulting library of grid masks is template matched to the grid bar segmentation of the image prediction (**Figure 4.2.2B**) and the image with the highest cross-correlation is used for subsequent processing (**Figure 4.2.2D**). This “idealization” of the grid bar segmentation resembles the interpolation that a user does intuitively. The cell instances (**Figure 4.2.2C**) can then be visualized on the original FIB image (**Figure 4.2.2E**) and compared against the grid bar model. Positions that overlap with the grid bar positions and a buffer to prevent lamella preparation too close to the grid bar are removed and the final lamella site remains (**Figure 4.2.2F**). Note that due to the possibility of data augmentation performed during training of the nnU-Net by e.g., randomly translating and rotating the FIB images, the Chlamy45 model allowed the subsequent algorithm to detect suitable lamella sites in spite of the observed overfitting (**Figure 4.2.2**). Future models based on larger dataset may mitigate this problem.

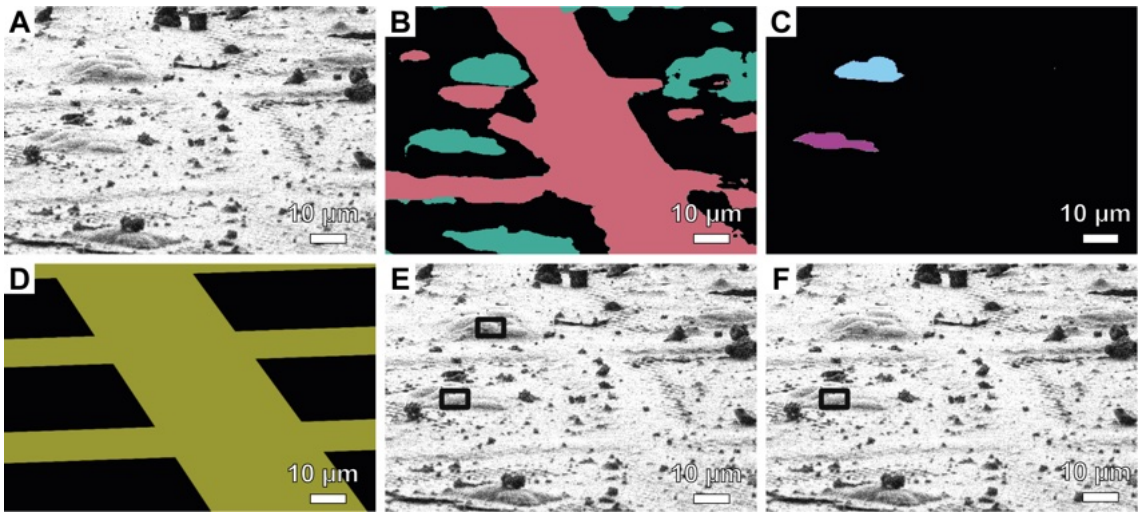

Figure 4.2.2 Site selection pipeline for cryo-FIB lamella positions: **A:** Image produced during the screening of a grid containing *C. reinhardtii* cells. **B:** Semantic segmentation of the image in A using the nn-UNet trained on 45 manually annotated images. **C:** Instance segmentation of the cell segmentation in B filtered for cell clumps of a certain size judged by the area of the cells. **D:** Highest scoring model for the grid bar orientation based on cross-correlation with a library of masks. The known grid dimensions are used to screen orientation based on a pre-defined angle step size, in this case 5°. **E:** Suitable lamella sites based on C. **F:** Lamella sites that do not overlap with the grid bar segmentation in D.

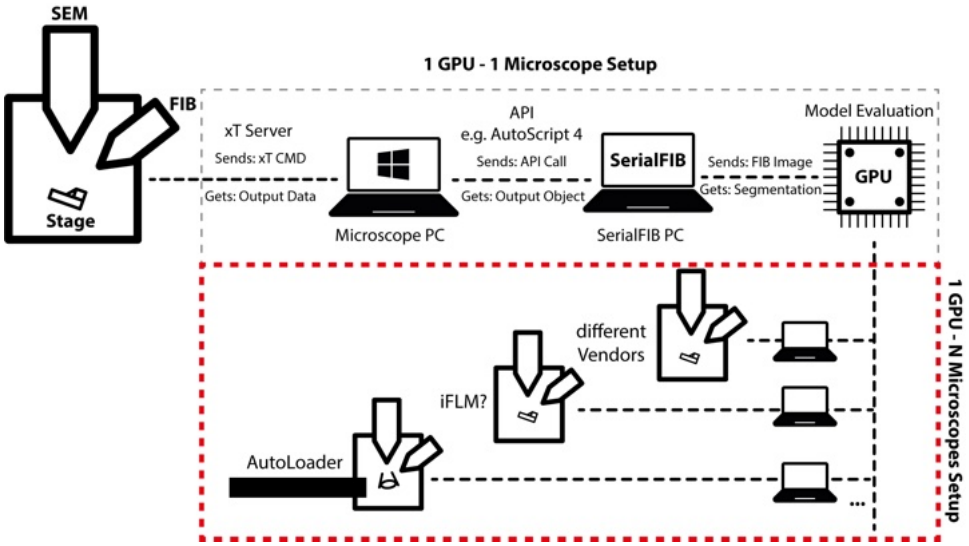

Figure 4.2.3 Setup for deploying the pipeline for automated lamella preparation with shared usage of a GPU for multiple cryo-FIB instruments. The dual-beam instrument is controlled via a Microscope PC running the vendor-specific software to control the instrument. SerialFIB is run on a computer that is connected to the network, either directly on the microscope computer or on a separate SerialFIB computer. It calls sends API calls to the dual-beam hardware using the the vendor specific API, for TFS instruments AutoScript 4. Images taken through the API are send to a different computer equipped with a CUDA ready GPU where the nnU-Net model is used to produce the semantic segmentation of the cryo-FIB image. The resulting segmentation is sent back to the SerialFIB PC where the result is used to proceed with the image processing steps for site selection based. The resulting lamella positions are prepared with the provided SerialFIB protocol via the vendor-specific API again. By design, this architecture allows for a single GPU to be deployed on multiple dual-beam systems with additional hardware if drivers for the equipment is developed. That includes the presented AutoLoader integration but also holds the potential to integrate e.g. integrated light microscopes and dual-beams from other vendors than the developed TFS driver. Note that SerialFIB drivers for e.g. the Zeiss Crossbeam are under development. Also, it is worth mentioning that the software architecture allows for deploying the code directly on the SerialFIB PC using e.g. the Windows Subsystem for Linux if desired. The requirement remains that the computer needs to be equipped with a GPU that can run the prediction using the nnU-Net architecture.

4.2.3. Deploying U-Net based automated site selection for lamella preparation

The microscope computer of modern cryo-FIB instruments is usually not equipped with a CUDA-ready graphical processing unit needed for the deployment of the U-Net model. While it is easy to upgrade existing computers with the necessary GPU hardware, it would be inefficient usage of the GPU as it is only rarely used during lamella production. The most time-consuming part is the milling process, which would leave the GPU idle except during the screening phase. Also, training can be performed "offline" as the microscope is not required for model training. In addition, the microscope computer shipped by a company is usually part of the warranty and/or service contract that comes with the microscope, making upgrades impractical or even impossible. To circumvent the troublesome and inefficient upgrade of cryo-FIB computers, we deployed the neural network in a centralized architecture (**Figure 4.2.3**). By mounting a GPU node to the computer running SerialFIB, images can be sent to a directory structure set up on the prediction server. A process running in the background on the GPU node checks for new images coming in from the microscope. If new images are found, they are predicted and saved to disk. The SerialFIB computer can subsequently take the predictions written to disk for lamella site selection. As facilities are starting to have multiple dual beam instruments, this not only allows for efficient usage of a single GPU node for training and deployment but also enables the GPU node to serve multiple cryo-FIB instruments, potentially even across more vendors as novel drivers for SerialFIB are in development.

To deploy the neural network on the microscope, we use SerialFIB's scripting interface to perform Pt deposition and grid screening. The acquired images are subsequently sent to the prediction GPU server. The resulting predictions are transferred back to the microscope computer and the necessary image processing steps to decide on suitable lamella sites are performed (**Figure 4.2.2**). Then, using previously described algorithms for automated lamella preparation (compare **Chapter 4.1**), SerialFIB prepares lamellae at the determined positions. If the software runs on hardware with automated sample exchange, the grids to be prepared can be selected and will be automatically exchanged during the workflow.

4.2.4. Fully automated workflow of cryo-lamella preparation of *C. reinhardtii* cells using gallium FIB

The trained U-Net model and site selection pipeline was deployed on grids of *C. reinhardtii* (**Figure 4.2.4**). The quality of the lamellae prepared are similar to automated lamellae from user setups and allowed for data collection. It needs to be noted that false positives will arise from the lamella site selection algorithm, especially for the

	Chlamy45	Chlamy45 with 5xCV	Chlamy164
Dice Score	0.34	0.31	0.41
Accuracy	0.65	0.66	0.69
Precision	0.67	0.83	0.88
Specificity	0.92	0.97	0.97
Sensitivity	0.23	0.19	0.27

Table 4.2.1 Performance of the lamella site selection pipeline. Performance is evaluated using the metrics dice score, accuracy, precision, specificity and sensitivity and compared between the model with 45 training cases, the model with 45 training cases and cross-validation and the model with 164 training cases. The metrics were derived from the true positive, true negative, false positive and false negative cell clusters selected by the pipeline. The classification from a human examiner was used as ground truth. Human examination and statistics performed by Marina Luchner.

small training data set (i.e. Chlamy45 model) but do not interfere with lamella preparation of true positives as the seperation of the field of view are chosen such that there is no overlap. As the images are produced in a systematic fashion during grid screening at the beginning of the workflow, images produced during production runs can be used to increase the size of the data set for training. This allows for the gradual increase of the data set size, potentially improving performance in the long run.

4.2.5. Models trained on Ga^+ images of C. reinhardtii are able to prepare lamellae of *S. cerevisiae* cells using Xe^+ ion beams

To explore the transferability of models trained on cryo-FIBs to other cell types and instruments, we tested the deployment of the Chlamy45 model trained on LMIS Ga^+-based FIBs on novel Xe^+-based cryo-plasma ion source. We observed that the machine learning model was indeed able to select suitable lamella sites from Xe^+ ion beam images, even though it was only trained with Ga^+-based images (**Figure 4.2.6**). A sample tomogram collected from a lamella prepared with xenon is shown in (**Figure 4.2.7**).

By using a novel cryo-PFIB instrument equipped with an AutoLoader, we explored the feasibility of the preparation of multiple grids with cryo-FIB lamellae without user intervention. The limitation in how long a grid can be on the stage and in the automated sample exchange for lamella preparation lies in the amorphous ice contamination rate inside those two vacuum systems. The ice contamination rate inside the chamber on our instrument is 3.8 nm/h (vendor specifications are 5 nm/h), while the growth of the contamination layer is 0.44 nm/h (vendor specifications 5 nm/h) when grids are stored in the AutoLoader (**Figure 4.2.5**). Thus, assuming an average lamella thickness of 200 nm, the maximum time that the first grid may spent in the chamber microscope to stay below 15% of additional lamella thickness by ice contamination (i.e. 30 nm) at

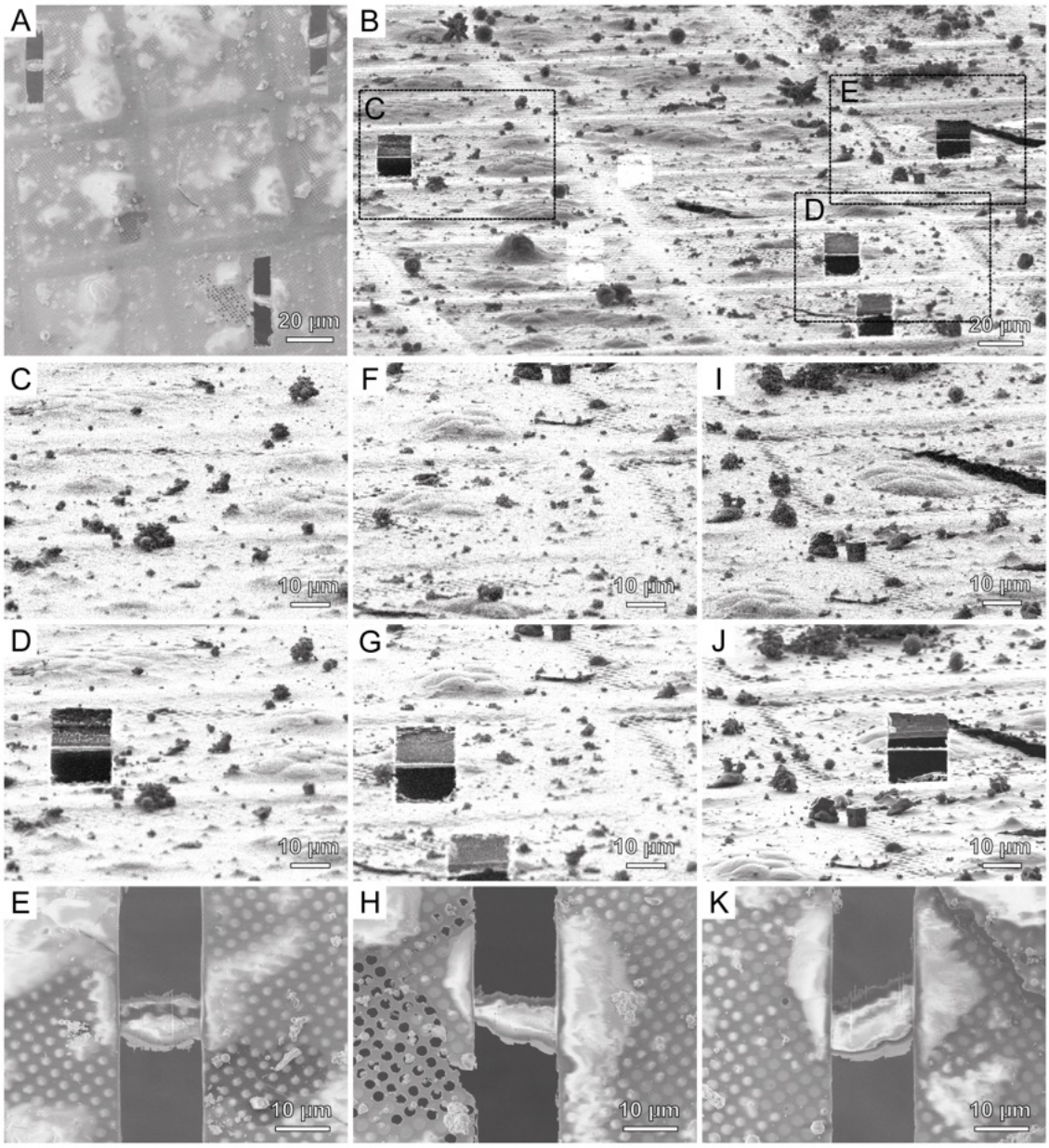

Figure 4.2.4 Fully automated lamella preparation workflow using a Ga+ focused ion beam instrument. A: SEM and **B:** FIB overview image of the automated lamellae prepared. (C)-(E) initial FIB image from grid screen performed during the workflow. (C') – (E') final FIB image of the lamella site after lamella preparation. (C")-(E") SEM image of the prepared lamellae.

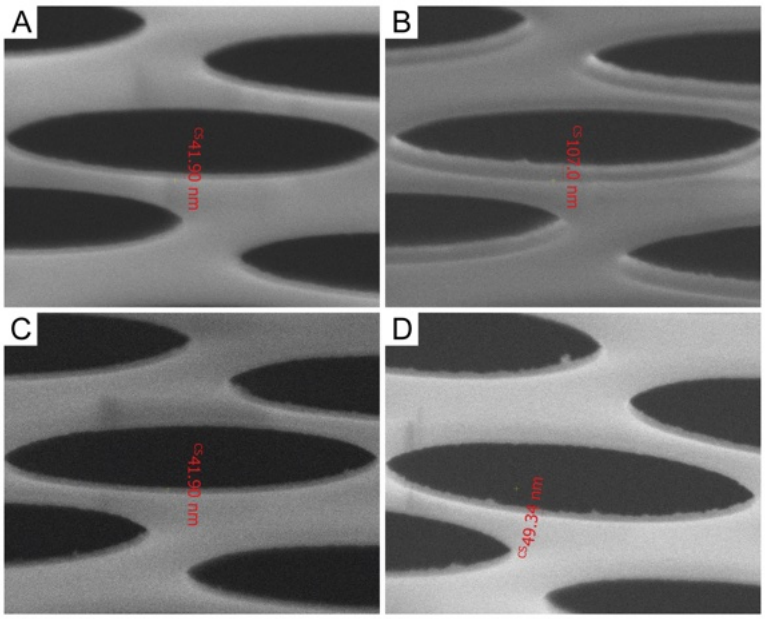

Figure 4.2.5 Redeposition measurements Arctis chamber and AutoLoader over 17 hours. A: SEM image of a grid kept within the chamber at the beginning of the measurement collected using the T2 detector. **B:** SEM image of a grid kept within the chamber after 17 hours collected using the T2 detector. The measured value for redeposition is $(107 - 41.9)/2 * 1/17 = 1.91nm/h$. **C:** SEM image of a grid kept within the AutoLoader at the beginning of the measurement collected using the T2 detector. **B:** SEM image of a grid kept within the AutoLoader after 17 hours collected using the T2 detector. The measured value for redeposition is $(49.3 - 41.9)/2 * 1/17 = 0.21nm/h$.

the end of the preparation of 12 grids is approximately 8h. Assuming from experience of several runs a lamella preparation time of 15 minute per lamella including screening and site selection steps, this would result in 3h preparation time if on average 12 suitable lamella sites per grid are found. If 3h preparation time is assumed, the first grid needs to be stored for 33 hours, adding 14.5 nm contamination. This allows for the grid to be stored in the AutoLoader during the preparation of the other grids without increasing contamination above 30 nm or 15$\%$ of the lamella thickness. Additionally, it is worth noting that the direct transfer from the plasma focused ion beam to the transmission electron microscope using the AutoLoader cassette and capsule also seems to circumvent extensive transfer ice contamination, though the transfer still requires reintroduction into liquid nitrogen. An in-vacuum transfer between the Arctis PFIB and the TEM would thus be desirable.

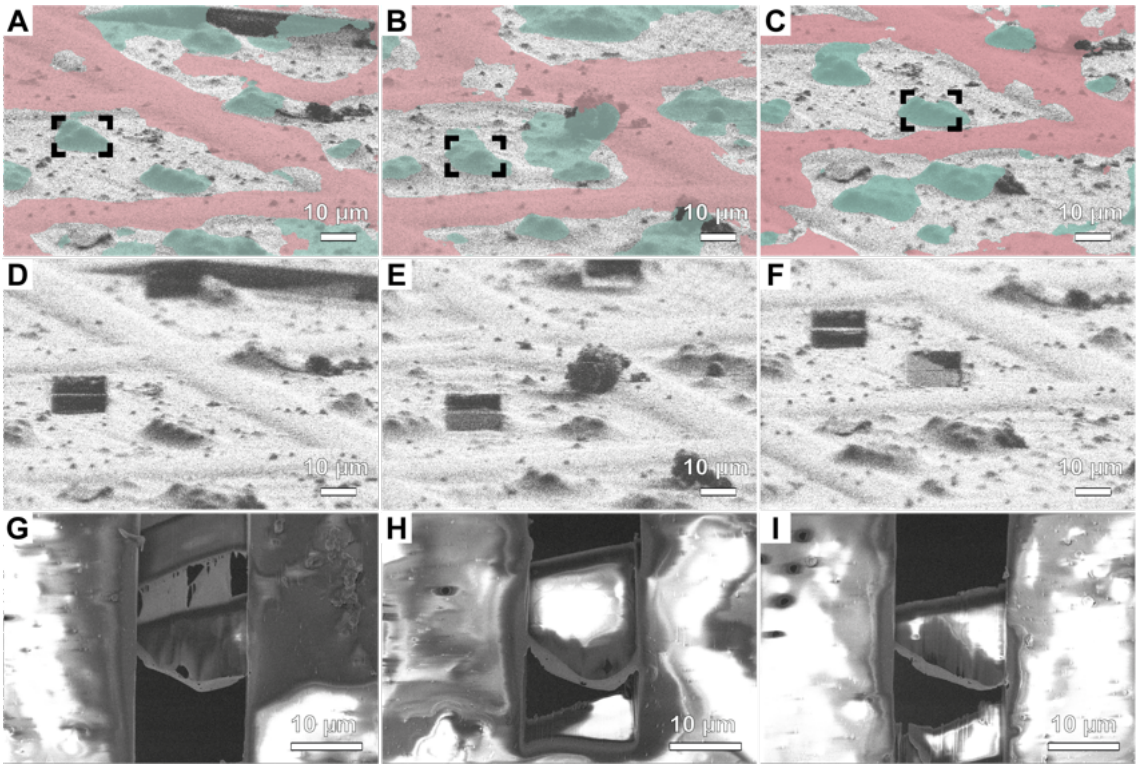

Figure 4.2.6 Example lamella from lamella milling job with Xe with the fully automated workflow presented here

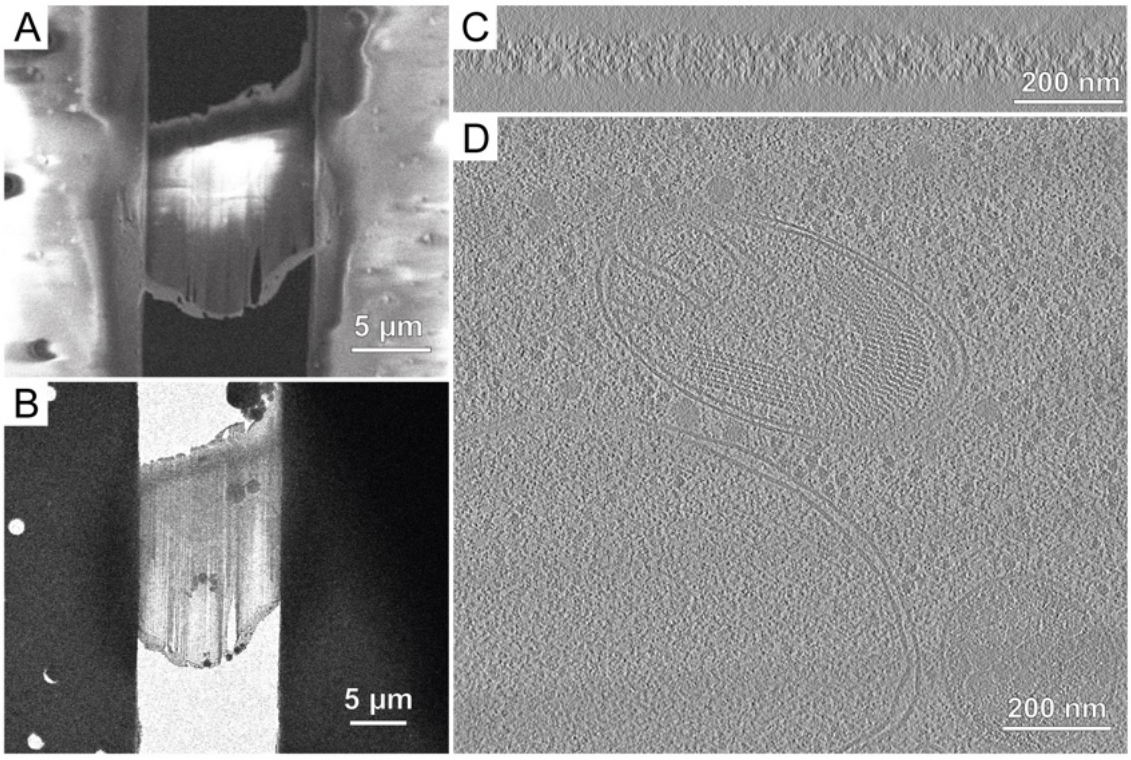

Figure 4.2.7 Sample tomogram from a fully automated lamella. A: SEM and **B:** TEM overview image of the milled lamella. Note the relatively strong curtaining artefacts that are still observed when using Xe^{+} PFIB lamella milling. **C:** XZ and **D:** XY section through a tomogram reconstructed from a tilt series acquired on the lamella in A and B. While curtaining will cause different regions on the lamella to be of varying thickness, high quality lamellae can still be acquired.

4.3. Structural basis of VIPP1 oligomerization and maintenance of thylakoid membrane integrity

This chapter is published as a highly collaborative article in Cell [242], encompassing five equally contributing authors, Dr. Tilak Kumar Gupta, Dr. Karin Gries, Dr. Steffen Heinz, Dr. Wojciech Wietrzynski and myself. Within this collaborative project, I performed the structural modelling and analysis work on all VIPP1 structures, suggested point mutations to generate based on the structural models for both the lipid binding and ATP hydrolysis sites of VIPP1, performed the comparison experiment of wildtype and mutant cyanobacteria *Synechocystis sp. 6803* strains by cryo-electron tomography and acquired the correlative light and electron microscopy data on the VIPP1-RFP *C. reinhardtii* strain.

4.3.1. High-resolution model of VIPP1 oligomerization

To gain a deeper understanding of VIPP1's various functions, structural insights at high resolution were needed. Previously, the only available 3D structures of VIPP1 was a low-resolution negative-stain electron microscopy (EM) single particle reconstruction that cannot reveal individual VIPP1 subunits (protomers) [243]. Consequently, we embarked on determining the structures of heterologously expressed *syn*VIPP1 rings using single-particle cryo-EM. Through iterative classification and refinement of approximately 337,000 particles from 8,120 images, Dr. Tilak Kumar Gupta and Dr. Jan Schuller obtained five distinct cryo-EM density maps representing VIPP1 rings with C14, C15, C16, C17, and C18 symmetries (**Figure 4.3.1**). These maps ranged in resolution from 3.8 Å to 5.0 Å, a resolution were *de novo* structural modelling on side-chain level is challenging. By employing a combination of techniques such as homology modeling, *ab initio* structure prediction, and refinement through molecular dynamics flexible fitting (MDFF), I successfully constructed atomic models for the two structures with resolutions better than 4 Å (C15 and C16) and extended this model building process to the other three symmetries (**Figure 4.3.1**).

In contrast to a previously discussed architecture that positioned VIPP1 monomers vertically along the ring's central axis [243], the obtained model shows that the monomers are horizontally arranged in stacked layers (**Figure 4.3.2D-E**). We observed six layers in C14-C16 and seven layers in C17 and C18 . The rings show a smaller diameter at the top (layer 1) compared to the bottom (layer 6 or 7). The density maps resolve five of the seven predicted helices of *syn*VIPP1, with the predicted H4 and H5 domains forming a single helix. The N-terminal H1 domains of each layer align to create vertical columns facing the ring's lumen (Fig. 1C). H2 and H3 form a coiled-coil hairpin, connected to H4/5 by a seven-amino-acid loop (**Figure 4.3.2G**). H6 protrudes on the outer surface of the ring (**Figure 4.3.2B**). Within a layer, H3 and H4/5 extend to pass

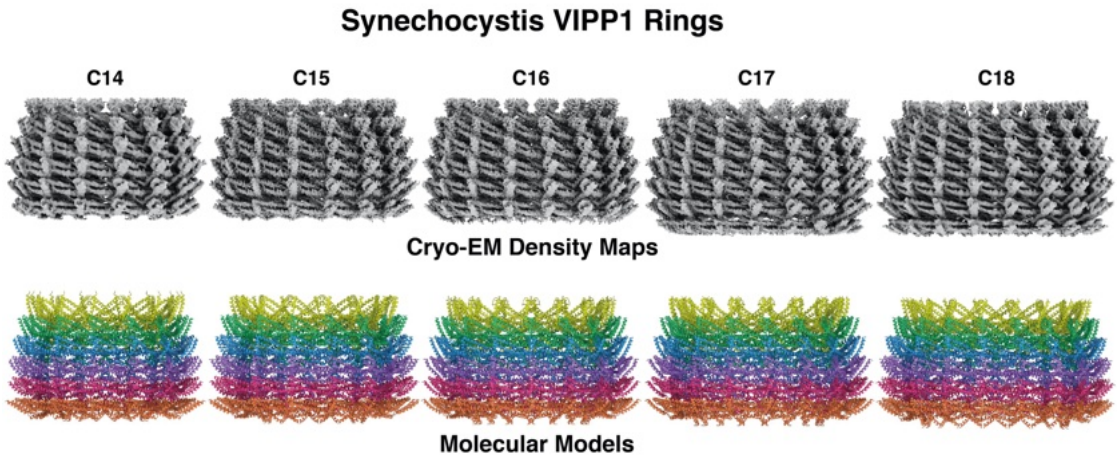

Figure 4.3.1 Maps and models for the different symmetries of VIPP1. Modeled structure range from C14 to C18 symmetric assemblies.

behind two adjacent monomers, while H6 points upward and binds the H2/H3 hairpin of the third neighboring monomer, creating the interwoven structure (**Figure 4.3.2D-E**). Additionally, the luminal H1 columns stabilize the ring internally and help hold the stacked layers together. In total, each VIPP1 monomer can interact with up to 16 other monomers from three layers (**Figure 4.3.3**).

H7 was not resolved in the cryo-EM map, most likely due to flexibility as it is connected to H6 via a 32 amino acid long, disordered linker which complicates the averaging in single particle analysis. The helix is not important for assembly of the oligomeric structure as rings can still be observed when deleting the helix. It is, thus, thought to interact with other factors in the cellular milieu such as chaperones that may regulate VIPP1's structural dynamics.

Comparing the different symmetries (C16-C18) of the *syn*VIPP1 structure, it is apparent that four regions of flexibility within the VIPP1 monomer allow for the structural rearrangements necessary to build both the layers within a symmetric structure (**Figure 4.3.2J**) and the differences across the different rotational symmetries (**Figure 4.3.2K**). While the former seems to be exploiting a combination of the flexible regions, the superposition of monomers in the same layer of different symmetries indicates that the latter mainly relies on the F3 region (**Figure 4.3.2K**).

4.3.2. VIPP1 assemblies show a nucleotide-binding pocket

During model building, an additional density between layer 1 and 2 (**Figure 4.3.4A-B**) was found. The additional density did not correspond to any of the protein residues (**Figure 4.3.4B**) and fitted in size to an additional bound molecule such as a nucleotide (**Figure 4.3.4C**). The vicinity and charge distribution around the ligand bind-

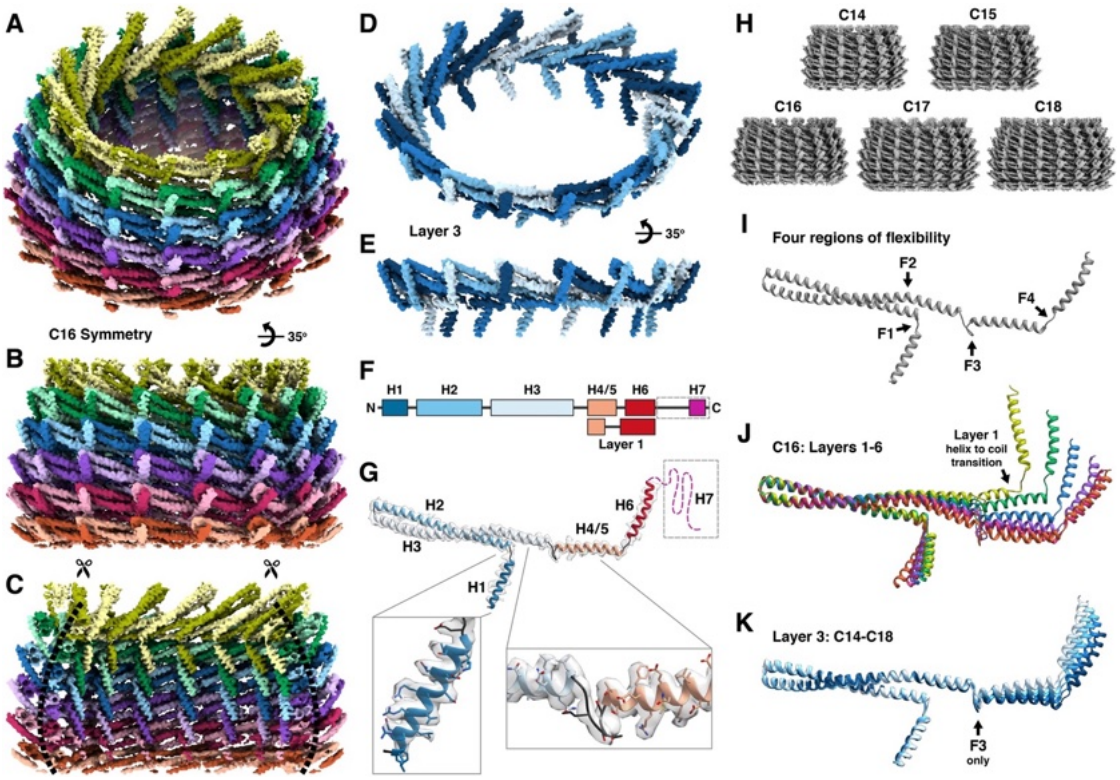

Figure 4.3.2 Structural basis of VIPP1 oligomerization. A: Structure of the C16 symmetric map colored by chain using the derived models. **B:** Side and **C:** luminal view of the VIPP1 C16 oligomer. **D:** Angled and **E:** side view of the segmentation of a single layer within the oligomeric structure shows the interwoven subunits. **F:** Schematic of the VIPP1 monomer from N- to C-terminus. The alpha helices are indicated as rectangles. **G:** Representative image of the map-to-model fit from a single subunit from layer 3 of the C16 symmetric structure. Zooms show the helices H1 and the region between H3 and H4/5. **H:** maps of the other symmetries. **I:** Flexible regions within the VIPP1 monomer. **J:** Superposition of the monomers from different layers showing the inherent flexibility that allows for the formation of the oligomeric structure. **K:** Superposition of the monomer from layer 3 across different assemblies (C14-C18) showing the flexible regions enabling the formation of the assemblies. Adapted from [242], with permission.

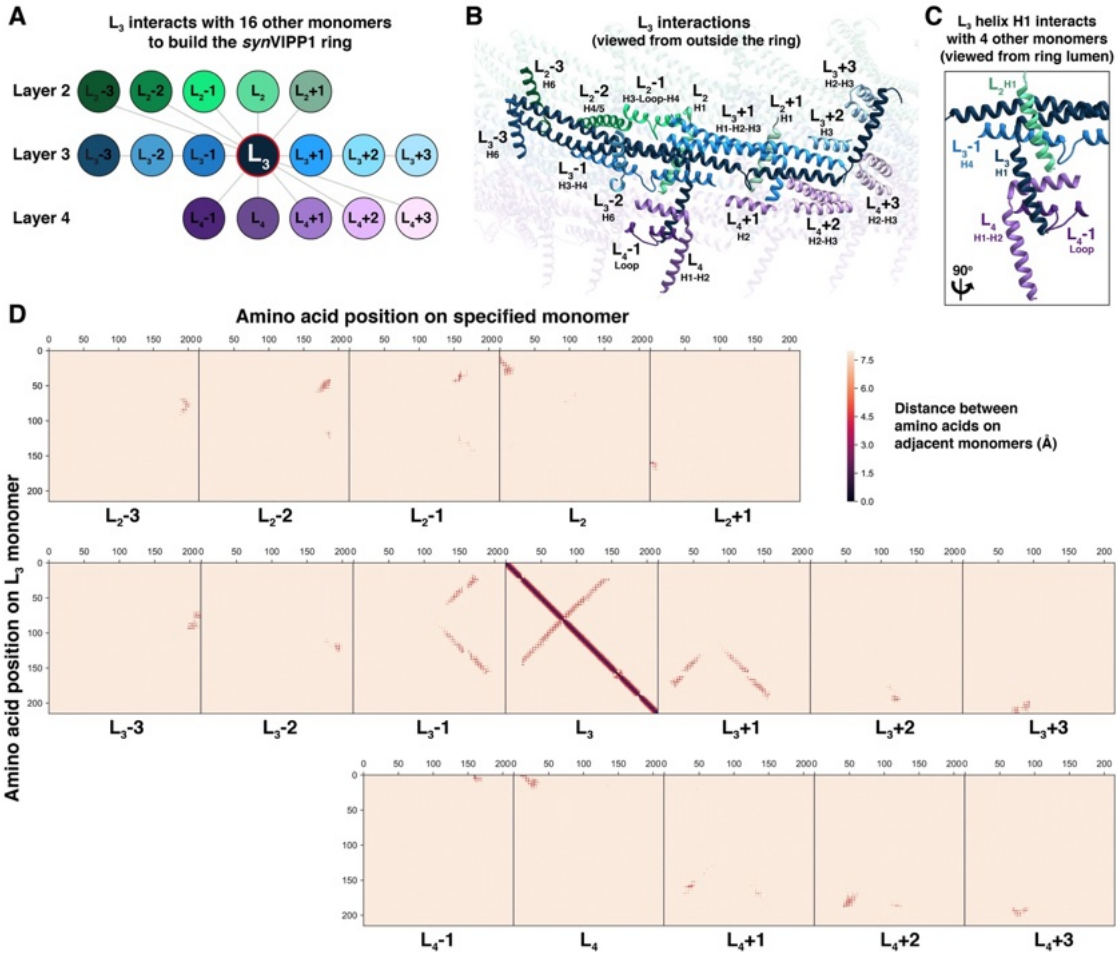

Figure 4.3.3 Interaction mapping of the C16 symmetric assembly of VIPP1. A: Schematic representation of the neighbors of a monomer within layer 3 (L3). **B:** Interactions of L3 viewed from outside the ring. **C:** Interactions of H1 from L3 viewed from the luminal side. **D:** Distance mapping of the amino acids within the different monomers. Y axis is always the L3 monomer numbering and X axis are the residues of the monomer as specified. Adapted from [242], with permission.

ing pocket suggested a nucleotide binding site (**Figure 4.3.4D-E**). With help from Dr. Elisabeth Weyher-Stingl and Dr. Maria Victoria Sanchez Caballero (MPI Biochemistry core facility), we performed additional mass spectrometry experiments using reversed-phase ion-pair high-performance liquid chromatography (RPIP-HPLC) coupled to electrospray ionization mass spectroscopy (ESI-MS) as previously described [244] and found a peak for ADP in the sample (**Figure 4.3.5A-B**). The nucleotide is likely incorporated during the ATP washing step in protein purification as part of the chitin-affinity chromatography. When sequentially washing with GTP, GDP is found in the mass spectrometry experiment (**Figure 4.3.4F**). In conjunction with these findings, nucleotide hydrolysis experiments performed by Dr. Norikazu Ohnishi and Dr. Wataru Sakamato (Okayama University, Japan) show that *syn*VIPP1 do hydrolyze ATP and GTP (**Figure 4.3.4G**). Comparing the additional density with other ADP and ATPγS densities available on the protein data base (p97 structures at 2.3 Å and 3.3 Å for ADP and ATPγS, respectively) further underlined the presence of a hydrolysed nucleotide and even helped identify a round density in the vicinity of the bound ligand that fits a magnesium ion bound to the diphosphate of ADP (**Figure 4.3.6A**). Based on the these results, I modelled the *syn*VIPP1 binding site with a bound ADP nucleotide. The model suggests Arg44 and Lys133 clamping the negatively charged diphosphate. Glu179 and Glu126 are positioned to act as proton acceptors in a hydrolysis reaction by nucleophilic attack of a water molecule at the γ-phosphate of an ATP molecule (**Figure 4.3.4E**). A schematic representation of the binding site is given in **Figure 4.3.6F**. To the best of our knowledge, the binding site does not correspond to any described ATP binding site, the most prominently being Walker A or P-loop motifs. Based on the model, I was able to suggest point mutations to probe our understanding of the nucleotide hydrolysis reaction in *syn*VIPP1 by site-directed mutagenesis experiment and subsequent phosphate release assays. Indeed, as is known for other ATPases, mutating the clamping residues while preserving their postively charged property (R44K and K133R) showed a decrease in phosphate release for R44K while not showing an effect for K133R. Similarly, mutating Glu126 and Glu179 to glutamine, therefore taking out their ability to accept protons, showed a decrease in phosphate release for E126Q and E179Q. Likely, these two residues are both able to act as proton acceptors in the hydrolysis reaction as only the double mutation E126Q+E179Q leads to no phosphate detectable in the release assay, thus destroying *syn*VIPP1's ATPase activity(**Figure 4.3.4H**). Interestingly, the binding pocket is formed between 3 monomers, two of layer 1 and one of layer 2 (**Figure 4.3.6E**). Only a structural rearrangement that happens on monomers of layer 1 (**Figure 4.3.6B-D**) and significantly shortens H4/5 enables the reach of Glu179 into the nucleotide binding site, giving possible insights into why ligand binding is only observed between layer 1 and 2 of the *syn*VIPP1 oligomer.

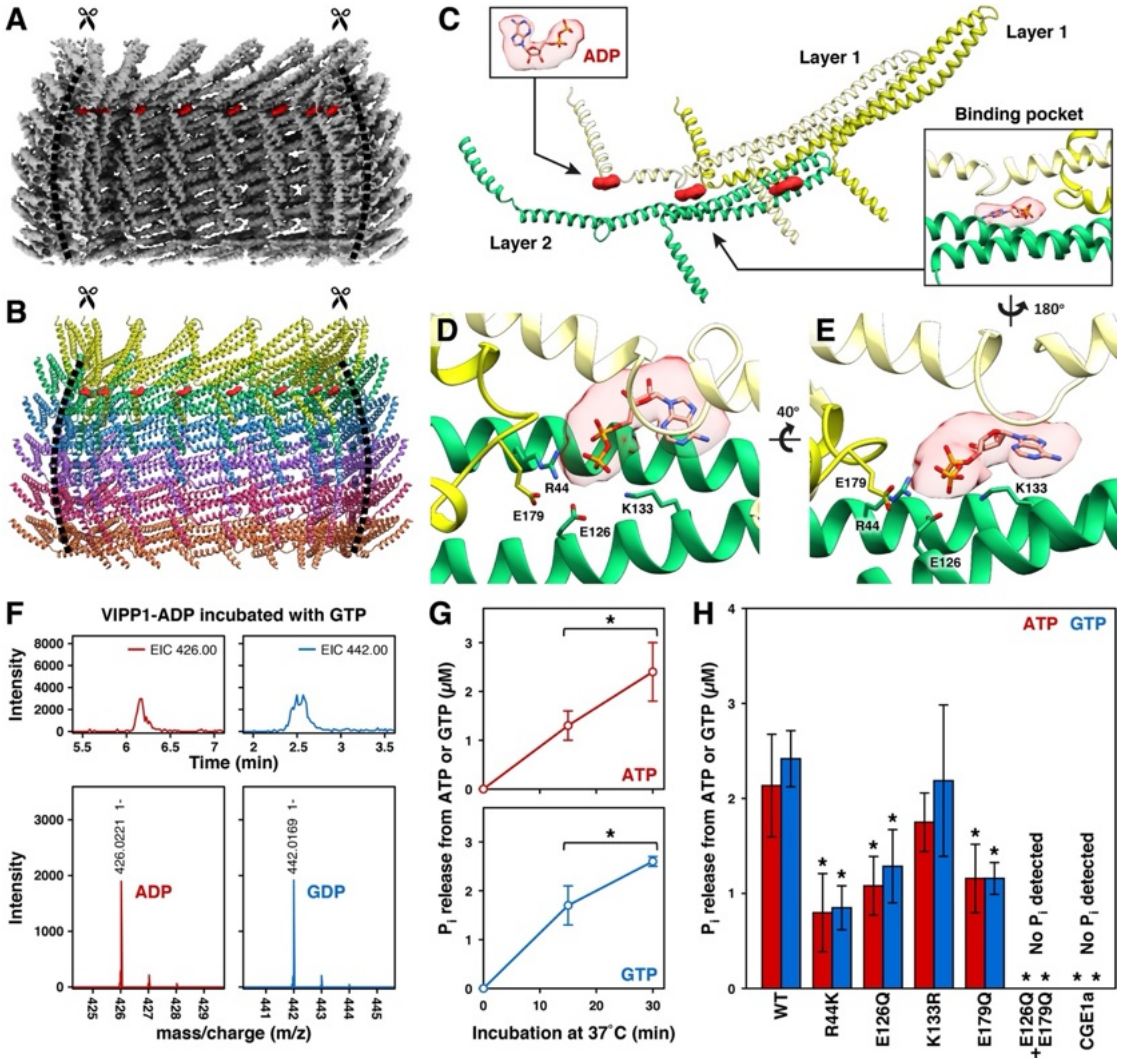

Figure 4.3.4 Structural aspects of VIPP1's nucleotide binding. A: Map of the C16 symmetric structure with the additional density between layer 1 and 2 of the oligomeric structure shown in red. **B:** View of the model of VIPP1 with the additonal density. **C:** The nucleotide binding site is formed by two monomers from layer 1 and one monomer from layer 2 coming together. Insets show the fit of ADP to the density. **D:** Side and **E:** Top view of the nucleotide binding site with the relevant residues for nucleophilic attack during nucleotide hydrolysis shown as sticks. **F:** RPIP-HPLC profiles (top panels) and subsequent ESI-MS (bottom panels) of wild-type (WT) synVIPP1 following incubation with GTP. Some of the bound ADP was exchanged for GDP. **G:** *In vitro* nucleotide hydrolysis assays show the release of phosphate from ATP and GTP by *syn*VIPP1. Error bars and standard deviation are from 3–4 replicates. Significant changes between the timepoints are indicated by the asterisks (*p < 0.05, Welch's t test). **H:** *In vitro* ATP and GTP hydrolysis by wildtype *syn*VIPP1 and mutations in the nucleotide binding pocket. Double mutations are indicated by a '+'. The nucleotide exchange factor of chloroplast Hsp70, CGE1a, was used as a negative control as it does not possess ATPase activity and is purified using the same protocol as for VIPP1. Error bars and standard deviation from 6–10 replicates. Significant changes are indicated by the asterisks (*p < 0.05, Welch's t test). Adapted from [242], with permission.

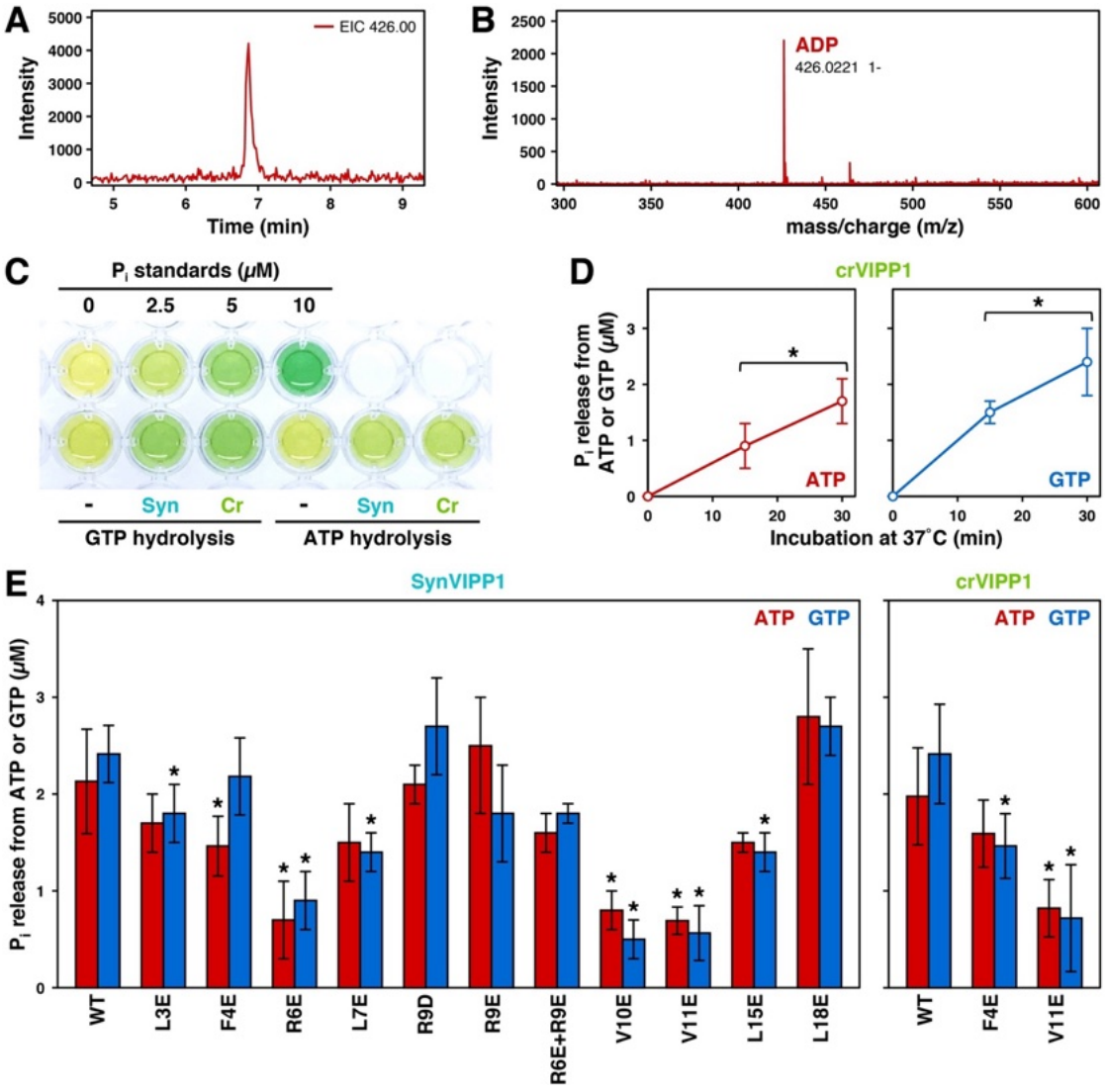

Figure 4.3.5 Mass spectrometry and nucleotide hydrolysis assay data of VIPP1. A: RPIP-HPLC profile and **B:** subsequent ESI-MS of isolated wildtype *syn*VIPP1. A distinct mass for ADP was observed. **C:** Microwell plate for *in vitro* nucleotide hydrolysis assay. Inorganic phosphate (Pi) standards are arrayed in the top row, and the hydrolysis of ATP and GTP by *syn*VIPP1 (Syn) and *C. reinhardtii* VIPP1 (Cr) are assayed on the bottom row. The control without protein shows no hydrolysis(-). **D:** Hydrolysis of ATP and GTP by crVIPP1. Error bars and standard deviation from 4–5 replicates. Significant changes are indicated by the asterisks (*p < 0.05, Welch's t test). **E:** *In vitro* ATP and GTP hydrolysis by wildtype and mutant synVIPP1 (left panel) and crVIPP1 (right panel). Error bars and standard deviation from 3-8 replicates. Significant changes are indicated by the asterisks (*p < 0.05, Welch's t test). Adapted from [242], with permission.

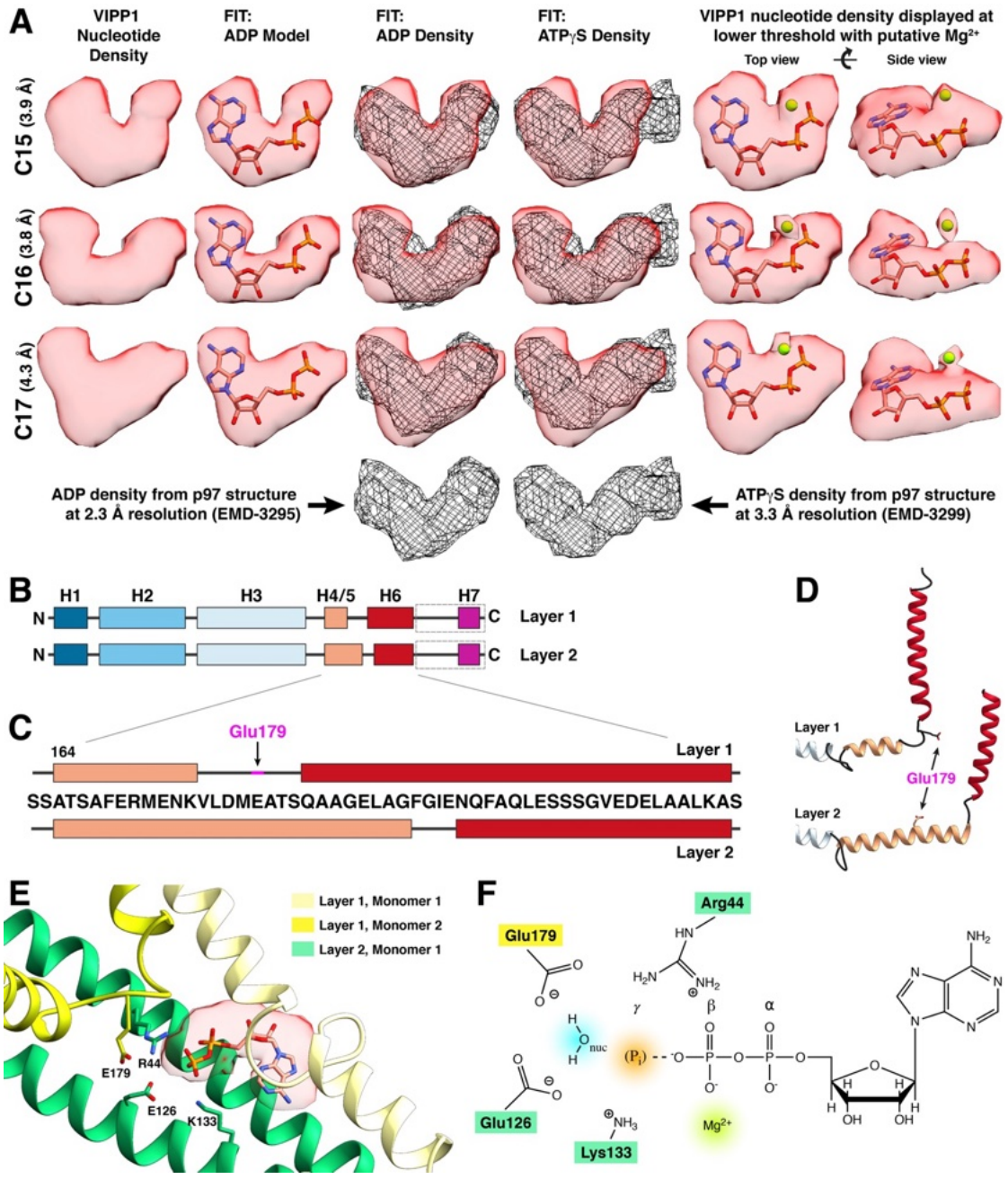

Figure 4.3.6 VIPP1 nucleotide density validation and detailed binding site description. A: Nucleotide density comparison to p97 structures (EMDB:3295 and EMDB:3299) show that a nucleotide di-phosphate fits the data better than a nucleotide tri-phosphate. **B:** Layer one shows a slight shift in secondary structure compared to the other layers, here represented by layer 2. **C:** Zoom into the sequence level of the shift in helix H4/5 between layer 1 and 2. **D:** Structural view of the representation in B and C. **E:** Top view of the binding site to illustrate the monomer positions schematically represented in E. **E:** Schematic of the nucleotide binding site of VIPP1. Adapted from [242], with permission.

4.3.3. Structural basis for VIPP1's lipid binding

Another additional density that did not fit to the protein model could be found on the lumenal side of the *syn*VIPP1 rings (**Figure 4.3.7A**). The N-terminal region of the *syn*VIPP1 monomer forms an amphiphatic helix required for lipid binding (**Figure 4.3.7B-C**). Due to the proximity of the additional density to the columns of amphiphatic helices on the luminal side of the oligomeric structure (**Figure 4.3.7D-E**), we interpret the density as residual endogenous lipids often detected when purifying VIPP1. Amphiphatic helices are known to induce membrane curvature. As the oligomeric assemblies tend to bind to and potentially even take in lipid bilayers, the N-terminal helices of *syn*VIPP1 are ideally positioned to interact with membranes. As it had previously been suggested that the N-terminal helix was required for VIPP1's function (compare **Chapter 3.7**), we decided to use the structure based model to determine positions that would disrupt the amphiphatic helix and, consequently, VIPP1's ability to bind membranes. Two mutations, F4E and V11E, where chosen for *in vivo* mutagenesis in *Synechocystis sp.* PCC 6803, prepared and tested under high-light stress by Dr. Steffen Heinz in Dr. Jörg Nickelsen's lab (LMU Munich, Germany). Indeed, the mutants showed a clear phenotype of decreased viability in spot growth assays under high-light condition but not under low-light conditions (**Figure 4.3.8A**). The relative abundance of VIPP1 for high-light to low-light conditions were unchanged for both mutations (**Figure 4.3.8B**). Subsequently, together with Dr. Wojciech Wietrzynski, I performed cryo-electron tomography experiments of FIB-milled cells (**Figure 4.3.8C**) to investigate whether the membrane architecture of these mutants shows similar phenotypes as previously described knock-down or knock-out experiments of VIPP1. Indeed, when comparing the membrane architecture of wild-type cyanobacteria (**Figure 4.3.8C-E**) to the *syn*VIPP1 F4E (**Figure 4.3.8F-H**) or V11E (**Figure 4.3.8I-K**) mutant, it is apparent that the thylakoid membranes are bloated dramatically. When quantifiying the membrane-to-membrane distances of wildtype and mutant strains under low- as well as high-light conditions, it is apparent that there is a slight increase in thylakoid lumen width going from low-light to high-light conditions in the wild-type. This effect, however, is much aggrevated in the mutant strains, leading to a higher mean and variance of thylakoid lumen width at both low and high-light conditions compared to the corresponding wild type measurements (**Figure 4.3.8L**). The phenotype in conjunction with previously observed phenotypes in cyanobacteria suggest that VIPP1's ability to bind and maintain thylakoid membranes is significantly impaired. In the reconstructed tomograms of the V11E mutant under low-light conditions, however, we did still observe multiple events of coated bilayers resembling *in vitro* reconstructions of *syn*VIPP1 bound to liposomes (**Figure 4.3.8M-O**). Thus, it is likely that some VIPP1 still shows some degree of membrane affinity, yet this remains to be quantified. In addition to the impaired stress response under high-light conditions, the mutants exhibited abnormal membrane topology at the thylakoid convergence zones, which had previously been implicated in their biogenesis. Instead of

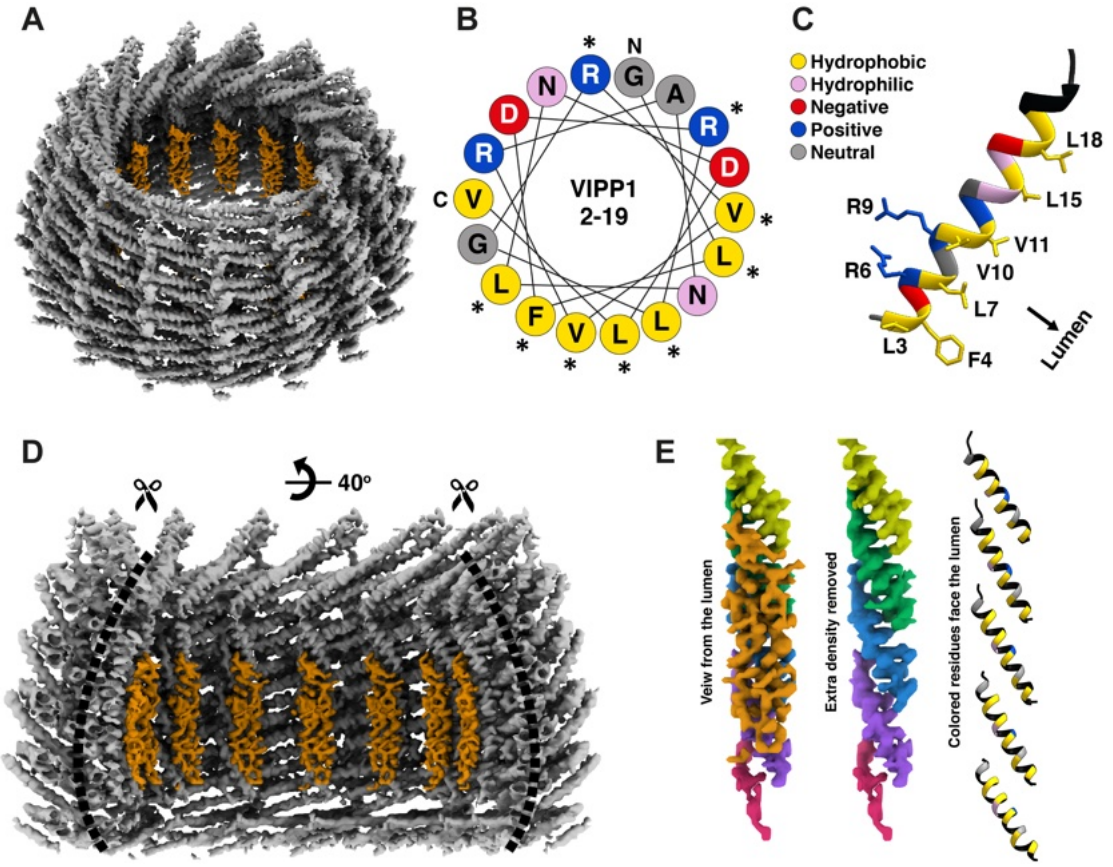

Figure 4.3.7 Structural basis of VIPP1's lipid binding. A: View of the C16 symemtric structure with the additional density (orange) highlighted on the luminal side of the oligomer. **B:** Helical wheel plot of the N-terminal helix (residues 2-19) of the VIPP1 monomer. Asterisks indicate the *in vitro* mutations analysed. *in vivo* mutations analysed are F4E and V11E. **C:** Representation of the model for the helix H1 of the VIPP1 monomer. **D:** Luminal view of the unassigned density shown in A. **E:** Density and model of the amphiphatic helix columns on the luminal side of the oligomer. Unassigned density in orange. Adapted from [242], with permission.

the usually observed convergence membranes that contact the plasma membrane, clusters of round membranes form (**Figure 4.3.8H**). Similar structures had been observed in *C. reinhardtii* for VIPP1 knockdown cells [225].

4.3.4. *In situ* observation of VIPP1 oligomers

To investigate the *in situ* structure of VIPP1 and confirm that it forms oligomeric structures inside the cell, we resorted to correlative light and electron microscopy experiments. Performing correlative cryo-FIB milling as discussed in previous chapters, we targeted the abundant fluorescent punctae that can be found in a *C. reinhardtii* strain that overexpresses a VIPP1-mCherry construct. Initially, we tried to visualize endogenously tagged VIPP1 in *Synechocytis sp.* PCC8603 but the punctae formed for endogenously tagged protein were too small to be targeted by the current state-of-the-art techniques. The fluorescent punctae in the VIPP1-mCherry overexpression *C. reinhardtii* cell line, however, were 200 nm to 500 nm in size and, thus, amenable to fluorescent guided lamella preparation. While the overexpression will lead to pro-

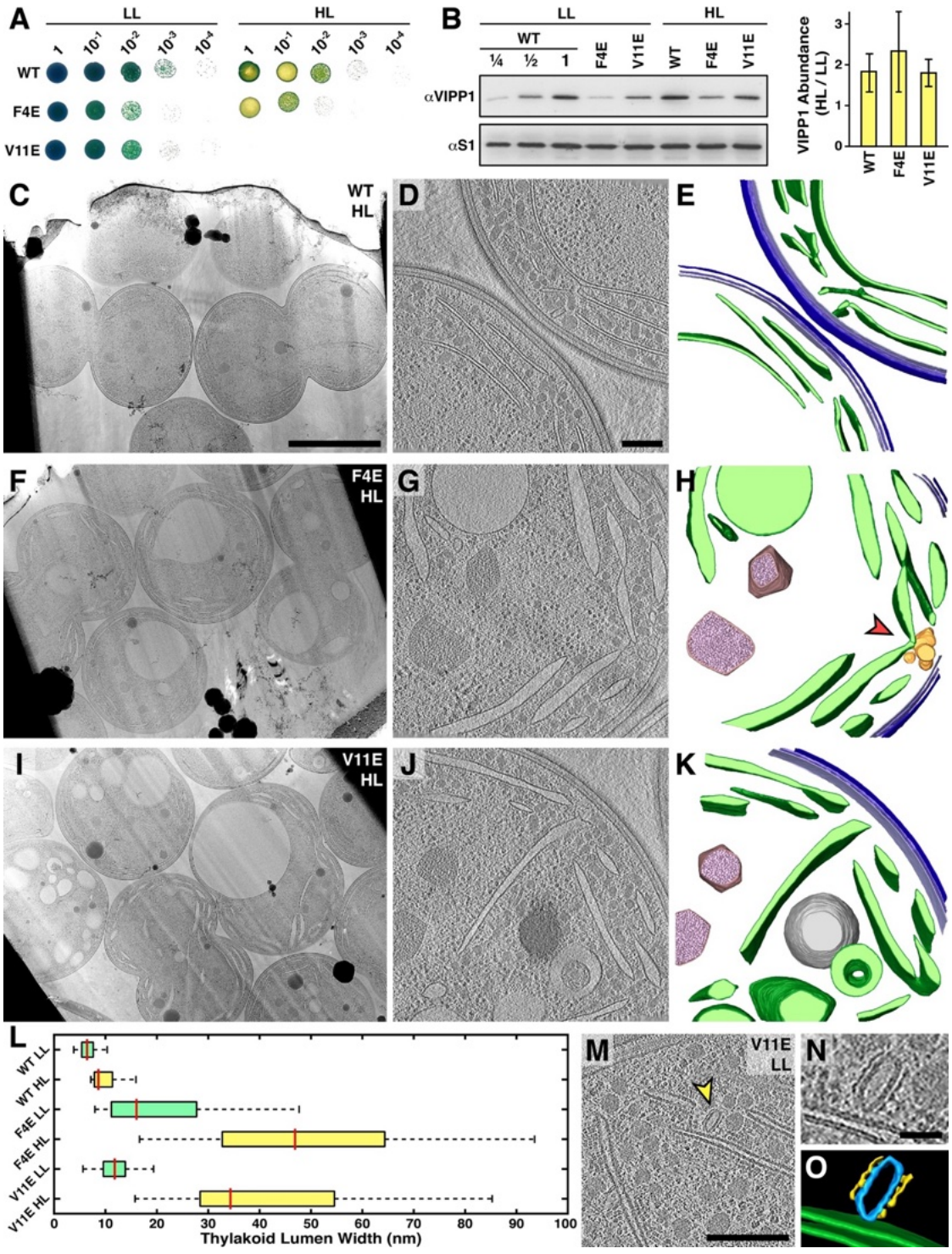

Figure 4.3.8 Interference of *syn*VIPP1 lipid interaction compromises thylakoid architecture under high-light stress. A: Spot growth tests of wildtype, F4E, and V11E mutant strains after 5 days on agar plates. Low light corresponds to 30 mmol photons m^{-2} s^{-1} and high light to 200 mmol photons m^{-2} s^{-1}. **B:** Protein level analysis of VIPP1 in liquid culture via Western blot at low light and 24 hour high light. The S1 ribosomal protein was used as a control. Relative abundance quantification in the bar plot on the right. Mean and standard deviation from 3 experiments. **C,F,I:** TEM overview, **D,G,J:** slice through a tomogram, and **E,H,K** segmentation for wildtype, F4E, and V11E strains under high-light stress. Note the thylakoid swelling of the mutants compared to the dense packing in the wildtype. Red arrowhead in H indicates the compromised thylakoid convergence zones, which had previously been implicated in thylakoid biogenesis. **L:** Quantification of thylakoid lumen width for low-light and high-light conditions of the wildtype, F4E, and V11E strains. Median shwon as red line with 25–75% percentiles (box) and 1.5 interquartile range (whiskers). 283 thylakoid membrane regions from 48 tomograms were analysed. **M:** Tomographic overview, **N:** close-up, and **O:** 3D segmentation of a structure resembling a protein coat (yellow) encapsulating membrane (blue) as observed in proximity to thylakoid membranes (green) *in situ*. Adapted from [242], with permission.

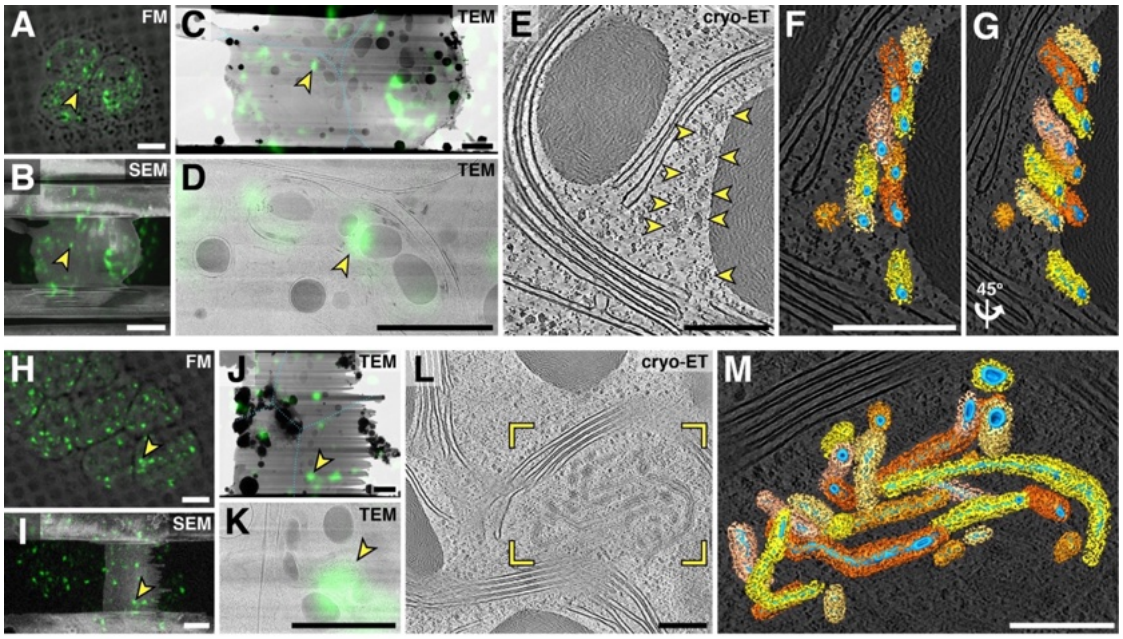

Figure 4.3.9 *In situ* observation of VIPP1 in *C. reinhardtii* by cryo-CLEM. A, H: Pre- and **B, I:** post-milling SEM image overlaid with the fluorescence maximum intensity projection (MIP) of a *C. reinhardtii* cell expressing mCherry-tagged VIPP1. **C, J:** TEM overview of the lamella and **D,K:** close up overlaid with the MIP. Yellow arrowheads indicate the fluorescent signal of the tilt series acquired. **E,L:** Slices through the tomogram collected on the fluorescent spots in D,K. Large assemblies (rectangle) of protein coated membrane tubes that can be clearly identified in the cross-section (arrowheads) are indicated. **F,G,M** Segmentations of the protein coated membrane tubes shown in E and L. Adapted from [242], with permission.

tein levels of VIPP1 that are far beyond the endogenous level, overexpression had previously been used to visualize the *in situ* architecture of mammalian ESCRT-III and bacterial ParM assemblies [245, 246].

The correlation in the CLEM experiemnt was guided by the VIPP1-mCherry signal and cellular features such as starch granules and cell boundaries (**Figure 4.3.9A, B, H, I**). The TEM overviews were subsequently correlated to obtain positions for cryo-electron tomography data acquisition that showed superposition with the fluorescence signal for VIPP1-mCherry (**Figure 4.3.9C, D, J, K**). Reconstructed tomograms from tilt series collected on those positions showed large clusters of membrane tubules coated with protein that resembles the *in vitro* structure observed for *C. reinhardtii* VIPP1 interacting with liposomes. Together with the co-localization of the fluorescent signal, we interpret the membrane coat likely consists of VIPP1, though they may contain other additional proteins known to interact with VIPP1 in *C. reinhardtii*. It clearly shows that the VIPP1 oligomeric structures can form *in situ* into helical assemblies within the native chloroplast. These helical assemblies encapsulate tubular membranes and have recently been solved for the bacterial homolog PspA by cryoEM using helical reconstruction. A comparison of the *syn*VIPP1 ring structure presented here with the helical structure shows that VIPP1 and PspA share a very similar fold, thus the molecular mechanisms identified here are likely relevant for the variety of VIPP1 architectures and their function inside the cell.

4.4. Advances in cryo-lift-out transfer without the use of GIS deposition

The following chapter is published as an overview article in Microscopy Today [22], available under the creative commons license (CC BY 4.0). I will be adopting the figures from the article to showcase the developments on gas injection system free transfer in cryo-lift-out.

4.4.1. Lift-Out Hardware

While lift-out is an established and wide-spread method in the materials science, its adaptation to samples at cryogenic temperatures proved to be challenging. There are two micromanipulation systems generally available for the process, a gripper and a needle (**Figure 4.4.1**). At room temperature, the attachment of the lift-out needle can be performed by site-specific deposition of platinum using ion or electron beam assisted vapour deposition from organometallic precursors (trimethyl(methylcyclopentadienyl)-(IV)-platinum) introduced into the chamber through the gas injection system (GIS). At cryogenic temperature, however, the precursor deposits unspecifically on the sample surface. Therefore, while transferring the room temperature approaches to cryogenic applications is possible, it will render the sample unusable after only a couple of lift-out experiments due to the vast amount of Pt-precursor deposits. As a result, other ways of transferring samples had to be explored that do not use the GIS to prevent the condensation of the sample surface (**Figure 4.4.1A**). Furthermore, previous approaches performed the experiment in half-moon grids without the AutoGrid cartridge **Figure 4.4.1B**). That meant that the fragile 200 nm lamella produced by cryo-lift-out needed to be assembled into the cartridge of modern 300 kV microscopes called AutoGrid (**Figure 4.4.1B**). As the assembly is a very manual and tedious process, this led to a low overall success rate of the workflow. Consequently, it was essential to move to pre-assembled receiver grids (**Figure 4.4.1B**). The cartridge, however, prevents approaching the half moon grid with the cryo-gripper towards slots inside the half-moon posts as previously explored [17]. Thus, other approaches of lamella transfer are needed.

4.4.2. Lift-Out using the cryo-gripper

One way of transfering the lift-out volume without GIS deposition is the cryo-gripper approach. Here, just like in the macroscopic world, a small tweezer that grips by applying forces in the pN range is coupled to a micromanipulator with three degrees of freedom in X, Y, and Z. This allows for the transfer of a small volume from the high-

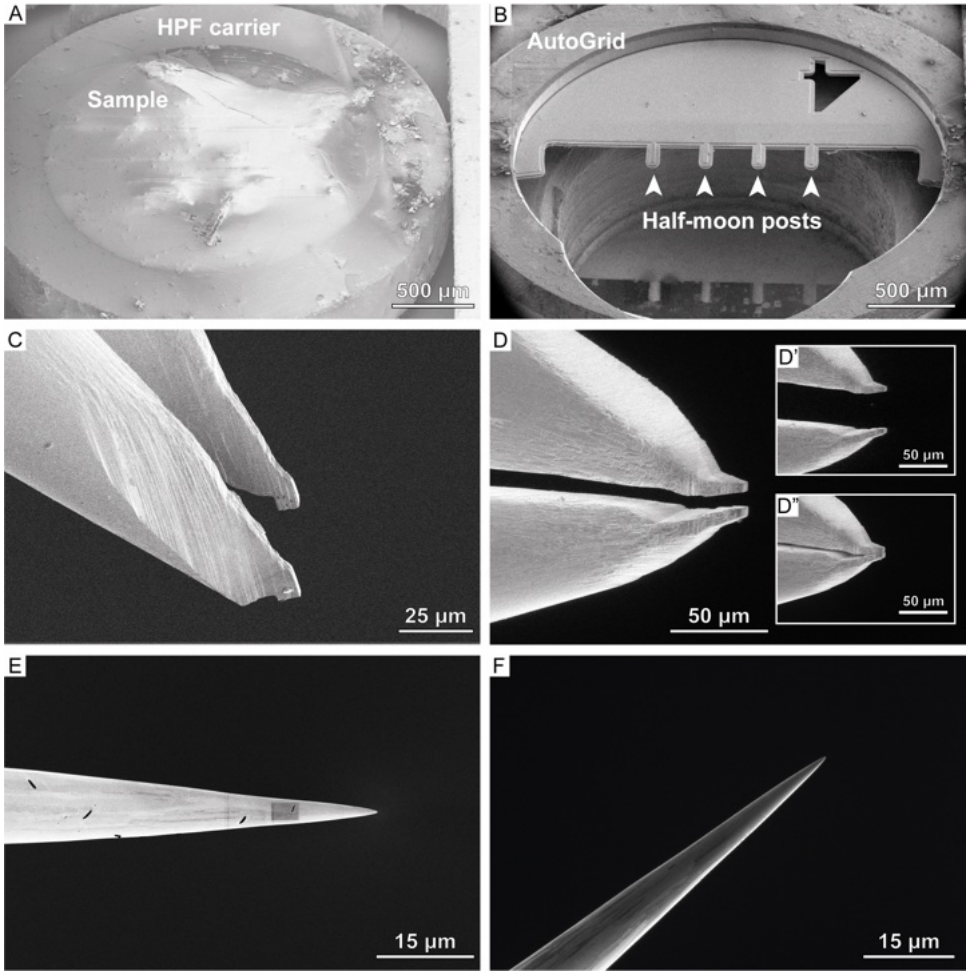

Figure 4.4.1 Samples and micro-manipulation devices for cryogenic applications. A: SEM image of a high-pressure freezing (HPF) planchette pre-trimming of the surface with a diamond knife. The carrier can be seen as a ring surrounding the sample within the cavity of the HPF planchette. **B:** SEM image of a typical half-moon grid used for lift-out assembled into a AutoGrid cartridge with 4 posts. **C:** SEM and **D:** FIB image of the Kleindiek gripper add another degree of freedom to micro-manipulation devices, namely the opening (D') and closing (D") of the gripper arms. **E:** SEM and **F:** FIB image of a tungsten needle from a EasyLift micro-manipulation device. Data collected with Jakub Kuba. Taken from [22], with permission.

pressure freezing carrier (**Figure 4.4.1A**, **Figure 4.4.2A-B**) to the receiver grid where the lift-out volume is attached to the halfmoon grid pin (**Figure 4.4.1B**) using FIB-mediated redeposition (**Figure 4.4.2C**). Here, a specific property of FIB milling is exploited, namely that material tends to deposit around the milling site during ion beam exposure (compare **Chapter 3.4.8**). In other applications such as lamella preparation, this redeposition is removed by scanning the exposed area multiple times. In the presented workflow, however, a single pass pattern is used to site-specficially micro-weld the copper material of the half-moon pin to the lift-out volume. After this attachment, the gripper can be opened and moved away from the pin (**Figure 4.4.1D**).

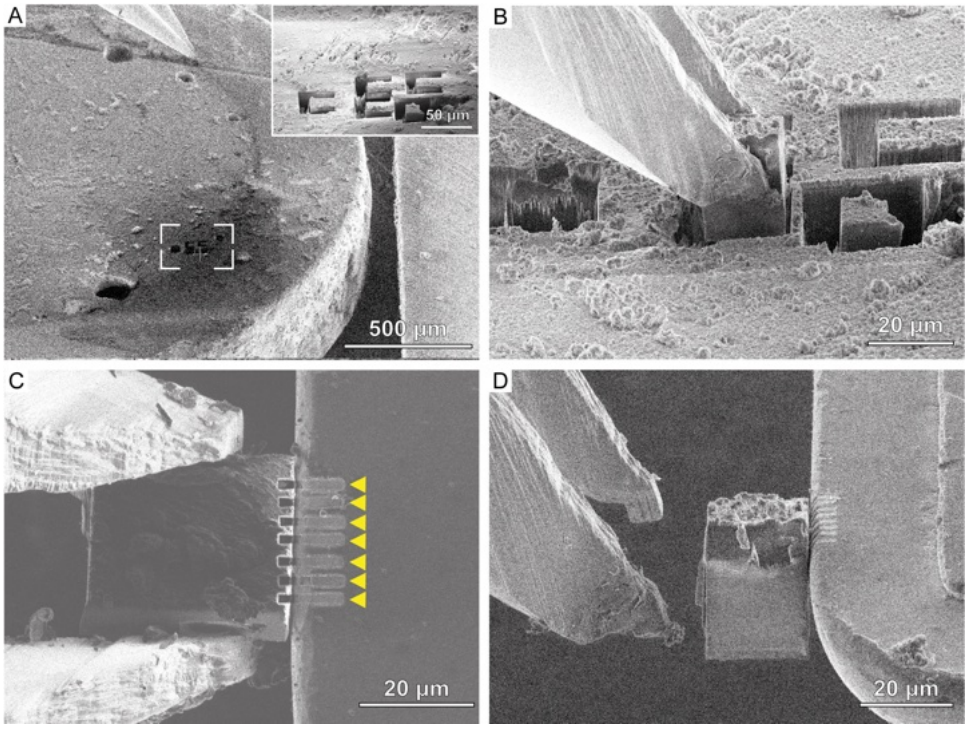

Figure 4.4.2 Lift-out workflow using a cryo-gripper micro-manipulation device. A: SEM image of a gripper approaching the prepared lift-out site on a HPF planchette. Inset shows a close-up of the prepared lamella sites. **B:** The sample is gripped and released via FIB milling from the bulk of the vitreous ice. **C:** After transfer to the half-moon grid, the lift-out volume is attached to the half-moon grid posts via redeposition milling of multiple patterns (yellow arrowheads). **D:** After attachment, the gripper can be opened and retracted from the post, leaving the volume attached to the half-moon grid for lamella preparation. Taken from [22], with permission.

4.4.3. Lift-Out using the cryo-needle

With the needle-type systems, the lift-out process can be performed similar to the gripper as shown above. An extraction volume, typically already in the size range of a lamella of 2-5 μm in thickness and around 20 μm in width, is prepared (**Figure 4.4.3A**). The additional step required is the attachment of the needle rather than the fixation of the lift-out volume by physical force as in the gripper approach. The needle is made of tungsten, a relatively low sputter yield material [247] and, thus, a weak source for redeposition attachment in the micro-welding approach. Thus, the biological material or vitreous ice is used for redeposition milling (**Figure 4.4.3B**). Once the biological material is attached, the lamella is milled free with the ion beam and transferred to the receiver grid, where the same technique as for the cryo-gripper approach is used. Since the copper has a higher sputtering yield [247] and, thus, redeposits stronger than vitreous ice, the attachment of the copper grid to the lift-out volume is generally much more sturdy. This will be deployed in **Chapter 4.5** via a copper adapter to allow for the extraction of larger volumes of biological material when using the cryo-needle systems. Subsequently, the needle is milled free from the biological sample (**Figure 4.4.3C-D**), leaving the sample on the pin.

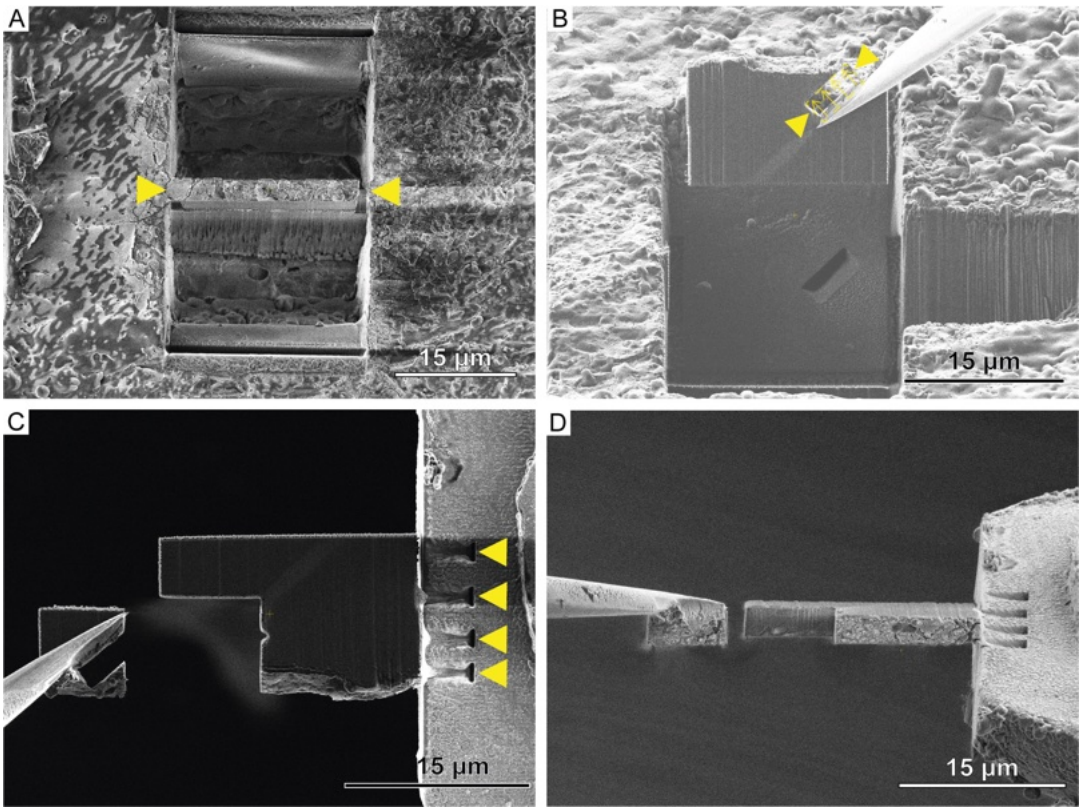

Figure 4.4.3 Lift-out workflow using a cryo-gripper micro-manipulation device. A: FIB image of a lamella (yellow arrowheads) prepared for lift-out. **B:** The lamella is approached with the tungsten needle, attached via redeposition milling (yellow arrowheads) with scanning direction away from the needle (arrows), released from the bulk by FIB milling and lifted out from the bulk. **C:** FIB and **D:** SEM image of a lamella that was attached via deposition (yellow arrowheads) to the half-moon pin and can subsequently be thinned to electron transparency. Data collected with Jakub Kuba. Taken from [22], with permission.

4.4.4. Examples of lamellae prepared

While the transfer mechanisms of cryo-gripper and cryo-needle differ slightly, the resulting lamellae for both approaches allow for the lamellae to be thinned to around 200 nm for subsequent cryo-electron tomography experiments (**Figure 4.4.4**). The imageable area in lamellae produced by this approach range between 5 μm x 5μm to 20 μm x 20 μm. The samples that the process was tested on was the *D. melanogaster* egg chamber (**Figure 4.4.4A-B**)and *M. musculus* brain (**Figure 4.4.4C-D**). SEM (**Figure 4.4.4A,C**) and TEM overviews are shown for both samples (**Figure 4.4.4B,D**). The integrity of the platinum layer, indicated as a yellow arrowhead in **Figure 4.4.4**, is very important for the stability of the lamella inside the TEM. Even with an intact platinum layer, the further away from the attachment point to the half-moon pin (rightern side of the lamellae), the higher was the beam-induced sample drift during exposure. Therefore, lamellae were generally aimed to be approximately 15 μm in size or double-sided attached, as will be further elaborated in **Chapter 4.5**. Clearly visible is the transfer contamination that accumulates on the surface of the sample, depicted in **Figure 4.4.4B** and **Figure 4.4.4D** as asteriks.
Transfer contamination is a remaining problem that can be reduced but to date not completely avoided by filtering the liquid nitrogen used to cool the tools through cloth

during transfers. Future developments, such as vacuum transfer from the FIB instrument to the TEM instrument by using automated sample exchange hardware such as the AutoLoader on both systems (compare **Chapter 3.4.5**), may circumvent this problem but are still requiring extensive technological development. However, to date, there is no FIB-SEM instrument that uses automated sample exchange hardware and allows for an integrated lift-out system.

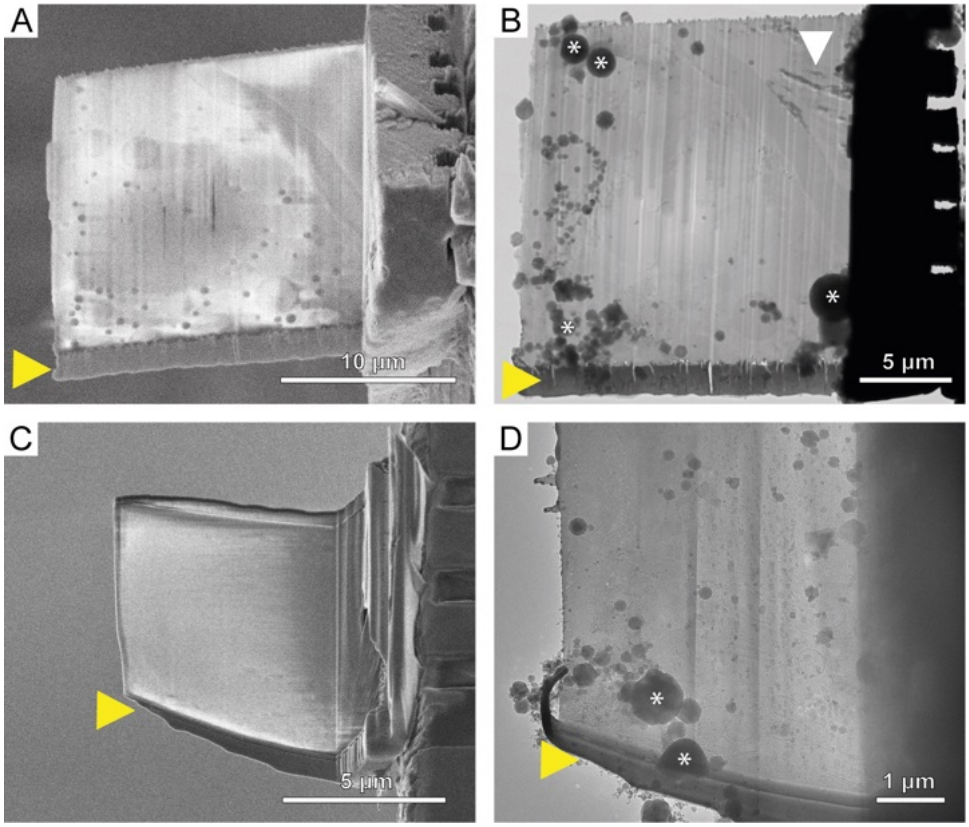

Figure 4.4.4 Example lamellae prepared by cryo-lift-out using needle and gripper micro-manipulation devices. A: SEM and **B:** TEM image of a lamella prepared using the Kleindiek cryo-gripper. **C:** SEM and **D:** TEM image of a lamella prepared using the EasyLift needle device. The protective platinum layer is depicted by yellow arrowheads and contamination by asterisks. Ice reflections from incomplete vitrification are indicated by a white arrowhead. Needle data collected with Jakub Kuba. Taken from [22], with permission.

4.5. Serial Lift-Out – Sampling the Molecular Anatomy of Whole Organisms

This chapter is based on an article accepted to be published in Nature Methods. In collaboration with my equal contributing co-authors Oda Helene Schioetz and Christoph Kaiser, I performed technological development, partook in the conceptualization of the presented work and the training of the researchers, collected, analyzed and visualized part of the data presented, wrote the initial manuscript draft, and handled the peer review process. The figures of the article are published under the Creative Commons license (CC BY-NC 4.0).

While the technical advances as described in **Chapter 4.1 and Chapter 4.4** have increased the throughput of cryo-lift-out experiments, it remains tedious and experimentally challenging. Therefore, to make the method applicable to biological questions and enable discoveries in native tissues, the success rate has to be increased by an order of magnitude. Inspired by classical serial sectioning in the preparation of thin sections of plastic embedded samples with diamond knifes (compare **Chapter 3.4.9**]), increasing the imageable area obtainable from cryo-lift-out experiments can be achieved by the preparation of multiple sections from a single lift-out transfer. Here, we formulate and demonstrate this idea on the *C. elegans* L1 larva as it shows ideal dimensions for an entire organism.

4.5.1. The concept of Serial Lift-Out

The general idea of the Serial Lift-Out method is schematically represented in **Figure 4.5.1**. An increased volume is lifted from the high-pressure frozen sample. The increased volume is going to be sectioned into multiple lamellae and thinned to electron transparency, yielding a number of sections along the length axis of the sample, in this case the antero-posterior axis of the *C. elegans* L1 larva (**Figure 4.5.1A-C**). To obtain multiple sections, the lift-out volume is transferred to the receiver grid, in this case a 400/100 mesh copper grid that allows for attachment of the lift-out material from both sides. By attaching the lowest 1-5 μm of the block of vitreous ice to the grid, that volume can be released from the lift-out needle by FIB milling while the rest of the volume remains attached to the lift-out device and can be transferred to the next lift-in position (**Figure 4.5.1D**).

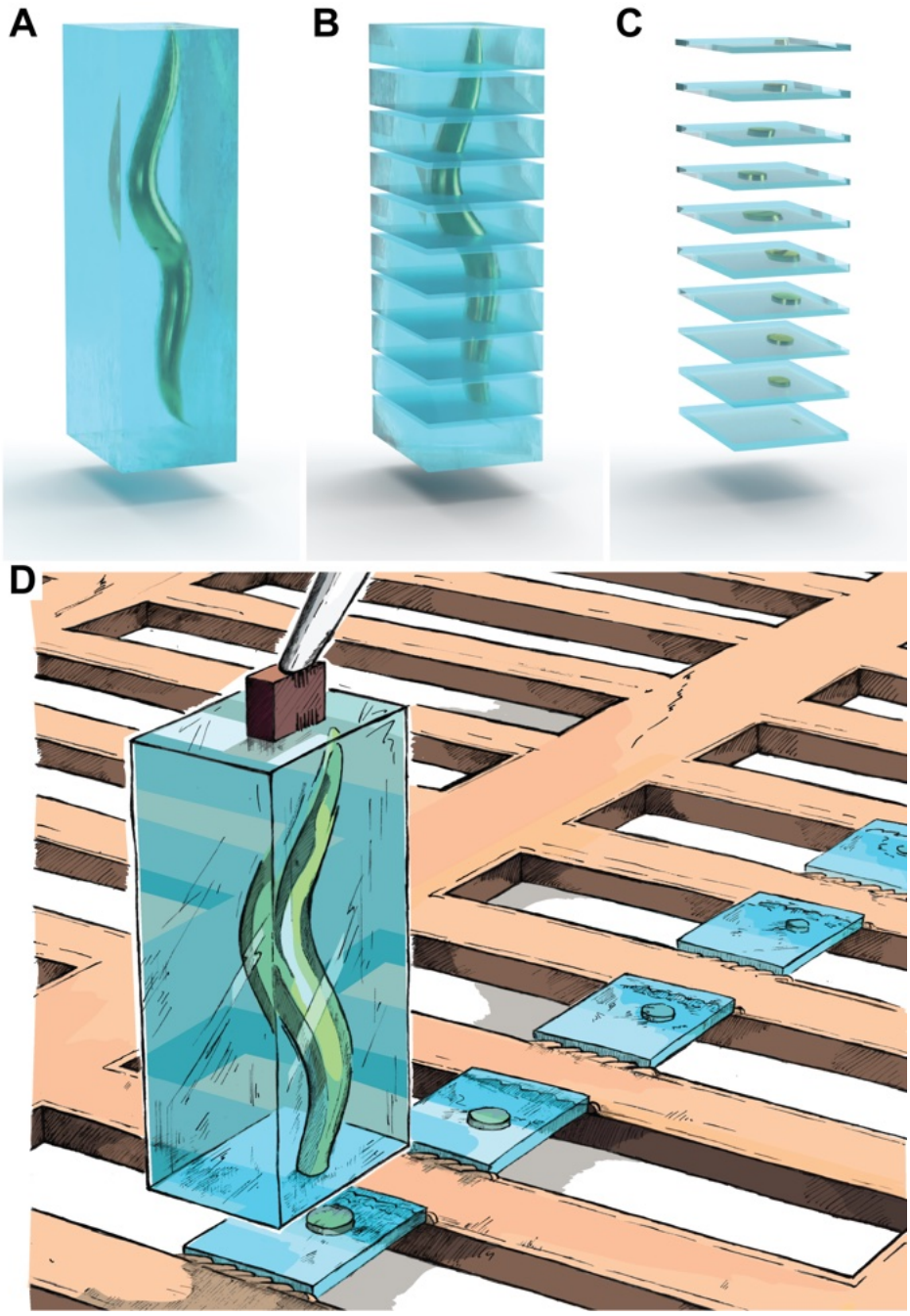

Figure 4.5.1 Visualization of the concept behind Serial Lift-Out. A: A large volume such as a *C. elegans* L1 larvae is attached to a micro-manipulation device and sectioned into **B:** several slices that can subsequently be **C:** thinned to electron transparency, yielding a number of **D:** quasi-sequential series of lamellae from the initial lift-out volume on a receiver grid. Produced with Dr. Jürgen M. Plitzko and adapted from [248].

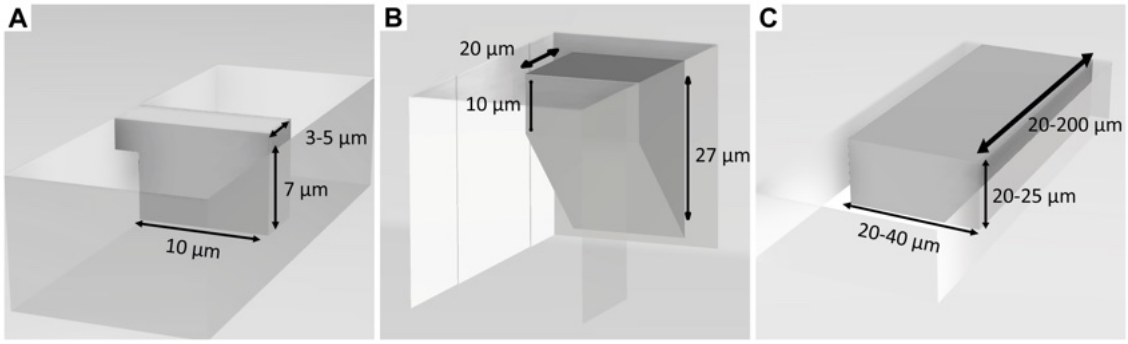

Figure 4.5.2 Dimensions of the lift-out volumes of previous works and the presented Serial Lift-Out approach. A: Lamella site prepared as presented in **Chapter 4.4** and described previously [17]. **B:** Increased volume for samples directly from HPF planchettes as demonstrated in **Chapter 4.4** for the cryo-gripper approach. **C:** For 'waffle' type samples, larger volumes up to 200 μm in length can be prepared, enabling lift-out of e.g. entire *C. elegans* L1 larvae. Data collected with Oda Schioetz and Dr. Christoph Kaiser and figure taken from [248].

4.5.2. Technical advances towards sequential sectioning in cryo-lift-out

To bring this concept into reality, a number of technical advances were needed. Compared to previous lamella site preparation inside high-pressure freezing planchettes that require an under-cut to be performed **Figure 4.5.2A-B**), a 'waffle'-type of freezing approach was used to allow for lifting large volumes without the need for an undercut (**Figure 4.5.2C**). The undercut is necessary due to the freezing process in high-pressure freezing: the sample gets embedded into a thick layer of ice depending on the cavity design of the planchette in traditional high-pressure freezing using Type A, B, or C carrier. For the waffle method, the flat side of two Type B carriers are used to sandwich a TEM grid during freezing. The TEM grid is subsequently retrieved. It contains a layer of ice approximately the thickness of the grid itself (10-30 μm), yielding windows of ice between the grid bars that do not have any material underneath. Thus, there is no need for an undercut, allowing for lift-out site preparation as shown in **Figure 4.5.2C**.

Second, in order to be able to transfer larger volumes using the redeposition method, the attachment surface and sputtering rate of the attaching materials had to be increased. As discussed in **Chapter 4.4**, previous approaches used the redeposition of the vitreous ice to attach the lift-out volume to the tungsten needle. Here, we used a copper block adapter as described in a patent (EP 4 207 243 A1). Since copper redeposits better due to a increased sputter yield than tungsten or vitreous ice, it is used for attaching the copper block from e.g. a standard TEM grid to the lift-out device (**Figure 4.5.3**). This can be performed at room-temperature prior cryogenic work. In the subsequent experiment, the copper block is used during lift-out to attach the biological material via redeposition (**Figure 4.5.4A**). Subsequently, the lift-out material is brought in contact to the grid bars of a 100/400 mesh TEM grid (**Figure 4.5.4B**). After redeposition attachment and milling off the section attached to the grid bars from the

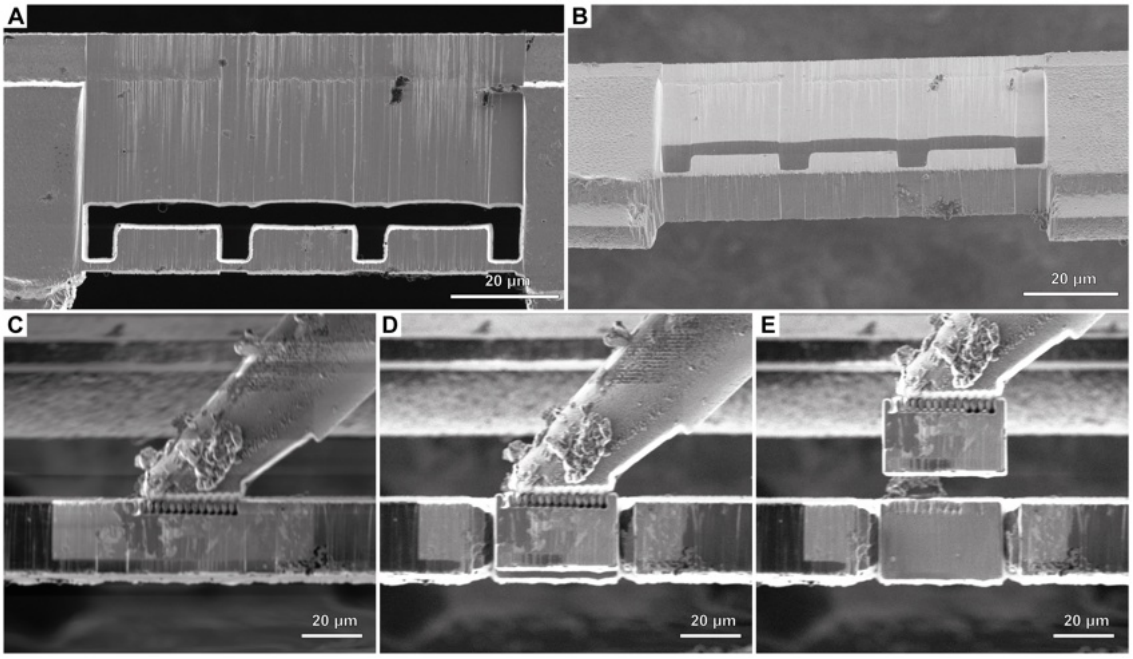

Figure 4.5.3 Copper block adapter attached to the lift-out needle. A: FIB and **B:** SEM image of three prepared copper blocks as needle adapters. **C:** The copper block is approached and attached via redeposition. **D:** Released copper block on the micro-manipulator needle. **E:** The needle can subsequently be moved up from the grid, yielding a copper block adapter attached to the needle. Data collected with Oda Schioetz and Dr. Christoph Kaiser and figure adapted from [248].

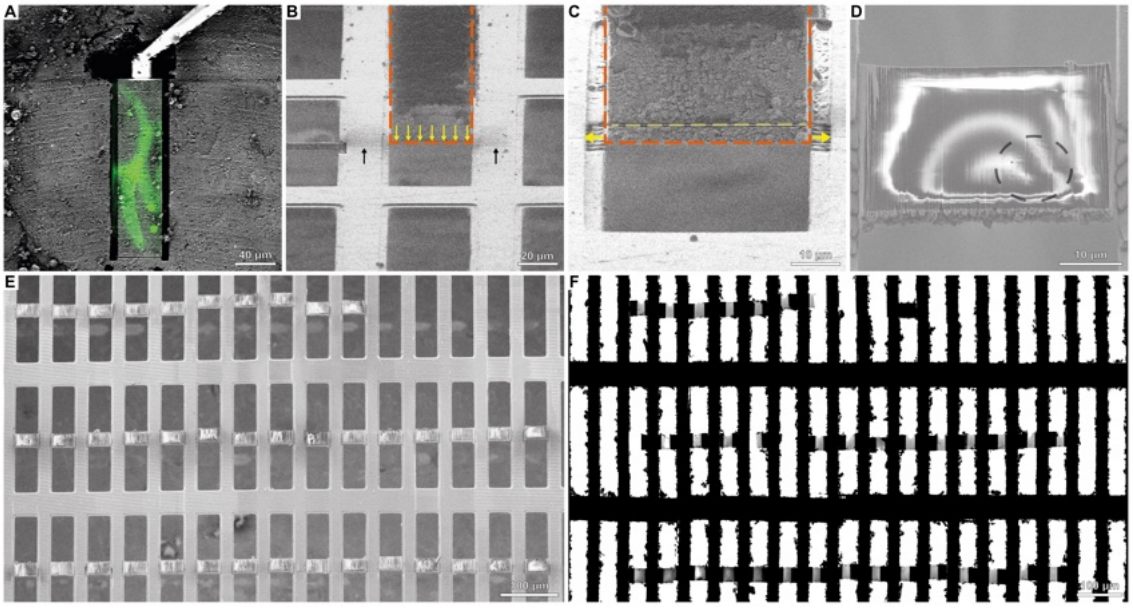

Figure 4.5.4 Serial Lift-Out experiment on *C. elegans* L1 larvae from 'waffle'-type samples. A: FIB image of the lift-out site with overlaid fluorescence maximum intensity projection collected with an in-chamber fluorescence light microscope. **B:** The lift-out block is brought into contact with 100/400 mesh receiver grid. **C:** After landing the bottom end of the lift-out volume on the grid bars of the recevier grid, redeposition milling (yellow arrow) is used to attach the bottom 3 μm of the volume to the grid. A line pattern is subsequently used to mill the lowest region off the block, leaving a lamella behind. **D:** SEM image of a representative slice from Serial Lift-Out. The black circle indicates the region of the worm. **E:** SEM and **F:** TEM overview of the series of thinned lamellae after a Serial Lift-Out experiment. Data collected with Oda Schioetz and Dr. Christoph Kaiser and figure taken from [248].

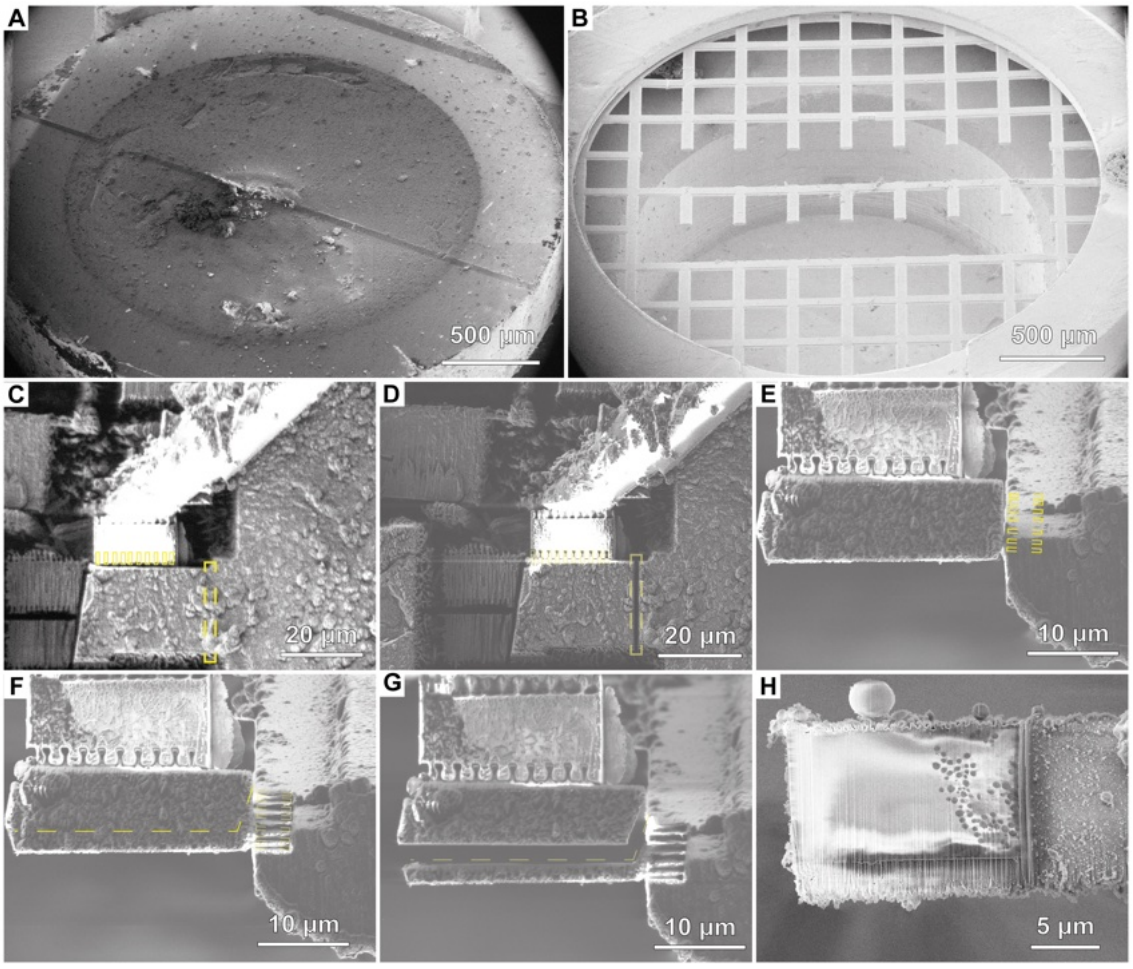

Figure 4.5.5 Serial Lift-Out experiment on *D. melanogaster* egg chambers from HPF planchettes. A: SEM image of the planchette. **B:** SEM image of the receiver grid, a 100 mesh square grid in which every second comb was milled out. **C:** The copper block adapter is brought into contact with the lift-out volume prepared. Essential is the undercut that needs to be performed in HPF planchettes but is not necessary in 'waffle'-type samples. **D:** The lift-out volume is released from the bulk by FIB milling. **E:** After transfer, the lift-out volume is brought into contact with the side of the grid and attached using redeposition milling (yellow rectangles). **F:** The lowest region is subsequently milled off the lift-out volume using a line pattern (yellow dashed line). **G:** After the section has been dispatched, the needle can be retracted and the next section prepared on the next pin. **H:** SEM image of a representative lamella from *D. melanogaster* egg chambers. Data collected with Oda Schioetz and Dr. Christoph Kaiser and figure taken from [248].

lift-out material (**Figure 4.5.4C**), the block can be lifted leaving behind the section that will be thinned to electron transparency (**Figure 4.5.4D**). In a sectional fashion, this allows for preparation of tens of lamellae (**Figure 4.5.4E**) readily imaged by TEM with just a single lift-out (**Figure 4.5.4F**). While the shown application is in samples frozen by the 'waffle' method where no undercut to free the lift-out volume from the bulk is needed, the same principles can be applied to high-pressure frozen material in planchettes (**Figure 4.5.5**). Here, a block as described for cryo-gripper devices (compare **Chapter 4.4**) with an undercut is prepared to yield multiple sections from a single transfer. While more time investment on the trench milling is needed similar to the cryo-gripper application, the yield in prepared lamellae is an order of magnitude higher.

4.5.3. Increasing the contextual information in the study of tissues

The applied sectioning allows for the approximate backmapping of the prepared sections of the *C. elegans* L1 larva to a schematic 3D model of the worm as anatomical features such as the pharynx, grinder, and other structures are discernible in the TEM lamella overviews (**Figure 4.5.6**). Based on these features, tilt series in specific cells and subcellular regions can be collected (**Figure 4.5.7A**) such as the nuclear periphery of neuronal cells (**Figure 4.5.7B**), the pharynx (**Figure 4.5.7C**), and the body wall muscle (**Figure 4.5.7D**).

Both single-sided (**Figure 4.5.5**) and double-sided (**Figure 4.5.4**) attachment was explored. While the tomogram thickness distribution seems to occasionally yield thinner tomograms for single-sided attachment (**Figure 4.5.8**), the consistency within the double-sided attachment experiments was higher as represented by less spread in the tomogram thickness distribution. This is likely due to more robust lamellae from double-sided attachment. The single-sided attached lamellae have a tendency to bend and, therefore, yield less even lamellae than when using double-sided attachment.

4.5.4. *In situ* structural biology in the *C. elegans* L1 larva

To demonstrate that the data from lamellae prepared by cryo-lift-out is comparable to on-grid preparations, we performed subtomogram averaging on the ribosomal particles within the reconstructed tomograms. A consensus map at subnanometer resolution of 6.9 Å yields a map that shows the secondary structure elements of the *C. elegans* ribosome (**Figure 4.5.9**). The classification of these ribosomes yielded different states of the elongation cycle at resolutions ranging from 8.4 Å to 15 Å (**Figure**

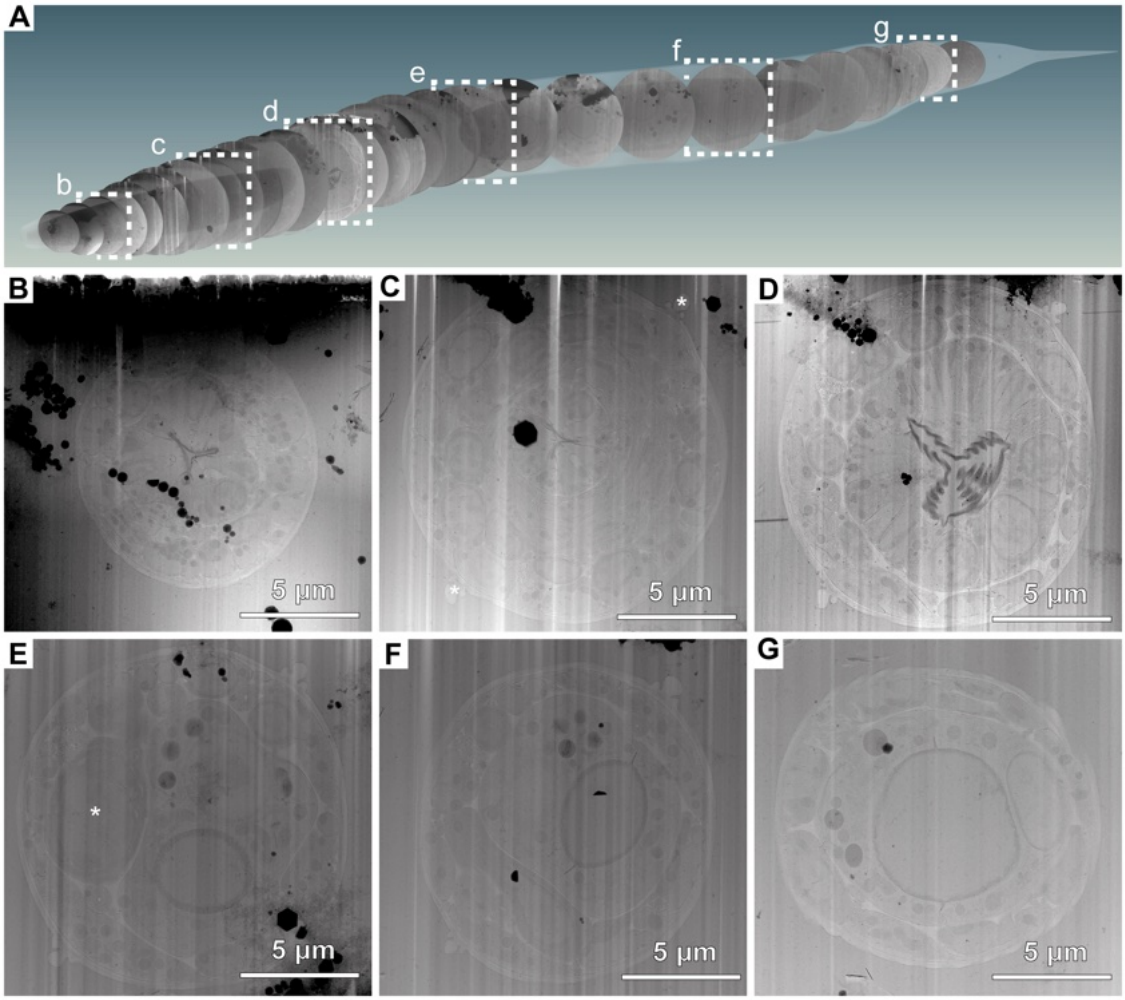

Figure 4.5.6 TEM overviews of the *C. elegans* L1 larva along the antero-posterior axis. A: Schematic representation of the TEM overviews backmapped to a model of the *C. elegans* worm. **B-G:** Representative examples of the TEM overviews from Serial Lift-Out lamellae. **C:** Asterisks indicate the worm's alae. **E:** Asterisk indicates a gonadal primordial cell. Data collected with Oda Schioetz and Dr. Christoph Kaiser and figure taken from [248].

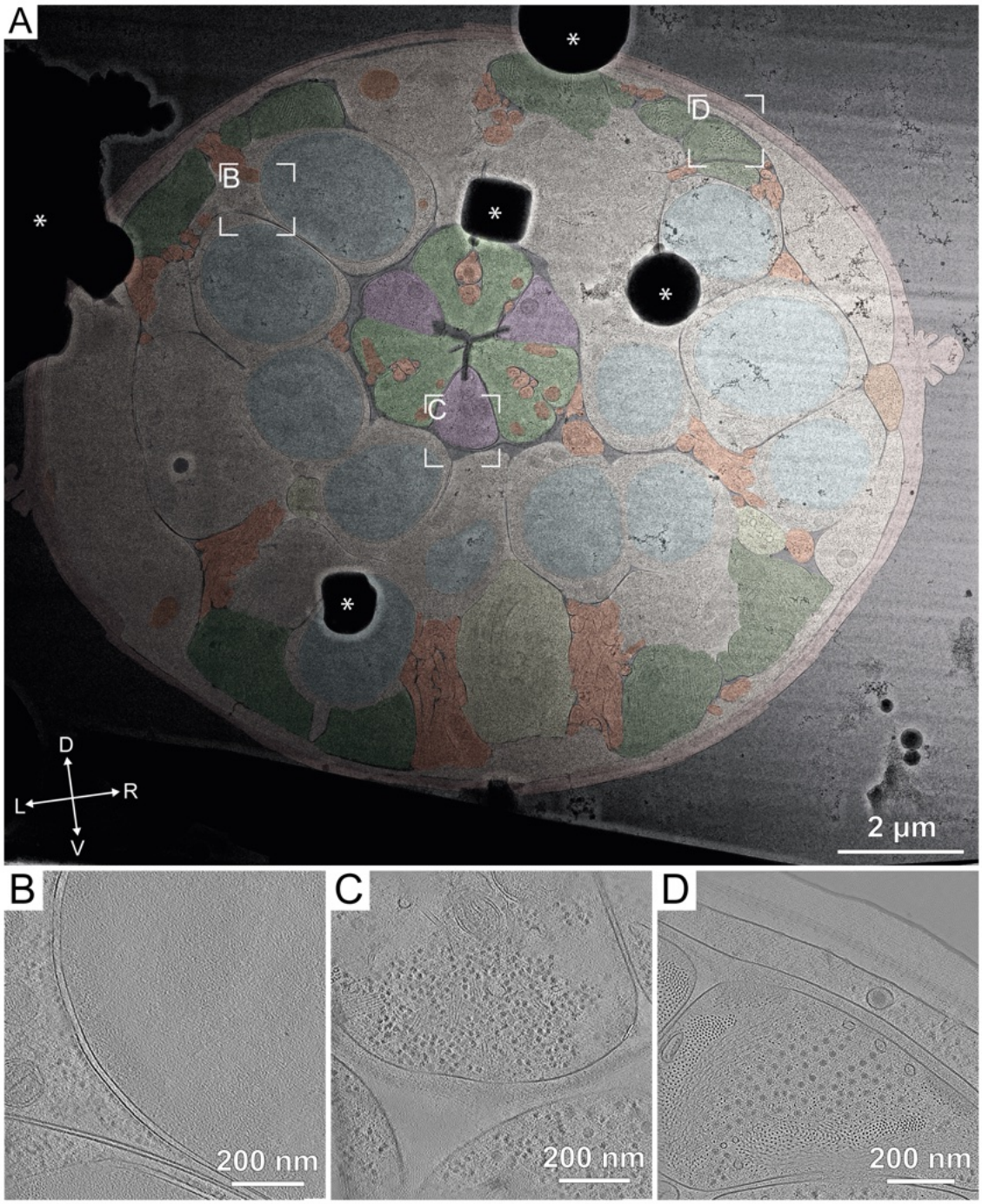

Figure 4.5.7 Exemplary cryo-ET data of the *C. elegans* L1 larva. A: Segmented overview montage (11.500x magnification) of a section prepared by Serial Lift-Out. The section originates from the head region. Cell types are colored according to the WormAtlas standard. Nuclei (blue) and mitochondria (orange) are arbitrarily colored, Pharyngeal muscle (light green), body wall muscle (dark green), excretory pore (yellow), marginal cells (purple). White rectangles indicate the tilt series positions. Asterisks label transfer ice contamination. **B:** Tomographic slice of the perinuclear region of most likely a neuronal cell. The nucleus exhibits a different granularity and density than the cytoplasm (Cyto). **C:** Tomographic slice of the pharynx. **D:** Tomographic slice of the body wall muscle. Data collected with Oda Schioetz and Dr. Christoph Kaiser and figure taken from [248].

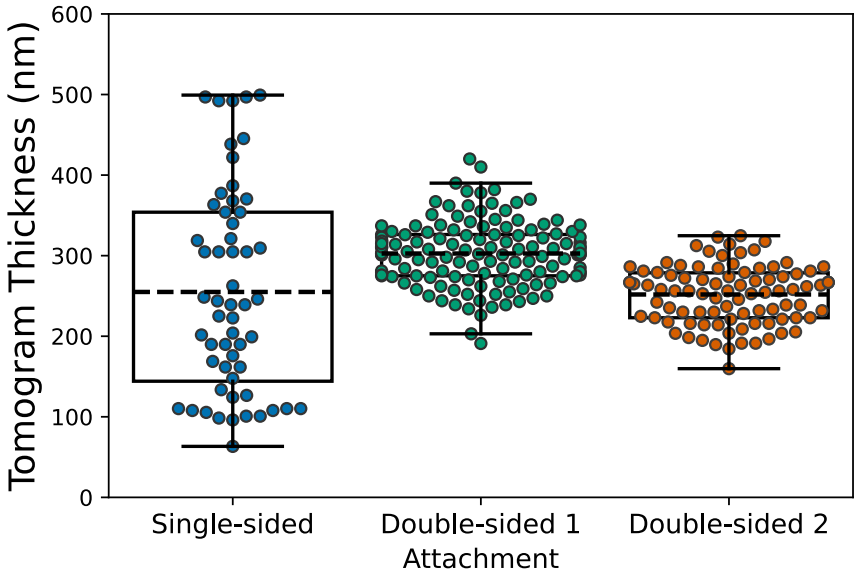

Figure 4.5.8 Tomogram thickness distribution for three Serial Lift-Out experiments. Box plot for the distribution of thickness measurements on single-sided and double-sided attachment Serial Lift-Out lamellae all for the single-sided attachment experiment (n=57) and double-sided attachment experiment 1 (n=132) and double-sided attachment experiment 2 (n=90). Average tomogram thickness for single-sided attachment (253 nm $\pm$ 125 nm), double-sided attachment 1 (303 nm $\pm$ 40 nm), and double sided attachment 2 (251 nm $\pm$ 36 nm). The box indicates the 25th and 75th percentile, the dashed line the mean of all measurements, and the whiskers indicate the observations within the 1.5x interquartile range. Data collected with Oda Schioetz and Dr. Christoph Kaiser and figure adapted from [248].

4.5.9, **Figure 4.5.10**).

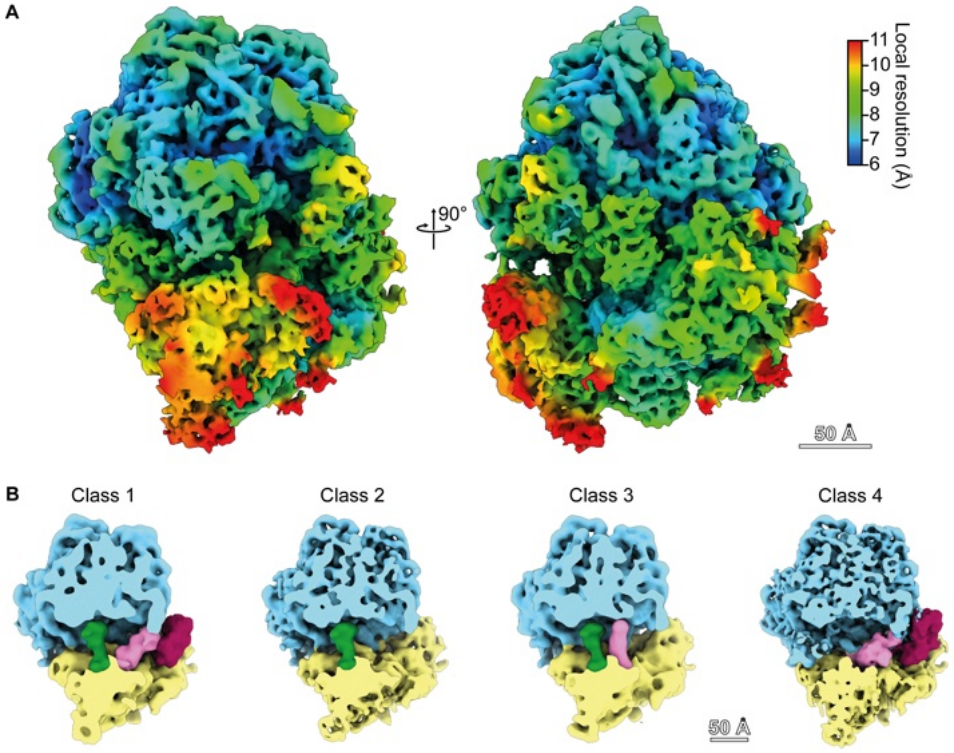

Figure 4.5.9 Ribosome structure and its translational states *in situ.* **A:** Resolution color coded *C. elegans* ribosome at 6.9 Å global resolution as measured by gold-standard fourier shell correlation. **B:** Four translational states of the *C. elegans* ribosome as obtained by 3D classification of the subtomograms. Ribosome Class 1 with occupied A, P and EF sites, Ribosome Class 2 with an occupied P site, Ribosome Class 3 with occupied A and P sites, Ribosome Class with occupied A and EF sites. Data collected with Oda Schioetz and Dr. Christoph Kaiser and figure taken from [248].

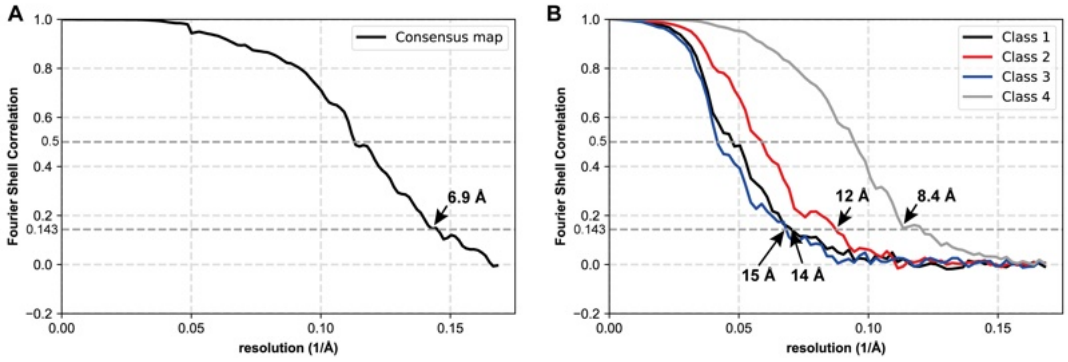

Figure 4.5.10 FSC curves of the *C. elegans* ribosome structures. **A:** FSC curve of the consensus map from subtomogram averaging. **B:** FSC curves of the different translational states shown in **Figure 4.5.9B**. Data collected with Oda Schioetz and Dr. Christoph Kaiser and figure taken from [248].

4.6. Correlative Lift-Out

In the pursue of targeting specific structures within bulk tissues, methods had to be developed from both the technological side but also in terms of workflow to enable the targeted production of lamellae from large, high-pressure frozen specimens. While many interesting questions will be able to be tackled with such methods, the development had two main questions as motivation. First, the fascinating variety of nuclear pore complex structure (NPC) across cell types and cellular environments, especially the structural comparison of germ-line NPCs, somatic NPCs and cytoplasmic NPCs (annulate lamellae) will be of special interest. Second, previous studies suggested that in the replication cycle of the *copia* retrotransposon, the capsids are assembled in the cytoplasm and form large clusters in the nucleus. This raises the question of how they are transported into the nucleus. To answer these questions, cryo-electron tomography of native tissue is required. The egg chamber is 150-200 μm in thickness, thus, high-pressure freezing is needed to achieve vitrification. While sample preparation of increasingly thick samples from high-pressure freezing through direct milling via the Waffle method using plasma FIBs are under development, cryo-lift-out is to date the only way to prepare samples from these very large samples. Though the quasi-sequential sectioning from **Chapter 4.5** speeds up the process, it is only applicable to targets that occur multiple times within short ranges in the 200 μm thick specimen. If unique events are targeted, the timeframe of preparation is still relatively long, anywhere between 5 h and 12 h of microscope time, depending on the sample. It involves trenching, lift-out transfer, volume imaging via FIB-SEM or fluorescence light microscopy of the extracted lift-out volume, thinning of the specimen and transfer to the TEM for tilt series acquisition. The workflow and time estimation for each step are summarized in **Figure 4.6.1**.

In order to target the follicle cell or germ-line nuclei from the voluminous material of a high-pressure frozen egg chamber, correlative microscopy methods are needed. As the nucleus is a membranous compartment, there are in principle two ways of targeting. The nuclear envelope can be distinguished in scanning electron microscopy images. Thus, milling the lift-out material from the top until the nucleus appears at the surface of the lamella as detected by scanning electron microscopy can be deployed to target the nucleus into the final lamella. The lamella can subsequently be produced by milling solely from the bottom of the lamella, only removing material from the top for polishing. If integrated light microscopes for the FIB-SEM instrument are available, the fluorescence signal of tagged proteins positive for, e.g. the nuclear envelope can be used to target the nucleus. Here, we deployed both methods as integrated light microscopes only became available throughout the execution of this project. It enables the preparation of nuclei within the approximately 200 nm lamella that is transferred to the TEM for data acquisition (**Figure 4.6.2**)

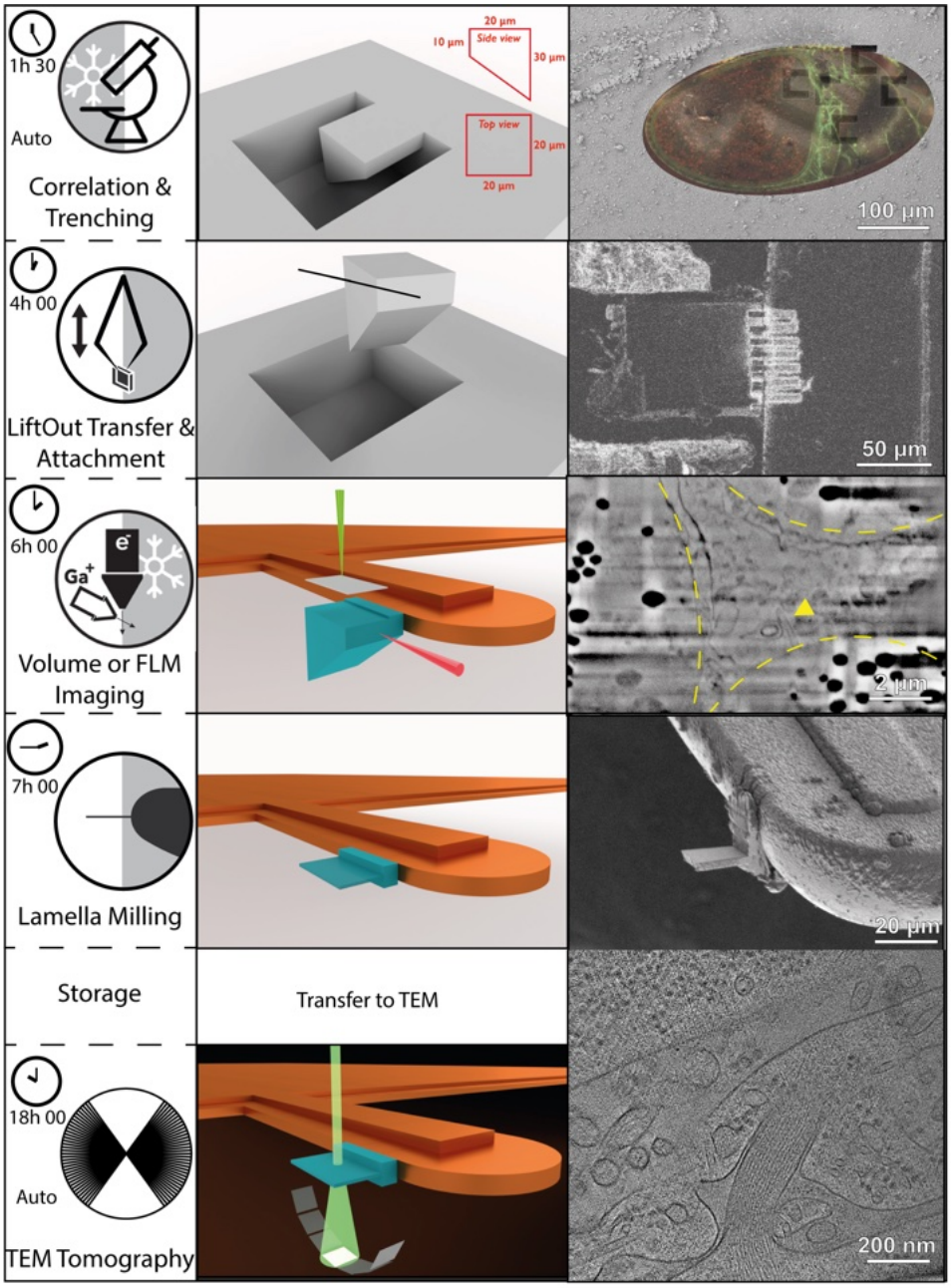

Figure 4.6.1 Preparation of site-specific lamellae by correlative cryo-lift-out. Time estimates are given in hours and minutes format. The steps along the workflow are schematically represented with an example image. The sample is a LifeAct-GFP expressing *D. melanogaster* egg chamber. After lift-out transfer, the final volume is targeted using FIB-SEM imaging from the surface of the extracted biological material. Yellow arrowheads indicates a targeted actin structure between the nurse cells. The final reconstructed tomogram from a tilt series collected on the lamella shows membrane protrusions driven by most likely actin filaments.

The workflow described here is used throughout the next chapter to study copia and the nuclear pore complex in the native environment of the egg chamber.

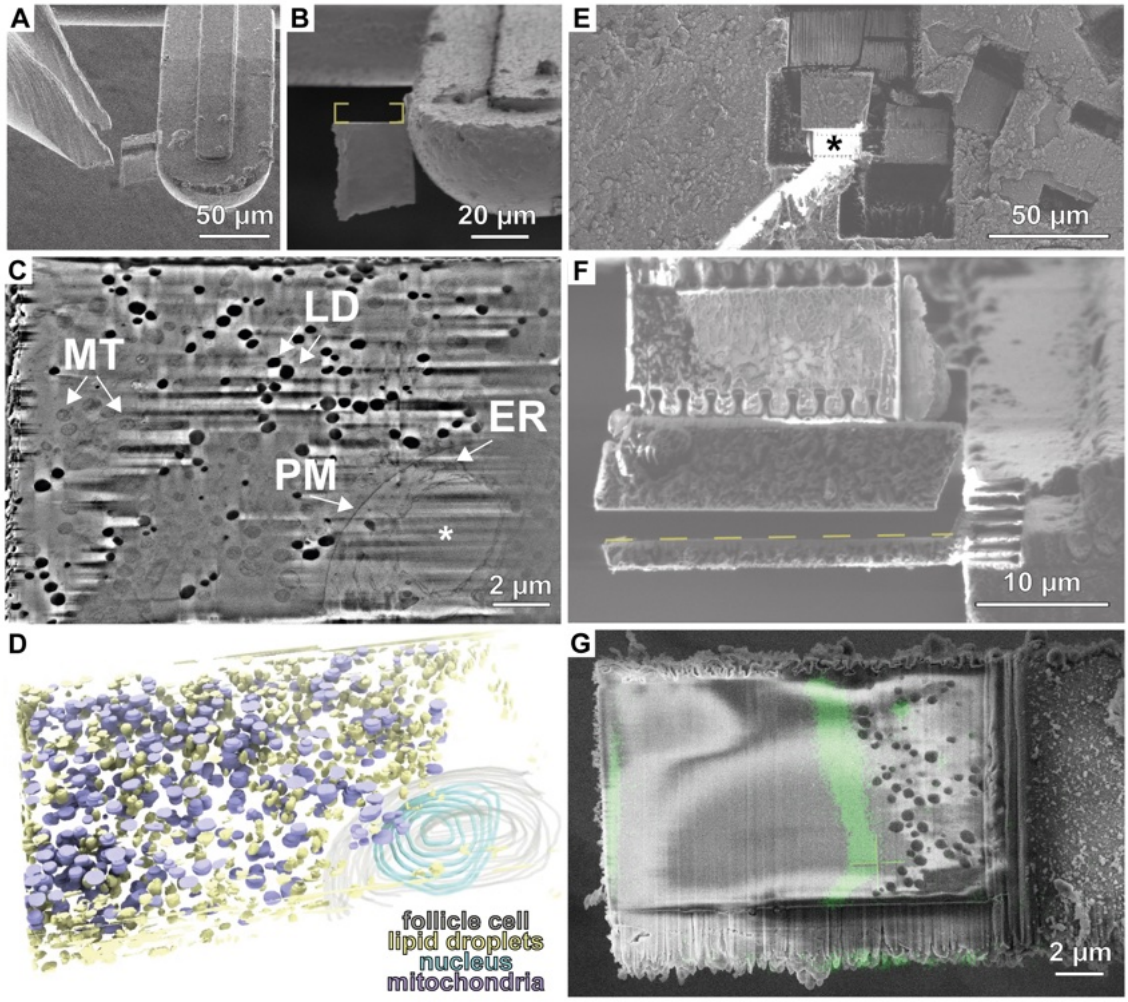

Figure 4.6.2 Targeting in cryo-lift-out using FIB-SEM volume imaging and in-chamber fluorescence microscopy. A: Kleindiek cryo-gripper lift-out from a bulk high-pressure frozen sample (compare **Chapter 4.4**). **B:** FIB image of the biological material after FIB-SEM volume imaging. The yellow square indicates the volume ablated during imaging. **C:** Sample SEM image from the volume imaging dataset. As soon as the feature of interest is identified in the SEM, the lamella is prepared by fine milling from the bottom. It is advisible to remove a damage layer caused by SEM imaging from the top of the lamella, usually around 50 nm. Asterisk indicates the nucleus. Further features are the plasma membrane (PM) of the follicle cells, mitochondria (MT), endoplasmic reticulum (ER), and lipid droplet (LD). **D:** FIB-SEM volume segmentation of C. **E:** Cryo-lift-out using the Serial Lift-Out approach (compare **Chapter 4.5**). The adaptor copper block (asterisk) is attached to the lift-out needle redeposition based lift-out transfer. **F:** After transfer and attachment to the receiver grid, the lift-out lamella is released from the bulk by FIB milling, indicated as a yellow line. **G:** Overlay of the in-chamber acquired fluorescence microscopy volume onto an SEM image of the section from F. The endogenously tagged Nup358 protein localizes to the nuclear envelope, thus the lipid droplets visible in the SEM are excluded from the inside of the nucleus on the left. Adapted from [249], with permission.

4.7. Structural studies of the transposable element *copia*

4.7.1. *Copia* retrotransposons are abundant transposable element in ovarian somatic follicle cells

Within the egg chamber, somatic support cells, also called follicle cells, engulf the oocyte, forming a specialized epithelial layer known as the follicle cell epithelium (**Figure 4.7.1A**). We employed various experimental approaches to investigate the expression and localization of retrotransposons within the egg chamber. Through re-analysis of a publically available single-cell RNA sequencing (scRNA-seq) data set of the *Drosophila* ovary (Jevitt et al. *PLoS Biology* 2020, compare key resource table) with recently developed tools to specifically detect transposable elements in scRNA-seq data, we identified high expression of the *copia* retrotransposon in somatic cells, most dominantly in somatic cells within the follicle cell epithelium and their precursors and successor cells (**Figure 4.7.1C-D**). To validate the scRNA-seq results and determine the spatial distribution of copia, Dr. Kirsten Senti and Dr. Julius Brennecke at the Institute of Molecular Biotechnology (IMBA) in Vienna, Austria, kindly shared data of single-molecule fluorescence *in situ* hybridization (smFISH) experiments. Remarkably, the smFISH data clearly showed *copia* signal enrichment within the follicle cells, while exhibiting minimal to no signal in the germ-line cells, comprising the nurse cells and oocyte (**Figure 4.7.1E**). These findings do suggest that *copia* retrotransposon expression is predominantly restricted to the somatic cells within the egg chamber. In agreement with the localization observed by smFISH, staining with commercially available antibody raised against the *copia* Pol protein shows localization of the *copia* signal within the follicle cell epithelium (**Figure 4.7.1F**). Strikingly, in addition to the cytoplasmic signal, *copia* was also detected in the nucleoplasm and at the nuclear envelope (**Figure 4.7.1E-F**) indicating a potential interaction with the nuclear pore complex of *copia* capsids within the follicle cell epithelium.

4.7.2. Electron tomography of follicle cells reveals large VLP clusters in their nucleus

Based on the indication of expression and localization in the follicle cells, along with a notably abundant nuclear signal of *copia* observed through immunofluorescence and smFISH, our subsequent investigation focused on resolving the nuclear periphery of the follicle cells by electron tomography of plastic embedded samples to determine if *copia* forms nuclear clusters as previously reported in overexpression systems in the commonly used *D. melanogaster* Schneider 2 (S2) cell line [190]. We performed sectioning of plastic-embedded stage 10 egg chambers (*tj-Gal4>UAS-Sec31.RFP* flies) (**Figure 4.7.2A**) to 300 nm and collected tilt series of the nuclear periphery of the follicle cells (**Figure 4.7.2B**). The reconstructed tomograms showed clearly distinguishable spheres that we interpret as capsids (**Figure 4.7.2C-F**). While cytoplasmic

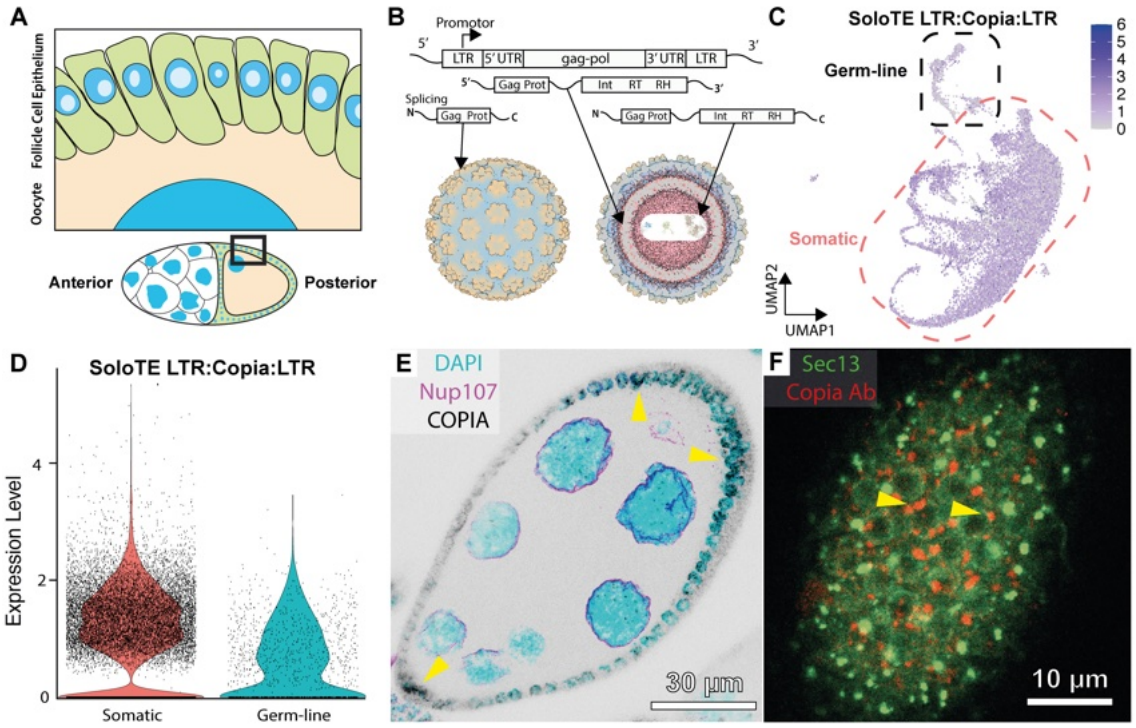

Figure 4.7.1 Copia is an abundant retrotransposon in the somatic follicle cells of the *D. melanogaster* egg chamber. **A:** Schematic of a stage 10 egg chamber. The ovaries come in pairs and are located within the abdomen. The egg chamber consists of somatic cells (green), the follicle cells, and germ-line cells, consisting of nurse cells (white) and the oocyte (beige). **B:** Overview of the copia genome and its expression. Alternative splicing has been described for other elements to lead to only Gag protein while a polypeptide is translated from the full length *copia* mRNA yielding the protease, integrase, and reverse transcriptase proteins that are packaged in capsids. **C:** Single-cell RNA seq analysis of transposable element *copia* in the *D. melanogaster* ovary. Color coded is corresponding to the expression level calculated by the scRNA-seq reads of LTR-copia-LTR according to the SoloTE pipeline. Note the high signal in the somatic cells compared to the germ-line cells. The copia genome is strongly detected in follicle cells but much less in germline cells. **D:** Violine plot shows expression levels in 2 clusters, germ-line and somatic cells. **E:** SmFISH of egg chambers expressing GFP::Nup107 maximum intensity projection of 12 optical slices from a confocal dataset. DAPI in cyan, GFP::Nup107 in magenta and smFISH for the *copia* genome in black. Arrowheads indicate signal in the somatic cells. Flies used express GFP::Nup107 (Bloomington ID: BL-35514). **F:** Immunofluorescence of the follicle cell epithelium of a tj>UAS-Sec13-EosFP positive egg chamber stained with an antibody raised against the *copia* polypeptide chain Pol region. Arrowheads indicate signal at the nuclear envelope and inside the nucleus.

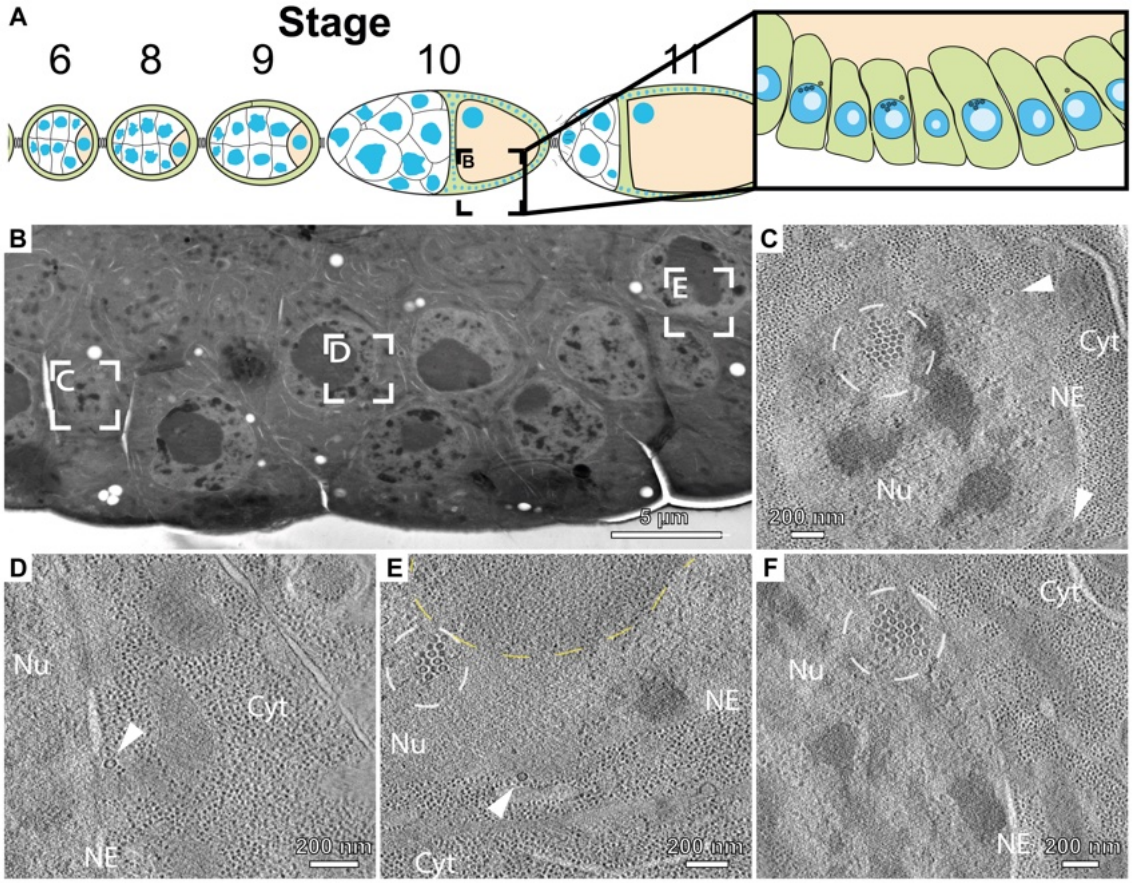

Figure 4.7.2 Electron tomography on thin sections of plastic-embedded egg chambers reveals large capsid clusters. **A:** Schematic of the origin of the section. The follicle cell epithelium of stage 10 egg chambers was targeted. **B:** Overview of the plastic section. Insets represent the location of the tomograms shown in C-E. **C:** Tomographic slices of the nuclear periphery of the follicle cell nucleus. Note the large clusters of presumably *copia* capsids in the nucleus (dashed circle). Cytoplasmic VLPs are indicated by white arrowheads. **D:** Tomographic slice showing a VLP (arrowhead) close to an opening of the nuclear envelope (NE). **E:** Tomographic slice showing VLP clusters (dashed white circle) excluded from the nucleolus (dashed yellow line). Cytoplasmic VLP indicated by white arrowhead. **F:** Tomogram showing another cluster of VLPs in the nucleus. The presented tomogram was collected on a different section than shown in B. Nucleus (Nu), nuclear envelope (NE) and cytoplasm (Cyt) are indicated in all tomograms. Flies used were driving Sec31.RFP expression under the tj-Gal4 promotor.

capsids seemed to be sparse and often close to the nuclear envelope, large clusters of capsids were found in the nuclei (**Figure 4.7.2B**). These particles seemed to be excluded from the nucleolus (**Figure 4.7.2D-E**). Additionally, we found the cytoplasmic capsids to be close to the nuclear envelope and even observed capsids close to an opening of the nuclear envelope (**Figure 4.7.2C**). As the high-pressure freezing and freeze substitution preparation technique used allowed for clear contrast of nucleic acids but limited contrast for proteins, it is tempting to interpret the clearly visible discontinuity in the nuclear envelope as a nuclear pore complex. The spheres detected are thus likely the bound RNA genome of *copia* rather than the capsid proteins themselves. Additionally, the region around the capsid structure at the nuclear envelope excluded ribosomes.

4.7.3. Leveraging the Gal4-UAS system to identify cell types on the grid

To examine the ultrastructure of follicle cells at the level of preservation of cryo-ET, the cells may be isolated and vitrified as their size is amenable to plunge freezing. In order to perform cryo-ET on the isolated follicle cells by on-grid lamella preparation, I developed a preparation method to dissociate tissue and identify tissue specific cells on-grid (**Figure 4.7.3A**). It is similar to protocols previously described for cell sorting [250]. In brief, the egg chambers (**Figure 4.7.3B**) are dissociated by trypsin digestion and filtered through a cell strainer with filter size of 40 μm (**Figure 4.7.3F**). The resulting cells can subsequently be plunge frozen (**Figure 4.7.3C**). By using transgenic Upstream Activation Sequence (UAS) reporter lines of a fluorescent protein, here Sec13-EosFP, and a Gal4 driver under the follicle cell specific *traffic jam* promotor, the cells originating from the follicle cell epithelium as well as precursor cells (e.g. follicle stem cells) will express Sec13-EosFP under UAS control and can thus be identified on the grid by correlative light and electron microscopy (CLEM) (**Figure 4.7.3D-J**). The Sec13-EosFP construct was chosen as it shows multiple features that can be checked for in the CLEM approach: cytoplasmic signal for COPII vesicles and ERES structures, nuclear rim signal as it is a component of the nuclear pore complex, and nuclear signal as Sec13 is known to act as a transcription factor. Cells isolated by this method showed similar localization patterns of Sec13-EosFP to the intact egg chamber (**Figure 4.7.3B,F**). Correlative light and electron microscopy was then used to identify the nuclear region within the FIB-SEM instrument (**Figure 4.7.3D,G,H**). By SEM imaging of the lamella surface, the nucleus can be targeted for the final lamella if no integrated light microscopy solutions are available (**Figure 4.7.3I**).

4.7.4. Isolated follicle cells contain large capsid clusters inside the nucleus

Cryo-FIB lamella produced from follicle cells prepared by the on-grid identification of tissue pipeline reveal large *copia* clusters that could already be seen in the low magnification overview (**Figure 4.7.4A**). The reconstructed tomogram (**Figure 4.7.4B**) showed large assemblies of capsids with very regular structure even yielding diffraction spots in the Fourier transform of the TEM image (**Figure 4.7.4E**) at 46 nm and 16 nm (**Figure 4.7.4E**). The capsids in these assemblies show typical features of retrotransposons such as immature (**Figure 4.7.4C**), and mature (**Figure 4.7.4D**) capsid structures. Additionally, putative binding proteins (**Figure 4.7.4F-G**) and elongated capsids deviating from the typical structure (**Figure 4.7.4H**) were observed. Seemingly incomplete capsids were also found in the reconstruction. Surprisingly, the capsid structures close to the nuclear pore complexes previously seen in the electron tomography data from high-pressure frozen and plastic-embedded egg chambers (**Figure 4.7.2**) were not observed in the cryo-ET tomograms of isolated follicle cells. Capsids were readily identified in the tomogram (**Figure 4.7.5A**) by template match-

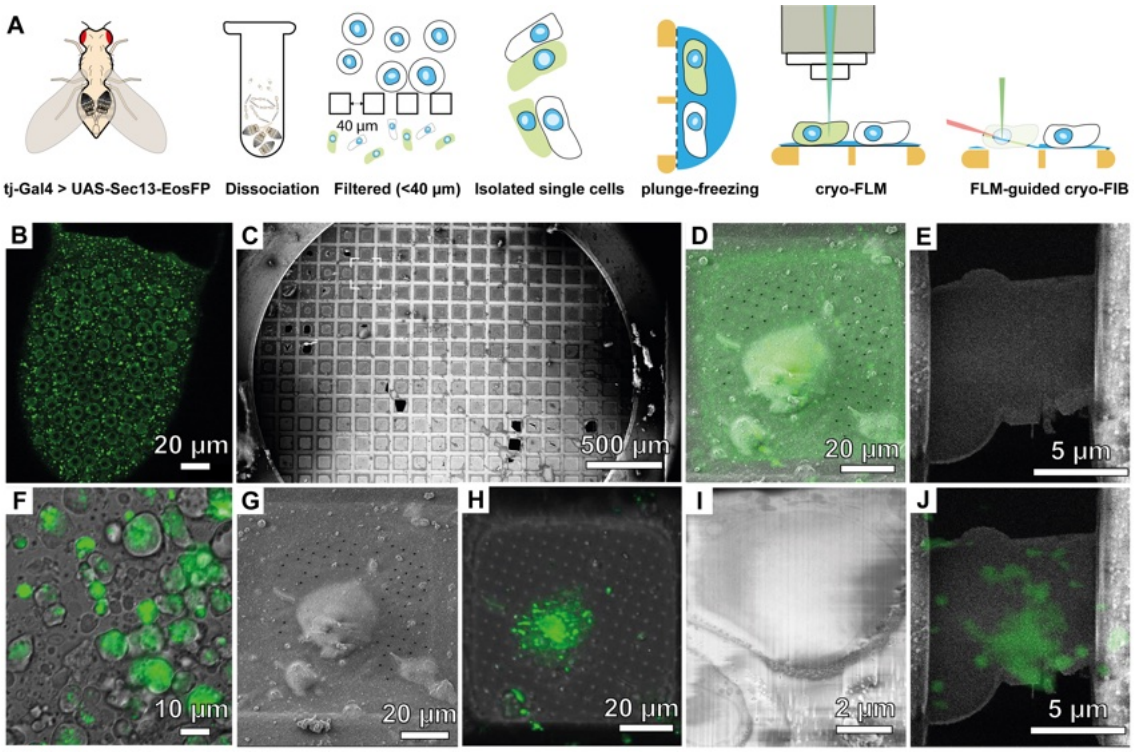

Figure 4.7.3 Isolation protocol for on-grid lamella preparation of tissue-specific cells using the UAS-GAL4 system. A: Schematic representation of the workflow. First, ovaries are extracted, digested and applied through a cell strainer. The resulting cellular suspension is plunge-frozen on an electron microscopy grid and subsequently, cells originated from the targeted tissue, in this case the follicle cell epithelium, can be identified by cryo-fluorescence microscopy. Lamella are prepared for subsequent cryo-ET correlative milling protocols as demonstrated throughout this thesis.**B:** Room temperature confocal microscopy image of a *D. melanogaster* egg chamber expressing EosFP-Sec13 in the follicle cell epithelium. **C:** Widefield fluorescence microscopy image of the isolated cells shown in from the workflow in A. **D:** SEM image of a grid prepared by the workflow in A. **E**: SEM and **F:** cryo-confocal image a grid square containing a EosFP-Sec13 positive and a negative cell directly next to each other. **G:** Overlay of D and E. **H:** SEM image of the lamella surface used to identify the nucleus for targeted lamella thinning. Note that in-chamber light microscopes were not available during this preparation. **I:** SEM image of the final thinned lamella. **J:** Image from I overlayed with the fluorescence image of the cell prior to milling.

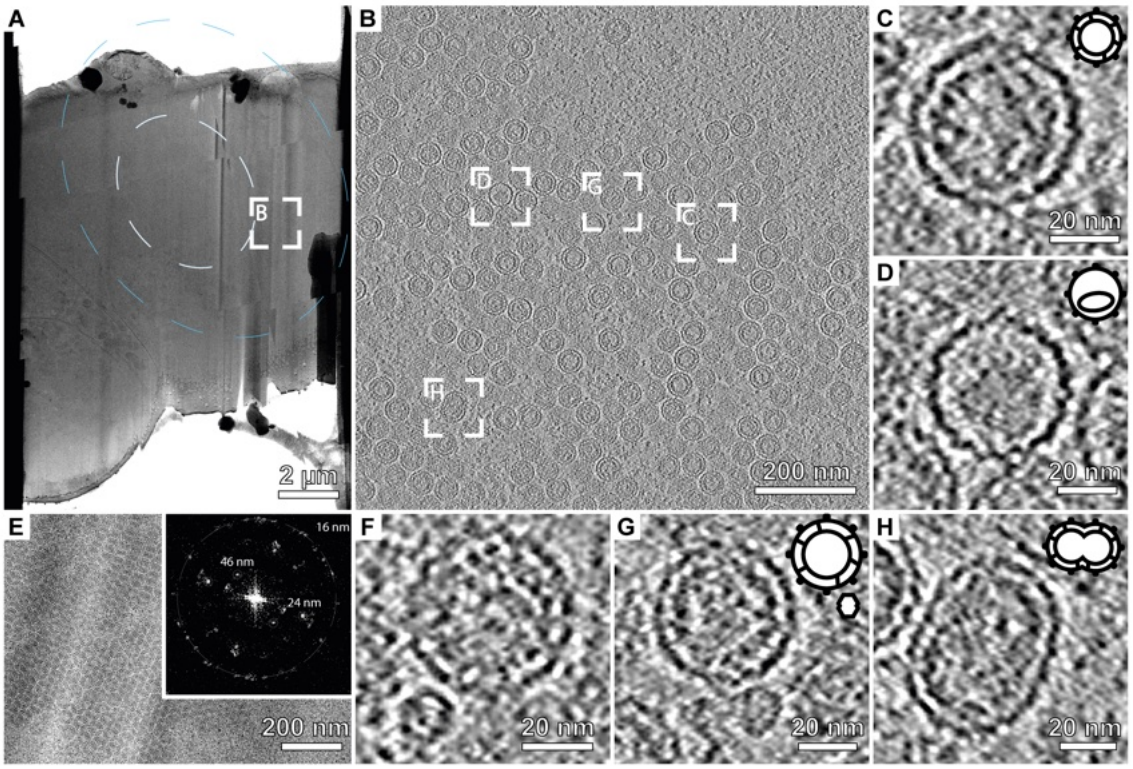

Figure 4.7.4 Tomogram of a large cluster of *copia* capsids collected on an isolated follicle cell. A: TEM overview of the lamella. **B:** Slice through the tomogram reconstruction of a tilt series collected on the lamella shown in A. **C:** A putative immature *copia* capsid. **D:** A putative mature *copia* capsid. **E:** Zero tilt image and its fast Fourier transformation (inset) of the tomogram shown in B. The fourier transform shows distinct peaks at 1/46nm and 1/24nm. **F-G** Sample images of unidentified potential interactors observed in the tomogram. **H:** Example of a potentially misassembled capsid.

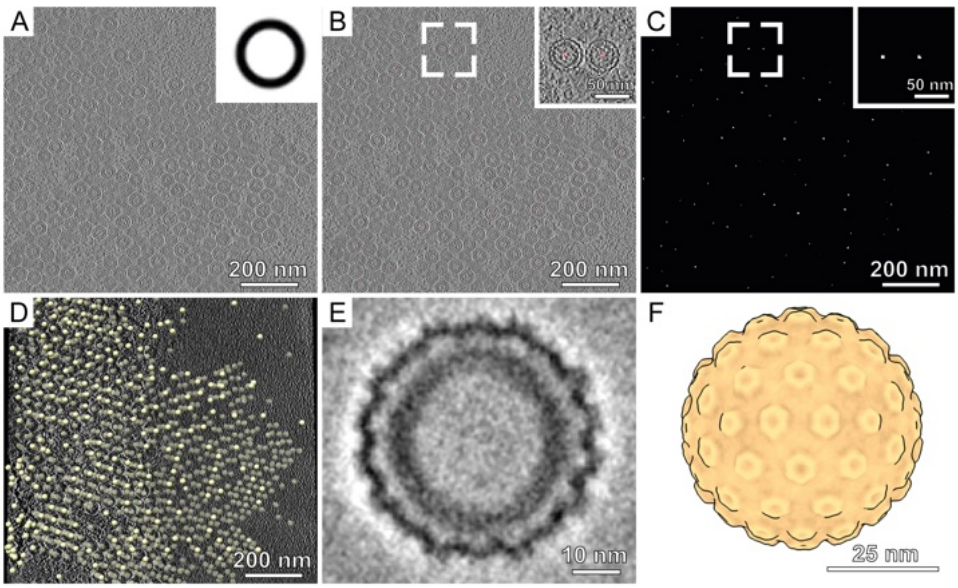

Figure 4.7.5 Particle identification of *copia* capsids by template matching. A: Slice through the tomogram reconstruction of a tilt series from *copia* clusters. Inset shows the template used for template matching, a hollow sphere **B:** Template matching results thresholded and overlaid to the initial tomogram. Inset shows the a magnified version of the indicated region. The tomogram is shown in gray values, the cross correlation map in red. **C:** Cross-correlation score map of the template matching in STOPGAP. Inset shows the same region as in B. **D:** Identified particles mapped in three dimensions into the tomogram. **E:** Intial subtomogram average obtained from the particle positions shown in D. **F:** 3D rendering of the symmetrised *copia* capsid shown in E.

ing with a hollow sphere as a reference (**Figure 4.7.5A inset**). These resulted in clear peaks in the cross-correlation map that coincided with the capsids (**Figure 4.7.5B-D**). Initial subtomogram analysis of the entire capsid without applied symmetry showed pentameric and hexameric structures, suggesting icosahedral symmetry of the capsids. Based on the size of the capsid, the triangulation number was determined as T=9 and applying that symmetry yielded a 16 Å initial *copia* capsid structure using the STOPGAP software package (**Figure 4.7.5E-F**).

4.7.5. Structure of the *copia* capsid

By re-visiting the tomograms of *copia* using Warp and Relion3.1, we were able to get a subnanometer structure of the *copia* capsid formed by the CA protein. While only approximately 20-30$\%$ of the capsids show icosahedral symmetry based on classification results, it yielded a 8 Å structure according to gold-standard FSC (**Figure 4.7.6A-B**). The structures show clear alpha helical features and, thus, allowed for model building of the capsid (**Figure 4.7.6C-D**). Predicted penta- and hexameric structures of the *D. melanogaster copia* gag sequence using the Alphafold-Multimer program were taken as initial model. Rigid body fitting structures for the hexameric structure were refined to the density (**Figure 4.7.8A**) using ISOLDE (**Figure 4.7.6B**). By examining surface models with electrostatic mapping, it is apparent that the pseudo-hexameric interfaces appear to be positively charged (**Figure 4.7.8C**).

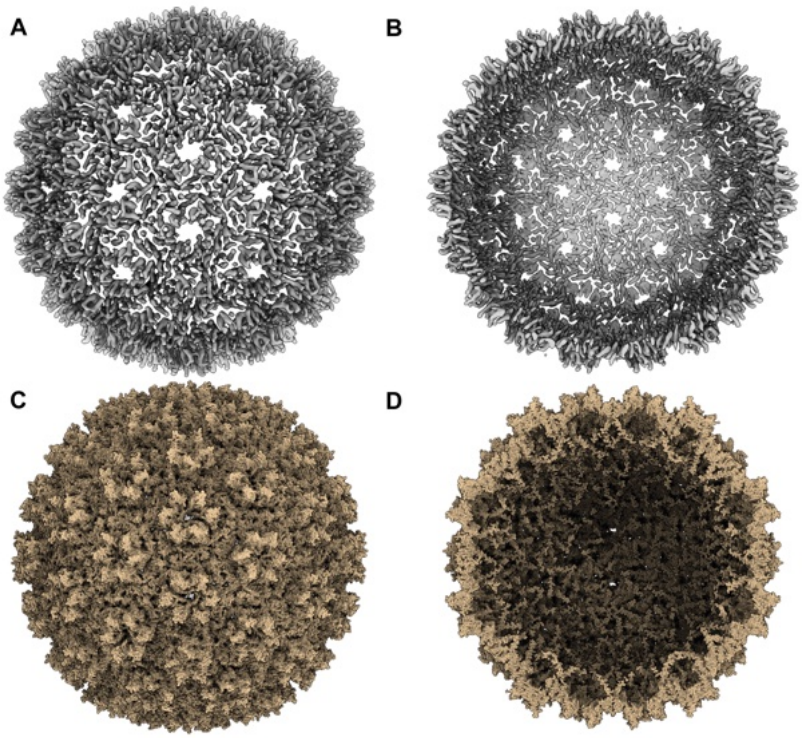

Figure 4.7.6 Structure of the entire icosahedral structure of the *copia* capsid. A: CryoEM map of the capsid structure looking at the C2 symmetry axis. **B:** CryoEM map of the capsid structure from the same angle as in A but cut in half. **C:** Atomic surface representation of the model derived from the density in A. **D:** Inside view of the atomic surface representation of the model derived from the density in C.

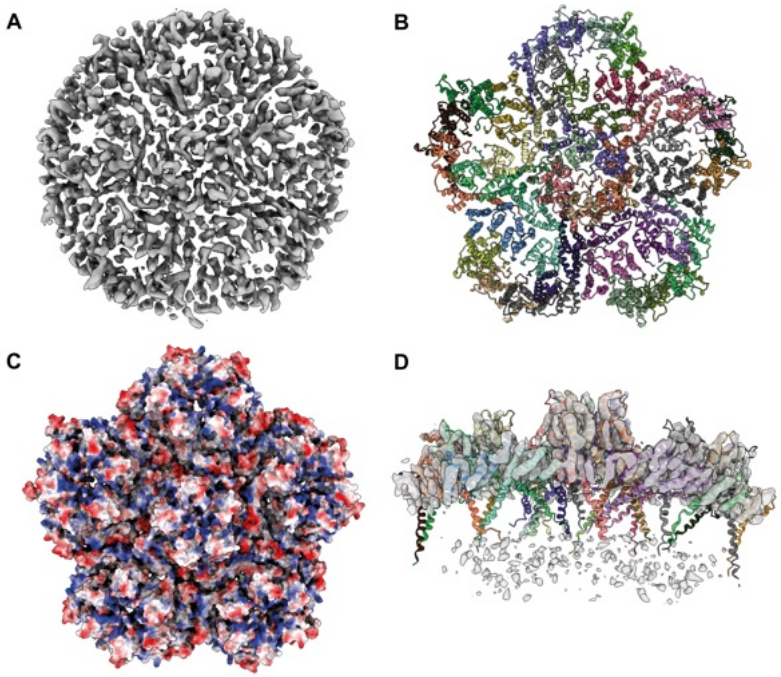

Figure 4.7.7 Structure of the C5 symmetric assembly of the *copia* capsid. A: CryoEM map from focused refinement on the C5 symmetry axis of the icosahedral *copia* capsids. **B:** Fitted structure based on interactive molecular dynamics flexible fitting simulations of rigid body fitted pentameric AlphaFold predictions of the *copia* protein. **C:** Surface representation of the model shown in B colored by charge from positive (blue) via neutral (white) to negative (red). **D:** Side view of the model to map fit from A and B. Note that the AlphaFold predicted helices are reaching towards the inner part of the *copia* structure where the nucleocapsid sits.

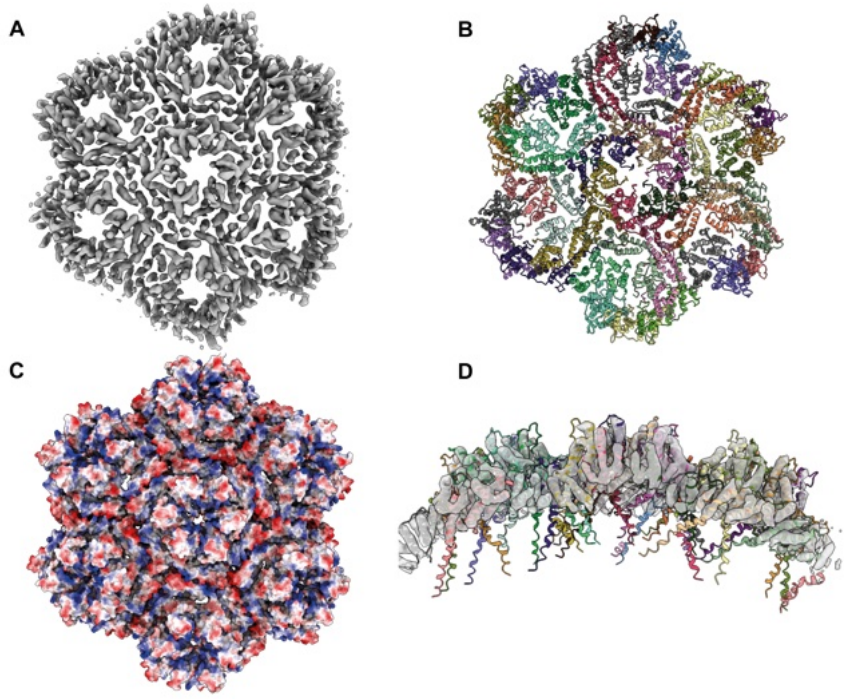

Figure 4.7.8 Structure of the hexameric environment of the *copia* capsid. A: CryoEM map masked from the icosahedral structure of the *copia* capsids for model generation. **B:** Fitted structure based on interactive molecular dynamics flexible fitting simulations of rigid body fitted hexameric AlphaFold predictions of the *copia* protein. **C:** Surface representation of the model shown in B colored by charge from positive (blue) via neutral (white) to negative (red). **D:** Side view of the model to map fit from A and B.

The helices distinguishable at the obtained resolution of 8 Å fitted the model (**Figure 4.7.8D**). For the pentameric structure (**Figure 4.7.7A**), the C-terminal domain of the *copia* CA protein needed to shift slightly, an adjustment that was done by interactive molecular dynamics flexible fitting in ISOLDE (**Figure 4.7.7B,D**). Similar trends in the electrostatic surface can be observed for the C5 symmetric structure, with the inside interfaces within the C5 symmetry being mostly positively charged (**Figure 4.7.7C**). The icosahedral symmetric structure of the entire capsid was then assembled from these parts and refined in a final fitting step to the entire capsid structure.

4.7.6. Visualizing the nuclear periphery of *D. melanogaster* egg chambers in its near-native state

Using the technical and technological developments to target specific structures in high-pressure frozen material described above (**Chapter 4.6**), we collected tomograms of the nuclear periphery of follicle cells (**Figure 4.7.9A-C**). As expected from the previous experiments, we observed capsids within the nucleus (**Figure 4.7.9B-D**). Capsids can also be distinguished in the cytoplasm, usually in close proximity of the nucleus (**Figure 4.7.9E**). Additionally, our tomograms showed capsids aligned with the central channel of the nuclear pore complex (**Figure 4.7.9B-E, G-H**). By measuring the particle sizes from intact tissue, we found that the *copia* particles in

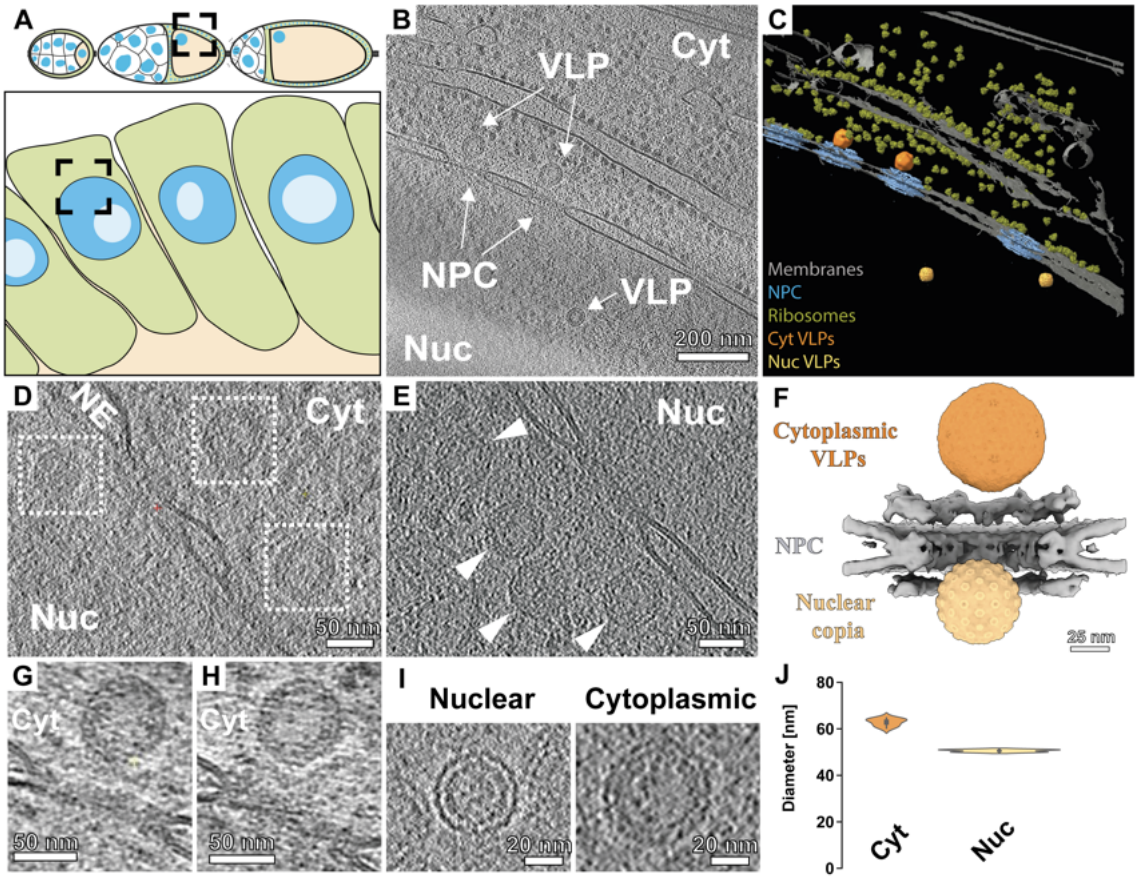

Figure 4.7.9 *In situ* observation of NPC interactions of *copia*. A: Schematic representation of the lift-out tomogram positions. Stage 10 oocytes were targeted. **B:** Tomographic slice of the nuclear periphery of a follicle cell from cryo-electron tomography of FIB lift-out lamellae. **C:** Segmentation of the tomogram shown in B. **D:** Close up on a nuclear envelope from a tomogram. Note the cytoplasmic and nucleoplasmic capsids that show a clear size difference. **E:** Close up of a tomographic reconstruction of the nuclear envelope region showing multiple cytoplasmic capsids. **F:** Visualization of cytoplasmic (orange) and nucleoplasmic (beige) averages compared to the subtomogram average of the nuclear pore complex (gray). **G-H:** Zoom in on capsids that are putatively interacting with the nuclear pore complex as they are perfectly aligned with the FG-Nup-rich central channel. **I:** Side-by-side comparison of nuclear and cytoplasmic *copia* capsids. **J:** Violin plot showing the size comparison of the observed nuclear and cytoplasmic capsids.

the nucleus were 50.5 nm $\pm$ 0.5 nm in diameter, while cytoplasmic capsids showed a diameter of 62.8 nm $\pm$ 1.5 nm (**Figure 4.7.9I-J**). When comparing the subtomogram averages of capsids found in the nucleoplasm and cytoplasm with the structure of the nuclear pore complex determined from the lift-out tomograms, it seems only the smaller capsids could pass through the central channel (**Figure 4.7.9F**).

4.7.7. Comparison of the nuclear morphology of somatic and germ-line nuclei reveal cell-type specific differences

As only the somatic cells within the egg chamber showed signal for *copia* (**Figure 4.7.1**), we were interested in how the nuclear periphery of somatic and germ-line cells compare morphologically. To compare nuclear pore complex structure between cell types, we collected tilt series of the nuclear periphery of the somatic and germ-line cells (**Figure 4.7.1A**). The nuclear envelope of the follicle cell nuclei (**Figure**

4.7.1B) shows a regular distance between inner nuclear membrane (INM) and outer nuclear membrane (ONM). The INM and ONM within the germ-line nucleus (**Figure 4.7.1E**), however, is extremely difficult to see due to the high number of nuclear pore complexes obscuring the reconstruction of the nuclear envelope. As seen in other eukaroytic cells, ribosomes coat the outer nuclear membrane in follicle cells (**Figure 4.7.1B-C**). Interestingly, the germ-line nucleus seems to form an exclusion zone of ribosomes (**Figure 4.7.1E-F**). No ribosomes are observed up about 35 nm distance from the nuclear envelope. Furthermore, the number of NPCs embedded into the nuclear envelope differs drastically between the cell types (**Figure 4.7.1C,G-H**). While the follicle cell nuclear envelope only shows sporadic NPC density (**Figure 4.7.1C**), the germ-line cells show a tight packing of NPCs within the nuclear envelope (**Figure 4.7.1G-H**). Additionally, a cytoplasmic NPC within a sheet of the endoplasmatic reticulum was observed (**Figure 4.7.1C yellow arrowhead**). When comparing the subtomogram averages obtained from germ-line and somatic cells (**Figure 4.7.1J-L**), a difference in membrane-to-membrane distance is detectable (**Figure 4.7.1L**).

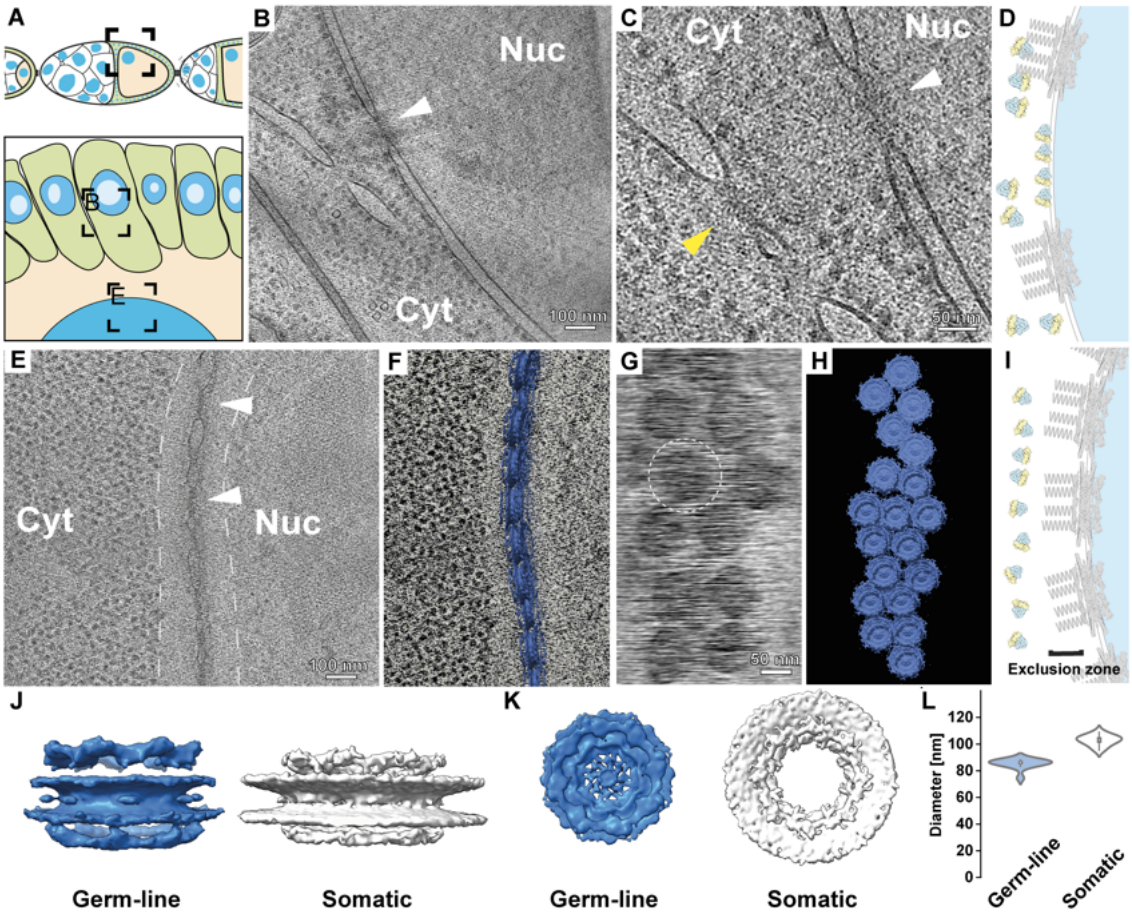

Figure 4.7.10 *In situ* observation of the nuclear morphology of somatic and germ-line cells in the *D. melanogaster* egg chamber. A: Schematic representation of the lift-out tomogram positions. Stage 10 oocytes were targeted. **B:** Tomographic slice of a follicle cell nucleus from an intact egg chamber by cryo-lift-out. Arrowhead indicates a nuclear pore complex. **C:** Different slice of the tomogram shown in B. The white arrowhead indicates an NPC in the nuclear envelope (NE), the yellow arrowhead indicates a cytoplasmic NPC in an ER sheet. Indicated in B-C are the nucleus (Nuc) and the cytoplasm (Cyt). **D:** Schematic model of the nuclear envelope ultrastructure in *Drosophila* somatic follicle cells. **E:** Tomographic slice of a tomogram collected in the periphery of the nuclear envelope of a germ-line cell. Arrowheads indicate NPCs. Dashed lines indicate the observed ribosome and chromatin exclusion zone around the nuclear envelope at the cytoplasmic (Cyt) and nuclear (Nuc) side, respectively. **F:** Rendering of the tomogram in E with backmapped germ-line nuclear pore complex average. **G:** Top view of the nuclear envelope from the tomogram in E. Dashed circle indicates an NPC. **H:** Rendering of the distribution of nuclear pore complexes within the germ-line NE in G. **I:** Schematic model of the nuclear envelope ultrastructure in *Drosophila* germ-line cells. **J-K:** Comparison of the subtomogram averages obtained from the germ-line and somatic cells in side-view (J) and top view (K). **L:** Quantification of the membrane-to-membrane diameter of the NPCs as manually measured.

5. Discussion and Outlook

5.1. Future developments in sample preparation for cryo-electron tomography

While cryo-electron tomography (cryo-ET) of on-grid cryo-FIB milled lamellae has become increasingly routine in specialized laboratories around the world, exemplified by the steady increase in publications that include the keyword “cryo-FIB” and “cryo-ET” in PubMed (**Figure 5.1.1**), many limitations still remain.

One of the major limitations lies in the targeting of specific events within the biological sample. Software solutions to target lamella preparation based on the signal in fluorescence cryo-microscopy exist with some of the recent developments presented in this thesis. However, the process of correlating the two imaging modalities of FIB and fluorescence microscopy, collected either outside or inside the FIB chamber, remains tedious, time-consuming, and highly user dependent. Future developments will be aimed at increasing the throughput of the procedure by reducing the need for user input to a minimum, potentially automating the entire process. The results in **Chapter 4.2** of this thesis may hint at how this could be achieved: The presented machine learning enabled workflow for on-grid lamella preparation by automated lamella site selection currently employs U-Net models that are trained to distinguish three classes in FIB images: cells, grid bars, and void. However, if fiducials that are visible in both FIB and FLM microscopy such as beads (compare **Chapter 4.1**) or other features such as sample topology can be identified on the sample surface, models could be trained to detect these fiducials. Subsequent analysis of these automatically determined fiducial positions yields the corresponding transformation to correlate the imaging modalities to not only inform lamella site selection as presented in **Chapter 4.1** but rather enable automated, site-specific lamella positioning in 3D. Creating large enough datasets to obtain models that are capable of confidently detecting fiducials within the single modalities will be of the essence.

While improved software solutions have the potential to increase the throughput of correlative approaches in lamella milling by reducing the operator’s input in the process, they are unlikely to increase the accuracy of correlation beyond the resolution of the fluorescence light microscopes used, be it in-chamber or on external dedicated widefield or confocal systems. Thus, narrowing down the resolution gap between light and electron microscopy by technical and technological improvements are needed to increase the detection capabilities of, e.g. macromolecular complexes of interest.

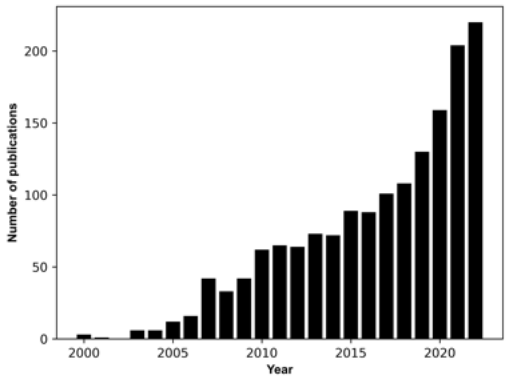

Figure 5.1.1 Number of publications per year involving cryo-ET and cryo-FIB from 2001 to 2022. PubMed search with the query: "cryo-ET"" or ""cryo-FIB"" or ""cryo-electron tomography"" or ""electron cryo-tomography"" or ""cryo-focused ion beam". Accessed on 8. October 2023.

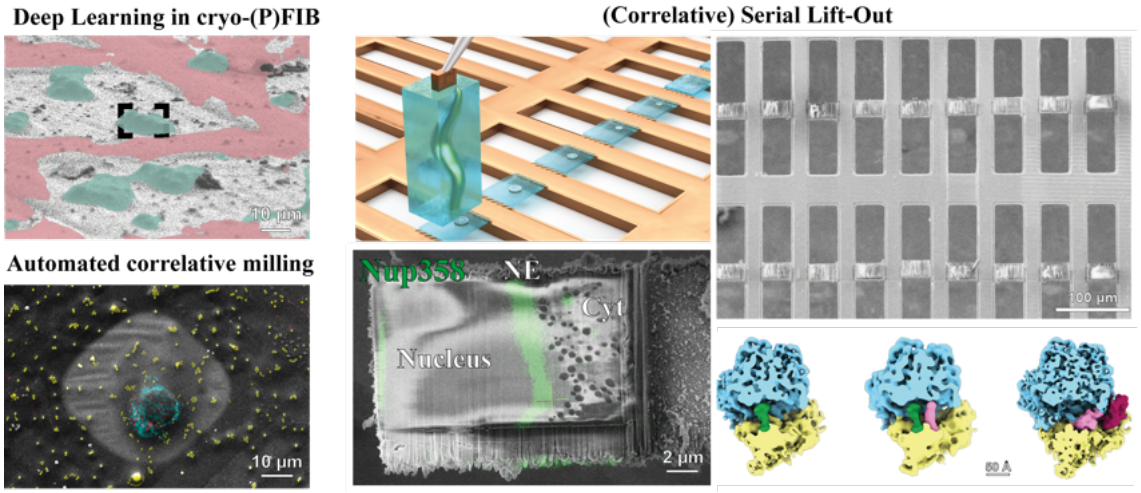

Figure 5.1.2 The prospects on sample preparation by cryo-FIB sample milling for cryo-ET. Future developments in lamella preparation by cryo-FIB milling that will help tackle biological questions may involve the optimisation and incorporation of Deep Learning tasks into the automation pipeline for on-grid preparation, site-directed 3D-CLEM preparations, and cryo-lift-out. Correlation will be especially important to elucidate rare events in tissues and whole organisms. A obvious starting point is the elucidation of cell-type specific structure (e.g. composition of complexes) and dynamics (e.g. translational states) of large macromolecular complexes such as the ribosome.

Super-resolution methods at cryogenic temperatures are being explored. There are promising approaches that have been demonstrated under cryo-conditions, including in-chamber structure illumination microscopy [251] and dedicated instruments for super resolution techniques such as photo-activated localization microscopy (PALM) [252] and reversible saturable optical fluorescence transition (RESOLFT). For the RESOLFT methods only cryo-STED has been demonstrated [253].

Limitations of sample preparation for cryo-electron tomography in cells and tissues beyond targeting are mainly in the throughput and automation for high-pressure frozen specimen and the efficient usage of plasma ion sources to prepare lamellae thereof. Characterization of milling properties and the associated damage with plasma ions is needed to establish best practices in sample preparation with plasma ion sources. Efforts to characterize the milling properties of plasma ion sources have been undertaken [254, 255]. Also, analyses to quantify the damage layer by both gallium and plasma ion sources have recently been described. However, both the gallium and plasma FIB characterization have used relatively large particles, namely ribosomes, to determine damage by decay of signal-to-noise ratio in high-resolution 2D template matching [256] or a Z-dependent Rosenthal-Henderson/B-factor plot, respectively [255]. As the size of the ribosome of approximately 25 nm is in the range of the damage layer determined (60 nm for gallium [256] and 30 nm for argon [255]), artifacts based on e.g. particles partially ablated by ion beam milling cannot be neglected. Thus, repeating the approaches systematically for different ion species and applying them to smaller particles will refine the determined damage layer.

A point of widespread interest will be to develop approaches that circumvent cryo-lift-out with the newest generation cryo-FIB instruments that encompass automated sample exchange hardware and plasma ion sources. As to date, no lift-out system can be installed on these instruments, so new workflows to enable the preparation of lamellae within tissues with these instruments have to rely on grid-based approaches. One of the techniques to achieve this is the “Waffle” method [116]. Due to the capability of eucentric rotation of the CompuStage equipped on newest generation cryo-PFIB-SEM instruments, the need for compucentric rotation in the Waffle preparation is circumvented. This renders the automation for Waffle samples much easier and preliminary results for such a lamella preparation developed as script in SerialFIB are shown in **Figure 5.1.3**. We anticipate that the preparation of lamellae from samples frozen by the Waffle method will eventually become highly automated and integrated into the structural cell biologist’s tool belt. As described above, targeting will become even more important in these type of preparations as the probability of retaining biological features of interest in the final volume for TEM imaging is decreased drastically by the increased volume of the sample compared to on-grid lamella approaches.

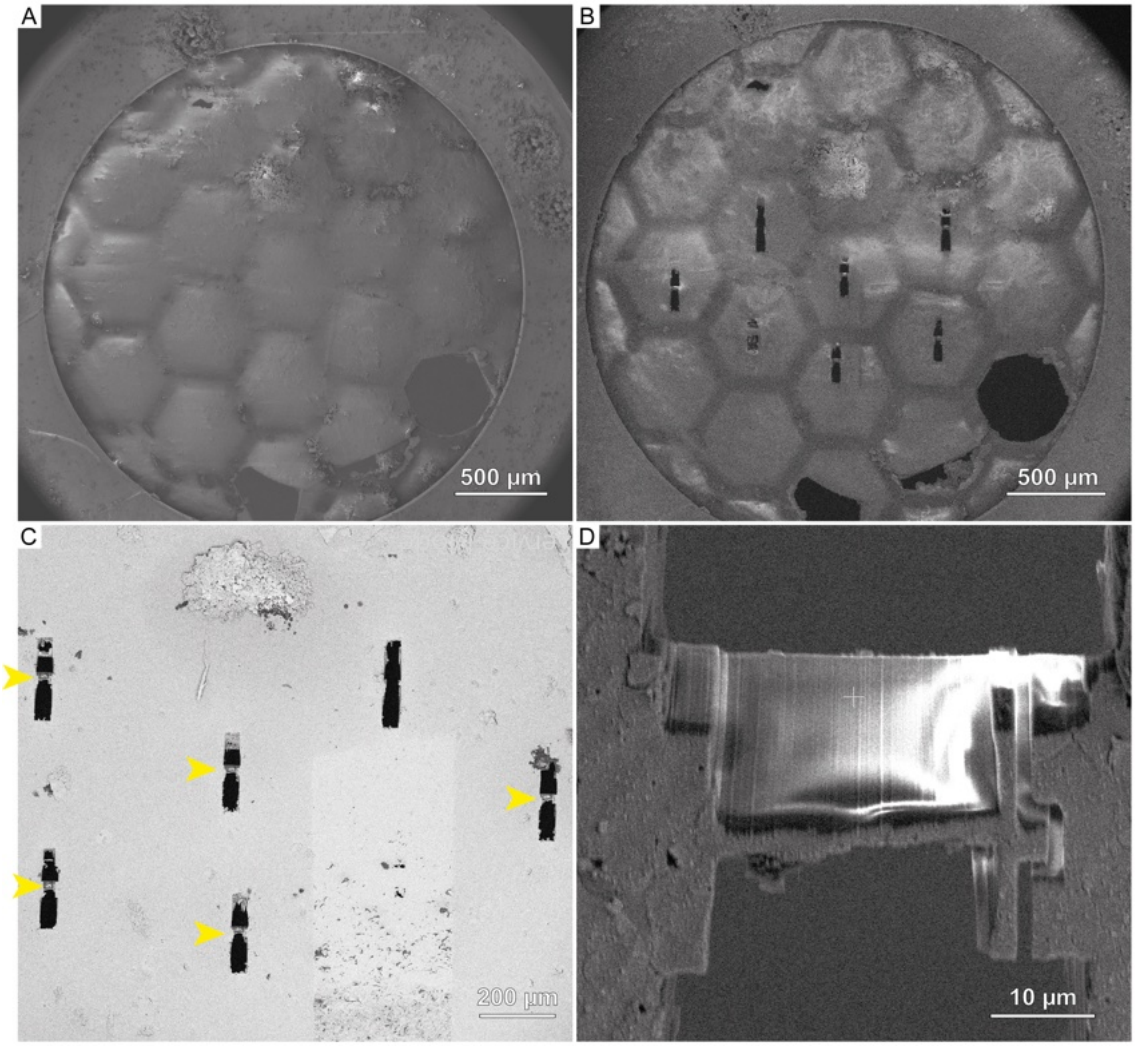

Figure 5.1.3 Automated 'waffle' milling in SerialFIB. As the CompuStage on the Arctis PFIB systems simplifies tilting the sample to a wide range of angles, automating the 'Waffle' method becomes easier. **A:** Pre- and **B:** post-milling SEM images showing automatically prepared 'Waffle' lamellae. **C:** 5 out of 6 of the 'Wafffle' rough lamella were successfully prepared. **D:** Representative SEM image of an automated 'Waffle' lamella.

Finally, cryo-lift-out in the current and future implementations will be automated to decrease the user expertise needed to successfully perform such experiments. First steps towards this goal have already been undertaken. As room temperature lift-out applications are already highly automated, it is only a matter of time until full automation becomes routinely available to cryogenic applications as well.

5.2. Open software for the cryo-FIB community: Extending SerialFIB to other microscope vendors

Open software is crucial for scientific progress as it enables researchers to collaborate, share, and reproduce findings across instrument platforms and research institutions. It makes developments accessible to scientists that can build up on previous

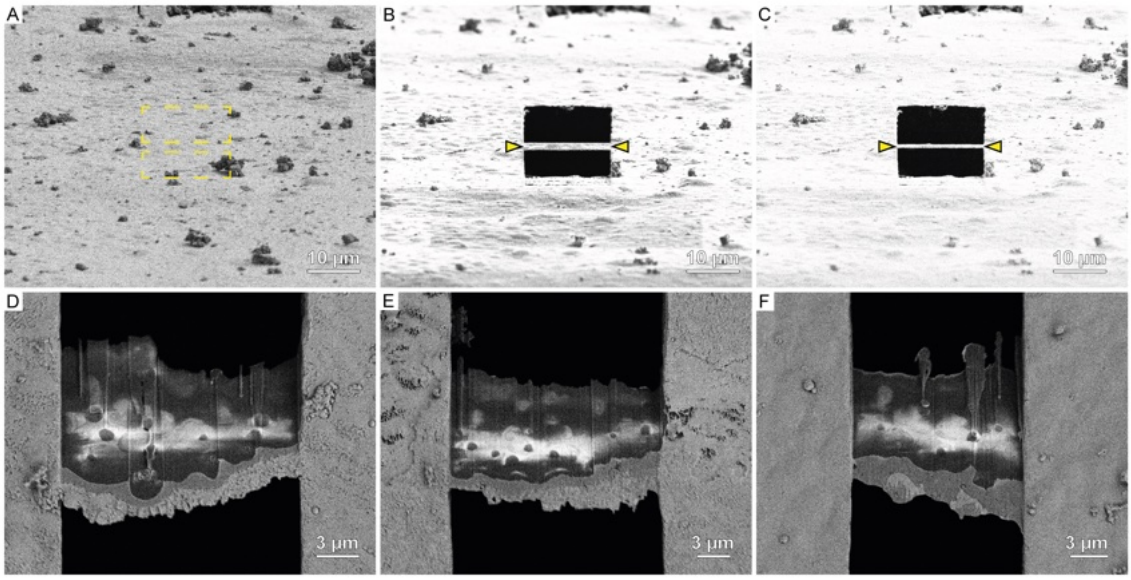

Figure 5.2.1 Exemplary lamellae prepared on a Zeiss CrossBeam instrument using SerialFIB. A: FIB image before rough milling. Yellow patterns show milled volume. **B:** FIB image of the rough milled lamella. Yellow arrowheads show the lamella position. **C:** FIB image of the final lamella. Yellow arrowheads indicate the lamella position. **D-F:** Three examples of automated lamellae milled with the SerialFIB CrossBeam implementation.

work and advance algorithm development in a timely manner. Thus, open software accelerates the pace of research and holds the potential to improve the transparency of developments. In microscopy, especially in light microscopy, many platforms for both data acquisition and analysis exist. An automation platform across microscope vendors for FIB technology such as SerialFIB has the potential to increase accessibility of newly developed preparation workflows where scripts can be shared and deployed across microscope platforms. SerialFIB (**Chapter 4.1**) was designed to be one of the first cross-platform software packages for cryogenic applications with the FIB. Work has already been undertaken to make the toolbox available to a larger scientific community. To date, a driver to allow for (correlative) cryo-FIB lamella preparation workflows on Zeiss CrossBeam FIB/SEM instruments has been developed (**Figure 5.2.1**) and protocols for milling are constantly optimized. Additionally, a driver for TESCAN FIB/SEM instruments is under construction. Not only does this provide researchers with software to automate repetitive tasks on the FIB and aid in further development but I anticipate it will also increase the speed with which new workflows such as the machine learning-based approaches presented in **Chapter 4.2** can be adapted to other microscopes available to the FIB/SEM community, demonstrating how open software can accelerate science.

5.3. Improving cryo-electron tomography for visual proteomics

Improving the imaging of weak phase objects will require significant hardware development. Since the contrast transfer function in the weak phase approximation in the description of imaging cryogenic biological samples starts off at 0 (**Figure 3.2.2**), the possibility of using phase plates to shift the CTF by 90° to obtain the maximum contrast transfer at low frequencies is being explored extensively. While both Zernike [257] and Volta phase plates [258] have been successfully applied, none of them proved ideal in the practical application. The main limitation of the Volta phase plate was two-fold: first, as a thin carbon film is introduced into the beam path, the signal-to-noise ratio of the final image is inevitably reduced [259]. This led to increased B-factors in practice and, though minor, an overall deterioration of the signal in the images. Second, the Volta phase plate relies on the Berriman effect, which leads to a phase shift in the electron beam by irradiating and charging a carbon film, creating the Volta potential causing the phase shift [258]. As the irradiation of the carbon film creates a time-dependent potential, keeping the phase shift constant over extended periods of time such as required for the acquisition of a tomogram is difficult. Recent advances in our understanding of the interaction of photons and electrons has yielded a novel design for phase plates: the laser phase plates [51]. By exploiting the pondermotive force that acts between a photon and an electron and deploying a Fabry-Perot cavity [260] to create a laser beam with high enough intensity to use this weak force to shift the phase of an electron, a first prototype of a laser phase plate that is capable of shifting a 300 kV electron beam by 90° has been realized and described [52].

Another important development is likely the integration of aberration correction into the imaging of biological specimen by TEM. When resolutions beyond 1 Å are obtained, the aberration of the microscope are starting to be limiting. Recently, structures obtained by SPA have been solved down to 1.2 Å resolution [41, 261]. The developments that allowed this achievement were the use of Cold FEGs [41] or a monochromator + BCORR spherical abberation corrector [261] to reduce the spread of the incident electron beam as well as novel detectors and energy filters [41]. Further advancements will likely need even more dedicated hardware. Another aspect that would benefit from aberration correction is the volume that can be studied by cryo-ET. Initial experiments showed that C_C correction can help in obtaining reconstructable tilt series from samples as thick as 400 nm (Dr. Peiyi Wang, Southern University of Science and Technology, China, personal communication). While quantitative analysis regarding downstream applications such as subtomogram averaging from such tomograms is still lacking, the possibility of obtaining more context of the biological sample seems promising.

Regarding sample preparation, the contextual information and, consequently, the descriptive ability of visual proteomics may be increased by improving the sectioning of Serial Lift-Out lamellae (**Chaper 4.5**). For example, one opportunity would be to mill lamellae of suitable thickness directly from the lift-out block rather than having to section and subsequently polish the obtained sections (compare **Figure 4.5.1**). While material will always be lost between the sections due to the ablation mechanism of the focused ion beam, it is desirable to keep it to a minimum. Anisotropically changing the dimensions of the ion beam by beam shaping may be one way to achieve this. While experiments along those lines can already be performed using the stigmator widely available in the cryo-FIB instruments, an optimized solution will likely require significant hardware development such as dedicated cylindrical lenses or beam shaping apertures.

Finally, the data analysis pipelines currently available for subtomogram analysis are slow, usually challenging to master, and require significant computational resources. There is a need for streamlined and easy-to-use software packages that allow for the reconstruction and analysis of cryo-ET tilt series in an automated fashion. Furthermore, since the amount of data collected is reaching the limits of what is managable, it is worthwhile to think about collaborative analysis and data sharing platforms, some of which have been explored for example in the volume electron microscopy community [262]. Together, this holds the potential to accelerate the route from sample to biological insights and discoveries by cryo-ET and expand the fraction of the proteome that is amenable to the visual proteomics approach.

5.4. Cryo-ET in multicellular organisms to understand cell-type specific structural differences

5.4.1. Nuclear pore complex structure and biogenesis

As described in **Chapter 4.7**, the ultrastructure of the nuclear envelope across the different nuclei in the egg chamber differ drastically. The follicle cell epithelium comprises somatic cells that show nuclear envelope morphology and nuclear pore complex distribution similar to previously studied organisms such as Baker's (*S. cerevisiae*) [263] and fission (*S. pombe*) yeast [264], human cell lines (HeLa) [204], and unicellular algae (*C. reinhardtii*)[165]. The nuclei of the germ-line cells in the *D. melanogaster* egg chamber, however, show a very different molecular morphology. The density of nuclear pore complexes in the nuclear envelope is significantly higher and almost resembles a hexagonal packing, similar to what has been seen in large cytoplasmic NPC assemblies called annulate lamellae [265]. Furthermore, the nuclear pore complexes seem to form a ribosome exclusion zone around the nucleus.

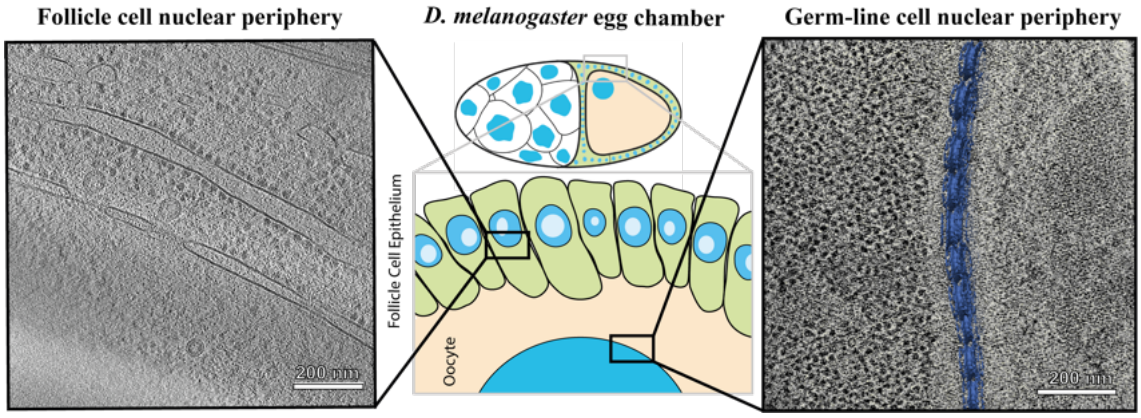

Figure 5.4.1 NPC structure across cell types in the *D. melanogaster* egg chamber. As macromolecular complexes may change their composition, structure, and dynamics dramatically across cell types, cell-type specific structural biology holds great potential. Here, we show that the morphology of the nuclear envelope and the nuclear pore complex structure seems to change dramatically in the egg chamber. Future research will help to understand the functional relevance of such differences.

It is thus tempting to ask the question whether little or even no translation happens at the outer nuclear membrane of germ-line nuclei or the germ vesicle. With the increased throughput of preparation methods presented throughout this thesis, further studies will enable a structural comparison of somatic and germ-line nuclear pores in the egg chamber (**Figure 5.4.1**). The preliminary results shown in **Chapter 4.7** already establish the clear differences in NPC distribution in the NE between somatic and germ-line nuclei. However, whether and how differences manifest at the structural level remains elusive and an interesting question. Finally, in light of the techniques of targeting events in biological tissue developed here, obtaining cryo-ET tilt series of other aspects of nuclear pore complex biogenesis, namely annulate lamellae [266–268] and their assembly in phase separated compartments [196, 269], becomes feasible.

5.4.2. Nucleocytoplasmic transport of large molecular complexes and the replication cycle of *copia*

The nucleocytoplasmic transport of macromolecules through the nuclear pore complex is a tightly regulated process. Generally, small molecules with a usually cited cut-off around 30 kDa can pass through the nuclear pore by passive diffusion [202]. Large macromolecules, however, require an active transport with the aid of nuclear transport receptors (NTRs) which are also referred to as importins and exportins of the karyopherin family. An increasing number of large protein assemblies are reported to be transported as a whole through the NPC. Some of the assemblies that are suggested to pass the nuclear envelope via the NPC are proteasomes [270], the TREX complex [271], and the mature HIV capsid [210]. Only the latter has to date been observed in close interaction with NPCs using transmission electron microscopy.

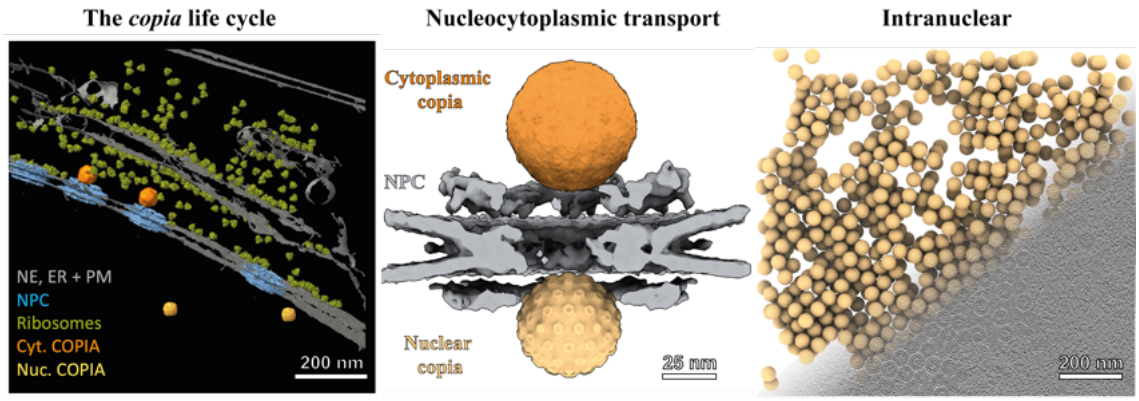

Figure 5.4.2 *In situ* studies of the nucleocytoplasmic transport of transposable elements. As transposable elements of class II, more specifically the LTR retrotransposons, share a evolutionary history with retroviruses, the replication cycle of transposons inside the cell may inform us on many aspects of cell biology. Thus, the study of the *copia* replication cycle as an example will be of interest as a model system.

As we saw in **Chapter 4.7**, the capsid of the *copia* retrotransposon seemingly interacts with the nuclear pore complex, raising the possibility that these are transported as entire capsids. In the presented work, multiple snapshots along the replication cycle of *copia* were obtained by cryo-ET (**Figure 5.4.2**). As capsids were observed outside and inside the nucleus as well as at the nuclear pore, a NPC-mediated nucleocytoplasmic transport is likely. While to date unclear, the size difference of cytoplasmic and nucleoplasmic capsids may be related to either a loss of an additional binding partner, different capsid assemblies, or a conformational change as reported for other icosahedral assemblies such as the plant virus CCMV [272]. Though unlikey as radial distribution plots look similar between nuclear and cytoplasmic VLPs, it can also not be completely ruled out that the cytoplasmic particles are not *copia* but a different capsid forming structure. Notably, cytoplasmic capsids were only observed in the intact tissue, not in isolated follicle cells. It suggests that transport of the capsids occurs relatively fast after assembly in the cytoplasm. Also, it suggests that the localization in the nucleus is favored. The detection of half assembled or disassembled lattices of the capsids in the nucleus further indicates that the capsids are stable in the nucleoplasm for extended periods of time.

The smaller diameter of germ-line nuclear pore complexes raises the question whether *copia* capsids can be transported into germ-line nuclei. Taken together, the presented work yields a preliminary model of the *copia* replication cycle in somatic follicle cells as follows: the genome is transcribed from the host DNA and transported into the cytoplasm where the *copia* polypeptide is produced. From the polypeptide, an immature capsid is formed. The cytoplasmic structure shows a difference in size from the nuclear VLPs that either is the result of additional binding factor on the surface, different T numbers yielding structures with changing sizes, or different conformations between outside and inside the nucleus. An interaction with the nuclear pore is likely, and the possibility of entire capsid being transported exists. Inside the nucleus, the capsids form large clusters from which the intasome is likely released after capsid

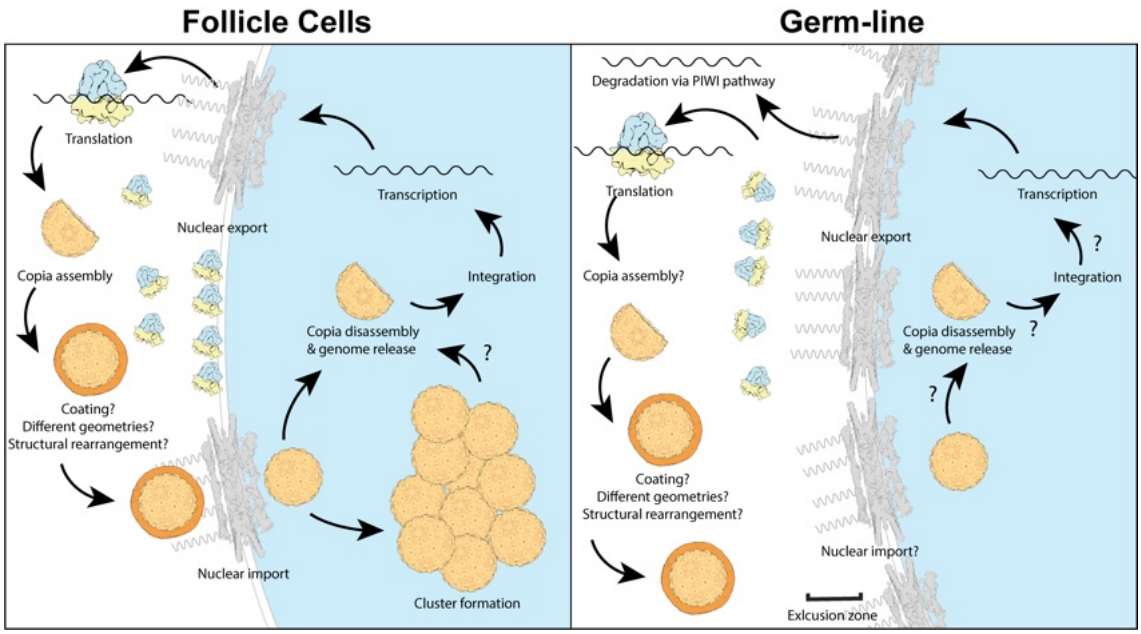

Figure 5.4.3 Model for the replication cycle of *copia*. In the somatic follicle cells, nucleocytoplasmic transport via the NPC seems to be possible for capsids that are of the right size, either due to their assembly, the release of a binding factor, or a conformational change. In the germ-line, the question whether nucleocytoplasmic transport is possible if capsids are produced remains.

disassembly, potentially leading to integration into the host genome. From there, the cycle can start anew (**Figure 5.4.3**). In the germ-line cells, however, no capsids are produced due to a specific protein that silences the retrotransposon (personal communication, Kirsten Senti). The question remains whether nucleocytoplasmic transport is possible in the germ-line cells if capsids are produced, e.g. under knockdown conditions of the repressing factors in the germ-line (**Figure 5.4.3**). Additionally puzzling is whether and how genome integrity is maintained with such a large number of TEs present in the nucleus.

The parallels to the replication cycle of HIV are striking (**Figure 5.4.4**) [210]. The mature HIV capsid is transported through the nuclear pore via specific interactions with Nup358, CPSF6, and Nup153 [209]. It then assembles in clusters, so called nuclear speckles, from which the intasome is released to allow for genome integration. The orientation of the cone-shaped capsid in this process is thereby thought to be achieved via differential affinities on the cone's surface to the different binding partners. A structure of the HIV CA protein bound to a Nup153-derived peptide from the FG-repeat region has recently become available [273]. Preliminary structural comparison of the pocket suggest similarity with the *copia* structure presented in **Chapter 4.7**, though further experiments and confirmations are needed. It raises the question whether the *copia* CA protein could show similar interactions to HIV that allows for its interaction with the nuclear pore complex.

Finally, the evolutionary logic of a transposable element would most probably be to

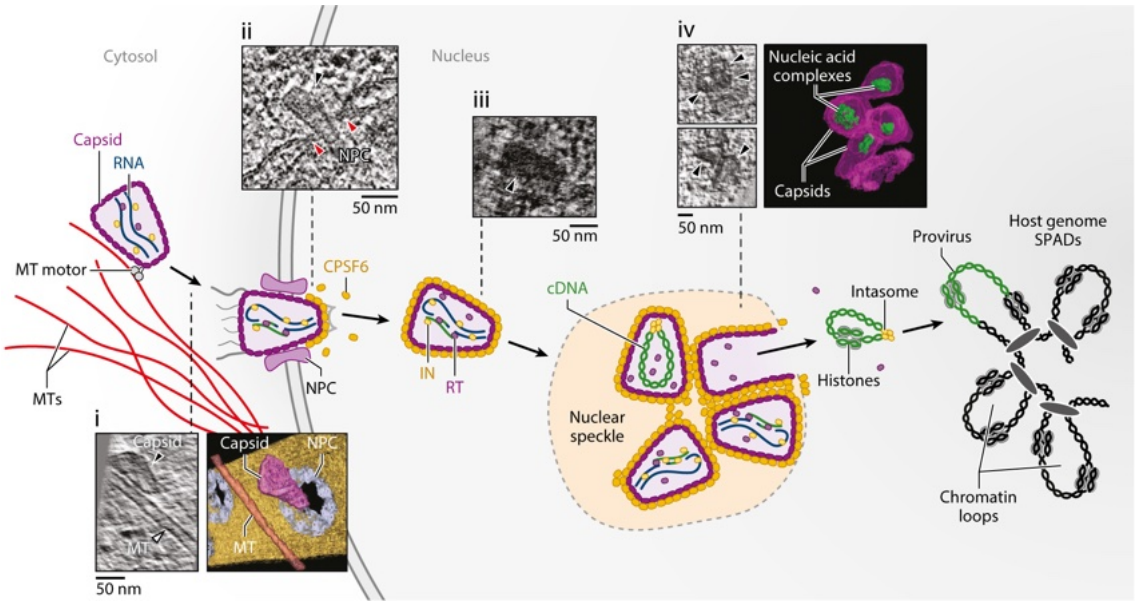

Figure 5.4.4 Model for the replication cycle of HIV. Adapted from [209] with permissions.

optimize for the capsids to reach the genetic information of the germ-line to allow for novel insertions. However, in the case of the *copia* capsids presented here, the localization in the follicle cell nucleus will make it unlikely that *copia* capsids reach the oocyte. However, as *copia* capsids have been detected in S2 cells [190] and the follicle cells as described here, they seem to be wide-spread in *Drosophila* and actively transcribed. The retrotransposition of *copia* was previously reported to happen almost exclusively in the male germ-line for the *D. melanogaster* 2b3 line [274]. The cell biological mechanisms of how *copia* transposes, however, remain elusive and will need to be addressed in future studies.

5.4.3. Other aspects of the biology of multicellular organisms

The study of multicellular organisms opens possibilities for understanding many aspects of cell biology that are inaccessible in unicellular organisms or immortalized cell lines. The advantage of doing structural biology directly within entire organisms is that the contextual information of cells and their environment is maintained, as demonstrated in **Chapter 4.5** and **Chapter 4.7**. In the *C. elegans* L1 larva, due to its limited size and, thus, simplified cryo-lift-out workflow, still many aspects of multicellular biology can be addressed. Multiple translational states could already be distinguished within the collected dataset (**Chapter 4.5**) but comparing the distribution of translational states among various tissues may reveal cell type-specific differences. The presence of cell type-specific structure has also been observed during revisions of the paper described in **Chapter 4.5**. For example, the difference in number of protofilaments of the microtubules in *C. elegans* previously described [275] was clearly visible in a tomographic reconstruction from two adjacent cells in a L1 larva section.

The study of the difference in the composition and structure of macromolecular complexes between germ-line and somatic cells or of cell-specific structures as presented in *D. melanogaster* egg chambers is another example of how structural cell biology can yield new insights if the preparation protocols are established. The methods presented here will aid the community in defining and further studying specific biological questions in various organisms.

5.5. Understanding VIPP1's role in thylakoid membrane biogenesis and maintenance

The structural model of VIPP1 presented here gives a first starting point to elucidate its vital function in thylakoid membrane biogenesis and maintenance. Thylakoid lipids originate in the chloroplast envelope membranes [276]. As we observed direct contacts of inner chloroplast membrane and the thylakoids by encapsulated membranes (**Figure 5.5.1A**), it is tempting to speculate that VIPP1 mediates this lipid exchange by direct contacts. Further indication is the apparent defect of the *Synechocystis sp.* PCC 8603 convergence zones in the F4E and V11E mutants under high-light conditions. Convergence zones have previously been described as high-curvature thylakoid membranes that make close contact with the plasma membrane. The convergence zones have been suggested to be sites of thylakoid biogenesis [221, 222]. Compromised VIPP1 function leading to defective convergence zones is consistent with the described pivotal function of the complex in membrane maintenance and biogenesis [224–230].

The presented results raise the question about the molecular cascade that leads to thylakoid swelling under high-light stress and how VIPP1 aids in relieving that stress. Thylakoid swelling has previously been described in *Synechocystis sp.* PCC 8603 [224] and *A. thaliana* [226] thylakoid membranes under high-light stress or VIPP1 knock-down. VIPP1 could potentially counteract thylakoid swelling by sensing proton leakage of stressed thylakoids and stabilizing damaged regions. How this would happen and whether membrane contacts are formed by VIPP1 and how the decoupling of the proton gradient is prevented in such contacts remains elusive. Further studies into the several aspects of VIPP1's function inside cells of the green lineage will be essential to answer these questions.

Finally, the assembly pathway of VIPP1 remains largely unknown. As both ring and rod structures are described for different species, the way of how VIPP1 encapsulates, deforms and protects membranes is unresolved. Recent AFM studies [277] suggest that monomers spiral on membranes similar to observations for mammalian ESCRT-III proteins and only form the ring structure in the center of the spiral (**Figure**

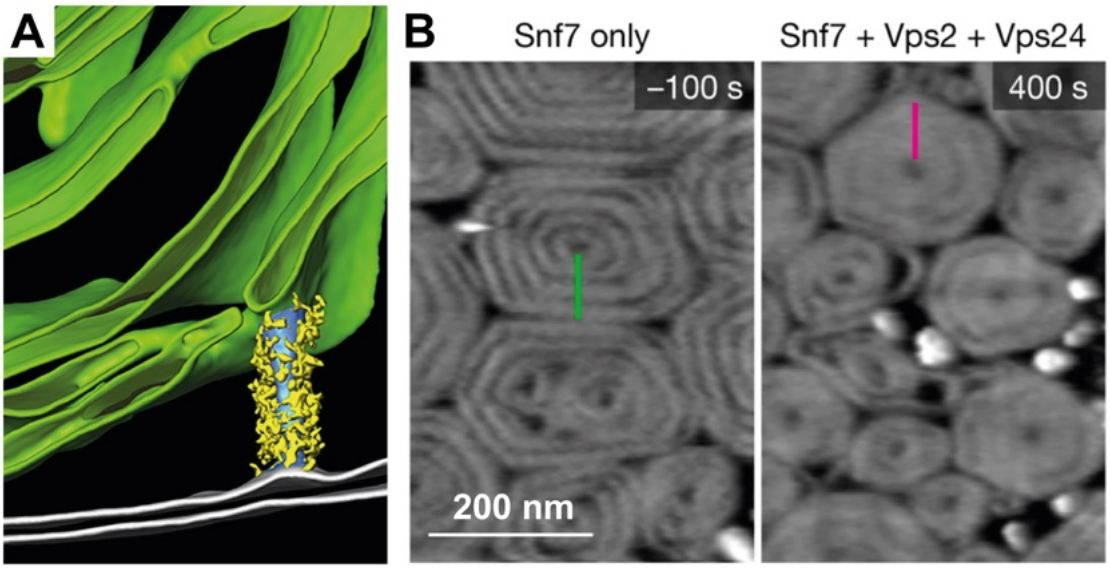

Figure 5.5.1 Hints at VIPP1's mode of action inside the cell. A: Segmentation of a cryo-ET tomogram from *C. reinhardtii* showing a direct connection of the inner chloroplast membrane with the thylakoids formed by an encapsulated membrane. The lamella was prepared used cryo-CLEM FIB milling. While the coat is not as regular as *in vitro* assembled VIPP1 on liposomes, it resembles the *in situ* structures described in **Chapter 4.3** and, thus, likely includes VIPP1. Adapted from [242], with permission. **B:** High speed AFM images of ESCRT-III polymers on supported lipid membranes. Left image shows snf7 that was polymerized on lipid membranes. Right image shows the effect of addition of Vps2 and Vps24 at t = 0 on the polymer structure. VIPP1 has been shown to form very similary structures in a recent pre-print [277] that is only available under the CC-BY-NC-ND 4.0 license and can therefore not be shown here. Images adapted from [279], with permission.

5.5.1B-C) [277, 278]. These studies are performed on isolated membranes, however, and leave the crucial question open whether such a mechanism would be possible in the crowded environment inside a cell.

6. Materials and Methods

Note that all software packages and essential reagents used are listed in the key resource table in the appendix.

6.1. Automating the cryo-FIB instrument

The methods for this chapter are detailed in [21] and will be summarized here and extended where necessary due to novel developments since the preparation of the manuscript. Especially for the preparation of the biological samples other than *S. cerevisiae* and *C. reinhardtii* used in automated milling that were prepared by collaborators, the reader is referred to the method section of the eLife publication [21].

6.1.1. Software implementation

For the development of the automation software presented in chapter 4.1 of this thesis, a number of different cryo-FIB instruments were used. Initial development was done on a Thermo Fisher Scientific Scios and Thermo Fisher Scientific Aquilos 1 instrument running the AutoScript4 software as a communication module with the FIB-SEM hardware. Subsequent adaption of the code to Zeiss instrumentation was performed in collaboration with Roland Salzer at Zeiss on a Zeiss CrossBeam 350 and Zeiss CrossBeam 550 instrument in Oberkochen, Germany. Generally, code development was done offline or on the instrument using either a silicon wafer or an empty grid as sample. The code developed is freely available on GitHub .

6.1.2. Automated lamella milling (with Dr. Sara K. Goetz and Dr. Herman K.H. Fung)

As general starting protocol, lamellae with thickness of around 1 μm were generated in 3 steps with FIB currents gradually decreasing from 1 to 0.3 nA as in manual operation [280]. After completion of rough milling for all positions, fine milling to the desired lamella thickness was performed in one or several steps with decreasing FIB currents (**Table 6.1.1**).

Sample	Micro-expansion joint milling				Rough milling				Polishing			
	distance from lamella [µm]	width [µm]	current [nA]	time [sec]	step	nominal lamella thickness [µm]	current [nA]	time [sec]	step	nominal lamella thickness [nm]	current [pA]	time [sec]
Sum159	4	0.3	1	30	1	5	1	480	1	400	100	210
					2	3	0.5	210	2	300	50	150
					3	1	0.3	210				
HeLa	4	0.3	1	30	1	5	1	540	1	300	50	360
					2	3	0.5	300				
					3	1	0.3	270				
E. huxleyi	4	0.3	1	120	1	5	1	600	1	800	100	240
					2	3	0.5	480	2	600	50	240
					3	1	0.3	480	3	300	30	240
C. rheinhardtii	5	0.5	0.3	60	1	5	0.3	210	1	800	50	180
					2	3	0.3	120	2	600	50	90
					3	1	0.1	120	3	400	50	60
S. cerevisiae	5	0.5	0.3	60	1	5	0.3	210	1	800	50	180
					2	3	0.3	120	2	600	50	90
					3	1	0.1	120	3	400	50	60

Table 6.1.1 Parameter summary for the automated lamella milling experiments from **Chapter 4.1**

6.1.3. Cryo-FIB-SEM volume imaging

Volume imaging was performed at 5 kV and 50 pA with a dwell time of 1 μs , 3072x2048 pixel for Sum159 and HeLa cells at 10.38 nm and 19.27 nm, respectively. Detection was done using the Everhart-Thornley detector with line integration of 16. Milling was performed at 0.5 nA, 30 kV with slice thickness of 100 nm for 10 and 20 seconds, respectively. The *C. reinhardtii* dataset was acquired at 3 kV, 13 pA, 0.25 μs dwell time, line integration of 64 and pixel size of 3.4 nm in OptiPlan mode using Everhart-Thornley, T1 and T2 in-lens detectors. Milling was done at 0.3 nA, 30 kV with slice thickness of 50 nm for 60 s.

Image analysis was inspired by a previous publication [145] and implemented in python using pywt for wavelet decomposition and gaussian blurring in scikit-image for charge compensation. Images were aligned using the SIFT algorithm in FIJI.

6.1.4. Preparation of *D. melanogaster* egg chambers for cryo-lift-out

Bloomington Drosophila Stock Center *D. melanogaster* fly strain (w*; P{w[+ mC]=sqh-mCherry.M}3, FlyBase ID: FBst0059024, BL-59024) expressing an mCherry-tagged

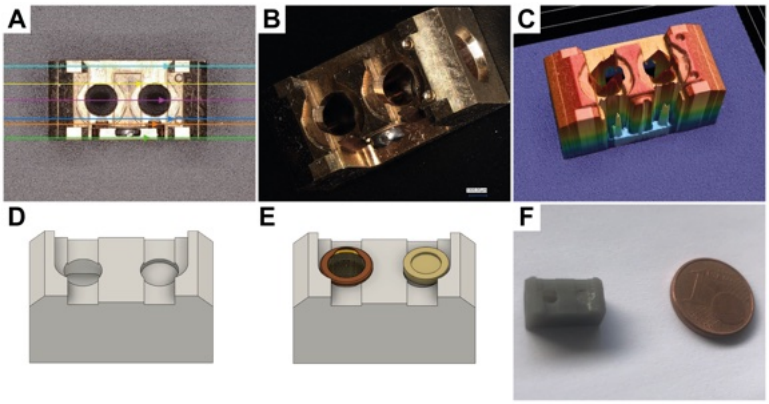

Figure 6.1.1 3D-printed Leica shuttle replica. A-B: Images from measurements of the Leica Cryo-CLEM shuttle. **C:** 3D rendering of the height profile of the Leica shuttle. Data collected by Dr. Frank Siedler (MPI of Biochemistry).**D:** 3D-CAD render of the replica of the Leica shuttle. **E:** 3D-CAD render of sample carriers glued to the shuttle using cryo-glue. **F:** Image of the 3D printed plastic replica. 1-cent coin for scale.

myosin regulator light chain protein named Sqh under the control of the endogenous sqh promotor were obtained and maintained at 22° on standard cornmeal agar. 24 hours prior to dissection of egg chambers, the flies were transferred into fresh vials supplemented with yeast paste. Ovaries were dissected from anesthesized females in S2 cell culture medium with subsequent isolation of ovarioles or single egg chambers. About 5 mid-oogenesis stage egg chambers were used for high-pressure freezing. The dissected egg chambers were high-pressure frozen in gold-cated copper Type A carriers (Engineering office M. Wohlwend) using the HPM010 (Abrafluid) or the EM Ice (Leica Microsystems). The 1.7 μl S2 cell culture medium containing egg chambers were added into the 100 μm cavity of the planchette and 20$\%$ Ficoll (70 kDa) was used for filling the carrier. After freezing, the planchettes were pre-trimmed using a cryo-microtome (EM UC6/FC6, Leica Microsystems) with a 45° trimming knife at 6 ° clearance angle.

The planchettes were glued to custom 3D printed plastic replicas of the Leica shuttle (**Chapter 6.1.1**) using cryo-glue (2:3 ethanol:isopropanol) and cryo-fluorescence light microscopy was done on a Leica TCS SP8 with a Leica EM cryo-CLEM stage, HC PL APO x50 / 0.9 NA dry objective lens and excitation laser strength of 17$\%$ (0.94 mW) at 552 nm and 6.8 $\%$ (0.38 mW) at 488 nm. Detection channels were set up at 650-751 nm and 495-545 nm for mCherry and autofluorescence, respectively. Custom 3D printed replicas were done using a Form2 (Formlabs) 3D printer using GreyProV1 resin at 50 μm slices and postprocessing for 20 minutes in IPA (FormWash) and 15 minutes curing at 80 °C (FormCure). 3D printing was performed by Dr. Frank Siedler, MPI of Biochemistry.

6.1.5. Cryo-lift-out sample preparation

The planchettes and a half-moon grid were transferred in a standard Aquilos 1 (Thermo Fisher Scientific) shuttle into the FIB-SEM instrument for lift-out experiments. Correlation with the acquired fluorescence images was done using 3DCT [138] and trench milling was automated in SerialFIB. The custom pattern file was chosen to create a roughly 20 μm by 20 μm block that could be undercut and lifted from the HPF sample. Lift-out device was a Kleindiek micromanipulator equipped with a cryo-gripper. After transfer and attachment using redeposition with multiple patterns at 0.3 nA, regular cross section, single pass, and a size of 1 μm, the final lamella was prepared with sequentially decreasing currents from 3 nA to 100 pA as for on-grid lamella preparation. The fine milled lamella was transferred to the TEM.

6.1.6. Cryo-ET data acquisition

Cryo-ET data was acquired in SerialEM [87] on a 300 kV Titan Krios G1 (Thermo Fisher Scientific) equipped with a K2 direct electron detector device (Gatan) and a Quantum post-column energy Gatan Imaging Filter (Gatan). A dose-symmetric tilt scheme was used starting at +10 $^\circ$ or -10 $^\circ$ to correct for the lamella pre-tilt depending on the loading orientation. Tilt range was -50° to +70° or -70° to +50°, respectively. 10 frames per second were collected at a magnification of 42.000x resulting in an object pixel size of 3.52 Å. The total dose of the tilt series was kept below 140 $e^-/Å^2$.

6.1.7. Subtomogram averaging of *D. melanogaster* ribosome

The frames of projection images were aligned using motion corrected using the Tomoman pipeline deploying MotionCor2 [47], NovaCTF [57] and CTFFIND4 [54]. Tomogram reconstructions were done in IMOD/etomo [89]. Four times binned move sums were aligned via patch tracking and tomograms were reconstructed with the weighted back projection algorithm. The positions of *Drosophila* ribosomal particles were determined by template matching in STOPGAP on 4x binned tomograms. A down-sampled reference obtained from a previously established structure of the D. melanogaster ribosome (EMD-5591) was used as a reference. A total of 20,284 ribosomal particles were selected from eight different tomograms. These particles were then extracted using a box size of 64 pixels, with a pixel size of 7.04 Å. Subsequent subtomogram alignment and averaging were carried out within the STOPGAP software. The resolution was assessed by Fourier shell cross-correlation of half-maps and determined to be 24.0 Å at the 0.5 FSC threshold and 20.8 Å at the 0.143 FSC threshold.

6.2. Machine Learning of cryo-FIB images

6.2.1. *Chlamydomonas reinhardtii* grid preparation

Cultures of *C. reinhardtii* mat3-4 strain were grown until mid-log phase in TAP media with 40 μmol photons / m^{-2} s -1 and 120 rpm shaking. 200 mesh copper grids with 2/1 silicon oxide film were glow discharged for 30 s. 4 μl of cells were applied on the electron microscopy grids for plunge freezing. Plunging was performed using a Vitrobot Mark 4 system (Thermo Fisher Scientific) at blot force 10, blotting time 10 s. Grids were assembled into AutoGrid cartridges and transferred into the cryo-FIB for image acquisition and lamella preparation.

6.2.2. Systematic screening of grids for training

In order to create the training data needed to produce a U-Net model capable of performing cryo-FIB image segmentation for cells and grid bars, a script for systematic screening of grids using the FIB was developed in SerialFIB. For this, spiral scans were performed. As the sample is generally viewed at a tilt to the FIB source, the image moves out of focus after every vertical movement of the sample stage. Thus, an autofocus function was necessary after every Y moment. Using the spiral scan script, images of 5 entire *C. reinhardtii* grids were collected. The resulting images were manually segmented for subsequent model generation. Images were collected after GIS deposition at a stage working distance of 9.6 mm for 30 seconds at 3 different horizontal field widths, 104 μm, 170 μm and 220 μm. The 104 μm dataset was annotated for subsequent use.

6.2.3. nnUNet model training of cryo-FIB images

For the machine learning model, we harnessed the software nnU-Net (Isensee et al. 2021). We implemented the nnU-Net pipeline according to the nnUNet documentation
(https://github.com/MIC-DKFZ/nnUNet). The cryo-FIB images were converted from 2D tif format to nii format using SimpleITK and nibable. Training and validation split was 80$\%$ to 20 $\%$. Initial models were trained on 45 images and validated on 12 images from the same grid. Subsequent models were trained using five-fold cross-validation. The model was used to predict and curate images to increase the dataset size. This increased the annotated images to a training dataset of 164 images and subsequent validation on 41 images. To evaluate model performance, prediction was run on 13 separate test images.

6.2.4. Lamella site detection from nnU-Net predictions

Cell clusters and grid bars were post-processed based on the nnU-Net prediction. Grid bar orientation was refined using cross-correlation with a mask based on measured grid dimensions. The mask was rotated in 1° steps and projected to the ion beam incidence angle of 11° to create a mask library and determine the most probable grid orientation based on the nnU-Net prediction via cross-correlation. Opencv-python was used for perspective transformation and cross-correlation. Next, cell clusters at the edges of the image and cell clusters with an area smaller than 500 pixels or larger than 1500 pixels were discarded. We then determined milling positions for the remaining cell clusters. Milling positions within a distance of 1 μm of the fitted grid bars were discarded. The remaining milling positions were used to mill the lamella. To assess the performance of the overall pipeline, a human examiner classified cell clusters manually into suitable and unsuitable cell clusters for milling, based on the original FIBSEM images. For each cell cluster, these classifications were compared with the classifications by our pipeline. Matching classifications as suitable cell clusters were counted as true positive, matching classifications as unsuitable cell clusters were counted as true negative and mismatching classifications were respectively counted as false positives and negatives. Based on these values, the metrics dice score, accuracy, precision, sensitivity and specificity were derived by Marina Luchner.

6.2.5. *S. cerevisiae* grid preparation

Yeast cultures were inoculated from overnight cultures and grown in YPD media at 30°C to an OD_{600} of 0.6. 200 mesh copper grids with 2/1 silicon oxide film were glow discharged for 30 s. 4 μl of cells were used for plunge freezing using a Vitrobot Mark 4 system (Thermo Fisher Scientific) at blot force 10, blotting time 10 s. Grids were assembled into AutoGrid cartridges and transferred into the AutoLoader of a Arctis cryo-PFIB (Thermo Fisher Scientific). Grids were inserted into the chamber, screened and milled automatically using the nnU-Net model trained on 45 images of *C. reinhardtii*.

6.2.6. Cryo-ET data acquisition and reconstruction

Resulting *S. cerevisiae* lamellae were transferred within the AutoLoader cassette into a Titan Krios G3i equipped with a Falcon 4i camera and Selectris X energy filter (Thermo Fisher Scientific). Tilt series were recorded at 300 kV using Tomo5 software package version 5.12.0 in EER file format using a dose-symmetric tilt scheme with an angular increment of 2 °, a dose of 2 e^- / ^{2} per tilt and a target defocus of -4 to -6 μm. The tilt range was -70 ° to 50 ° with a starting pre-tilt of -10 °, though the actual

pre-tilt of the lamella calculated from the cryo-PFIB geometry was closer to -20 °. Resulting EER frames were pre-processed with Tomoman version 0.7, rendered into 10 tif frames with an approximate dose per frame of 0.2 e^{-} / ^{2}, motion corrected using MotionCor2 version 1.4.7. Tilt series were aligned, reconstructed, and visualized in IMOD version 4.12.32.

6.3. VIPP1 modeling and *in situ* observation

6.3.1. VIPP1 modeling

The initial model of *syn*VIPP1 was based on a homology model using the Modeler software using the *E. coli* PspA crystal structure (PDB: 4WHE) as a reference and the *syn*VIPP1 sequence (UniProt ID: A0A68MW27). The additional helices of *syn*VIPP1 that are not resolved in the PspA crystal structure (residues 1-25 adn 142-216) were modeled using Rosetta *ab initio* structure prediction implemented into a VMD plugin called ModelMaker. The modeled residues correspond to helices H1, H4/5 and H6. 10.000 structures were predicted and clustered by the k-means algorithm, which gave a continuous model for the *syn*VIPP1 monomer. The monomers were subsequently fitted by molecular dynamics flexible fitting to masked regions for a monomer for each of the layers in the C16 symmetric structure. 2000 minimization steps with harmonic potentials on the C_α atoms were followed by fitting without C_α restraints until the trajectory root mean square deviation (RMSD) stabilized. Timestep was 1 fs, rigid bonds were imposed on the water molecules, Langevin dynamics were used with a damping coefficient of 5 per ps and hydrogens were not coupled to the langevin bath. Simulations were performed at a temperature of 300 K, a gscale of 0.3, and restraints imposed on secondary structure, cispeptides, and chirality to reduce overfitting. The full structure was assembled by applying C16 symmetry to model a single column and a MDFF run was performed on the entire oligomeric structure. 10000 minimization steps with harmonic potentials on the C_α atoms were followed by simulation with released restraints. The resulting structure was refined by PHENIX real space refinement and re-adjusted to the density using MDFF. The structure was subsequently re-symmetrized from a single column extracted from the fitted MDFF run using BioMT within the PDB from a custom python script. Based on these initial models, all additional symmetries (C14,C15,C17,C18) were assembled and refined. Distance plotting was performed using MDAnalysis and ProDy. The nucleotide binding site was predicted using GTPbinder and ATPint web servers. In order to get initial configurations of the nucleotide, an AutoDock4 run was used to evaluate possible binding modes. An ADP model from PDB 5L4G was aligned with the best scoring result and replaced in the final PDB. The nucleotide binding site was then refined using interactive MDFF simulations in VMD. Simulations were done in NAMD2 using CHARMM36 force field parameters. For all other measurements such as mass spec-

trometry experiments, physiological and biochemical analysis of the *Synechocystis* mutants, and nucleotide hydrolysis assays, the reader is referred to [242].

6.3.2. Cryo-FIB milling and cryo-ET data acquistion of *Synechocystis* (Performed with Dr. Wojciech Wietrzynski)

Wildtype, *vipp1-F4E*, and *vipp1-V11E* strains were grown in low light (30 μmol photons m^{-2} s^{-1}) for two days until they reached log phase. The cultures were inoculated to OD_{750} of 0.1 and grown in low light or high light (200 μmol photons m^{-2} s^{-1}) for 24 hours. The cells were subsequently harvested by centrifugation, and plunged into liquid ethane-propane mixture using a Vitrobot Mark 4 (Thermo Fisher Scientific) by applying 4 μl of cell suspension onto 200-mesh R 1/4 SiO_2 gold grids. Grids were assembled into AutoGrid cartridges and loaded into a Aquilos 1 cryo-FIB-SEM instrument (Thermo Fisher Scientfic). Lamella were prepared as described in **Chapter 6.1.2** but all milling steps were performed manually as no automated solutions were available at the time. Cryo-ET data was acquired as described in **Chapter 6.1.6**.

6.3.3. Correlative lamella preparation and cryo-ET of *C. reinhardtii) cells (Performed with Dr. Wojciech Wietrzynski)*

A VIPP1-mCherry expressing *Chlamydomonas reinhardtii* strain was grown as described in **Chapter 6.2.1**. After clipping into AutoGrid cartridges, the grids were transferred into a Leica TCS SP8 confocal microscope (**Chapter 6.1.5**). Excitation was done with a 552 nm laser at 0.6 $\%$ intensity (0.033 mW). Two detection channels were set up: 610-633 nm for the mCherry signal and 710-720 nm to detect autofluorescence. The pinhole was kept at 0.9 Airy units. 10 μm stacks with system optimised z-spacing were acquired using LAS X (Leica). Z-stacks were deconvolved using Huygens (Scientific Volume Imaging). Cryo-FIB lamella sites were chosen based on the fluorescence data correlation using 3DCT and Fiji, correlating fiducial coordinates and other features identifiable in both FIB and FLM imaging. Lamellae were prepared as described before. Cryo-ET data collection based on the overlay of the fluorescence data with the TEM overviews (6500x magnification) was performed as described in **Chapter 6.3.2**. Tomogram reconstructions were done as described in **Chapter 6.1.7**. Tomograms were filtered using tom_deconv (*Synechocystis*) or denoised using Cryo-CARE (*C. reinhardtii*). Segmentations were done with TomoSegMemTV and Amira. Thylakoid membrane measurements were done on 2D slices oriented to yield the cross-section of the thylakoids and line scan profiles were done in FIJI. From these, bilayer thickness and lumen width was measured.

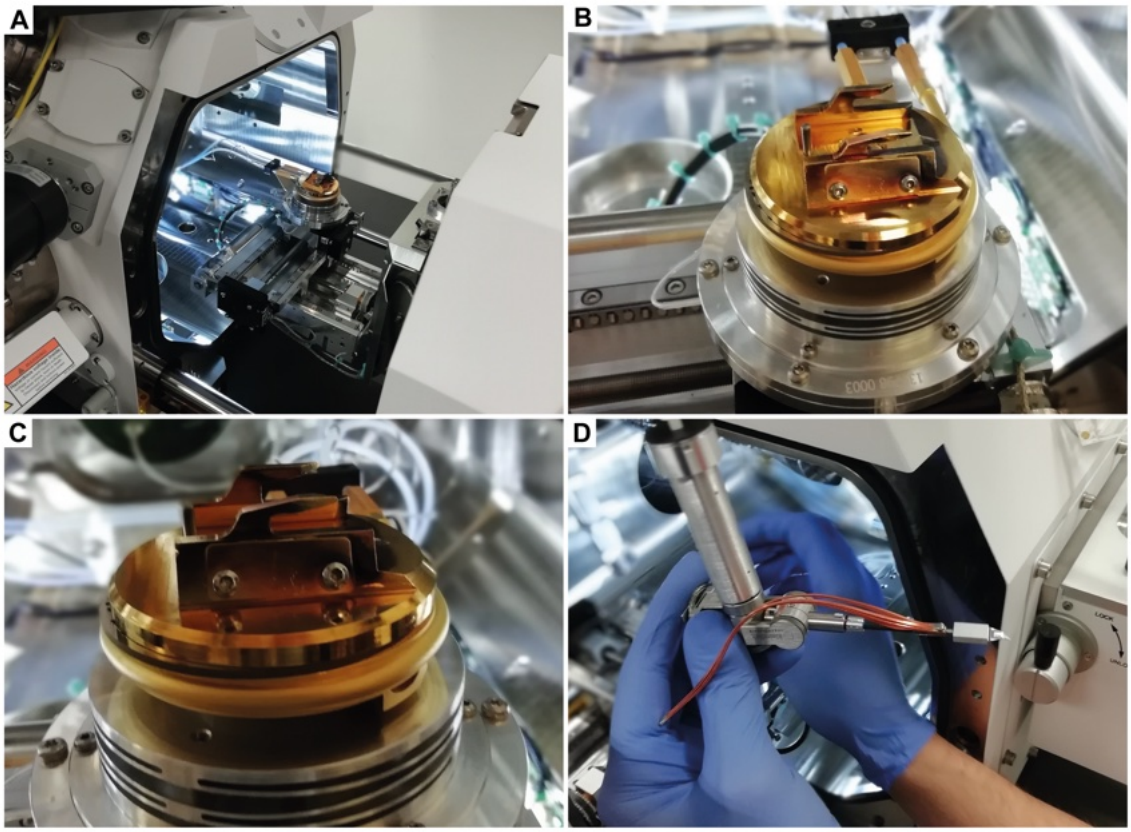

Figure 6.4.1 Adjusting the Aquilos stage to incorporate the Kleindiek cryo-gripper

6.4. Cryo-lift-out without GIS deposition

6.4.1. Hardware implementation of the cryo-gripper on the Aquilos

Due to the change in working distance of the SEM column of 7 mm in the Aquilos cryo-FIB compared to previous installation on the Quanta cryo-FIB of 10 mm, the installation of the Kleindiek cryo-gripper posed a number of problems. The main problem arises from the fact that, when trying to reach the grid positions in the standard Aquilos shuttle, the additional arms holding the lid of the cryo-shuttle open on the stage are blocking the way for the micromanipulator. As the cryo-stage arms are a lot bigger than necessary, we removed some of that material to allow the cryo-gripper to access the positions on the grid (compare **Figure 6.4.1**). While a higher cryo-shuttle may circumvent this problem as well, we aimed at establishing workflows for the standard configurations of the Aquilos and, consequently, the modification of the cryo-stage was chosen.

6.4.2. Lift-Out experiments (with Jakub Kuba)

Drosophila ovary samples were prepared by high-pressure freezing on an EM Ice (Leica Microsystems) and pre-trimming with a diamond knife as described above.

The fly strain used was a LiveAct-GFP line kindly provided by Dr. Anne Ephrussi. The mouse brain was from a wildtype lab mouse and kindly provided by Dr. Jana Nebesarova.

The cryo-gripper experiments were performed on an TFS Aquilos 1 with modified cryo-stage as descirbed above. Cryo-fluorescence light microscopy was performed on an Leica SP8 equipped with a cryo-stage and by gluing the high-pressure freezing planchette to a 3D printed replica of the Leica shuttle design using cryo-glue (2:3 Ethanol to 2-Isopropanol mixture) as described above. High-pressure frozen samples were transferred into the cryo-FIB chamber in a standard Aquilos 45 $^\circ$ pre-tilted shuttle. Trenches to allow the cryo-gripper to access the material were milled at 1 nA to create an approximately 20 μm by 20 μm block. The attachment to the half moon grid after transfer was done using cross-section patterns with the milling direction pointing away from the transferred block. Thinning of the lamellae was done as described in **Chapter 6.1.5**. The needle lift-out was performed with Jakub Kuba in Brno, Thermo Fisher Scientific, on a Aquilos 2 cryo-FIB-SEM instrument equipped with an EasyLift system (Thermo Fisher Scientific). Trenching was performed using regular cross sections at 3 nA, 1 nA and 0.5 nA with sequentially decreasing the current the closer it was to the final volume (8 μm, 5 μm and 3 μ, respectively). The undercut was performed at 0.3 nA. The needle of the EasyLift was brought into contact with the lamella and redeposition milling at 0.3 nA, regular cross section, single pass, with milling direction pointing away from the lift-out needle. Attachment after transfer was done as described in **Chapter 6.1.5**. TEM overviews were aquired on a Titan Krios G3 equipped with a Gatan K2 camera and a GIF energy filter (Gatan) or a Titan Krios G4 equipped with Falcon 4i camera and SelectrisX energy filter (Thermo Fisher Scientific).

6.5. Sequential sections in cryo-lift-out

6.5.1. Sample vitrification (with Dr. Christoph J.O. Kaiser)

C. elegans L1 larvae were high-pressure frozen by Dr. Christoph J.O. Kaiser. Adults of *C. elegans* strains AM140 (allele rmIs132[unc-54p::Q53::YFP]) and NK2476 (allele qy46[ina1::mKate+loxP]) were collected in M9 medium and larvae were obtained by bleaching in 3.75 ml (1M NaOH, 0.3 ml houdhold bleach, 8.25 ml H_2O) and subsequent addition of egg-buffer (118 mM NaCl, 48 mM KCl, 2 mM MgCl2, 25 mM HEPES, pH 7.3). After floating on 60$\%$ sucrose solution, the purified eggs are withdrawn from the surface and hatched in M9 buffer at 20 $^\circ$ for 24 hours. High-pressure freezing was performed on an EM Ice (Leica Microsystems) using a 50 mesh square or 75 mesh hexagonal grid. The larvae were applied to the grid in 20 $\%$ Ficoll 400 in M9 medium and the grid was sandwiched between the flat sides of two Type B HPF

carriers with 6 mm diameter. After high pressure freezing, the grid was retrieved and assembled into an AutoGrid cartridge for further processing. Those were loaded into a Leica TCS SP8 for cryo-light microscopy.

D. melanogaster egg chambers were frozen as described in **Chapter 6.1.4**. Cryo-fluorescence light microscopy was performed as explained in **Chapter 6.1.4**.

6.5.2. Single-sided attachment

The single-sided attachment experiment on *D. melanogaster* egg chambers was done on a Scios cryo-FIB-SEM equipped with an EasyLift system (Thermo Fisher Scientific). Lift-in grids were prepared from 100 square mesh copper grids (Agar Scientific) by milling out two grid bar combs yielding 14 pins for sequential sectioning. The copper block was prepared and attached from the lift-in grid using up to 15 nA for shaping. Attachment was done by bringing the lift-out needle into contact with the copper block and milling at 1 nA, 30 kV, single pass cross section patterns at the interface of needle and copper block with the milling direction pointing away from the needle. Trenching of the *D. melanogaster* egg chamber was performed as described in **Chapter 6.1.4**. For lift-out, the copper block was brought into contact with the volume of vitrified biological material and the same parameters as for copper block attachment were used, with the milling direction pointing away from the biological material. After transfer, the sections are attached from lamella milling orientation (18 $^\circ$ tilt, 0° rotation relative to the loading rotation). Sectioning was performed at 0.3 nA to 0.5 nA with a line pattern, yielding sections of approximately 1 μm to 3 μm thickness. Sections were subsequently thinned to electron transparency as described in **Chapter 6.4.2**.

6.5.3. Double-sided attachment (performed by Oda H. Schioetz and Dr. Christoph J.O. Kaiser)

Double sided attachment experiments of high-pressure frozen *C. elegans* L1 larvae were done on an Aquilos 2 cryo-FIB-SEM system equipped with a EasyLift system (Thermo Fisher Scientific). Trench milling was performed at 3 nA to yield a approximately 20 μm thick ('waffle' freezing thickness), 40 μm wide and approximately 200 μm in length. Rather than a modified grid as in single-sided attachment, a 100/400 rectangular mesh copper grid was used. This allows for attachment of a approximately 40 μm section between the two grid bars, leading to more stable lamellae. The grid needs to be oriented such that the slots within the grid are aligned with the FIB view. Attachment, sectioning and thinning of the lamellae is therein performed as described above (**Chapter 6.5.2**).

6.5.4. TEM data acquistion, tomogram reconstruction, and subtomogram averaging (with Florian Beck)

Tilt series were acquired on a G3 Titan Krios equipped with a Falcon 4i and SelectrisX energy filter (Thermo Fisher Scientific). Tilt series were acquired using Tomo5 software package 5.12.0 (Thermo Fisher Scientifc) in at two magnifications, 42.000x resulting in an object pixel size of 2.95 Å and 64.000x resulting in an object pixel size of 1.89 Å. Total dose was 120 $e^{-}/Å^{2}$ to 132 $e^{-}/Å^{2}$ with a tilt increment of 2 $^{\circ}$ and 3°, respectively, and a target defocus of -1 to -5.5 μm. Data was preprocessed using the Tomoman pipeline employing MotionCorr2, CTFFIND4, or Warp. Tomograms were reconstructed in IMOD version 4.12.32 or AreTomo version 1.3.3. Initial subtomogram averages of ribosomal particles were reconstructied in STOPGAP similar to **Chapter 6.1.7**. The particles were subsequently extracted via Warp to Relion 3.0 to perform classification and refinement. A total of 35,350 particles were obtained and subsequently extracted using a pixel size of 2.98 Å and a box size of 160 pixels. The alignment of subtomograms was conducted using Relion version 3.0 with the application of a spherical mask with a radius of 340 Å. Following this, the particles were imported into M version 1.0.9, where geometric and CTF parameters underwent a sequential refinement process. Corrected subtomograms were then extracted from M and subjected to classification within Relion 3.0. During two rounds of classification, employing a spherical mask with a diameter of 340 Å, a total of 8,256 particles were eliminated from the dataset. After the aforementioned steps, the final classes were combined manually based on their structural similarity, resulting in 5 distinct classes with particle counts of 2.175, 20.638, 877, 1.119, and 2.285 particles, with the class containing 877 particles being excluded from further analysis.

6.6. Correlative approaches for targeting in cryo-lift-out

6.6.1. LiftOut

LiftOut was performed as described in **Chapter 6.4.2** but with a Kleindiek manipulator with a cryo-gripper or tungsten needle attached at the tip.

6.6.2. Volume Imaging

Volume imaging on the lift-out volume's surface was performed at 3 kV, 13 pA, 200 ns dwell time, line integration 64, pixel size of 7.81 nm, 3072x2188 image dimensions. Milling was done at 30 kV, 0.5 nA for 60 seconds using regular cross section patterns at a pattern thickness of 100 nm and a milling step size for volume imaging of 100 nm. Data was collected for initial testing via manual acquisition. Once acquisition

parameters were established, the cryo-FIB-SEM volume imaging was automated in SerialFIB.

6.6.3. In-chamber fluorescence microscopy

In-chamber fluorescence microscopy was done on a Scios cryo-FIB-SEM instrument (Thermo Fisher Scientific) equipped with a METEOR integrated light microscope (Delmic) in the GFP and reflection channel at a power of 73.6 mW, 310 ms exposure, excitation at 485 nm and emission at 525 nm. Reflection was collected at an empty filter wheel position with excitation at 485 nm, power of 2 mW and exposure time of 100 ms.

6.6.4. Cryo-ET data acquisition

Positions were chosen based on the correlation of the TEM overview with the fluorescence stacks or previous SEM images. Data was collected and processed as described in **Chapter 6.5.4** at a magnification of 42.000x resulting in a object pixel size of 2.95 Å.

6.7. *In situ* study of the transposable element *copia*

6.7.1. Fly husbandry and used fly lines (with Dr. Bernhard Hampoelz)

Used fly lines:

- w*; P{w[+ mC]=sqh-mCherry.M}3 (FlyBase ID: FBst0059024) (BL-59024)
- w* P{UAS-Sec31.RFP}13.5; snaSco/CyO, P{ftz-lacB}E3 (FlyBase ID: FBst0086533)
- emGFP::nup358 PBac{y[+mDint2] = vas-Cas9}VK00027 [269]
- ;tj-Gal4/CyO;; [281] (gift of Dr. Anne Ephrussi)
- w* P{UASp-Sec13::EosFP}/ CyO ; (generated by Dr. JM Philippe and Dr. Bernhard Hampoelz, provided by BH)
- w*; P{GFP-Nup107.K}9.1 (BL-35514)
- w*; P{w+, sqhp>LifeAct::mNeonGreen}; MKRS/TM6. [282]

Flies were maintained at 22°C on standard cornmeal agar. Flies from stocks or crosses were transferred into a fresh vial supplemented with yeast paste 24 h prior to dissection of egg chambers for experiments.

6.7.2. Bioinformatic analysis of scRNA-seq data from *D. melanogaster* ovaries (performed with Dr. Assa Yeroslaviz)

The standard analysis workflow discards features such as transposable elements due to their repetitive nature. Even though there are a few other tools for scRNA-Seq, soloTE outperforms such tools both in its computational resources, but the main advantage of this tool is keeping the locus-specific position of the identified TEs. Raw data files were obtained from a public data set (SRX7814226, GSE146040) and aligned using the STAR aligner (STARsolo) against the *D. melanogaster* genome (Build dm6).

soloTE takes two files as input. The first one, a RepeatMasker file is converted into bed format using an internal script. The bed file contains in its fourth column the location of the TE as well as its class and family information. The second file is the output of the STARsolo run in bam format, containing the CB and GN tags. Further important for a successful run is the possibility to distinguish uniquely and multi-mapped reads (those reads must not be discarded). soloTE collect reads, not mapped to genes (those were discarded) and assessed their overlap to TE elements using bedtools. TE expression is than summarized on the locus level (similar to gene expression intensities).

The resulted folder containing the expression matrix containing the gene- as well as the TE-expression intensities was analyzed using the R package Seurat. First the expression matrix was filtered removing low-quality cells using the default analysis pipeline. Data was normalized and scaled to prevent highly-expressed genes from dominating the results. Dimensionality reduction resulting in a PCA. A KNN-Graph was constructed based on the Euclidean distances in PCA space to identify the clusters of the cells. Marker analysis was carried out using the FindAllMarkers command keeping only the results with logFC$\geq$0.25 and a p-value$\leq$0.01.

6.7.3. Plastic tomography (with Dr. Paolo Ronchi)

Drosophila egg chambers were dissected from ovaries in Schneider's medium and subsequently high-pressure frozen (HPM010, AbraFluid) using the Schneider's medium supplemented with 20% Ficoll (70kDa) as a cryoprotectant. Following high-pressure freezing, the samples underwent freeze-substitution (EM-AFS2 - Leica Microsystems) with 0.1% Uranyl Acetate (UA) in acetone at -90°C for 48 hours. Then, the temperature was increased to -45°C at a rate of 3.5°C per hour, followed by a further incubation for 5 hours. After rinsing in acetone, infiltration with Lowicryl HM20 resin was performed with the temperature rising to -25°C. UV light for 48 hours at -25°C and an additional 9 hours with a gradual temperature increase to 20°C (5°C per

hour) polymerized the Lowicryl. Thick sections (300nm) were cut from the polymerized resin block using a FC7/UC7 microtome (Leica Microsystems, Vienna, Austria) and placed on carbon-coated mesh grids. Subsequent to post-staining, tilt series of the designated areas were obtained using a TECNAI F30 TEM (FEI, Thermo Fisher Scientific, Eindhoven, The Netherlands), and tomograms were reconstructed using the IMOD software package [89].

6.7.4. smFISH of egg chambers (performed by Dr. Kirsten Senti)

Single molecule fluorescence *in situ* hybridization probes (smFISH) were prepared and experiments performed as described previously [283, 284]. SmFISH experiments were done by Dr. Kirsten Senti (Institute of Molecular Biotechnology of the Austrian Academy of Sciences, Vienna, Austria). Probe sets were designed on the LGC Stellaris website. The full length copia Open Reading Frame (ORF) was chosen due to its more homogenous GC content. 20 nucleotide long, antisense oligo probes were designed to be perfectly complementary for copia consensus sequence in respect to the transcribed strand with zero mismatches. Mapping of all initial copia probes were bioinformatically analyzed against all other TE consensus sequences and probes that detected any other TE with less than 2 mismatches were omitted from the pool. Also, probes with less than 35$\%$ GC content were removed. The total number of oligo probes were restricted to 48, typically chosen within a stretch of 1.5 to 3kb and CAL Fluor Red 590-labeled probe sets were ordered from Stellaris. Oligos were dissolved in 200 μl of TE buffer (10 mM Tris, 1 mM EDTA, pH 8.0). The stock concentration should be 25 μM (100x). Dissect the ovaries in PBS on ice, minimizing disruption. Ovaries were washed two times with cold PBS. After removal of PBS, 500ul of 4$\%$ PFA with 0.3$\%$ TX100 was added and ovaries were pipetted up and down approximately 10 times using a 1000μl low retention pipette tip to dissociate ovaries into ovarioles (to later allowing for more even penetration of probes into all the tissue). After that, further 500 μl of fixative were added and fixation was allowed to continue for 20 minutes at room temperature. Ovaries were then washed three times for 10 minutes with PBS with 0.3$\%$ TX100 at room temperature. The ovaries were incubated in 70$\%$ EtOH at 4 °C for at least four hours. 0.5 μl of probe stock were mixed with 50 μl RNA FISH hybridization buffer (10 w$\%$ Dextran Sulfate, 1 ml saline-sodium citrate (SSC) 20x (3 M sodium chloride and 300 mM trisodium citrate (adjusted to pH 7.0 with HCl)), 1 ml Formamide (deionized), 8 ml H2O). Ovaries were equilibrated with RNA FISH wash buffer for 5 minutes. Remove excess buffer and add probe hybridization solution, ensuring thorough mixing. Hybridization was done at 37 °C for a minimum of 6 hours, preferably overnight in 200μl PCR tubes with end over end rotation. After hybridization ovaries were rinsed two times with RNA FISH wash buffer at room temperature. Ovaries were then washed twice for 30 minutes with RNA FISH wash buffer at 37°C. Ovaries were then counterstained with DAPI

(1:10,000 in 2xSSC) at room temperature for 5 minutes, followed by three ten minutes washes with 2xSSC. After complete removal of 2xSSC, 40μl of ProLong Gold or ProLong Diamond was added. Ovaries were then carefully taken up into a cut tip 100 μl pipette tip, added on a glass slide and carefully evenly distributed using a 10 μl tip, and covered with a 18x18mm coverslip. The mounting medium was allowed to harden for one to several days in the dark at room temperature. Later storage was done in the dark at 4 °C.

6.7.5. Immunofluorescence staining of egg chambers

Prior to dissection, flies were transferred to fresh cornmeal agar vials supplemented with yeast paste. Ovaries were dissected from flies in PBS and transferred to a 1.5 ml tube containing 100 μl 0.05 $\%$ TX-100 in PBS. The ovaries sediment and the supernatant is removed. 500 μl of 4$\%$ paraform aldehyde (PFA)s in PBS were added and incubated for 30 minutes at room temperature on a rotating wheel. The PFA solution was discarded and 1 ml 1$\%$ Triton is added. The ovaries were subsequently incubated at room temperature for 1 hour. Subsequently, the supernatant was removed and the ovaries are blocked with blocking solution, PBS supplemented with 10 $\%$ native goat serum and 0.1 $\%$ TX-100 and incubated for 1 hour on the rotating wheel. The ovaries are subsequently transfered to PCR tubes with at least 5 ovaries per tube and 200 μl of primary antibody at a 1:2000 dilution in blocking solution was added. The primary antibody was incubated on the wheel over night at 4°C. Control experiments were blocking solution without primary antibody. After overnight incubation, the primary antibody was taken off and the ovaries were rinsed three times with 0.1$\%$ TX-100 in PBS and subsequently washed using 0.1$\%$ TX-100 in PBS with incubation on the wheel for 10 minutes at room temperature. The rinse and wash process was repeated three times. Then, 200 μl of secondary antibody at 1:500 dilution in blocking solution was added and incubated for 2 hours on the rotating wheel at room temperature. The secondary antibody was removed, and the rinse and wash steps in 0.1$\%$ TX-100 in PBS were repeated three times. The ovaries were transferred to a glass slide containing a drop of mounting medium. The ovarioles were then separated to yield isolated egg chambers and covered with cover glasses. The final preparation was stored overnight in the dark. Optionally, nail polish was applied around the cover glasses afterwards for longer lifetime of the sample.

6.7.6. Follicle cell isolation for cryo-CLEM

The UAS-Gal4 system (Brand and Perrimon) was used for tissue specific expression of a fluorescently labelled target protein, Sec13. To generate females expressing Sec13::EosFP in follicle cells, w* P$\{$UAS-Sec13::EosFP$\}$/ CyO ; flies (provided by Dr.

Bernhard Hampoelz) were crossed to ;tj-gal4/CyO;; [281] flies, a follicle cell specific Gal-4 driver lines. Adult female F1 progeny carrying both transgenes were scored for subsequent experiments.

For follicle cell isolation, ovaries were dissected in Schneider's medium supplemented with 10% fetal bovine serum, 50 units / ml penicillin, 50 mg/ml streptomycin, 0.25 mg/ml fungizone and 0.4 μM insulin. 10-15 ovaries were dissected into fresh 2 ml Eppendorf tubes and subsequently washed three times with phosphate buffered saline (PBS). 0.137 M NaCl, 0.0027 M KCl, 0.01 Na_2HPO_4 M, 0.0018 M KH_2PO_4). The digestion of the tissue was done in 0.5 % Trypsin in PBS. First, the oocytes were sedimented and the supernatant was removed. Subsequently, 0.7 ml 0.5 % Trypsin in PBS was added to the tube and incubated for 15 minutes at room temperature in a shaker at 400 rpm. Then, the supernatant was filtered through a cell strainer with mesh size 40 μm. 0.7 ml of Schneider's S2 medium was added through the cell strainer and the 1.4 ml were transferred from a falcon tube to a fresh 1.5 ml eppendorf tube. The filtrate was centrifuged for 7 minutes at 5000 rcf, washed with fresh 1.4 ml S2 medium and centrifuged again for 7 minutes at 5000 rcf. The pellet contained the obtained cells. The remaining tissue was digested again for 15 minutes with fresh 0.7 ml of 0.5% Trypsin in PBS. This process was repeated 2 times. The final pellet was resuspended in 20 μl fresh S2 medium and subsequently used for plunge freezing.

Plunge freezing of cells was performed on R2/1 SiO_2 copper 200 mesh grids (Quantifoil) glow discharged for 30 seconds. 4 μl of cell suspension were applied and plunging using a Vitrobot Mark 4 system (Thermo Fisher Scientific) at blot force 10, blotting time 10 s with blotting paper brought into contact with the grid on the backside only and teflon sheets on both sides.

6.7.7. On-grid (correlative) FIB milling

Plunge frozen grids were assembled into AutoGrid cartridges and subjected to cryo-FLM imaging on a Leica SP8 equipped with a cryo-stage, a 50x objective with an NA of 0.9, and two HyD hybrid detectors. An overview was recorded using transmission light as well as fluorescence and reflection channels. Transmission channel gain was 560 using a PMT. Images were collected at an excitation wavelength of 552 nm, detection between 582 nm and 652 nm at unidirectional scan speed of 400, a pinhole size of 1, and a zoom of 2.

Grids were subsequently loaded into a Aquilos 1 cryo-FIB instrument (Thermo Fisher Scientific) and lamella were prepared. Lamella were prepared as described previous at a stage tilt of 18 $^\circ$ corresponding to a pre-tilt angle of 11°.

6.7.8. Lift-out experiments

Lift-Out experiments were performed as described in **Chapter 6.1.5** using a Kleindiek manipulator with either a cryo-gripper at the tip or a needle at the tip. For the needle approach, an identical methodology as described in **Chapter 6.4.2** was used, with the only difference being that larger blocks were extracted by redeposition milling compared to the described coarse lamella lift-out. After lift-out transfer, the coarse milling and polishing of the lamellae were performed using a correlative approach with SEM data acquisition to target the follicle cell nuclear envelope as described in **Chapter 6.6**. Approximately 4 μm of volume imaging was performed prior to lamella preparation at a section thickness of 100 nm and SEM imaging at 3 kV, 13 pA, 50 line integration at 200 ns dwell time, pixel width of 6.84 nm, and an image dimension of 3072x2188 pixels. Images were aquired with the ET detector in Standard mode or with optional addition of T1 and T2 detector in OptiPlan mode. Milling for volume imaging was performed at 30 kV 0.5 nA using regular cross-sections. Once the feature of interest, here the nuclear envelope, was visible in the SEM image, further imaging and milling was stopped, approximately 200 nm were taken from the top and the rest of the lamella preparation was done from the bottom with sequentially decreasing milling currents of 0.5 nA to 3 μm thickness, 0.3 nA to 1 μm, and 0.1 nA to 500 nm. Final polishing was done at 50 pA until the contrast fainted at 3 kV 13 pA SEM image. Usually, this yields a lamella below 200 nm that may be transferred to the TEM.

6.7.9. Cryo-electron tomography data acquisition and reconstruction

Cryo-ET data was acquired on a Titan Krios G3i equipped with a Falcon 4i and Selectris X energy filter. A dose-symmetric scheme was used with a 3° increment for on-grid lamellae and a 2° increment for lift-out lamellae. Total dose in both cases was 120 $e^{-}/^{2}$. Tilt range was from -50° to +70° or -70° to +50° depending on the loading direction with a pre-tilt of +10° and -10°, respectively. Tomograms were recorded at a magnification of 42.000x resulting in a pixel size of 2.95 Å.

Data was pre-processed using the Tomoman version 0.7 pipeline. EER files were rendered as frames aiming at 0.2 e/Å^2 dose per frame and motion-corrected using the MotionCor2 version 1.4.7. The CTF was estimated with CTFFIND4 version 4.14. Bad tilts that were e.g. obstructed by ice particles, were removed using the dedicated Tomoman scripts. Dose weighting was performed in either Tomoman or Warp version 1.0.9. Tomograms for initial subtomogram averaging were reconstructed using AreTomo version 1.3.3. Tomograms for visualization were reconstructed using patch tracking in IMOD version 4.12.32 at pixel size of 11.8 Å using patches of 200x200 and a fractional overlap of 0.45 in X and Y. Membrane segmentation was performed

using TomoSegMemTV and cleaned manually in Amira.

6.7.10. Subtomogram averaging of the nuclear pore complex

The nuclear pore complex subtomogram averaging was performed as described in [264]. In brief, particles were picked manually in IMOD using custom scripts developed by Dr. Beata Turonova (MPI of Biophysics, Frankfurt, Germany). Subtomogram averaging was performed in STOPGAP v0.7 and an in-house subtomogram averaging code at MPI of Biophysics, novaSTA. Manually picked particles were aligned at pixel size 23.6 Å (bin8) in a box of 72^3 voxels with C8 symmetry applied. The alignment was refined at 11.8Å (bin4). As the particle number was limited, the entire pores were averaged with applied symmetry and not split into asymmetric subunits.

6.7.11. Subtomogram averaging of ribosomes

Subtomogram averaging of ribosomes was performed as described in **Chapter 6.1.7**. In brief, template matching was performed with the subtomogram average from the previous dataset resampled to the bin8 pixel size of 23.6 Å. Particles were extracted and aligned in STOPGAP v0.7 as described above and backmapped to the tomogram for visualization in ArtiaX version 0.1.

6.7.12. Subtomogram averaging of *copia* capsid

Copia capsid positions were detected at a pixel size of 23.6 Å via template matching with a hollow sphere with inner radius of 8 pixels and out radius of 12 pixels in a 32^3 voxel box size and a spherical mask with radius of 14 pixels. As the reference is symmetric, only a single angle was matched. A lamella mask was created in IMOD to prevent matching outside the lamella region. The particle positions were extracted from the score map with a threshold adjusted per tomogram to avoid false positives, generally with a cross correlation score of around 0.23. The Euler angles of the extracted particles were randomized to prevent alignment to the missing wedge. The particles were first aligned for 10 iterations with an angular increment for cone-search of 5 and 12 iterations and a in-plane search increment of 5 and 12 iterations. Icosahedral symmetry was applied.

The data was then re-processed using Warp version 1.0.9 and the particle positions from STOPGAP template matching were used to extract the capsid particles. Re-alignment of the particles in Relion version 3.0 and classified using a spherical mask of 600 Å in diameter. This reconstructing yielded an average at a resolution of 7.8 Å

from around 30% of the particles that showed icosahedral symmetry. Other particles showed defects in their assembly that are currently still investigated.

6.7.13. Model building of the *copia* pentameric and hexameric structures

Based on the 7.8 Å reconstruction of the *copia* capsid, models for the *copia* capsid were created starting off with the pseudo C5 and C6 symmetric parts of the structure. Five and six copies of the N-terminal 270 residues of the *copia* Gag protein were predicted using alphafold-multimer version 2.2.0 and rigid body fitted into the electron microscopy map. While the structure of six monomers fitted well into the density, the five fold symmetric map showed a discrepancy between the prediction and the reconstructed map. The C-terminal domain needed to shift slightly towards the center of the capsid in order to make the secondary structure elements of prediction fit the cryoEM map. The structures were fitted in ISOLDE version 1.5 [76] within ChimeraX [285] version 1.5. Simulations were run at 100 K using the AMBER ff14sb force field [286]. The solvent is treated using GB-Neck2 implicit solvent [287]. Additionally, grid-based protein backbone corrections are used [288]. The entire capsid structure was assembled from these subunits using BioMT matrices for icosahedral symmetry.

7. Acronyms

ART	Algebraic reconstruction techniques
2D	Two-dimensional
3D	Three-dimensional
3DCT	Three-dimensional correlation toolbox
ADP	Adenosine diphosphate
AFM	Atom force microscopy
API	Application (or advanced) programming interface
ATP	Adenosine triphosphate
CCMV	Cowpea chlorotic mottle virus
CLAHE	Contrast limited adaptive histogram equalization
CLEM	Correlative light and electron microscopy
CPU	Central processing unit
cryo-EM	Cryo-Electron microscopy
cryo-ET	Cryo-electron tomography
CTF	Contrast transfer function
CUDA	Compute Unified Device Architecture
CVD	Chemical vapour deposition
DNA	Deoxyribonucleic acid
ECR	Electron cyclotron resonance

EER	Electron event representation
EFTEM	Energy-filtered transmission electron microscopy
ENV	Envelope gene
ERES	Endoplasmic reticulum exit sites
ERV	Endogenous retrovirus
ESI-MS	Electron spray ionization mass spectrometry
ETD	Everhart-Thornley detector
FIB	Focused ion beam
FLM	Fluorescence light microscopy
FSC	Fourier shell correlation
Gal4	Yeast transcription activator protein Gal4
GFIS	Gas-field ion source
GFP	Green fluorescent protein
GIP	Gag-int-pol
GIS	Gas-injection system
GPU	Graphical processing unit
GTP	Guanosine triphosphate
GUI	Graphical user interface
HIV	Human immunodeficiency virus
HPF	High-pressure freezing
ICP	inductively coupled plasma
INM	Inner nuclear membrane
KNN	K-nearest neighbors

LINE	Long intersperesed nuclear element
LMIS	Liiquid metal ion source
LTR	Long terminal repeats
MD	Molecular dynamics
MDFF	Molecular dynamics flexible fitting
MIP	Maximum intensity projection
MPI	Max-Planck-Instititute
NADPH	Nicotinamide adenine dinucleotide phosphate
NE	Nuclear envelope
NPC	Nuclear pore complex
ONM	Outer nuclear membrane
PALM	Photoactivated localization microscopy
PBS	Phosphate-buffered saline
PCA	Principle component analysis
PCC	Pasteur Culture Collection of cyanobacteria
PCR	Polymerase chain reaction
PDB	Protein database
PFA	Para-formaldehyde
PFIB	Plasma focused ion beam
piRNA	PIWI(P-element induced Wimpy)-interacting ribonucleic acid
PIWI	P-element induced Wimpy testis
PLE	Penelope-like element
PMT	Photomultiplier

RESOLFT	Reversible saturable optical fluorescence transitions
RMSD	Root mean square deviation
RNA	Ribonucleic acid
RPIP-HPLC	Reverse-phase ion pair high-performance liquid chromatography
SART	Simultaneous algebraic reconstruction technique
SEM	Scanning electron microscopy
SIFT	Scale-invariant feature transform
SIMS	Secondary ion mass spectrometry
SINE	Short intersperesed nuclear element
siRNA	Small interfering ribonucleic acid
smFISH	Single molecule fluorescence *in situ* hybridization
SPA	Single particle analysis
STED	Stimulated emission depletion
TE	Transposable element
TEM	Transmission electron microscopy
TFS	Thermo Fisher Scientific
TIC	Translocon on the inner chloroplast membrane
TOC	Translocon on the outer chloroplast membrane
TOF	Time-of-flight
UAS	Upstream activating sequence
vEM	Volume electron microscopy
VMD	Visual molecular dynamics
VLP	Viral-like particle

WBP	Weighted backprojection

9. Acknowledgement

Quite honestly, where to start acknowledging all the amazing people that helped make this journey happen and made it so fun along the way? And what a journey it has been.

I want to express my deepest gratitude to:

First and foremost, **Prof. Dr. Jürgen Plitzko** and **Prof. Dr. Martin Beck** for believing in me and giving me the opportunity and the freedom to work on such an exciting project in some of the most exciting environments for *in situ* structural biology out there: MPI of Biochemistry, MPI of Biophysics, and EMBL Heidelberg.
Jürgen a.k.a. **JP**, being one of the most supportive scientists I had the pleasure of meeting, has truly been a mentor and continuous advocate throughout my time in Martinsried. I will keep fond memories of the times that he built me up when I found myself in a deep dive of doubt but also kept me grounded whenever I was getting ahead of myself. **Thank you** for immense positive impact you have had on my personal and professional trajectory.
Martin truly made me start to think about problems from a biologist's perspective. I have learnt enormously simply by observing how he approaches science and it truly inspired me to strive to become a structural cell biologist. I admire his leadership style and the atmosphere he manages to spread in his lab by not only being a great scientist but simply by being a great person to interact with. **Thank you** for letting me be a part of it.
Prof. Dr. Wolfgang Baumeister for hosting me during my Master's thesis and supervising my PhD. Thank you for letting me part of the unmatchable creative environment you uphold for so long.
Dr. John Briggs for teaching me about virus structure, symmetries, and retrotransposons. He was instrumental in helping me navigate the jungle of endogenous retroviruses and transposable elements.
Dr. Julia Mahamid for the mentorship and teaching me a lot on writing throughout uncountable hours of Zoom sessions. You have been an enormous influence on me and I greatly appreciate your leadership and all the things you have taught me.
Dr. Ben Engel, who showed me early on what it takes to create a biological story and embrace the diverse angles on scientific problems that come with a collaborative group of scientists.
Dr. Philipp Erdmann for all the great fun we had at the FIB, the many scientific discussions and mentorship. He has put enormous efforts into maintaining the microscopes at the institute and was, thus, instrumental to many of the works coming

out of the department during his time in Martinsried.
Dr. Bernhard Hampoelz for teaching me everything I know on working with *D. melanogaster* as a model organism, for invaluable feedback on this thesis, and for enduring through my many questions on everything regarding flies.
Dr. Kirsten Senti, **Dr. Julius Brennecke**, and **Dr. Maya Shinan Voicheck** for opening my eyes to the fascinating world of PIWI and endogenous retroviruses in *Drosophila* over many great discussions.
Dr. Will Wan for the image processing beer sessions in the rain.
Dr. Paolo Ronchi and **Dr. Yannick Schwab** at the EMBL EM core facility for the tomography data collection of plastic sectioned egg chambers.
All the great academic collaborators that i had the pleasure of working with on a variety of projects: **Dr. Maud Dumoux**, **Dr. Sebastian Tacke**, **Dr. Michael Grange**,**Dr. Tom Glen**, **Dr. Zhexin Wang**, **Dr. Luca Zinzula**, **Dr. Eri Sakata**, **Dr. Till Rudack**, **Dr. Mike Strauss**, **Dr. Jan Schuller**, **Dr. Michael Schroda**, **Dr. Jörg Nickelson**, **Dr. Wataru Sakamoto**, **Dr. Karin Gries**, **Dr. Steffen Heinz**, **Dr. Liwen Jiang**, **Dr. Florian Wilfling**, **Dr. Rado Danev**, **Dr. Jim Naismith**, **Jake Smith**, **Dr. Anna Steyer**, **Dr. Simone Mattei**, **Dr. Gregor Weiss**, **Dr. Martin Pilhofer**, **Dr. Wioleta Dudka**, **Dr. Michelle Darrow**, **Dr. Caitie McCafferty**, **Dr. Wanda Kukulski**, **Dr. Edoardo d'Imprima Dr. Lucy Collinson**, **Dr. Rommie Amaro**, and everyone else that crossed my path along the way!
Our collaborators at various companies: **Jakub Kuba**, **Dr. John Mitchells**, **Dr. Abhay Kotecha**, **Dr. Alex Rigort**, **Dr. Veronika Vrbroska**, **Dr. Rado Spurny**, **Dr. Andreas Schertel**, **Dr. Endre Majorovits**, **Samuel Zachej**, **Martina Zanova**, **Jakub Javurek**, and all the other people that help push the boundaries of cryo-ET.
Especially the SerialFIB crew, **Dr. Sara Götz** & **Dr. Herman Fung**, and the Serial Lift-Out squad, **Oda Schioetz** & **Dr. Christoph Kaiser**, for the great environment that we created together to pull through with developments. Technology development can be extremely frustrating, but it never gets you down as much if you are surrounded by wonderful people that lift you up. Furthermore, **Florian Beck** for all the help with computation and image processing. Words can't express how much I appreciate you guys. Thank you!
Everyone in the Department. I feel like I have spent multiple PhD times in Martinsried (and no, it hasn't been THAT long), but this is most likely the result of meeting so many wonderful people. I got to see the last years of the Baumeister Department, which were some of the most fun times of my life. So thank you to **Dr. Javier Collado**, **Dr. Christos Papantoniou**, **Dr. Wojciech Wietrzynski**, **Dr. Manon Demulder**, **Dr. Ricardo Righetto**, **Dr. Tat Cheng**, **Dr. Tilak Gupta**, **Dr. Hugo van den Hoek**, and **Dr. Vicky Trinkaus** (who are now deeply missed in Martinsried!) and **Dr. Matthias Pöge**, **Dr. Markus Eisele**, **Caro Klose**, **Cristina Capitanio**, **Anna Bieber**, **Sagar Khavnekar**, **Chuan Liu**, **Jonathan Schneider**, **Dr. Daniel Bollschweiler**, **Dr. Tillman**

Schäfer, **Jonathan Wagner**, **Dr. Stefan Bohn**, **Dr. Marius Boicu**, **Robin Mohr** and **Inga Wolf**. You guys made the time at MPI truly memorable. Though the reconstructions weren't a particularly timid time in the Department, seeing the transition into the Briggs Department and Plitzko group and experiencing what John and Jürgen built up together was a unique experience that I wouldn't miss for the world. It led to meeting new colleagues and making new friends: **Joe Brenner**, **Dr. David Klebl**, **Davide Torre**, **Elena Shmakova**, **Dr. Grigory Tagiltsev**, **Dr. Zunlong Ke**, **Dr. Yoko Fujiharu**, **Dr. Hui Guo**, **Dr. Rebecca Taylor**, **Dustin Morado**, **Dr. Dominik Hrebik**, **Hannah Kugler**, **Dr. Raffaella Villa**, and **Dr. Iosune Ibiricu**.
The Frankfurt crowd. While it wasn't too often that I showed up, I was always welcomed with open arms by **Dr. Christian Zimmerli**, **Dr. Matteo Allegretti**, **Dr. Erica Margiotta**, **Jenny Sachweh**, **Dr. Patrick Hoffmann**, **Dr. Iskander Khusainov**, **Carmen Ortiz-Cantos**, **Dr. Beata Turonova**, **Dr. Maarten Tuijtel**, **Anja Becker**, **Eva Kaindl**, **Dr. Reiya Taniguchi**, **Dr. Max Seidel**, and **Dr. Agnieszka Obarska-Kosinska**.
The amazing students I had the privilege of working with. Thank you **Annika Elimelech**, **Sarah Brajkovic**, **Benedikt Müller**, **Marina Luchner**, **Peter Takacs**, **Adrian Müller**, and **Michael Rheinberger**. Furthermore, the iGEM Team 2017 and 2018 as being both student and advisor in the competition were the best and most fun preparation for this PhD journey I could ask for.

Chez Stratmann for always being so inviting.

The Brussels crew, **Aaron**, **Ben**, **Lara**, **Alex**, **Leif**, **Sebastian**, and **Julia** (yeah, you count now), it is crazy that it has been more than 1.5 decades already.
The Biochem nerds, especially **Thomas**, **Tuan**, **Sebi**, **Max**, and **Marie-Lena**.

My parents, **Eva-Maria** and **Michael**, and family, **Patrick**, **Gerda**, **Hermann**, who have always supported me in everything I do. I would not have made it here without you.

Finally, I want to thank **Liya** for the tremendous support throughout my PhD journey. Thank you for coping with my (sometimes almost obsessive) focus, for being the amazing person that you are and for always being there for me in any and every life situation. **Thank you!**

Bibliography

[1] Vinicius Duval da Silva. *Van Leeuwenhoek, Antonie (1632–1723)*, pages 505–510. Springer International Publishing, Cham, 2017. ISBN 978-3-319-41995-4. doi: 10.1007/978-3-319-41995-4_562. URL https://doi.org/10.1007/978-3-319-41995-4_562.

[2] M.J. Schleiden, T. Schwann, M. Schultze, and I. Jahn. *Klassische Schriften zur Zellenlehre*. Akademische Verlagsgesellschaft Geest Portig K.-G., 1987. ISBN 9783321000348. URL https://books.google.de/books?id=LkG4AAAAIAAJ.

[3] Max Knoll and Ernst Ruska. Das elektronenmikroskop. *Zeitschrift für physik*, 78:318–339, 1932. ISSN 0044-3328.

[4] B Von Borries, E Ruska, and H Ruska. Bakterien und virus in Übermikroskopischer aufnahme: Mit einer einführung in die technik des Übermikroskops. *Klinische Wochenschrift*, 17:921–925, 1938. ISSN 0023-2173.

[5] J. C. Kendrew, G. Bodo, H. M. Dintzis, R. G. Parrish, H. Wyckoff, and D. C. Phillips. A three-dimensional model of the myoglobin molecule obtained by x-ray analysis. *Nature*, 181(4610):662–666, 1958. ISSN 1476-4687. doi: 10.1038/181662a0. URL https://doi.org/10.1038/181662a0.

[6] Werner Kühlbrandt. The resolution revolution. *Science*, 343(6178):1443–1444, 2014. doi: doi:10.1126/science.1251652. URL https://www.science.org/doi/abs/10.1126/science.1251652.

[7] Friedrich Förster, Bong-Gyoon Han, and Martin Beck. *Chapter Eleven - Visual Proteomics*, volume 483, pages 215–243. Academic Press, 2010. ISBN 0076-6879. doi: https://doi.org/10.1016/S0076-6879(10)83011-3. URL https://www.sciencedirect.com/science/article/pii/S0076687910830113.

[8] Ohad Medalia, Igor Weber, Achilleas S. Frangakis, Daniela Nicastro, Günther Gerisch, and Wolfgang Baumeister. Macromolecular architecture in eukaryotic cells visualized by cryoelectron tomography. *Science*, 298(5596):1209–1213, 2002. doi: doi:10.1126/science.1076184. URL https://www.science.org/doi/abs/10.1126/science.1076184.

[9] A. Al-Amoudi, J. J. Chang, A. Leforestier, A. McDowall, L. M. Salamin, L. P. Norlén, K. Richter, N. S. Blanc, D. Studer, and J. Dubochet. Cryo-electron microscopy of vitreous sections. *Embo j*, 23(18):3583–8, 2004. ISSN 0261-4189 (Print) 0261-4189. doi: 10.1038/sj.emboj.7600366.

[10] A. Rigort, F. J. Bauerlein, E. Villa, M. Eibauer, T. Laugks, W. Baumeister, and J. M. Plitzko. Focused ion beam micromachining of eukaryotic cells for cryo-electron tomography. *Proc Natl Acad Sci U S A*, 109(12):4449–54, 2012. ISSN 1091-6490 (Electronic) 0027-8424 (Linking). doi: 10.1073/pnas.1201333109. URL https://www.ncbi.nlm.nih.gov/pubmed/22392984.

[11] M. Marko, C. Hsieh, R. Schalek, J. Frank, and C. Mannella. Focused-ion-beam thinning of frozen-hydrated biological specimens for cryo-electron microscopy. *Nat Methods*, 4(3):215–7, 2007. ISSN 1548-7091 (Print) 1548-7091 (Linking). doi: 10.1038/nmeth1014. URL https://www.ncbi.nlm.nih.gov/pubmed/17277781.

[12] A. Al-Amoudi, D. Studer, and J. Dubochet. Cutting artefacts and cutting process in vitreous sections for cryo-electron microscopy. *J Struct Biol*, 150(1):109–21, 2005. ISSN 1047-8477 (Print) 1047-8477 (Linking). doi: 10.1016/j.jsb.2005.01.003. URL https://www.ncbi.nlm.nih.gov/pubmed/15797735.

[13] Alexander Rigort and Jürgen M. Plitzko. Cryo-focused-ion-beam applications in structural biology. *Archives of Biochemistry and Biophysics*, 581: 122–130, 2015. ISSN 0003-9861. doi: https://doi.org/10.1016/j.abb.2015.02.009. URL https://www.sciencedirect.com/science/article/pii/S0003986115000715.

[14] M. W. Phaneuf. *FIB for Materials Science Applications - a Review*, pages 143–172. Springer US, Boston, MA, 2005. ISBN 978-0-387-23313-0. doi: 10.1007/0-387-23313-X_8. URL https://doi.org/10.1007/0-387-23313-X_8.

[15] Robert Krueger. Dual-column (fib–sem) wafer applications. *Micron*, 30(3):221–226, 1999. ISSN 0968-4328. doi: https://doi.org/10.1016/S0968-4328(98)00044-4. URL https://www.sciencedirect.com/science/article/pii/S0968432898000444.

[16] M. Beck and W. Baumeister. Cryo-electron tomography: Can it reveal the molecular sociology of cells in atomic detail? *Trends Cell Biol*, 26(11):825–837, 2016. ISSN 1879-3088 (Electronic) 0962-8924 (Linking). doi: 10.1016/j.tcb.2016.08.006. URL https://www.ncbi.nlm.nih.gov/pubmed/27671779.

[17] M. Schaffer, S. Pfeffer, J. Mahamid, S. Kleindiek, T. Laugks, S. Albert, B. D. Engel, A. Rummel, A. J. Smith, W. Baumeister, and J. M. Plitzko. A cryo-fib lift-out technique enables molecular-resolution cryo-et within native caenorhabditis elegans tissue. *Nat Methods*, 16(8):757–762, 2019. ISSN 1548-7105 (Electronic) 1548-7091 (Linking). doi: 10.1038/s41592-019-0497-5. URL https://www.ncbi.nlm.nih.gov/pubmed/31363205.

[18] J. Mahamid, R. Schampers, H. Persoon, A. A. Hyman, W. Baumeister, and J. M. Plitzko. A focused ion beam milling and lift-out approach for site-specific

preparation of frozen-hydrated lamellas from multicellular organisms. *J Struct Biol*, 192(2):262–9, 2015. ISSN 1095-8657 (Electronic) 1047-8477 (Linking). doi: 10.1016/j.jsb.2015.07.012. URL https://www.ncbi.nlm.nih.gov/pubmed/26216184.

[19] J. Kuba, J. Mitchels, M. Hovorka, P. Erdmann, L. Berka, R. Kirmse, K. Onig J, D. E. Bock J, B. Goetze, and A. Rigort. Advanced cryo-tomography workflow developments - correlative microscopy, milling automation and cryo-lift-out. *J Microsc*, 281(2):112–124, 2021. ISSN 1365-2818 (Electronic) 0022-2720 (Linking). doi: 10.1111/jmi.12939. URL https://www.ncbi.nlm.nih.gov/pubmed/32557536.

[20] Andrej Sali. From integrative structural biology to cell biology. *Journal of Biological Chemistry*, 296, 2021. ISSN 0021-9258. doi: 10.1016/j.jbc.2021.100743. URL https://doi.org/10.1016/j.jbc.2021.100743.

[21] S. Klumpe, H. K. H. Fung, S. K. Goetz, I. Zagoriy, B. Hampoelz, X. J. Zhang, P. S. Erdmann, J. Baumbach, C. W. Müller, M. Beck, J. M. Plitzko, and J. Mahamid. A modular platform for automated cryo-fib workflows. *Elife*, 10, 2021. ISSN 2050-084X. doi: 10.7554/eLife.70506;10.7554/eLife.70506.sa0;10.7554/eLife.70506.sa1;10.7554/eLife.70506.sa2. URL <GotoISI>://WOS:000747134800001.

[22] Sven Klumpe, Jakub Kuba, Oda H. Schioetz, Philipp S. Erdmann, Alexander Rigort, and Jürgen M. Plitzko. Recent advances in gas injection system-free cryo-fib lift-out transfer for cryo-electron tomography of multicellular organisms and tissues. *Microscopy Today*, 30(1):42–47, 2022. ISSN 1551-9295. doi: 10.1017/S1551929521001528. URL https://www.cambridge.org/core/article/recent-advances-in-gas-injection-systemfree-cryofib-liftout-transfer-for-53E42EB56650CC198B81EDD6FE638419.

[23] Baptiste Gault, Ann Chiaramonti, Oana Cojocaru-Mirédin, Patrick Stender, Renelle Dubosq, Christoph Freysoldt, Surendra Kumar Makineni, Tong Li, Michael Moody, and Julie M. Cairney. Atom probe tomography. *Nature Reviews Methods Primers*, 1(1):51, 2021. ISSN 2662-8449. doi: 10.1038/s43586-021-00047-w. URL https://doi.org/10.1038/s43586-021-00047-w.

[24] Bernd Reif, Sharon E. Ashbrook, Lyndon Emsley, and Mei Hong. Solid-state nmr spectroscopy. *Nature Reviews Methods Primers*, 1(1):2, 2021. ISSN 2662-8449. doi: 10.1038/s43586-020-00002-1. URL https://doi.org/10.1038/s43586-020-00002-1.

[25] Florent Delhommel, Frank Gabel, and Michael Sattler. Current approaches for integrating solution nmr spectroscopy and small-angle scattering to study the structure and dynamics of biomolecular complexes. *Journal of Molecular Biology*, 432(9):2890–2912, 2020. ISSN 0022-2836. doi: https://doi.org/10.1016/j.jmb.2020.03.014. URL https://www.sciencedirect.com/science/article/pii/S0022283620302357.

[26] Jan Drenth. *Principles of protein X-ray crystallography*. Springer Science Business Media, 2007. ISBN 0387337466.

[27] Philip J. Withers, Charles Bouman, Simone Carmignato, Veerle Cnudde, David Grimaldi, Charlotte K. Hagen, Eric Maire, Marena Manley, Anton Du Plessis, and Stuart R. Stock. X-ray computed tomography. *Nature Reviews Methods Primers*, 1(1):18, 2021. ISSN 2662-8449. doi: 10.1038/s43586-021-00015-4. URL https://doi.org/10.1038/s43586-021-00015-4.

[28] Ernst H. K. Stelzer, Frederic Strobl, Bo-Jui Chang, Friedrich Preusser, Stephan Preibisch, Katie McDole, and Reto Fiolka. Light sheet fluorescence microscopy. *Nature Reviews Methods Primers*, 1(1):73, 2021. ISSN 2662-8449. doi: 10.1038/s43586-021-00069-4. URL https://doi.org/10.1038/s43586-021-00069-4.

[29] Sheng Liu, Philipp Hoess, and Jonas Ries. Super-resolution microscopy for structural cell biology. *Annual Review of Biophysics*, 51 (1):301–326, 2022. doi: 10.1146/annurev-biophys-102521-112912. URL https://www.annualreviews.org/doi/abs/10.1146/annurev-biophys-102521-112912.

[30] B. Titze and C. Genoud. Volume scanning electron microscopy for imaging biological ultrastructure. *Biol Cell*, 108(11):307–323, 2016. ISSN 0248-4900. doi: 10.1111/boc.201600024.

[31] Louis K. Scheffer, C. Shan Xu, Michal Januszewski, Zhiyuan Lu, Shin-ya Takemura, Kenneth J. Hayworth, Gary B. Huang, Kazunori Shinomiya, Jeremy Maitlin-Shepard, Stuart Berg, Jody Clements, Philip M. Hubbard, William T. Katz, Lowell Umayam, Ting Zhao, David Ackerman, Tim Blakely, John Bogovic, Tom Dolafi, Dagmar Kainmueller, Takashi Kawase, Khaled A. Khairy, Laramie Leavitt, Peter H. Li, Larry Lindsey, Nicole Neubarth, Donald J. Olbris, Hideo Otsuna, Eric T. Trautman, Masayoshi Ito, Alexander S. Bates, Jens Goldammer, Tanya Wolff, Robert Svirskas, Philipp Schlegel, Erika Neace, Christopher J. Knecht, Chelsea X. Alvarado, Dennis A. Bailey, Samantha Ballinger, Jolanta A. Borycz, Brandon S. Canino, Natasha Cheatham, Michael Cook, Marisa Dreher, Octave Duclos, Bryon Eubanks, Kelli Fairbanks, Samantha Finley, Nora Forknall, Audrey Francis, Gary Patrick Hopkins, Emily M. Joyce, SungJin Kim,

Nicole A. Kirk, Julie Kovalyak, Shirley A. Lauchie, Alanna Lohff, Charli Maldonado, Emily A. Manley, Sari McLin, Caroline Mooney, Miatta Ndama, Omotara Ogundeyi, Nneoma Okeoma, Christopher Ordish, Nicholas Padilla, Christopher M. Patrick, Tyler Paterson, Elliott E. Phillips, Emily M. Phillips, Neha Rampally, Caitlin Ribeiro, Madelaine K. Robertson, Jon Thomson Rymer, Sean M. Ryan, Megan Sammons, Anne K. Scott, Ashley L. Scott, Aya Shinomiya, Claire Smith, Kelsey Smith, Natalie L. Smith, Margaret A. Sobeski, Alia Suleiman, Jackie Swift, Satoko Takemura, Iris Talebi, Dorota Tarnogorska, Emily Tenshaw, Temour Tokhi, John J. Walsh, Tansy Yang, Jane Anne Horne, Feng Li, Ruchi Parekh, Patricia K. Rivlin, Vivek Jayaraman, Marta Costa, Gregory S. X. E. Jefferis, et al. A connectome and analysis of the adult drosophila central brain. *eLife*, 9:e57443, 2020. ISSN 2050-084X. doi: 10.7554/eLife.57443. URL https://doi.org/10.7554/eLife.57443.

[32] H. M. Vergara, C. Pape, K. I. Meechan, V. Zinchenko, C. Genoud, A. A. Wanner, K. N. Mutemi, B. Titze, R. M. Templin, P. Y. Bertucci, O. Simakov, W. Dürichen, P. Machado, E. L. Savage, L. Schermelleh, Y. Schwab, R. W. Friedrich, A. Kreshuk, C. Tischer, and D. Arendt. Whole-body integration of gene expression and single-cell morphology. *Cell*, 184(18):4819–4837.e22, 2021. ISSN 0092-8674 (Print) 0092-8674. doi: 10.1016/j.cell.2021.07.017.

[33] Jürgen M. Plitzko, Benjamin Schuler, and Philipp Selenko. Structural biology outside the box—inside the cell. *Current Opinion in Structural Biology*, 46:110–121, 2017. ISSN 0959-440X. doi: https://doi.org/10.1016/j.sbi.2017.06.007. URL https://www.sciencedirect.com/science/article/pii/S0959440X16301920.

[34] Francis J. O'Reilly, Liang Xue, Andrea Graziadei, Ludwig Sinn, Swantje Lenz, Dimitry Tegunov, Cedric Blötz, Neil Singh, Wim J. H. Hagen, Patrick Cramer, Jörg Stülke, Julia Mahamid, and Juri Rappsilber. In-cell architecture of an actively transcribing-translating expressome. *Science*, 369(6503):554–557, 2020. doi: doi:10.1126/science.abb3758. URL https://www.science.org/doi/abs/10.1126/science.abb3758.

[35] Patrick C. Hoffmann, Jan Philipp Kreysing, Iskander Khusainov, Maarten W. Tuijtel, Sonja Welsch, and Martin Beck. Structures of the eukaryotic ribosome and its translational states in situ. *Nature Communications*, 13(1):7435, 2022. ISSN 2041-1723. doi: 10.1038/s41467-022-34997-w. URL https://doi.org/10.1038/s41467-022-34997-w.

[36] Casper Berger, Maud Dumoux, Thomas Glen, Neville B. y Yee, John M. Mitchels, Zuzana Patáková, Michele C. Darrow, James H. Naismith, and Michael Grange. Plasma fib milling for the determination of structures in situ. *Nature Communications*, 14(1):629, 2023. ISSN 2041-

1723. doi: 10.1038/s41467-023-36372-9. URL https://doi.org/10.1038/s41467-023-36372-9.

[37] S. K. Goetz and J. Mahamid. Visualizing molecular architectures of cellular condensates: Hints of complex coacervation scenarios. *Dev Cell*, 55(1):97–107, 2020. ISSN 1534-5807. doi: 10.1016/j.devcel.2020.09.003.

[38] David B. Williams and C. Barry Carter. *Transmission Electron microscopy*. doi: 10.1007/978-0-387-76501-3.

[39] A. I. Kirkland, S. Haigh, and L. Y. Chang. Aberration corrected tem: current status and future prospects. *Journal of Physics: Conference Series*, 126(1): 012034, 2008. ISSN 1742-6596 1742-6588. doi: 10.1088/1742-6596/126/1/012034. URL https://dx.doi.org/10.1088/1742-6596/126/1/012034.

[40] Knut W. Urban, Juri Barthel, Lothar Houben, Chun-Lin Jia, Lei Jin, Markus Lentzen, Shao-Bo Mi, Andreas Thust, and Karsten Tillmann. Progress in atomic-resolution aberration corrected conventional transmission electron microscopy (ctem). *Progress in Materials Science*, 133:101037, 2023. ISSN 0079-6425. doi: https://doi.org/10.1016/j.pmatsci.2022.101037. URL https://www.sciencedirect.com/science/article/pii/S0079642522001189.

[41] T. Nakane, A. Kotecha, A. Sente, G. McMullan, S. Masiulis, Pmge Brown, I. T. Grigoras, L. Malinauskaite, T. Malinauskas, J. Miehling, T. Uchanski, L. B. Yu, D. Karia, E. V. Pechnikova, E. de Jong, J. Keizer, M. Bischoff, J. McCormack, P. Tiemeijer, S. W. Hardwick, D. Y. Chirgadze, G. Murshudov, A. R. Aricescu, and S. H. W. Scheres. Single-particle cryo-em at atomic resolution. *Nature*, 587(7832):152–+, 2020. ISSN 0028-0836. doi: 10.1038/s41586-020-2829-0. URL <GotoISI>://WOS:000580948100003.

[42] Miloš Vulović, Lenard M. Voortman, Lucas J. van Vliet, and Bernd Rieger. When to use the projection assumption and the weak-phase object approximation in phase contrast cryo-em. *Ultramicroscopy*, 136:61–66, 2014. ISSN 0304-3991. doi: https://doi.org/10.1016/j.ultramic.2013.08.002. URL https://www.sciencedirect.com/science/article/pii/S0304399113002088.

[43] Peter W Hawkes and John CH Spence. *Springer handbook of microscopy*. Springer Nature, 2019. ISBN 3030000699.

[44] Y. Kang, G. Wu, X. Zhang, Y. Liu, C. Shi, W. Wei, and G. Gao. Verification and analysis of flowing gas discharge – part ii. *IEEE Transactions on Dielectrics and Electrical Insulation*, 26(4):1056–1064, 2019. ISSN 1558-4135. doi: 10.1109/TDEI.2019.007833.

[45] T Shimojima, A Nakamura, and K Ishizaka. Development and applications of ultrafast transmission electron microscopy. *Microscopy*, 72(4):287–298, 2023.

ISSN 2050-5701. doi: 10.1093/jmicro/dfad021. URL https://doi.org/10.1093/jmicro/dfad021.

[46] G. McMullan, A. R. Faruqi, D. Clare, and R. Henderson. Comparison of optimal performance at 300kev of three direct electron detectors for use in low dose electron microscopy. *Ultramicroscopy*, 147:156–163, 2014. ISSN 0304-3991. doi: https://doi.org/10.1016/j.ultramic.2014.08.002. URL https://www.sciencedirect.com/science/article/pii/S030439911400151X.

[47] S. Q. Zheng, E. Palovcak, J. P. Armache, K. A. Verba, Y. F. Cheng, and D. A. Agard. Motioncor2: anisotropic correction of beam-induced motion for improved cryo-electron microscopy. *Nature Methods*, 14(4):331–332, 2017. ISSN 1548-7091. doi: 10.1038/nmeth.4193. URL <GotoISI>://WOS:000397900500004.

[48] Radostin Danev, Matthew Belousoff, Yi-Lynn Liang, Xin Zhang, Fabian Eisenstein, Denise Wootten, and Patrick M. Sexton. Routine sub-2.5Å cryo-em structure determination of gpcrs. *Nature Communications*, 12(1):4333, 2021. ISSN 2041-1723. doi: 10.1038/s41467-021-24650-3. URL https://doi.org/10.1038/s41467-021-24650-3.

[49] R. H. Wade. A brief look at imaging and contrast transfer. *Ultramicroscopy*, 46(1):145–156, 1992. ISSN 0304-3991. doi: https://doi.org/10.1016/0304-3991(92)90011-8. URL https://www.sciencedirect.com/science/article/pii/0304399192900118.

[50] Bart Buijsse, Piet Trompenaars, Veli Altin, Radostin Danev, and Robert M. Glaeser. Spectral dqe of the volta phase plate. *Ultramicroscopy*, 218:113079, 2020. ISSN 0304-3991. doi: https://doi.org/10.1016/j.ultramic.2020.113079. URL https://www.sciencedirect.com/science/article/pii/S0304399120302308.

[51] O. Schwartz, J. J. Axelrod, S. L. Campbell, C. Turnbaugh, R. M. Glaeser, and H. Müller. Laser phase plate for transmission electron microscopy. *Nature Methods*, 16(10):1016–+, 2019. ISSN 1548-7091. doi: 10.1038/s41592-019-0552-2. URL <GotoISI>://WOS:000488225900032.

[52] O. Schwartz, J. J. Axelrod, D. R. Tuthill, P. Haslinger, C. Ophus, R. M. Glaeser, and H. Müller. Near-concentric fabry-px000e9;rot cavity for continuous-wave laser control of electron waves. *Optics Express*, 25(13):14453–14462, 2017. doi: 10.1364/OE.25.014453. URL https://opg.optica.org/oe/abstract.cfm?URI=oe-25-13-14453.

[53] Mark V. de Ruiter, Robin Klem, Daniel Luque, Jeroen J. L. M. Cornelissen, and José R. Castón. Structural nanotechnology: three-dimensional cryo-em and

its use in the development of nanoplatforms for in vitro catalysis. *Nanoscale*, 11(10):4130–4146, 2019. ISSN 2040-3364. doi: 10.1039/C8NR09204D. URL http://dx.doi.org/10.1039/C8NR09204D.

[54] A. Rohou and N. Grigorieff. Ctffind4: Fast and accurate defocus estimation from electron micrographs. *Journal of Structural Biology*, 192(2):216–221, 2015. ISSN 1047-8477. doi: 10.1016/j.jsb.2015.08.008. URL <GotoISI>://WOS:000364607400012.

[55] D. Tegunov and P. Cramer. Real-time cryo-electron microscopy data preprocessing with warp. *Nature Methods*, 16(11):1146–+, 2019. ISSN 1548-7091. doi: 10.1038/s41592-019-0580-y. URL <GotoISI>://WOS:000493902600028.

[56] J. Zivanov, T. Nakane, B. O. Forsberg, D. Kimanius, W. J. H. Hagen, E. Lindahl, and S. H. W. Scheres. New tools for automated high-resolution cryo-em structure determination in relion-3. *Elife*, 7, 2018. ISSN 2050-084X. doi: 10.7554/eLife.42166. URL <GotoISI>://WOS:000450857100001.

[57] B. Turonova, F. K. M. Schur, W. Wan, and J. A. G. Briggs. Efficient 3d-ctf correction for cryo-electron tomography using novactf improves subtomogram averaging resolution to 3.4a. *J Struct Biol*, 199(3):187–195, 2017. ISSN 1095-8657 (Electronic) 1047-8477 (Linking). doi: 10.1016/j.jsb.2017.07.007. URL https://www.ncbi.nlm.nih.gov/pubmed/28743638.

[58] A. Punjani, J. L. Rubinstein, D. J. Fleet, and M. A. Brubaker. cryosparc: algorithms for rapid unsupervised cryo-em structure determination. *Nature Methods*, 14(3):290–+, 2017. ISSN 1548-7091. doi: 10.1038/nmeth.4169. URL <GotoISI>://WOS:000395661700027.

[59] S. H. W. Scheres. Relion: Implementation of a bayesian approach to cryo-em structure determination. *Journal of Structural Biology*, 180(3):519–530, 2012. ISSN 1047-8477. doi: 10.1016/j.jsb.2012.09.006. URL <GotoISI>://WOS:000311471000014.

[60] T. Nakane and S. H. W. Scheres. *Multi-body Refinement of Cryo-EM Images in RELION*, volume 2215 of *Methods in Molecular Biology*, pages 145–160. 2021. ISBN 978-1-0716-0966-8; 978-1-0716-0965-1. doi: 10.1007/978-1-0716-0966-8_7. URL <GotoISI>://WOS:000678844000008.

[61] T. Nakane, D. Kimanius, E. Lindahl, and S. H. W. Scheres. Characterisation of molecular motions in cryo-em single-particle data by multi-body refinement in relion. *Elife*, 7, 2018. ISSN 2050-084X. doi: 10.7554/eLife.36861. URL <GotoISI>://WOS:000435436100001.

[62] Daniel Cressey and Ewen Callaway. Cryo-electron microscopy wins chemistry nobel. *Nature*, 550(7675):167–167, 2017. ISSN 1476-4687. doi: 10.1038/nature.2017.22738. URL https://doi.org/10.1038/nature.2017.22738.

[63] Siewert J. Marrink, H. Jelger Risselada, Serge Yefimov, D. Peter Tieleman, and Alex H. de Vries. The martini force field: coarse grained model for biomolecular simulations. *The Journal of Physical Chemistry B*, 111(27):7812–7824, 2007. ISSN 1520-6106. doi: 10.1021/jp071097f. URL https://doi.org/10.1021/jp071097f.

[64] B. Webb and A. Sali. Comparative protein structure modeling using modeller. *Curr Protoc Bioinformatics*, 47:5 6 1–32, 2014. ISSN 1934-340X (Electronic) 1934-3396 (Linking). doi: 10.1002/0471250953.bi0506s47. URL https://www.ncbi.nlm.nih.gov/pubmed/25199792.

[65] John Jumper, Richard Evans, Alexander Pritzel, Tim Green, Michael Figurnov, Olaf Ronneberger, Kathryn Tunyasuvunakool, Russ Bates, Augustin Žídek, Anna Potapenko, Alex Bridgland, Clemens Meyer, Simon A. A. Kohl, Andrew J. Ballard, Andrew Cowie, Bernardino Romera-Paredes, Stanislav Nikolov, Rishub Jain, Jonas Adler, Trevor Back, Stig Petersen, David Reiman, Ellen Clancy, Michal Zielinski, Martin Steinegger, Michalina Pacholska, Tamas Berghammer, Sebastian Bodenstein, David Silver, Oriol Vinyals, Andrew W. Senior, Koray Kavukcuoglu, Pushmeet Kohli, and Demis Hassabis. Highly accurate protein structure prediction with alphafold. *Nature*, 596(7873):583–589, 2021. ISSN 1476-4687. doi: 10.1038/s41586-021-03819-2. URL https://doi.org/10.1038/s41586-021-03819-2.

[66] Minkyung Baek, Frank DiMaio, Ivan Anishchenko, Justas Dauparas, Sergey Ovchinnikov, Gyu Rie Lee, Jue Wang, Qian Cong, Lisa N. Kinch, R. Dustin Schaeffer, Claudia Millán, Hahnbeom Park, Carson Adams, Caleb R. Glassman, Andy DeGiovanni, Jose H. Pereira, Andria V. Rodrigues, Alberdina A. van Dijk, Ana C. Ebrecht, Diederik J. Opperman, Theo Sagmeister, Christoph Buhlheller, Tea Pavkov-Keller, Manoj K. Rathinaswamy, Udit Dalwadi, Calvin K. Yip, John E. Burke, K. Christopher Garcia, Nick V. Grishin, Paul D. Adams, Randy J. Read, and David Baker. Accurate prediction of protein structures and interactions using a three-track neural network. *Science*, 373(6557):871–876, 2021. doi: doi:10.1126/science.abj8754. URL https://www.science.org/doi/abs/10.1126/science.abj8754.

[67] Carol A. Rohl, Charlie E. M. Strauss, Kira M. S. Misura, and David Baker. *Protein Structure Prediction Using Rosetta*, volume 383, pages 66–93. Academic Press, 2004. ISBN 0076-6879. doi: https://doi.org/10.1016/S0076-6879(04)83004-0. URL https://www.sciencedirect.com/science/article/pii/S0076687904830040.

[68] Garrett M. Morris, Ruth Huey, William Lindstrom, Michel F. Sanner, Richard K. Belew, David S. Goodsell, and Arthur J. Olson. Autodock4 and autodocktools4: Automated docking with selective receptor flexibility. *Journal of Computational*

Chemistry, 30(16):2785–2791, 2009. ISSN 0192-8651. doi: https://doi.org/10.1002/jcc.21256. URL https://onlinelibrary.wiley.com/doi/abs/10.1002/jcc.21256.

[69] G. C. P. van Zundert, A. S. J. Melquiond, and Amjj Bonvin. Integrative modeling of biomolecular complexes: Haddocking with cryo-electron microscopy data. *Structure*, 23(5):949–960, 2015. ISSN 1878-4186 (Electronic) 0969-2126 (Linking). doi: 10.1016/j.str.2015.03.014. URL https://www.ncbi.nlm.nih.gov/pubmed/25914056.

[70] S. J. de Vries, M. van Dijk, and A. M. Bonvin. The haddock web server for data-driven biomolecular docking. *Nat Protoc*, 5(5):883–97, 2010. ISSN 1750-2799 (Electronic) 1750-2799 (Linking). doi: 10.1038/nprot.2010.32. URL https://www.ncbi.nlm.nih.gov/pubmed/20431534.

[71] B. Webb, K. Lasker, D. Schneidman-Duhovny, E. Tjioe, J. Phillips, S. J. Kim, J. Velazquez-Muriel, D. Russel, and A. Sali. Modeling of proteins and their assemblies with the integrative modeling platform. *Methods Mol Biol*, 781:377–97, 2011. ISSN 1940-6029 (Electronic) 1064-3745 (Linking). doi: 10.1007/978-1-61779-276-2_19. URL https://www.ncbi.nlm.nih.gov/pubmed/21877292https://link.springer.com/content/pdf/10.1007%2F978-1-61779-276-2_19.pdf.

[72] B. Webb, S. Viswanath, M. Bonomi, R. Pellarin, C. H. Greenberg, D. Saltzberg, and A. Sali. Integrative structure modeling with the integrative modeling platform. *Protein Sci*, 27(1):245–258, 2018. ISSN 1469-896X (Electronic) 0961-8368 (Linking). doi: 10.1002/pro.3311. URL https://www.ncbi.nlm.nih.gov/pubmed/28960548https://www.ncbi.nlm.nih.gov/pmc/articles/PMC5734277/pdf/PRO-27-245.pdf.

[73] I. Farabella, D. Vasishtan, A. P. Joseph, A. P. Pandurangan, H. Sahota, and M. Topf. Tempy: a python library for assessment of three-dimensional electron microscopy density fits. *J Appl Crystallogr*, 48(Pt 4):1314–1323, 2015. ISSN 0021-8898 (Print) 0021-8898. doi: 10.1107/s1600576715010092.

[74] Vasileios Rantos, Kai Karius, and Jan Kosinski. Integrative structural modeling of macromolecular complexes using assembline. *Nature Protocols*, 17(1):152–176, 2022. ISSN 1750-2799. doi: 10.1038/s41596-021-00640-z. URL https://doi.org/10.1038/s41596-021-00640-z.

[75] J. C. Phillips, R. Braun, W. Wang, J. Gumbart, E. Tajkhorshid, E. Villa, C. Chipot, R. D. Skeel, L. Kale, and K. Schulten. Scalable molecular dynamics with namd. *J Comput Chem*, 26(16):1781–802, 2005. ISSN 0192-8651 (Print) 0192-8651 (Linking). doi: 10.1002/jcc.20289. URL https://www.ncbi.nlm.nih.gov/pubmed/16222654.

[76] T. I. Croll. isolde: a physically realistic environment for model building into low-resolution electron-density maps. *Acta Crystallographica Section D-Structural Biology*, 74:519–530, 2018. ISSN 2059-7983. doi: 10.1107/s2059798318002425. URL <GotoISI>://WOS:000434348800004.

[77] Maxim Igaev, Carsten Kutzner, Lars V. Bock, Andrea C. Vaiana, and Helmut Grubmüller. Automated cryo-em structure refinement using correlation-driven molecular dynamics. *eLife*, 8:e43542, 2019. ISSN 2050-084X. doi: 10.7554/eLife.43542. URL https://doi.org/10.7554/eLife.43542.

[78] Roger G. Hart. Electron microscopy of unstained biological material: The polytropic montage. *Science*, 159(3822):1464–1467, 1968. doi: doi:10.1126/science.159.3822.1464. URL https://www.science.org/doi/abs/10.1126/science.159.3822.1464.

[79] Montserrat Bárcena and Abraham J. Koster. Electron tomography in life science. *Seminars in Cell Developmental Biology*, 20(8):920–930, 2009. ISSN 1084-9521. doi: https://doi.org/10.1016/j.semcdb.2009.07.008. URL https://www.sciencedirect.com/science/article/pii/S1084952109001554.

[80] K. Dierksen, D. Typke, R. Hegerl, J. Walz, E. Sackmann, and W. Baumeister. Three-dimensional structure of lipid vesicles embedded in vitreous ice and investigated by automated electron tomography. *Biophysical Journal*, 68(4):1416–1422, 1995. ISSN 0006-3495. doi: https://doi.org/10.1016/S0006-3495(95)80314-0. URL https://www.sciencedirect.com/science/article/pii/S0006349595803140.

[81] Patricia Abellan, Eric Gautron, and Jay A. LaVerne. Radiolysis of thin water ice in electron microscopy. *The Journal of Physical Chemistry C*, 127(31):15336–15345, 2023. ISSN 1932-7447. doi: 10.1021/acs.jpcc.3c02936. URL https://doi.org/10.1021/acs.jpcc.3c02936.

[82] M. Mishyna, O. Volokh, Ya Danilova, N. Gerasimova, E. Pechnikova, and O. S. Sokolova. Effects of radiation damage in studies of protein-dna complexes by cryo-em. *Micron*, 96:57–64, 2017. ISSN 0968-4328. doi: https://doi.org/10.1016/j.micron.2017.02.004. URL https://www.sciencedirect.com/science/article/pii/S0968432816303626.

[83] Robert M. Glaeser. Limitations to significant information in biological electron microscopy as a result of radiation damage. *Journal of Ultrastructure Research*, 36(3):466–482, 1971. ISSN 0022-5320. doi: https://doi.org/10.1016/S0022-5320(71)80118-1. URL https://www.sciencedirect.com/science/article/pii/S0022532071801181.

[84] B. Turonová, W. J. H. Hagen, M. Obr, S. Mosalaganti, J. W. Beugelink, C. E. Zimmerli, H. G. Kräusslich, and M. Beck. Benchmarking tomographic ac-

quisition schemes for high-resolution structural biology. *Nature Communications*, 11(1), 2020. ISSN 2041-1723. doi: 10.1038/s41467-020-14535-2. URL <GotoISI>://WOS:000514928000017.

[85] Kangkang Song, Zhiguo Shang, Xiaofeng Fu, Xiaochu Lou, Nikolaus Grigorieff, and Daniela Nicastro. In situ structure determination at nanometer resolution using tygress. *Nature Methods*, 17(2):201–208, 2020. ISSN 1548-7105. doi: 10.1038/s41592-019-0651-0. URL https://doi.org/10.1038/s41592-019-0651-0.

[86] W. J. H. Hagen, W. Wan, and J. A. G. Briggs. Implementation of a cryo-electron tomography tilt-scheme optimized for high resolution subtomogram averaging. *J Struct Biol*, 197(2):191–198, 2017. ISSN 1095-8657 (Electronic) 1047-8477 (Linking). doi: 10.1016/j.jsb.2016.06.007. URL https://www.ncbi.nlm.nih.gov/pubmed/27313000.

[87] D. N. Mastronarde. Automated electron microscope tomography using robust prediction of specimen movements. *J Struct Biol*, 152(1):36–51, 2005. ISSN 1047-8477 (Print) 1047-8477 (Linking). doi: 10.1016/j.jsb.2005.07.007. URL https://doi.org/10.1016/j.jsb.2005.07.007.

[88] Christian Suloway, Jian Shi, Anchi Cheng, James Pulokas, Bridget Carragher, Clinton S. Potter, Shawn Q. Zheng, David A. Agard, and Grant J. Jensen. Fully automated, sequential tilt-series acquisition with leginon. *Journal of Structural Biology*, 167(1):11–18, 2009. ISSN 1047-8477. doi: https://doi.org/10.1016/j.jsb.2009.03.019. URL https://www.sciencedirect.com/science/article/pii/S1047847709000975.

[89] J. R. Kremer, D. N. Mastronarde, and J. R. McIntosh. Computer visualization of three-dimensional image data using imod. *Journal of Structural Biology*, 116(1):71–76, 1996. ISSN 1047-8477. doi: 10.1006/jsbi.1996.0013. URL <GotoISI>://WOS:A1996TX60600013.

[90] Shawn Zheng, Georg Wolff, Garrett Greenan, Zhen Chen, Frank G. A. Faas, Montserrat Bárcena, Abraham J. Koster, Yifan Cheng, and David A. Agard. Aretomo: An integrated software package for automated marker-free, motion-corrected cryo-electron tomographic alignment and reconstruction. *Journal of Structural Biology: X*, 6:100068, 2022. ISSN 2590-1524. doi: https://doi.org/10.1016/j.yjsbx.2022.100068. URL https://www.sciencedirect.com/science/article/pii/S2590152422000095.

[91] Richard Gordon, Robert Bender, and Gabor T. Herman. Algebraic reconstruction techniques (art) for three-dimensional electron microscopy and x-ray photography. *Journal of Theoretical Biology*, 29(3):471–481, 1970. ISSN 00225193. doi: 10.1016/0022-5193(70)90109-8.

[92] Euan Pyle and Giulia Zanetti. Current data processing strategies for cryo-electron tomography and subtomogram averaging. *Biochemical Journal*, 478 (10):1827–1845, 2021. ISSN 0264-6021. doi: 10.1042/bcj20200715. URL https://doi.org/10.1042/BCJ20200715.

[93] Colin M. Palmer and Jan Löwe. A cylindrical specimen holder for electron cryo-tomography. *Ultramicroscopy*, 137:20–29, 2014. ISSN 0304-3991. doi: https://doi.org/10.1016/j.ultramic.2013.10.016. URL https://www.sciencedirect.com/science/article/pii/S0304399113002933.

[94] T. O. Buchholz, M. Jordan, G. Pigino, F. Jug, and Ieee. Cryo-care: Content-aware image restoration for cryo-transmission electron microscopy data. In *16th IEEE International Symposium on Biomedical Imaging (ISBI)*, IEEE International Symposium on Biomedical Imaging, pages 502–506, 2019. ISBN 978-1-5386-3641-1. doi: 10.1109/isbi.2019.8759519. URL <GotoISI>://WOS:000485040000111.

[95] Yun-Tao Liu, Heng Zhang, Hui Wang, Chang-Lu Tao, Guo-Qiang Bi, and Z. Hong Zhou. Isotropic reconstruction for electron tomography with deep learning. *Nature Communications*, 13(1):6482, 2022. ISSN 2041-1723. doi: 10.1038/s41467-022-33957-8. URL https://doi.org/10.1038/s41467-022-33957-8.

[96] Achilleas S. Frangakis. It's noisy out there! a review of denoising techniques in cryo-electron tomography. *Journal of Structural Biology*, 213(4):107804, 2021. ISSN 1047-8477. doi: https://doi.org/10.1016/j.jsb.2021.107804. URL https://www.sciencedirect.com/science/article/pii/S104784772100109X.

[97] Stephan Nickell, Christine Kofler, Andrew P. Leis, and Wolfgang Baumeister. A visual approach to proteomics. *Nature Reviews Molecular Cell Biology*, 7 (3):225–230, 2006. ISSN 1471-0080. doi: 10.1038/nrm1861. URL https://doi.org/10.1038/nrm1861.

[98] William J. Rice, Anchi Cheng, Alex J. Noble, Edward T. Eng, Laura Y. Kim, Bridget Carragher, and Clinton S. Potter. Routine determination of ice thickness for cryo-em grids. *Journal of Structural Biology*, 204(1):38–44, 2018. ISSN 1047-8477. doi: https://doi.org/10.1016/j.jsb.2018.06.007. URL https://www.sciencedirect.com/science/article/pii/S1047847718301552.

[99] J. Dubochet. High-pressure freezing for cryoelectron microscopy. *Trends in Cell Biology*, 5(9):366–368, 1995. ISSN 0962-8924. doi: 10.1016/s0962-8924(00)89071-6. URL <GotoISI>://WOS:A1995RQ88200007.

[100] J. Dubochet and A. W. McDowall. Vitrification of pure water for electron-microscopy. *Journal of Microscopy-Oxford*, 124(DEC):RP3–RP4, 1981. ISSN 0022-2720. URL <GotoISI>://WOS:A1981MU68700017.

[101] Bruno M. Humbel, Heinz Schwarz, Erin M. Tranfield, and Roland A. Fleck. *Chemical Fixation*, pages 191–221. 2019. doi: https://doi.org/10.1002/9781118663233.ch10. URL https://onlinelibrary.wiley.com/doi/abs/10.1002/9781118663233.ch10.

[102] J. Dubochet, J. Lepault, R. Freeman, J. A. Berriman, and J.-C. Homo. Electron microscopy of frozen water and aqueous solutions. *Journal of Microscopy*, 128(3):219–237, 1982. ISSN 0022-2720. doi: https://doi.org/10.1111/j.1365-2818.1982.tb04625.x. URL https://onlinelibrary.wiley.com/doi/abs/10.1111/j.1365-2818.1982.tb04625.x.

[103] H. Kanno, R. J. Speedy, and C. A. Angell. Supercooling of water to -92degreesc under pressure. *Science*, 189(4206):880–881, 1975. ISSN 0036-8075. doi: 10.1126/science.189.4206.880. URL <GotoISI>://WOS:A1975AN78500015.

[104] William F Tivol, Ariane Briegel, and Grant J Jensen. An improved cryogen for plunge freezing. *Microscopy and Microanalysis*, 14(5):375–379, 2008. ISSN 1431-9276. doi: 10.1017/s1431927608080781. URL https://doi.org/10.1017/S1431927608080781.

[105] H. Moor. Die gefrier-fixation lebender zellen und ihre anwendung in der elektronenmikroskopie. *Zeitschrift Fur Zellforschung Und Mikroskopische Anatomie*, 62(4):546–580, 1964. doi: 10.1007/bf00338850. URL <GotoISI>://WOS:A1964WP90600010.

[106] Hans Moor. *Theory and Practice of High Pressure Freezing*, pages 175–191. Springer Berlin Heidelberg, Berlin, Heidelberg, 1987. ISBN 978-3-642-72815-0. doi: 10.1007/978-3-642-72815-0_8. URL https://doi.org/10.1007/978-3-642-72815-0_8.

[107] Daniel Studer, Bruno M. Humbel, and Matthias Chiquet. Electron microscopy of high pressure frozen samples: bridging the gap between cellular ultrastructure and atomic resolution. *Histochemistry and Cell Biology*, 130(5):877–889, 2008. ISSN 1432-119X. doi: 10.1007/s00418-008-0500-1. URL https://doi.org/10.1007/s00418-008-0500-1.

[108] Giulia Weissenberger, Rene J. M. Henderikx, and Peter J. Peters. Understanding the invisible hands of sample preparation for cryo-em. *Nature Methods*, 18 (5):463–471, 2021. ISSN 1548-7105. doi: 10.1038/s41592-021-01130-6. URL https://doi.org/10.1038/s41592-021-01130-6.

[109] Robert M. Glaeser. Preparing better samples for cryo–electron microscopy: Biochemical challenges do not end with isolation and purification. *Annual Review of Biochemistry*, 90(1):451–474, 2021. doi: 10.1146/annurev-biochem-072020-020231. URL https://www.annualreviews.org/doi/abs/10.1146/annurev-biochem-072020-020231.

[110] David P. Klebl, Louie Aspinall, and Stephen P. Muench. Time resolved applications for cryo-em; approaches, challenges and future directions. *Current Opinion in Structural Biology*, 83:102696, 2023. ISSN 0959-440X. doi: https://doi.org/10.1016/j.sbi.2023.102696. URL https://www.sciencedirect.com/science/article/pii/S0959440X23001707.

[111] Sascha Josef Amann, Demian Keihsler, Tatyana Bodrug, Nicholas G. Brown, and David Haselbach. Frozen in time: analyzing molecular dynamics with time-resolved cryo-em. *Structure*, 31(1):4–19, 2023. ISSN 0969-2126. doi: https://doi.org/10.1016/j.str.2022.11.014. URL https://www.sciencedirect.com/science/article/pii/S0969212622004853.

[112] M. Fuest, M. Schaffer, G. M. Nocera, R. I. Galilea-Kleinsteuber, J. E. Messling, M. Heymann, J. M. Plitzko, and T. P. Burg. In situ microfluidic cryofixation for cryo focused ion beam milling and cryo electron tomography. *Sci Rep*, 9(1):19133, 2019. ISSN 2045-2322 (Electronic) 2045-2322 (Linking). doi: 10.1038/s41598-019-55413-2. URL https://www.ncbi.nlm.nih.gov/pubmed/31836773https://www.ncbi.nlm.nih.gov/pmc/articles/PMC6911106/pdf/41598_2019_Article_55413.pdf.

[113] A. Al-Amoudi, L. P. O. Norlen, and J. Dubochet. Cryo-electron microscopy of vitreous sections of native biological cells and tissues. *Journal of Structural Biology*, 148(1):131–135, 2004. ISSN 1047-8477. doi: 10.1016/j.jsb.2004.03.010. URL <GotoISI>://WOS:000224065100011.

[114] M. Marko, C. Hsieh, W. Moberlychan, C. A. Mannella, and J. Frank. Focused ion beam milling of vitreous water: prospects for an alternative to cryo-ultramicrotomy of frozen-hydrated biological samples. *J Microsc*, 222(Pt 1):42–7, 2006. ISSN 0022-2720 (Print) 0022-2720 (Linking). doi: 10.1111/j.1365-2818.2006.01567.x. URL https://www.ncbi.nlm.nih.gov/pubmed/16734713https://onlinelibrary.wiley.com/doi/pdf/10.1111/j.1365-2818.2006.01567.x.

[115] A. Schertel, N. Snaidero, H. M. Han, T. Ruhwedel, M. Laue, M. Grabenbauer, and W. Möbius. Cryo fib-sem: Volume imaging of cellular ultrastructure in native frozen specimens. *Journal of Structural Biology*, 184(2):355–360, 2013. ISSN 1047-8477. doi: 10.1016/j.jsb.2013.09.024. URL <GotoISI>://WOS:000327171000029.

[116] K. Kelley, A. M. Raczkowski, O. Klykov, P. Jaroenlak, D. Bobe, M. Kopylov, E. T. Eng, G. Bhabha, C. S. Potter, B. Carragher, and A. J. Noble. Waffle method: A general and flexible approach for improving throughput in fib-milling. *Nature Communications*, 13(1), 2022. doi: 10.1038/s41467-022-29501-3. URL <GotoISI>://WOS:000779311200031.

[117] Vladimir K. Zworykin. The scanning electron microscope. *Scientific American*, 167(3):111–113, 1942. ISSN 00368733, 19467087. URL http://www.jstor.org/stable/24967890.

[118] C. W. Oatley. The early history of the scanning electron microscope. *Journal of Applied Physics*, 53(2):R1–R13, 1982. ISSN 0021-8979. doi: 10.1063/1.331666. URL https://doi.org/10.1063/1.331666.

[119] C. A. Volkert and A. M. Minor. Focused ion beam microscopy and micromachining. *MRS Bulletin*, 32(5):389–399, 2007. ISSN 1938-1425. doi: 10.1557/mrs2007.62. URL https://doi.org/10.1557/mrs2007.62.

[120] J. H. Orloff and L. W. Swanson. Study of a field-ionization source for microprobe applications. *Journal of Vacuum Science and Technology*, 12(6):1209–1213, 1975. ISSN 0022-5355. doi: 10.1116/1.568497. URL https://doi.org/10.1116/1.568497.

[121] R. L. Seliger, J. W. Ward, V. Wang, and R. L. Kubena. A high-intensity scanning ion probe with submicrometer spot size. *Applied Physics Letters*, 34(5):310–312, 2008. ISSN 0003-6951. doi: 10.1063/1.90786. URL https://doi.org/10.1063/1.90786.

[122] Noel S. Smith, John A. Notte, and Adam V. Steele. Advances in source technology for focused ion beam instruments. *MRS Bulletin*, 39(4):329–335, 2014. ISSN 1938-1425. doi: 10.1557/mrs.2014.53. URL https://doi.org/10.1557/mrs.2014.53.

[123] R Geller. Ecris: The electron cyclotron resonance ion sources. *Annual Review of Nuclear and Particle Science*, 40(1):15–44, 1990. doi: 10.1146/annurev.ns.40.120190.000311. URL https://www.annualreviews.org/doi/abs/10.1146/annurev.ns.40.120190.000311.

[124] Katja Höflich, Gerhard Hobler, Frances I Allen, Tom Wirtz, Gemma Rius, Arkady V Krasheninnikov, Matthias Schmidt, Ivo Utke, Nico Klingner, and Markus Osenberg. Roadmap for focused ion beam technologies. *arXiv preprint arXiv:2305.19631*, 2023.

[125] Boo Ki Min, Ju Sung Kim, Seung Ju Lim, Hyun OH Joo, Sang Jung Ahn, Doyoung Kim, Sung Duk Kwon, Seung Oun Kang, and Eun Ha Choi. Ion beam

characteristics of liquid metal (gallium) ion source with inclusion of suppressor. *Nanoscience and Nanotechnology Letters*, 7(12):945–949, 2015. ISSN 1941-4900.

[126] Adelajda Polkowska, Małgorzata Warmuzek, Julia Kalarus, Wojciech Polkowski, and Natalia Sobczak. A comparison of various imaging modes in scanning electron microscopy during evaluation of selected si/refractory sessile drop couples after wettability tests at ultra-high temperature. *Prace Instytutu Odlewnictwa*, 57(4), 2017. ISSN 1899-2439.

[127] Agnieszka Priebe and Johann Michler. Review of recent advances in gas-assisted focused ion beam time-of-flight secondary ion mass spectrometry (fib-tof-sims). *Materials*, 16(5):2090, 2023. ISSN 1996-1944. URL https://www.mdpi.com/1996-1944/16/5/2090.

[128] J. L. Carson. Fundamental technical elements of freeze-fracture/freeze-etch in biological electron microscopy. *J Vis Exp*, (91):51694, 2014. ISSN 1940-087x. doi: 10.3791/51694.

[129] V. Baena, R. L. Schalek, J. W. Lichtman, and M. Terasaki. Serial-section electron microscopy using automated tape-collecting ultramicrotome (atum). *Methods Cell Biol*, 152:41–67, 2019. ISSN 0091-679X (Print) 0091-679x. doi: 10.1016/bs.mcb.2019.04.004.

[130] Lucy M. Collinson, Carles Bosch, Anwen Bullen, Jemima J. Burden, Raffaella Carzaniga, Cheng Cheng, Michele C. Darrow, Georgina Fletcher, Errin Johnson, Kedar Narayan, Christopher J. Peddie, Martyn Winn, Charles Wood, Ardan Patwardhan, Gerard J. Kleywegt, and Paul Verkade. Volume em: a quiet revolution takes shape. *Nature Methods*, 20(6):777–782, 2023. ISSN 1548-7105. doi: 10.1038/s41592-023-01861-8. URL https://doi.org/10.1038/s41592-023-01861-8.

[131] Christopher J. Peddie, Christel Genoud, Anna Kreshuk, Kimberly Meechan, Kristina D. Micheva, Kedar Narayan, Constantin Pape, Robert G. Parton, Nicole L. Schieber, Yannick Schwab, Benjamin Titze, Paul Verkade, Aubrey Weigel, and Lucy M. Collinson. Volume electron microscopy. *Nature Reviews Methods Primers*, 2(1):51, 2022. ISSN 2662-8449. doi: 10.1038/s43586-022-00131-9. URL https://doi.org/10.1038/s43586-022-00131-9.

[132] Benjamin Titze and Christel Genoud. Volume scanning electron microscopy for imaging biological ultrastructure. *Biology of the Cell*, 108(11):307–323, 2016. ISSN 0248-4900. doi: https://doi.org/10.1111/boc.201600024. URL https://onlinelibrary.wiley.com/doi/abs/10.1111/boc.201600024.

[133] V. Lam and E. Villa. Practical approaches for cryo-fib milling and applications for cellular cryo-electron tomography. *Methods Mol Biol*, 2215:49–82, 2021. ISSN 1064-3745 (Print) 1064-3745. doi: 10.1007/978-1-0716-0966-8_3.

[134] F. R. Wagner, R. Watanabe, R. Schampers, D. Singh, H. Persoon, M. Schaffer, P. Fruhstorfer, J. Plitzko, and E. Villa. Preparing samples from whole cells using focused-ion-beam milling for cryo-electron tomography. *Nat Protoc*, 15(6):2041–2070, 2020. ISSN 1754-2189 (Print) 1750-2799. doi: 10.1038/s41596-020-0320-x.

[135] M. Schaffer, J. Mahamid, B. D. Engel, T. Laugks, W. Baumeister, and J. M. Plitzko. Optimized cryo-focused ion beam sample preparation aimed at in situ structural studies of membrane proteins. *J Struct Biol*, 197(2):73–82, 2017. ISSN 1047-8477. doi: 10.1016/j.jsb.2016.07.010.

[136] Georg Wolff, Ronald W. A. L. Limpens, Shawn Zheng, Eric J. Snijder, David A. Agard, Abraham J. Koster, and Montserrat Bárcena. Mind the gap: Micro-expansion joints drastically decrease the bending of fib-milled cryo-lamellae. *Journal of Structural Biology*, 208(3):107389, 2019. ISSN 1047-8477. doi: https://doi.org/10.1016/j.jsb.2019.09.006. URL https://www.sciencedirect.com/science/article/pii/S104784771930200X.

[137] M. Dumoux, T. Glen, J. L. R. Smith, E. M. L. Ho, L. M. A. Perdigao, A. Pennington, S. Klumpe, N. B. Y. Yee, D. A. Farmer, P. Y. A. Lai, W. Bowles, R. Kelley, J. M. Plitzko, L. Wu, M. Basham, D. K. Clare, C. A. Siebert, M. C. Darrow, J. H. Naismith, M. Grange, and G. Zanetti. Cryo-plasma fib/sem volume imaging of biological specimens. *Elife*, 12, 2023. ISSN 2050-084X. doi: 10.7554/eLife.83623. URL <GotoISI>://WOS:000946348400001.

[138] J. Arnold, J. Mahamid, V. Lucic, A. de Marco, J. J. Fernandez, T. Laugks, T. Mayer, A. A. Hyman, W. Baumeister, and J. M. Plitzko. Site-specific cryo-focused ion beam sample preparation guided by 3d correlative microscopy. *Biophys J*, 110(4):860–9, 2016. ISSN 1542-0086 (Electronic) 0006-3495 (Linking). doi: 10.1016/j.bpj.2015.10.053. URL https://www.ncbi.nlm.nih.gov/pubmed/26769364.

[139] J. Yang, V. Vrbovská, T. Franke, B. Sibert, M. Larson, A. Hall, A. Rigort, J. Mitchels, and E. R. Wright. Integrated fluorescence microscopy (iflm) for cryo-fib-milling and in-situ cryo-et. *bioRxiv*, 2023. doi: 10.1101/2023.07.11.548578.

[140] Jie E. Yang, Matthew R. Larson, Bryan S. Sibert, Samantha Shrum, and Elizabeth R. Wright. Correlator: Interactive software for real-time high precision cryo-correlative light and electron microscopy. *Journal of Structural Biology*, 213(2):107709, 2021. ISSN 1047-8477. doi: https://doi.org/10.

1016/j.jsb.2021.107709. URL https://www.sciencedirect.com/science/article/pii/S1047847721000149.

[141] Julia Mahamid, Stefan Pfeffer, Miroslava Schaffer, Elizabeth Villa, Radostin Danev, Luis Kuhn Cuellar, Friedrich Förster, Anthony A. Hyman, Jürgen M. Plitzko, and Wolfgang Baumeister. Visualizing the molecular sociology at the hela cell nuclear periphery. *Science*, 351(6276):969–972, 2016. doi: doi:10.1126/science.aad8857. URL https://www.science.org/doi/abs/10.1126/science.aad8857.

[142] A. Sartori, R. Gatz, F. Beck, A. Rigort, W. Baumeister, and J. M. Plitzko. Correlative microscopy: Bridging the gap between fluorescence light microscopy and cryo-electron tomography. *Journal of Structural Biology*, 160(2):135–145, 2007. ISSN 1047-8477. doi: 10.1016/j.jsb.2007.07.011. URL <GotoISI>://WOS:000250456300003.

[143] Patrick C. Hoffmann, Stefano L. Giandomenico, Iva Ganeva, Michael R. Wozny, Magdalena Sutcliffe, Madeline A. Lancaster, and Wanda Kukulski. Electron cryo-tomography reveals the subcellular architecture of growing axons in human brain organoids. *eLife*, 10:e70269, 2021. ISSN 2050-084X. doi: 10.7554/eLife.70269. URL https://doi.org/10.7554/eLife.70269.

[144] M. R. Wozny, A. Di Luca, D. R. Morado, A. Picco, R. Khaddaj, P. Campomanes, L. Ivanović, P. C. Hoffmann, E. A. Miller, S. Vanni, and W. Kukulski. In situ architecture of the er-mitochondria encounter structure. *Nature*, 618(7963):188–192, 2023. ISSN 0028-0836 (Print) 0028-0836. doi: 10.1038/s41586-023-06050-3.

[145] D. Spehner, A. M. Steyer, L. Bertinetti, I. Orlov, L. Benoit, K. Pernet-Gallay, A. Schertel, and P. Schultz. Cryo-fib-sem as a promising tool for localizing proteins in 3d. *Journal of Structural Biology*, 211(1), 2020. ISSN 1047-8477. doi: 10.1016/j.jsb.2020.107528. URL <GotoISI>://WOS:000540690600003.

[146] Y. N. Zhu, D. P. Sun, A. Schertel, J. Y. Ning, X. F. Fu, P. P. Gwo, A. M. Watson, L. C. Zanetti-Domingues, M. L. Martin-Fernandez, Z. Freyberg, and P. J. Zhang. Serial cryofib/sem reveals cytoarchitectural disruptions in leigh syndrome patient cells. *Structure*, 29(1):82–+, 2021. ISSN 0969-2126. doi: 10.1016/j.str.2020.10.003. URL <GotoISI>://WOS:000606462800010.

[147] Anna M. Steyer, Andreas Schertel, Christos Nardis, and Wiebke Möbius. *Chapter 1 - FIB-SEM of mouse nervous tissue: Fast and slow sample preparation*, volume 152, pages 1–21. Academic Press, 2019. ISBN 0091-679X. doi: https://doi.org/10.1016/bs.mcb.2019.03.009. URL https://www.sciencedirect.com/science/article/pii/S0091679X19300317.

[148] C. D. Parmenter, M. W. Fay, C. Hartfield, and H. M. Eltaher. Making the practically impossible "merely difficult"–cryogenic fib lift-out for "damage free" soft matter imaging. *Microsc Res Tech*, 79(4):298–303, 2016. ISSN 1097-0029 (Electronic) 1059-910X (Linking). doi: 10.1002/jemt.22630. URL https://www.ncbi.nlm.nih.gov/pubmed/26875988.

[149] C. D. Parmenter and Z. A. Nizamudeen. Cryo-fib-lift-out: practically impossible to practical reality. *J Microsc*, 2020. ISSN 1365-2818 (Electronic) 0022-2720 (Linking). doi: 10.1111/jmi.12953. URL https://www.ncbi.nlm.nih.gov/pubmed/32815145.

[150] S. Rubino, S. Akhtar, P. Melin, A. Searle, P. Spellward, and K. Leifer. A site-specific focused-ion-beam lift-out method for cryo transmission electron microscopy. *J Struct Biol*, 180(3):572–6, 2012. ISSN 1095-8657 (Electronic) 1047-8477 (Linking). doi: 10.1016/j.jsb.2012.08.012. URL https://www.ncbi.nlm.nih.gov/pubmed/23000702.

[151] D. K. Schreiber, D. E. Perea, J. V. Ryan, J. E. Evans, and J. D. Vienna. A method for site-specific and cryogenic specimen fabrication of liquid/solid interfaces for atom probe tomography. *Ultramicroscopy*, 194:89–99, 2018. ISSN 1879-2723 (Electronic) 0304-3991 (Linking). doi: 10.1016/j.ultramic.2018.07.010. URL https://www.ncbi.nlm.nih.gov/pubmed/30092393.

[152] Tobias Zachs, Andreas Schertel, João Medeiros, Gregor L. Weiss, Jannik Hugener, Joao Matos, and Martin Pilhofer. Fully automated, sequential focused ion beam milling for cryo-electron tomography. *eLife*, 9:e52286, 2020. ISSN 2050-084X. doi: 10.7554/eLife.52286. URL https://doi.org/10.7554/eLife.52286.

[153] Genevieve Buckley, Gediminas Gervinskas, Cyntia Taveneau, Hariprasad Venugopal, James C. Whisstock, and Alex de Marco. Automated cryo-lamella preparation for high-throughput in-situ structural biology. *Journal of Structural Biology*, 210(2):107488, 2020. ISSN 1047-8477. doi: https://doi.org/10.1016/j.jsb.2020.107488. URL https://www.sciencedirect.com/science/article/pii/S104784772030054X.

[154] Patrick Cleeve, David Dierickx, Genevieve Buckley, Sergey Gorelick, Lucile Naegele, Lachlan Burne, James C Whisstock, and Alex de Marco. Openfibsem: an application programming interface for easy fib/sem automation. *bioRxiv*, page 2022.11.01.514681, 2022. doi: 10.1101/2022.11.01.514681. URL https://www.biorxiv.org/content/biorxiv/early/2022/11/02/2022.11.01.514681.full.pdf.

[155] J. Hanske, Y. Sadian, and C. W. Müller. The cryo-em resolution revolution and

transcription complexes. *Curr Opin Struct Biol*, 52:8–15, 2018. ISSN 0959-440X (Print) 0959-440x. doi: 10.1016/j.sbi.2018.07.002.

[156] Liang Xue, Swantje Lenz, Maria Zimmermann-Kogadeeva, Dimitry Tegunov, Patrick Cramer, Peer Bork, Juri Rappsilber, and Julia Mahamid. Visualizing translation dynamics at atomic detail inside a bacterial cell. *Nature*, 610(7930): 205–211, 2022. ISSN 1476-4687. doi: 10.1038/s41586-022-05255-2. URL https://doi.org/10.1038/s41586-022-05255-2.

[157] E. R. J. Quemin, E. A. Machala, B. Vollmer, V. Pražák, D. Vasishtan, R. Rosch, M. Grange, L. E. Franken, L. A. Baker, and K. Grünewald. Cellular electron cryo-tomography to study virus-host interactions. *Annu Rev Virol*, 7(1):239–262, 2020. ISSN 2327-056x. doi: 10.1146/annurev-virology-021920-115935.

[158] J. Wagner, M. Schaffer, and R. Fernández-Busnadiego. Cryo-electron tomography-the cell biology that came in from the cold. *FEBS Lett*, 591(17): 2520–2533, 2017. ISSN 0014-5793. doi: 10.1002/1873-3468.12757.

[159] S. Pfeffer and J. Mahamid. Unravelling molecular complexity in structural cell biology. *Curr Opin Struct Biol*, 52:111–118, 2018. ISSN 1879-033X (Electronic) 0959-440X (Linking). doi: 10.1016/j.sbi.2018.08.009. URL https://www.ncbi.nlm.nih.gov/pubmed/30339965.

[160] B. D. Engel, M. Schaffer, L. K. Cuellar, E. Villa, J. M. Plitzko, and W. Baumeister. Native architecture of the chlamydomonas chloroplast revealed by in situ cryo-electron tomography. *Elife*, 4, 2015. ISSN 2050-084X. doi: 10.7554/eLife.04889. URL <GotoISI>://WOS:000347917200002.

[161] Yury S. Bykov, Miroslava Schaffer, Svetlana O. Dodonova, Sahradha Albert, Jürgen M. Plitzko, Wolfgang Baumeister, Benjamin D. Engel, and John A. G. Briggs. The structure of the copi coat determined within the cell. *eLife*, 6: e32493, 2017. ISSN 2050-084X. doi: 10.7554/eLife.32493. URL https://doi.org/10.7554/eLife.32493.

[162] E. S. Freeman Rosenzweig, B. Xu, L. Kuhn Cuellar, A. Martinez-Sanchez, M. Schaffer, M. Strauss, H. N. Cartwright, P. Ronceray, J. M. Plitzko, F. Förster, N. S. Wingreen, B. D. Engel, L. C. M. Mackinder, and M. C. Jonikas. The eukaryotic co(2)-concentrating organelle is liquid-like and exhibits dynamic reorganization. *Cell*, 171(1):148–162.e19, 2017. ISSN 0092-8674 (Print) 0092-8674. doi: 10.1016/j.cell.2017.08.008.

[163] J. Theis, T. K. Gupta, J. Klingler, W. Wan, S. Albert, S. Keller, B. D. Engel, and M. Schroda. Vipp1 rods engulf membranes containing phosphatidylinositol phosphates. *Scientific Reports*, 9, 2019. ISSN 2045-2322. doi: 10.1038/s41598-019-44259-3. URL <GotoISI>://WOS:000472029100004.

[164] Wojciech Wietrzynski, Miroslava Schaffer, Dimitry Tegunov, Sahradha Albert, Atsuko Kanazawa, Jürgen M. Plitzko, Wolfgang Baumeister, and Benjamin D. Engel. Charting the native architecture of chlamydomonas thylakoid membranes with single-molecule precision. *eLife*, 9:e53740, 2020. ISSN 2050-084X. doi: 10.7554/eLife.53740. URL https://doi.org/10.7554/eLife.53740.

[165] Shyamal Mosalaganti, Jan Kosinski, Sahradha Albert, Miroslava Schaffer, Daniela Strenkert, Patrice A. Salomé, Sabeeha S. Merchant, Jürgen M. Plitzko, Wolfgang Baumeister, Benjamin D. Engel, and Martin Beck. In situ architecture of the algal nuclear pore complex. *Nature Communications*, 9(1): 2361, 2018. ISSN 2041-1723. doi: 10.1038/s41467-018-04739-y. URL https://doi.org/10.1038/s41467-018-04739-y.

[166] S. Albert, M. Schaffer, F. Beck, S. Mosalaganti, S. Asano, H. F. Thomas, J. M. Plitzko, M. Beck, W. Baumeister, and B. D. Engel. Proteasomes tether to two distinct sites at the nuclear pore complex. *Proc Natl Acad Sci U S A*, 114(52): 13726–13731, 2017. ISSN 0027-8424 (Print) 0027-8424. doi: 10.1073/pnas.1716305114.

[167] Sahradha Albert, Wojciech Wietrzynski, Chia-Wei Lee, Miroslava Schaffer, Florian Beck, Jan M. Schuller, Patrice A. Salomé, Jürgen M. Plitzko, Wolfgang Baumeister, and Benjamin D. Engel. Direct visualization of degradation microcompartments at the er membrane. *Proceedings of the National Academy of Sciences*, 117(2):1069–1080, 2020. doi: doi:10.1073/pnas.1905641117. URL https://www.pnas.org/doi/abs/10.1073/pnas.1905641117.

[168] Stefan Pfeffer, Johanna Dudek, Miroslava Schaffer, Bobby G. Ng, Sahradha Albert, Jürgen M. Plitzko, Wolfgang Baumeister, Richard Zimmermann, Hudson H. Freeze, Benjamin D. Engel, and Friedrich Förster. Dissecting the molecular organization of the translocon-associated protein complex. *Nature Communications*, 8(1):14516, 2017. ISSN 2041-1723. doi: 10.1038/ncomms14516. URL https://doi.org/10.1038/ncomms14516.

[169] Johann Milhelm Meigen. Systematische beschreibung der bekannten europäischen zweiflügeligen insekten. v. 6. *123456789/807*, 1830.

[170] R. Stephenson and N. H. Metcalfe. Drosophila melanogaster: a fly through its history and current use. *J R Coll Physicians Edinb*, 43(1):70–5, 2013. ISSN 1478-2715. doi: 10.4997/jrcpe.2013.116.

[171] Tonse N. J. Raju. The nobel chronicles. *The Lancet*, 353(9147):157, 1999. ISSN 0140-6736. doi: https://doi.org/10.1016/S0140-6736(05)76205-X. URL https://www.sciencedirect.com/science/article/pii/S014067360576205X.

[172] Stephanie Elizabeth Mohr. *First in fly: Drosophila research and biological discovery*. Harvard University Press, 2018. ISBN 0674971019.

[173] Elizabeth T Ables, Grace H Hwang, Danielle S Finger, Taylor D Hinnant, and Daniela Drummond-Barbosa. A genetic mosaic screen reveals ecdysone-responsive genes regulating drosophila oogenesis. *G3 Genes|Genomes|Genetics*, 6(8):2629–2642, 2016. ISSN 2160-1836. doi: 10.1534/g3.116.028951. URL https://doi.org/10.1534/g3.116.028951.

[174] Yukiko M Yamashita. Subcellular specialization and organelle behavior in germ cells. *Genetics*, 208(1):19–51, 2018. ISSN 1943-2631. doi: 10.1534/genetics.117.300184. URL https://doi.org/10.1534/genetics.117.300184.

[175] John M McLaughlin and Diana P Bratu. Drosophila melanogaster oogenesis: an overview. *Drosophila oogenesis: methods and protocols*, pages 1–20, 2015. ISSN 1493928503.

[176] Rebecca Bastock and Daniel St Johnston. Drosophila oogenesis. *Current Biology*, 18(23):R1082–R1087, 2008. ISSN 0960-9822.

[177] Diane Patricia Vig Lebo and Kimberly McCall. Murder on the ovarian express: A tale of non-autonomous cell death in the drosophila ovary. *Cells*, 10(6): 1454, 2021. ISSN 2073-4409. URL https://www.mdpi.com/2073-4409/10/6/1454.

[178] Taylor D Hinnant, Julie A Merkle, and Elizabeth T Ables. Coordinating proliferation, polarity, and cell fate in the drosophila female germline. *Frontiers in cell and developmental biology*, 8:19, 2020. ISSN 2296-634X.

[179] L. Cooley and W. E. Theurkauf. Cytoskeletal functions during drosophila oogenesis. *Science*, 266(5185):590–6, 1994. ISSN 0036-8075 (Print) 0036-8075. doi: 10.1126/science.7939713.

[180] A. Stathopoulos and D. Iber. Studies of morphogens: keep calm and carry on. *Development*, 140(20):4119–24, 2013. ISSN 0950-1991 (Print) 0950-1991. doi: 10.1242/dev.095141.

[181] Jonathan N. Wells and Cédric Feschotte. A field guide to eukaryotic transposable elements. *Annual review of genetics*, 2020.

[182] A. C. Spradling and G. M. Rubin. Transposition of cloned p elements into drosophila germ line chromosomes. *Science*, 218(4570):341–7, 1982. ISSN 0036-8075 (Print) 0036-8075. doi: 10.1126/science.6289435.

[183] Robert J Ross, Molly M Weiner, and Haifan Lin. Piwi proteins and piwi-interacting rnas in the soma. *Nature*, 505(7483):353–359, 2014. ISSN 0028-0836.

[184] Alexei A. Aravin, Gregory J. Hannon, and Julius Brennecke. The piwi-pirna pathway provides an adaptive defense in the transposon arms race. *Science*, 318(5851):761–764, 2007. doi: doi:10.1126/science.1146484. URL https://www.science.org/doi/abs/10.1126/science.1146484.

[185] Deniz M. Ozata, Ildar Gainetdinov, Ansgar Zoch, Dónal O'Carroll, and Phillip D. Zamore. Piwi-interacting rnas: small rnas with big functions. *Nature Reviews Genetics*, 20(2):89–108, 2019. ISSN 1471-0064. doi: 10.1038/s41576-018-0073-3. URL https://doi.org/10.1038/s41576-018-0073-3.

[186] David J. Finnegan. Eukaryotic transposable elements and genome evolution. *Trends in Genetics*, 5:103–107, 1989. ISSN 0168-9525. doi: https://doi.org/10.1016/0168-9525(89)90039-5. URL https://www.sciencedirect.com/science/article/pii/0168952589900395.

[187] Vincent Mérel, Matthieu Boulesteix, Marie Fablet, and Cristina Vieira. Transposable elements in drosophila. *Mobile DNA*, 11(1):23, 2020. ISSN 1759-8753. doi: 10.1186/s13100-020-00213-z. URL https://doi.org/10.1186/s13100-020-00213-z.

[188] M. J. Curcio, S. Lutz, and P. Lesage. The ty1 ltr-retrotransposon of budding yeast, saccharomyces cerevisiae. *Microbiol Spectr*, 3(2):1–35, 2015. ISSN 2165-0497. doi: 10.1128/microbiolspec.MDNA3-0053-2014.

[189] J. Ashley, B. Cordy, D. Lucia, L. G. Fradkin, V. Budnik, and T. Thomson. Retrovirus-like gag protein arc1 binds rna and traffics across synaptic boutons. *Cell*, 172(1-2):262–+, 2018. ISSN 0092-8674. doi: 10.1016/j.cell.2017.12.022. URL <GotoISI>://WOS:000419840100024.

[190] André S. Bachmann, Gloria Corpuz, Wade P. Hareld, Gordon Wang, and Beth-Ann Coller. A simple method for the rapid purification of copia virus-like particles from drosophila schneider 2 cells. *Journal of Virological Methods*, 115(2):159–165, 2004. ISSN 0166-0934. doi: https://doi.org/10.1016/j.jviromet.2003.09.025. URL https://www.sciencedirect.com/science/article/pii/S0166093403003082.

[191] Kristina Clemens, Liza Larsen, Min Zhang, Yurii Kuznetsov, Virginia Bilanchone, Arlo Randall, Adam Harned, Rhonda DaSilva, Kunio Nagashima, Alexander McPherson, Pierre Baldi, and Suzanne Sandmeyer. The ty3 gag3 spacer controls intracellular condensation and uncoating. *Journal of Virology*, 85(7):3055–3066, 2011. doi: doi:10.1128/jvi.01055-10. URL https://journals.asm.org/doi/abs/10.1128/jvi.01055-10.

[192] Svetlana O. Dodonova, Simone Prinz, Virginia Bilanchone, Suzanne Sandmeyer, and John A. G. Briggs. Structure of the ty3/gypsy retrotransposon capsid and the evolution of retroviruses. *Proceedings of the National Academy*

of Sciences, 116(20):10048–10057, 2019. doi: doi:10.1073/pnas.1900931116. URL https://www.pnas.org/doi/abs/10.1073/pnas.1900931116.

[193] Liza S. Z. Larsen, Nadejda Beliakova-Bethell, Virginia Bilanchone, Min Zhang, Anne Lamsa, Rhonda DaSilva, G. Wesley Hatfield, Kunio Nagashima, and Suzanne Sandmeyer. Ty3 nucleocapsid controls localization of particle assembly. *Journal of Virology*, 82(5):2501–2514, 2008. doi: doi:10.1128/jvi.01814-07. URL https://journals.asm.org/doi/abs/10.1128/jvi.01814-07.

[194] Becky Irwin, Michael Aye, Pierre Baldi, Nadejda Beliakova-Bethell, Henry Cheng, Yimeng Dou, Willy Liou, and Suzanne Sandmeyer. Retroviruses and yeast retrotransposons use overlapping sets of host genes. *Genome research*, 15(5):641–654, 2005. ISSN 1088-9051.

[195] Sudhir Kumar Rai, Maya Sangesland, Michael Lee Jr, Caroline Esnault, Yujin Cui, Atreyi Ghatak Chatterjee, and Henry L Levin. Host factors that promote retrotransposon integration are similar in distantly related eukaryotes. *PLoS Genetics*, 13(12):e1006775, 2017. ISSN 1553-7390.

[196] Andre Schwarz. *Nucleoporin mRNA localization and Annulate Lamellae biosynthesis during Drosophila melanogaster oogenesis*. Thesis, 2020.

[197] Yoan Diekmann and José B. Pereira-Leal. Evolution of intracellular compartmentalization. *Biochemical Journal*, 449(2):319–331, 2012. ISSN 0264-6021. doi: 10.1042/bj20120957. URL https://doi.org/10.1042/BJ20120957.

[198] N Amy Yewdall, Alexander F Mason, and Jan CM Van Hest. The hallmarks of living systems: towards creating artificial cells. *Interface Focus*, 8(5):20180023, 2018. ISSN 2042-8898.

[199] Sven B Gould. Membranes and evolution. *Current Biology*, 28(8):R381–R385, 2018. ISSN 0960-9822.

[200] Jonathan Lombard, Purificación López-García, and David Moreira. The early evolution of lipid membranes and the three domains of life. *Nature Reviews Microbiology*, 10(7):507–515, 2012. ISSN 1740-1526.

[201] Damien P Devos, Ralph Gräf, and Mark C Field. Evolution of the nucleus. *Current opinion in cell biology*, 28:8–15, 2014. ISSN 0955-0674.

[202] B. Hampoelz, A. Andres-Pons, P. Kastritis, and M. Beck. Structure and assembly of the nuclear pore complex. *Annu Rev Biophys*, 48:515–536, 2019. ISSN 1936-122x. doi: 10.1146/annurev-biophys-052118-115308.

[203] M. Beck, F. Förster, M. Ecke, J. M. Plitzko, F. Melchior, G. Gerisch, W. Baumeister, and O. Medalia. Nuclear pore complex structure and dynamics revealed by

cryoelectron tomography. *Science*, 306(5700):1387–90, 2004. ISSN 0036-8075. doi: 10.1126/science.1104808.

[204] A. von Appen, J. Kosinski, L. Sparks, A. Ori, A. L. DiGuilio, B. Vollmer, M. T. Mackmull, N. Banterle, L. Parca, P. Kastritis, K. Buczak, S. Mosalaganti, W. Hagen, A. Andres-Pons, E. A. Lemke, P. Bork, W. Antonin, J. S. Glavy, K. H. Bui, and M. Beck. In situ structural analysis of the human nuclear pore complex. *Nature*, 526(7571):140–143, 2015. ISSN 1476-4687 (Electronic) 0028-0836 (Linking). doi: 10.1038/nature15381. URL https://www.ncbi.nlm.nih.gov/pubmed/26416747.

[205] A. von Appen and M. Beck. Structure determination of the nuclear pore complex with three-dimensional cryo electron microscopy. *J Mol Biol*, 428(10 Pt A):2001–10, 2016. ISSN 1089-8638 (Electronic) 0022-2836 (Linking). doi: 10.1016/j.jmb.2016.01.004. URL https://www.ncbi.nlm.nih.gov/pubmed/26791760.

[206] J. Kosinski, S. Mosalaganti, A. von Appen, R. Teimer, A. L. DiGuilio, W. Wan, K. H. Bui, W. J. Hagen, J. A. Briggs, J. S. Glavy, E. Hurt, and M. Beck. Molecular architecture of the inner ring scaffold of the human nuclear pore complex. *Science*, 352(6283):363–5, 2016. ISSN 1095-9203 (Electronic) 0036-8075 (Linking). doi: 10.1126/science.aaf0643. URL https://www.ncbi.nlm.nih.gov/pubmed/27081072.

[207] Khanh Huy Bui, Alexander Von Appen, Amanda L DiGuilio, Alessandro Ori, Lenore Sparks, Marie-Therese Mackmull, Thomas Bock, Wim Hagen, Amparo Andrés-Pons, and Joseph S Glavy. Integrated structural analysis of the human nuclear pore complex scaffold. *Cell*, 155(6):1233–1243, 2013. ISSN 0092-8674.

[208] Martin Beck, Shyamal Mosalaganti, and Jan Kosinski. From the resolution revolution to evolution: structural insights into the evolutionary relationships between vesicle coats and the nuclear pore. *Current Opinion in Structural Biology*, 52:32–40, 2018. ISSN 0959-440X. doi: https://doi.org/10.1016/j.sbi.2018.07.012. URL https://www.sciencedirect.com/science/article/pii/S0959440X17301471.

[209] Thorsten G. Müller, Vojtech Zila, Barbara Müller, and Hans-Georg Kräusslich. Nuclear capsid uncoating and reverse transcription of hiv-1. *Annual Review of Virology*, 9(1):261–284, 2022. doi: 10.1146/annurev-virology-020922-110929. URL https://www.annualreviews.org/doi/abs/10.1146/annurev-virology-020922-110929.

[210] V. Zila, E. Margiotta, B. Turoňová, T. G. Müller, C. E. Zimmerli, S. Mattei, M. Allegretti, K. Börner, J. Rada, B. Müller, M. Lusic, H. G. Kräusslich, and

M. Beck. Cone-shaped hiv-1 capsids are transported through intact nuclear pores. *Cell*, 184(4):1032–1046.e18, 2021. ISSN 0092-8674 (Print) 0092-8674. doi: 10.1016/j.cell.2021.01.025.

[211] Ryan C. Burdick, Chenglei Li, MohamedHusen Munshi, Jonathan M. O. Rawson, Kunio Nagashima, Wei-Shau Hu, and Vinay K. Pathak. Hiv-1 uncoats in the nucleus near sites of integration. *Proceedings of the National Academy of Sciences*, 117(10):5486–5493, 2020. doi: doi:10.1073/pnas.1920631117. URL https://www.pnas.org/doi/abs/10.1073/pnas.1920631117.

[212] R. Bayliss, T. Littlewood, L. A. Strawn, S. R. Wente, and M. Stewart. Glfg and fxfg nucleoporins bind to overlapping sites on importin-beta. *J Biol Chem*, 277 (52):50597–606, 2002. ISSN 0021-9258 (Print) 0021-9258. doi: 10.1074/jbc.M209037200.

[213] B. Boettcher and Y. Barral. The cell biology of open and closed mitosis. *Nucleus*, 4(3):160–5, 2013. ISSN 1949-1034 (Print) 1949-1034. doi: 10.4161/nucl.24676.

[214] S. Manhas, L. Ma, and V. Measday. The yeast ty1 retrotransposon requires components of the nuclear pore complex for transcription and genomic integration. *Nucleic Acids Res*, 46(7):3552–3578, 2018. ISSN 1362-4962 (Electronic) 0305-1048 (Linking). doi: 10.1093/nar/gky109. URL https://www.ncbi.nlm.nih.gov/pubmed/29514267.

[215] Marzia Munafo, Victoria R. Lawless, Alessandro Passera, Serena MacMillan, Susanne Bornelöv, Irmgard U. Haussmann, Matthias Soller, Gregory J. Hannon, and Benjamin Czech. Channel nuclear pore complex subunits are required for transposon silencing in drosophila. *eLife*, 10:e66321, 2021. ISSN 2050084X. doi: 10.7554/eLife.66321. URL https://doi.org/10.7554/eLife.66321.

[216] V. Guida, F. M. Cernilogar, A. Filograna, R. De Gregorio, H. Ishizu, M. C. Siomi, G. Schotta, G. C. Bellenchi, and D. Andrenacci. Production of small noncoding rnas from the flamenco locus is regulated by the gypsy retrotransposon of drosophila melanogaster. *Genetics*, 204(2):631–644, 2016. ISSN 0016-6731 (Print) 0016-6731. doi: 10.1534/genetics.116.187922.

[217] Amandine Bonnet, Carole Chaput, Noé Palmic, Benoit Palancade, and Pascale Lesage. A nuclear pore sub-complex restricts the propagation of ty retrotransposons by limiting their transcription. *PLOS Genetics*, 17(11):e1009889, 2021. doi: 10.1371/journal.pgen.1009889. URL https://doi.org/10.1371/journal.pgen.1009889.

[218] Padmapriya Varadarajan, Sundarasamy Mahalingam, Peiyun Liu, Sarah Boon Hsi Ng, Sheetal Gandotra, Desmond Suresh Kumar Dorairajoo, and

David Balasundaram. The functionally conserved nucleoporins nup124p from fission yeast and the human nup153 mediate nuclear import and activity of the tf1 retrotransposon and hiv-1 vpr. *Molecular Biology of the Cell*, 16 (4):1823–1838, 2005. doi: 10.1091/mbc.e04-07-0583. URL https://www.molbiolcell.org/doi/abs/10.1091/mbc.e04-07-0583.

[219] A. Stirbet, D. Lazár, Y. Guo, and G. Govindjee. Photosynthesis: basics, history and modelling. *Ann Bot*, 126(4):511–537, 2020. ISSN 0305-7364 (Print) 0305-7364. doi: 10.1093/aob/mcz171.

[220] Martin F. Hohmann-Marriott and Robert E. Blankenship. Evolution of photosynthesis. *Annual Review of Plant Biology*, 62(1):515–548, 2011. doi: 10.1146/annurev-arplant-042110-103811. URL https://www.annualreviews.org/doi/abs/10.1146/annurev-arplant-042110-103811.

[221] A. Rast, S. Heinz, and J. Nickelsen. Biogenesis of thylakoid membranes. *Biochimica Et Biophysica Acta-Bioenergetics*, 1847(9):821–830, 2015. ISSN 0005-2728. doi: 10.1016/j.bbabio.2015.01.007. URL <GotoISI>://WOS:000357751800008.

[222] A. Rast, M. Schaffer, S. Albert, W. Wan, S. Pfeffer, F. Beck, J. M. Plitzko, J. Nickelsen, and B. D. Engel. Biogenic regions of cyanobacterial thylakoids form contact sites with the plasma membrane. *Nat Plants*, 5(4):436–446, 2019. ISSN 2055-0278 (Electronic) 2055-0278 (Linking). doi: 10.1038/s41477-019-0399-7. URL https://www.ncbi.nlm.nih.gov/pubmed/30962530.

[223] Jotham R Austin and L Andrew Staehelin. Three-dimensional architecture of grana and stroma thylakoids of higher plants as determined by electron tomography. *Plant physiology*, 155(4):1601–1611, 2011. ISSN 1532-2548.

[224] S. Westphal, L. Heins, J. Soll, and U. C. Vothknecht. Vipp1 deletion mutant of synechocystis: a connection between bacterial phage shock and thylakoid biogenesis? *Proc Natl Acad Sci U S A*, 98(7):4243–8, 2001. ISSN 0027-8424 (Print) 0027-8424 (Linking). doi: 10.1073/pnas.061501198. URL https://www.ncbi.nlm.nih.gov/pubmed/11274448.

[225] A. Nordhues, M. A. Schottler, A. K. Unger, S. Geimer, S. Schonfelder, S. Schmollinger, M. Rutgers, G. Finazzi, B. Soppa, F. Sommer, T. Muhlhaus, T. Roach, A. Krieger-Liszkay, H. Lokstein, J. L. Crespo, and M. Schroda. Evidence for a role of vipp1 in the structural organization of the photosynthetic apparatus in chlamydomonas. *Plant Cell*, 24(2):637–59, 2012. ISSN 1532-298X (Electronic) 1040-4651 (Linking). doi: 10.1105/tpc.111.092692. URL https://www.ncbi.nlm.nih.gov/pubmed/22307852.

[226] L. Zhang, Y. Kato, S. Otters, U. C. Vothknecht, and W. Sakamoto. Essential role of vipp1 in chloroplast envelope maintenance in arabidopsis. *Plant*

Cell, 24(9):3695–707, 2012. ISSN 1532-298X (Electronic) 1040-4651 (Linking). doi: 10.1105/tpc.112.103606. URL https://www.ncbi.nlm.nih.gov/pubmed/23001039.

[227] B. Junglas, S. T. Huber, T. Heidler, L. Schlösser, D. Mann, R. Hennig, M. Clarke, N. Hellmann, D. Schneider, and C. Sachse. Pspa adopts an escrt-iii-like fold and remodels bacterial membranes. *Cell*, 184(14):3674–+, 2021. ISSN 0092-8674. doi: 10.1016/j.cell.2021.05.042. URL <GotoISI>://WOS:000671212300010.

[228] J. Liu, M. Tassinari, D. P. Souza, S. Naskar, J. K. Noel, O. Bohuszewicz, M. Buck, T. A. Williams, B. Baum, and H. H. Low. Bacterial vipp1 and pspa are members of the ancient escrt-iii membrane-remodeling superfamily. *Cell*, 184(14):3660–3673.e18, 2021. ISSN 0092-8674 (Print) 0092-8674. doi: 10.1016/j.cell.2021.05.041.

[229] Eva Fuhrmann, Jelle B. Bultema, Uwe Kahmann, Eva Rupprecht, Egbert J. Boekema, and Dirk Schneider. The vesicle-inducing protein 1 from synechocystis sp. pcc 6803 organizes into diverse higher-ordered ring structures. *Molecular Biology of the Cell*, 20(21):4620–4628, 2009. doi: 10.1091/mbc.e09-04-0319. URL https://www.molbiolcell.org/doi/abs/10.1091/mbc.e09-04-0319.

[230] Daniela Kroll, Karin Meierhoff, Nicole Bechtold, Mikio Kinoshita, Sabine Westphal, Ute C Vothknecht, Jürgen Soll, and Peter Westhoff. Vipp1, a nuclear gene of arabidopsis thaliana essential for thylakoid membrane formation. *Proceedings of the National Academy of Sciences*, 98(7):4238–4242, 2001. ISSN 0027-8424.

[231] Jennifer Heidrich, Adrien Thurotte, and Dirk Schneider. Specific interaction of im30/vipp1 with cyanobacterial and chloroplast membranes results in membrane remodeling and eventually in membrane fusion. *Biochimica et Biophysica Acta (BBA) - Biomembranes*, 1859(4):537–549, 2017. ISSN 0005-2736. doi: https://doi.org/10.1016/j.bbamem.2016.09.025. URL https://www.sciencedirect.com/science/article/pii/S0005273616303273.

[232] O. Sandoval-Ibáñez, A. Sharma, M. Bykowski, G. Borràs-Gas, Jbyh Behrendorff, S. Mellor, K. Qvortrup, J. C. Verdonk, R. Bock, Ł Kowalewska, and M. Pribil. Curvature thylakoid 1 proteins modulate prolamellar body morphology and promote organized thylakoid biogenesis in arabidopsis thaliana. *Proc Natl Acad Sci U S A*, 118(42), 2021. ISSN 0027-8424 (Print) 0027-8424. doi: 10.1073/pnas.2113934118.

[233] B. Klinkert, F. Ossenbühl, M. Sikorski, S. Berry, L. Eichacker, and J. Nickelsen. Prata, a periplasmic tetratricopeptide repeat protein involved in biogenesis of

photosystem ii in synechocystis sp. pcc 6803. *J Biol Chem*, 279(43):44639–44, 2004. ISSN 0021-9258 (Print) 0021-9258. doi: 10.1074/jbc.M405393200.

[234] A. Thurotte, T. Seidel, R. Jilly, U. Kahmann, and D. Schneider. Dnak3 is involved in biogenesis and/or maintenance of thylakoid membrane protein complexes in the cyanobacterium synechocystis sp. pcc 6803. *Life (Basel)*, 10(5), 2020. ISSN 2075-1729 (Print) 2075-1729. doi: 10.3390/life10050055.

[235] Klaas Jan van Wijk. *Proteins Involved in Biogenesis of the Thylakoid Membrane*, pages 153–175. Springer Netherlands, Dordrecht, 2001. ISBN 978-0-306-48148-2. doi: 10.1007/0-306-48148-0_9. URL https://doi.org/10.1007/0-306-48148-0_9.

[236] Elena Kreis, Katharina König, Melissa Misir, Justus Niemeyer, Frederik Sommer, and Michael Schroda. Turboid reveals the proxiomes of chlamydomonas proteins involved in thylakoid biogenesis and stress response. *Plant Physiology*, 193(3):1772–1796, 2023. ISSN 0032-0889. doi: 10.1093/plphys/kiad335. URL https://doi.org/10.1093/plphys/kiad335.

[237] S. J. Bryan, N. J. Burroughs, D. Shevela, J. Yu, E. Rupprecht, L. N. Liu, G. Mastroianni, Q. Xue, I. Llorente-Garcia, M. C. Leake, L. A. Eichacker, D. Schneider, P. J. Nixon, and C. W. Mullineaux. Localisation and interactions of the vipp1 protein in cyanobacteria. *Mol Microbiol*, 94(5):1179–95, 2014. ISSN 0950-382X (Print) 0950-382x. doi: 10.1111/mmi.12826.

[238] Ute C. Vothknecht, Stephanie Otters, Raoul Hennig, and Dirk Schneider. Vipp1: a very important protein in plastids?! *Journal of Experimental Botany*, 63(4):1699–1712, 2011. ISSN 0022-0957. doi: 10.1093/jxb/err357. URL https://doi.org/10.1093/jxb/err357.

[239] Carmen Siebenaller, Benedikt Junglas, and Dirk Schneider. Functional implications of multiple im30 oligomeric states. *Frontiers in Plant Science*, 10:1500, 2019. ISSN 1664-462X.

[240] Jennifer Heidrich, Adrien Thurotte, and Dirk Schneider. Specific interaction of im30/vipp1 with cyanobacterial and chloroplast membranes results in membrane remodeling and eventually in membrane fusion. *Biochimica et Biophysica Acta (BBA) - Biomembranes*, 1859(4):537–549, 2017. ISSN 0005-2736. doi: https://doi.org/10.1016/j.bbamem.2016.09.025. URL https://www.sciencedirect.com/science/article/pii/S0005273616303273.

[241] N. Ohnishi, L. G. Zhang, and W. Sakamoto. Vipp1 involved in chloroplast membrane integrity has gtpase activity in vitro. *Plant Physiology*, 177(1):328–338, 2018. ISSN 0032-0889. doi: 10.1104/pp.18.00145. URL <GotoISI>://WOS:000431347500029.

[242] T. K. Gupta, S. Klumpe, K. Gries, S. Heinz, W. Wietrzynski, N. Ohnishi, J. Niemeyer, B. Spaniol, M. Schaffer, A. Rast, M. Ostermeier, M. Strauss, J. M. Plitzko, W. Baumeister, T. Rudack, W. Sakamoto, J. Nickelsen, J. M. Schuller, M. Schroda, and B. D. Engel. Structural basis for vipp1 oligomerization and maintenance of thylakoid membrane integrity. *Cell*, 184(14):3643–3659 e23, 2021. ISSN 1097-4172 (Electronic) 0092-8674 (Linking). doi: 10.1016/j.cell.2021.05.011. URL https://www.ncbi.nlm.nih.gov/pubmed/34166613.

[243] M. Saur, R. Hennig, P. Young, K. Rusitzka, N. Hellmann, J. Heidrich, N. Morgner, J. Markl, and D. Schneider. A janus-faced im30 ring involved in thylakoid membrane fusion is assembled from im30 tetramers. *Structure*, 25(9):1380–1390 e5, 2017. ISSN 1878-4186 (Electronic) 0969-2126 (Linking). doi: 10.1016/j.str.2017.07.001. URL https://www.ncbi.nlm.nih.gov/pubmed/28803692.

[244] Y. Gat, J. M. Schuller, M. Lingaraju, E. Weyher, F. Bonneau, M. Strauss, P. J. Murray, and E. Conti. Insp₆ binding to pikk kinases revealed by the cryo-em structure of an smg1-smg8-smg9 complex. *Nature Structural Molecular Biology*, 26(12):1089–+, 2019. ISSN 1545-9993. doi: 10.1038/s41594-019-0342-7. URL <GotoISI>://WOS:000501349100005.

[245] J. McCullough, A. K. Clippinger, N. Talledge, M. L. Skowyra, M. G. Saunders, T. V. Naismith, L. A. Colf, P. Afonine, C. Arthur, W. I. Sundquist, P. I. Hanson, and A. Frost. Structure and membrane remodeling activity of escrt-iii helical polymers. *Science*, 350(6267):1548–1551, 2015. ISSN 0036-8075. doi: 10.1126/science.aad8305. URL <GotoISI>://WOS:000366591100064.

[246] J. Salje, B. Zuber, and J. Löwe. Electron cryomicroscopy of e-coli reveals filament bundles involved in plasmid dna segregation. *Science*, 323 (5913):509–512, 2009. ISSN 0036-8075. doi: 10.1126/science.1164346. URL <GotoISI>://WOS:000262587900044.

[247] Nabil Bassim, Keana Scott, and Lucille A. Giannuzzi. Recent advances in focused ion beam technology and applications. *MRS Bulletin*, 39(4):317–325, 2014. ISSN 1938-1425. doi: 10.1557/mrs.2014.52. URL https://doi.org/10.1557/mrs.2014.52.

[248] Oda Helene Schiøtz, Christoph J.O. Kaiser, Sven Klumpe, Dustin R. Morado, Matthias Poege, Jonathan Schneider, Florian Beck, Christopher Thompson, and M. Jürgen Plitzko. Serial lift-out – sampling the molecular anatomy of whole organisms. *bioRxiv*, page 2023.04.28.538734, 2023. doi: 10.1101/2023.04.28.538734. URL https://www.biorxiv.org/content/biorxiv/early/2023/04/30/2023.04.28.538734.full.pdf.

[249] Sven Klumpe, Oda H. Schioetz, Christoph Kaiser, Marina Luchner, Johann Brenner, and Jürgen M. Plitzko. Developments in cryo-fib sample preparation: Targeting in cryo-lift-out preparation of tissues and machine learning models for fully automated on-grid lamella preparation. *Microscopy and Microanalysis*, 29(Supplement1):511–513, 2023. ISSN 1431-9276. doi: 10.1093/micmic/ozad067.243. URL https://doi.org/10.1093/micmic/ozad067.243.

[250] Zev Bryant, Lakshman Subrahmanyan, Michael Tworoger, Leah LaTray, Chun-Rong Liu, Meng-Jin Li, Ger van den Engh, and Hannele Ruohola-Baker. Characterization of differentially expressed genes in purified drosophila follicle cells: Toward a general strategy for cell type-specific developmental analysis. *Proceedings of the National Academy of Sciences*, 96(10):5559–5564, 1999. doi: doi:10.1073/pnas.96.10.5559. URL https://www.pnas.org/doi/abs/10.1073/pnas.96.10.5559.

[251] M. A. Phillips, M. Harkiolaki, D. M. S. Pinto, R. M. Parton, A. Palanca, M. Garcia-Moreno, I. Kounatidis, J. W. Sedat, D. I. Stuart, A. Castello, M. J. Booth, I. Davis, and I. M. Dobbie. Cryosim: super-resolution 3d structured illumination cryogenic fluorescence microscopy for correlated ultrastructural imaging. *Optica*, 7(7):802–812, 2020. ISSN 2334-2536. doi: 10.1364/optica.393203. URL <GotoISI>://WOS:000550690300002.

[252] Y. W. Chang, S. Y. Chen, E. I. Tocheva, A. Treuner-Lange, S. Loebach, L. Sogaard-Andersen, and G. J. Jensen. Correlated cryogenic photoactivated localization microscopy and cryo-electron tomography. *Nature Methods*, 11(7):737–U179, 2014. ISSN 1548-7091. doi: 10.1038/nmeth.2961. URL <GotoISI>://WOS:000338321400017.

[253] Arnold Giske. *CryoSTED microscopy-a new spectroscopic approach for improving the resolution of STED microscopy using low temperature*. Thesis, 2007.

[254] S. M. Vitale and J. D. Sugar. Using xe plasma fib for high-quality tem sample preparation. *Microsc Microanal*, pages 1–13, 2022. ISSN 1435-8115 (Electronic) 1431-9276 (Linking). doi: 10.1017/S1431927622000344. URL https://www.ncbi.nlm.nih.gov/pubmed/35289261.

[255] Casper Berger, Maud Dumoux, Thomas Glen, Neville B.-y. Yee, John M. Mitchels, Zuzana Patáková, James H Naismith, and Michael Grange. Plasma fib milling for the determination of structures in situ. *bioRxiv*, page 2022.08.01.502333, 2022. doi: 10.1101/2022.08.01.502333. URL https://www.biorxiv.org/content/biorxiv/early/2022/08/01/2022.08.01.502333.full.pdf.

[256] B. A. Lucas and N. Grigorieff. Quantification of gallium cryo-fib milling damage in biological lamellae. *Proc Natl Acad Sci U S A*, 120(23):e2301852120, 2023. ISSN 0027-8424 (Print) 0027-8424. doi: 10.1073/pnas.2301852120.

[257] Radostin Danev and Kuniaki Nagayama. Transmission electron microscopy with zernike phase plate. *Ultramicroscopy*, 88(4):243–252, 2001. ISSN 0304-3991. doi: https://doi.org/10.1016/S0304-3991(01)00088-2. URL https://www.sciencedirect.com/science/article/pii/S0304399101000882.

[258] R. Danev, B. Buijsse, M. Khoshouei, J. M. Plitzko, and W. Baumeister. Volta potential phase plate for in-focus phase contrast transmission electron microscopy. *Proceedings of the National Academy of Sciences of the United States of America*, 111(44):15635–15640, 2014. ISSN 0027-8424. doi: 10.1073/pnas.1418377111. URL <GotoISI>://WOS:000344088100022.

[259] B. Buijsse, P. Trompenaars, V. Altin, R. Danev, and R. M. Glaeser. Spectral dqe of the volta phase plate. *Ultramicroscopy*, 218, 2020. ISSN 0304-3991. doi: 10.1016/j.ultramic.2020.113079. URL <GotoISI>://WOS:000588015200005.

[260] C. Turnbaugh, J. J. Axelrod, S. L. Campbell, J. Y. Dioquino, P. N. Petrov, J. Remis, O. Schwartz, Z. L. Yu, Y. F. Cheng, R. M. Glaeser, and H. Mueller. High-power near-concentric fabry-perot cavity for phase contrast electron microscopy. *Review of Scientific Instruments*, 92(5), 2021. ISSN 0034-6748. doi: 10.1063/5.0045496. URL <GotoISI>://WOS:000692122200001.

[261] Ka Man Yip, Niels Fischer, Elham Paknia, Ashwin Chari, and Holger Stark. Atomic-resolution protein structure determination by cryo-em. *Nature*, 587 (7832):157–161, 2020. ISSN 1476-4687. doi: 10.1038/s41586-020-2833-4. URL https://doi.org/10.1038/s41586-020-2833-4.

[262] C. Shan Xu, Song Pang, Gleb Shtengel, Andreas Müller, Alex T. Ritter, Huxley K. Hoffman, Shin-ya Takemura, Zhiyuan Lu, H. Amalia Pasolli, Nirmala Iyer, Jeeyun Chung, Davis Bennett, Aubrey V. Weigel, Melanie Freeman, Schuyler B. van Engelenburg, Tobias C. Walther, Robert V. Farese, Jennifer Lippincott-Schwartz, Ira Mellman, Michele Solimena, and Harald F. Hess. An open-access volume electron microscopy atlas of whole cells and tissues. *Nature*, 599(7883):147–151, 2021. ISSN 1476-4687. doi: 10.1038/s41586-021-03992-4. URL https://doi.org/10.1038/s41586-021-03992-4.

[263] M. Allegretti, C. E. Zimmerli, V. Rantos, F. Wilfling, P. Ronchi, H. K. H. Fung, C. W. Lee, W. Hagen, B. Turonova, K. Karius, M. Bormel, X. Zhang, C. W. Muller, Y. Schwab, J. Mahamid, B. Pfander, J. Kosinski, and M. Beck. In-cell architecture of the nuclear pore and snapshots of its turnover. *Nature*, 586 (7831):796–800, 2020. ISSN 1476-4687 (Electronic) 0028-0836 (Linking). doi:

10.1038/s41586-020-2670-5. URL https://www.ncbi.nlm.nih.gov/pubmed/32879490.

[264] Christian E. Zimmerli, Matteo Allegretti, Vasileios Rantos, Sara K. Goetz, Agnieszka Obarska-Kosinska, Ievgeniia Zagoriy, Aliaksandr Halavatyi, Gerhard Hummer, Julia Mahamid, Jan Kosinski, and Martin Beck. Nuclear pores dilate and constrict in cellulo. *Science*, 374(6573):eabd9776, 2021. doi: doi:10.1126/science.abd9776. URL https://www.science.org/doi/abs/10.1126/science.abd9776.

[265] G. G. Maul. Ultrastructure of pore complexes of annulate lamellae. *J Cell Biol*, 46(3):604–10, 1970. ISSN 0021-9525 (Print) 0021-9525 (Linking). doi: 10.1083/jcb.46.3.604. URL https://www.ncbi.nlm.nih.gov/pubmed/4949849http://jcb.rupress.org/content/jcb/46/3/604.full.pdf.

[266] G. Tanifuji, N. T. Onodera, T. J. Wheeler, M. Dlutek, N. Donaher, and J. M. Archibald. Complete nucleomorph genome sequence of the nonphotosynthetic alga cryptomonas paramecium reveals a core nucleomorph gene set. *Genome Biol Evol*, 3:44–54, 2011. ISSN 1759-6653 (Electronic) 1759-6653 (Linking). doi: 10.1093/gbe/evq082. URL https://www.ncbi.nlm.nih.gov/pubmed/21147880https://www.ncbi.nlm.nih.gov/pmc/articles/PMC3017389/pdf/evq082.pdf.

[267] R. G. Kessel. Annulate lamellae: a last frontier in cellular organelles. *Int Rev Cytol*, 133:43–120, 1992. ISSN 0074-7696 (Print) 0074-7696 (Linking). URL https://www.ncbi.nlm.nih.gov/pubmed/1374369.

[268] B. Hampoelz, M. T. Mackmull, P. Machado, P. Ronchi, K. H. Bui, N. Schieber, R. Santarella-Mellwig, A. Necakov, A. Andres-Pons, J. M. Philippe, T. Lecuit, Y. Schwab, and M. Beck. Pre-assembled nuclear pores insert into the nuclear envelope during early development. *Cell*, 166(3):664–678, 2016. ISSN 1097-4172 (Electronic) 0092-8674 (Linking). doi: 10.1016/j.cell.2016.06.015. URL https://www.ncbi.nlm.nih.gov/pubmed/27397507.

[269] B. Hampoelz, A. Schwarz, P. Ronchi, H. Bragulat-Teixidor, C. Tischer, I. Gaspar, A. Ephrussi, Y. Schwab, and M. Beck. Nuclear pores assemble from nucleoporin condensates during oogenesis. *Cell*, 179(3):671–686 e17, 2019. ISSN 1097-4172 (Electronic) 0092-8674 (Linking). doi: 10.1016/j.cell.2019.09.022. URL https://doi.org/10.1016/j.cell.2019.09.022.

[270] P. Wendler and C. Enenkel. Nuclear transport of yeast proteasomes. *Front Mol Biosci*, 6:34, 2019. ISSN 2296-889X (Print) 2296-889x. doi: 10.3389/fmolb.2019.00034.

[271] B. Pacheco-Fiallos, M. K. Vorländer, D. Riabov-Bassat, L. Fin, F. J. O'Reilly, F. I. Ayala, U. Schellhaas, J. Rappsilber, and C. Plaschka. mrna recogni-

tion and packaging by the human transcription-export complex. *Nature*, 616 (7958):828–835, 2023. ISSN 0028-0836 (Print) 0028-0836. doi: 10.1038/s41586-023-05904-0.

[272] Oliver F. Harder, Sarah V. Barrass, Marcel Drabbels, and Ulrich J. Lorenz. Fast viral dynamics revealed by microsecond time-resolved cryo-em. *Nature Communications*, 14(1):5649, 2023. ISSN 2041-1723. doi: 10.1038/s41467-023-41444-x. URL https://doi.org/10.1038/s41467-023-41444-x.

[273] James C. V. Stacey, Aaron Tan, John M. Lu, Leo C. James, Robert A. Dick, and John A. G. Briggs. Two structural switches in hiv-1 capsid regulate capsid curvature and host factor binding. *Proceedings of the National Academy of Sciences*, 120(16):e2220557120, 2023. doi: doi:10.1073/pnas.2220557120. URL https://www.pnas.org/doi/abs/10.1073/pnas.2220557120.

[274] E. Pasyukova, S. Nuzhdin, W. Li, and A. J. Flavell. Germ line transposition of the copia retrotransposon in drosophila melanogaster is restricted to males by tissue-specific control of copia rna levels. *Mol Gen Genet*, 255(1): 115–24, 1997. ISSN 0026-8925 (Print) 0026-8925 (Linking). doi: 10.1007/s004380050479. URL https://www.ncbi.nlm.nih.gov/pubmed/9230904.

[275] Lisa R Girard, Tristan J Fiedler, Todd W Harris, Felicia Carvalho, Igor Antoshechkin, Michael Han, Paul W Sternberg, Lincoln D Stein, and Martin Chalfie. Wormbook: the online review of caenorhabditis elegans biology. *Nucleic acids research*, 35(suppl1):D472–D475, 2007. ISSN 1362-4962.

[276] Georg Hölzl and Peter Dörmann. Chloroplast lipids and their biosynthesis. *Annual Review of Plant Biology*, 70(1):51–81, 2019. doi: 10.1146/annurev-arplant-050718-100202. URL https://www.annualreviews.org/doi/abs/10.1146/annurev-arplant-050718-100202.

[277] Naskar Souvik, Merino Andrea, Espadas Javier, Singh Jayanti, Roux Aurelien, Colom Adai, and H. Low Harry. Mechanism for vipp1 spiral formation, ring biogenesis and membrane repair. *bioRxiv*, page 2023.09.26.559607, 2023. doi: 10.1101/2023.09.26.559607. URL http://biorxiv.org/content/early/2023/09/26/2023.09.26.559607.abstract.

[278] B. Junglas, R. Orru, A. Axt, C. Siebenaller, W. Steinchen, J. Heidrich, U. A. Hellmich, N. Hellmann, E. Wolf, S. A. L. Weber, and D. Schneider. Im30 idps form a membrane-protective carpet upon super-complex disassembly. *Communications Biology*, 3(1), 2020. doi: 10.1038/s42003-020-01314-4. URL <GotoISI>://WOS:000585235700003.

[279] Beata E. Mierzwa, Nicolas Chiaruttini, Lorena Redondo-Morata, Joachim Moser von Filseck, Julia König, Jorge Larios, Ina Poser, Thomas Müller-

Reichert, Simon Scheuring, Aurélien Roux, and Daniel W. Gerlich. Dynamic subunit turnover in escrt-iii assemblies is regulated by vps4 to mediate membrane remodelling during cytokinesis. *Nature Cell Biology*, 19(7):787–798, 2017. ISSN 1476-4679. doi: 10.1038/ncb3559. URL https://doi.org/10.1038/ncb3559.

[280] M. Schaffer, J. Mahamid, B. D. Engel, T. Laugks, W. Baumeister, and J. M. Plitzko. Optimized cryo-focused ion beam sample preparation aimed at in situ structural studies of membrane proteins. *J Struct Biol*, 197(2):73–82, 2017. ISSN 1095-8657 (Electronic) 1047-8477 (Linking). doi: 10.1016/j.jsb.2016.07.010. URL https://doi.org/10.1016/j.jsb.2016.07.010.

[281] L. Cassella and A. Ephrussi. Subcellular spatial transcriptomics identifies three mechanistically different classes of localizing rnas. *Nat Commun*, 13(1):6355, 2022. ISSN 2041-1723. doi: 10.1038/s41467-022-34004-2.

[282] D. Krueger, C. Pallares Cartes, T. Makaske, and S. De Renzis. h-spectrin is required for ratcheting apical pulsatile constrictions during tissue invagination. *EMBO Rep*, 21(8):e49858, 2020. ISSN 1469-221X (Print) 1469-221x. doi: 10.15252/embr.201949858.

[283] F. Mohn, G. Sienski, D. Handler, and J. Brennecke. The rhino-deadlock-cutoff complex licenses noncanonical transcription of dual-strand pirna clusters in drosophila. *Cell*, 157(6):1364–1379, 2014. ISSN 0092-8674. doi: 10.1016/j.cell.2014.04.031.

[284] K. A. Senti, D. Jurczak, R. Sachidanandam, and J. Brennecke. pirna-guided slicing of transposon transcripts enforces their transcriptional silencing via specifying the nuclear pirna repertoire. *Genes Dev*, 29(16):1747–62, 2015. ISSN 0890-9369 (Print) 0890-9369. doi: 10.1101/gad.267252.115.

[285] E. F. Pettersen, T. D. Goddard, C. R. C. Huang, E. E. C. Meng, G. S. Couch, T. I. Croll, J. H. Morris, and T. E. Ferrin. Ucsf chimerax: Structure visualization for researchers, educators, and developers. *Protein Science*, 30(1):70–82, 2021. ISSN 0961-8368. doi: 10.1002/pro.3943. URL <GotoISI>://WOS:000580702900001.

[286] James A. Maier, Carmenza Martinez, Koushik Kasavajhala, Lauren Wickstrom, Kevin E. Hauser, and Carlos Simmerling. ff14sb: Improving the accuracy of protein side chain and backbone parameters from ff99sb. *Journal of Chemical Theory and Computation*, 11(8):3696–3713, 2015. ISSN 1549-9618. doi: 10.1021/acs.jctc.5b00255. URL https://doi.org/10.1021/acs.jctc.5b00255.

[287] H. Nguyen, D. R. Roe, and C. Simmerling. Improved generalized born solvent model parameters for protein simulations. *J Chem Theory Comput*, 9(4):2020–2034, 2013. ISSN 1549-9618 (Print) 1549-9618. doi: $10.1021/\mathrm{ct3010485}$.

[288] Alberto Perez, Justin L. MacCallum, Emiliano Brini, Carlos Simmerling, and Ken A. Dill. Grid-based backbone correction to the ff12sb protein force field for implicit-solvent simulations. *Journal of Chemical Theory and Computation*, 11 (10):4770–4779, 2015. ISSN 1549-9618. doi: $10.1021/\mathrm{acs.jctc.5b00662}$. URL `https://doi.org/10.1021/acs.jctc.5b00662`.

List of Figures

List of Tables

10. Appendix

smFISH probes

Probeset	Probe sequences
copiaORF2kbse590 (total 41 probes)	atattacgtttagccttgtc
	gtacttctcgccatcaaacg
	gccctaattctaaatttcca
	tttaagcacatcttgctcgg
	cgttaggcattaaaccatca
	tttttccaggagtcatctac
	tacttttgcacaacgctct
	gtcgcttaggtactctatta
	gtcgcttgttgcgaaattta
	caagaatctgacgcgccgta
	gttcataaacggcgtccaaa
	agttgcgacgccaaactttt
	aagcaaacgttttcgcagcg
	atctcactcgatagcttcag
	agctgccaacaattcactta
	tccatctcttctatttttgc
	acgaaggcaatgtgatcagt
	cgctgtaataattccatcgt
	tttcacaaacgccaatgtca
	atttcttgatccagcaatct
	gtatcgttgtggtcattttt
	cgcgttcataactttcttgc
	gtgttattattgttgtgcac
	tggtttagttacccgatttt
	cacagtggtgacacttgact
	ctttttaatgtggccttct
	gttgcagtttgaacttgttt
	cataaacgcaatgccgtgtg
	gtccatcactgaagtattat
	aatcaaggacaaacccgcag
	ataagatggtcactagcacc
	ggtatacagcgactcatcat
	gcaatcttaagtggaggcac
	aataaattcgccttgcttgg
	gacaataccacgcttagtgg
	atctcatggtcattccgtag
	aaagagtacatcctccagtg
	aaattaccagcagcttcctt
	ttggagacgctttacggaca
	aattcgatcgacattcctgc
	cgaaatggttacaccgcttt
	ttttgacaaccattaaccca
	tgatcacaggtacattgttt
	cctctcatgccataaacgaa
	atttgccatcgcttatatgg
	ccatttaaacagggttcaca
	aaaaggaagtcttgcctgtt
	gggtcttatctttcaattgt

Key Resource Table

Reagent type (species) or resource	Designation	Source or reference	Identifiers	Additional information
Cell line(*Homo sapiens*)	HeLa Kyoto	Hyman Lab, MPI-CBG	RRID:CVCL_1922	
Cell line(*H. sapiens*)	Sum159	Walter and Farese Lab, Harvard T.H. Chan School of Public Health	RRID:CVCL_5423	
Strain, strain background (*Saccharomyces cerevisiae*)	Ede1-eGFP	Wilfling lab, MPI for Biophysics	FWY0153	MATα, his3-Δ200, leu2-3,2-112, lys2-801, trp1-1(am), ura3-52, yap1801Δ::kanMX4, yap1802Δ::hphNT1, apl3Δ::HIS3MX6, Ede1::EGFP::TRP1, atg15Δ::natNT2, atg19Δ::URA3
Strain, strain background (*Emiliania huxleyi*)	Eh1	Vardi Lab, Weizmann Institute of Science		Isolated in June 2018 at Espegrend, Norway
Strain, strain background (*Chlamydomonas reinhardtii*)	mat3-4	Chlamydomonas Resource Center, University of Minnesota, MN	CC-3994	
Strain, strain background (*C. reinhardtii*)	CW15	Chlamydomonas Resource Center, University of Minnesota, MN	CC-400	Reference cell-wall deficient WT strain of Chlamydomonas
Strain, strain background (*Chlamydomonas reinhardtii*)	UVM4	Neupert J et al. *Plant J.* (2009) 57: 1140-1150		
Strain, strain background (*Chlamydomonas reinhardtii*)	UVM4 – Vipp1-mCherry			
Strain, strain background (*Synechocystis* sp. PCC 6803)	*vipp1-F4E*	Rippka R. et al. *Microbiology* (1979) 111:1-61	-	
Strain, strain background (*Synechocystis* sp. PCC 6803)	*vipp1-V11E*	Gupta TK, Klumpe S et al. *Cell* (2021) 184(14): 3643-3659	-	
Strain, strain background (*Synechocystis* sp. PCC 6803)	*vipp1-GFP*	Bryan SJ et al. *Mol Microbiol.* (2014) 94:1179-1195	-	
Genetic reagent (*Drosophila melanogaster*)	sqh-mCherry	Bloomington Drosophila Stock Center	FlyBase ID: FBst0059024	FlyBase genotype: w*; P{sqh-mCherry.M}3
		Bloomington Drosophila Stock Center	FlyBase ID: FBst0059024)	w*; P{w[+ mC]=sqh-mCherry.M}3
Genetic reagent (*Drosophila melanogaster*)	UAS-Sec31::RFP	Bloomington Drosophila Stock Center	FlyBase ID: FBst0086533	w* P{UAS-Sec31.RFP}13.5; snaSco/CyO, P{ftz-lacB}E3
Genetic reagent (*Drosophila melanogaster*)	GFP::nup358	Hampoelz B et al. *Cell* (2019) 179(3):671-686	-	emGFP::nup358 PBac{y[+mDint2] = vas-Cas9}VK00027
Genetic reagent (*Drosophila melanogaster*)	Tj-gal4	Casella L & Ephrussi A *Nat. Comm.* (2022) 26;13(1):6355 Gift of Dr. Anne Ephrussi	-	;tj-Gal4/CyO;;
Genetic reagent (*Drosophila melanogaster*)	UASp-Sec13::EosFP	generated by Dr. JM Philippe and Dr. Bernhard Hampoelz, provided by BH	-	w* P{UASp-Sec13::EosFP}/ CyO ;)
Genetic reagent (*Drosophila melanogaster*)	GFP-Nup107	Bloomington Drosophila Stock Center	FlyBase ID: FBst0035514	w*; P{GFP-Nup107.K}9.1 (BL-35514)
Genetic reagent	LifeAct-GFP	Provided by Dr. Cristina Pallares Cartes	-	w*; P{w+, sqhp>LifeAct::mNeonGreen}; MKRS/TM6.

Reagent type (species) or resource	Designation	Source or reference	Identifiers	Additional information
(*Drosophila melanogaster*)				
Commercial assay or kit	ATPase assay kit	Expedeon, acquired by Abcam in Jan 2020	Cat# Expedeon: 601-0120 Abcam: ab270551	
Commercial assay or kit	GTPase assay kit	Expedeon, acquired by Abcam in Jan 2020	Cat# Expedeon: 602-0120 Abcam: ab270553	
Commercial assay or kit	QuikChange XL Site-Directed Mutagenesis Kit	Agilent Technologies	Cat# 200517	
Antibody	Copia Antibody`	Cusabio	CSB-PA366106XA01DLU	
Probes	smFISH	Stellaris	-	CAL Fluor Red 590-labeled probe sets, see probe table for sequence.
Other	BODIPY 558/568C12	Thermo Fisher Scientific	D3835	Lipid droplet live stain (1:2000)
Other	Mito Tracker Green(490/516)	Thermo Fisher Scientific	M7514	Mitochondria live stain (1:2000)
Other	Carboxylate-Modified Microspheres, 1.0 µm, crimson fluorescent (625/645)	Thermo Fisher scientific	F8816	Fluorescence bead fiducials for 3D correlation (1:30)
Software, algorithm	SerialFIB	https://github.com/sklumpe/SerialFIB (copy archived at swh:1:rev:0eaaaf66afa2d803440cea18af85c444df10478f, Klumpe, 2021)		This study
Software, algorithm	AutoScript4	Thermo Fisher Scientific		https://www.thermofisher.com/de/de/home/electron-microscopy/products/software-em-3d-vis/autoscript-4-software.html
Software, algorithm	LAS X	Leica Microsystems		https://www.leica-microsystems.com/products/microscope-software/p/leica-las-x-ls/
Software, algorithm	Fiji	https://imagej.net/software/fiji/		
Software, algorithm	3DCT	https://3dct.semper.space/index.html		
Software, algorithm	SerialEM	https://bio3d.colorado.edu/SerialEM/		
Software, algorithm	Warp	http://www.warpem.com/warp/		
Software, algorithm	TOMOMAN	https://github.com/williamnwan/TOMOMAN		
Software, algorithm	MotionCorr2	https://emcore.ucsf.edu/ucsf-software		
Software, algorithm	NovaCTF	Turoňová et al., 2017b		
Software, algorithm	CTFFIND4	https://grigoriefflab.umassmed.edu/ctffind4		
Software, algorithm	IMOD	https://bio3d.colorado.edu/imod		
Software, algorithm	pyTOM	https://pytom.sites.uu.nl/		
Software, algorithm	RELION	https://www3.mrc-lmb.cam.ac.uk/relion/index.php/Main_Page		
Software, algorithm	STOPGAP	Wan, 2020		
Software, algorithm	UCSF ChimeraX	https://www.rbvi.ucsf.edu/chimerax/		
Software, algorithm	nnU-Net	https://github.com/MIC-DKFZ/nnUNet		
Software, algorithm	ISOLDE	https://tristanic.github.io/isolde/		
Software, algorithm	Biopython	https://biopython.org/		
Software, algorithm	MDAnalysis	https://www.mdanalysis.org/		
Software, algorithm	GTPbinder	http://crdd.osdd.net/raghava/gtpbinder/		

Reagent type (species) or resource	Designation	Source or reference	Identifiers	Additional information
Software, algorithm	ATPint	http://crdd.osdd.net/raghava/atpint/		
Software, algorithm	AutoDock4	http://autodock.scripps.edu/		
Software, algorithm	TomoSegMemTV software package	https://sites.google.com/site/3demimageprocessing/tomosegmemtv		
Dataset	scRNAseq *D. melanogaster* ovary	Jevitt A et al. *PLoS Biology* (2020)	SRA ID: SRX7814226 GEO ID: GSE146040	